Site-Directed Spin Labeling of Large Riboswitches Using Click Chemistry

Dissertation

zur
Erlangung des Doktorgrades (Dr. rer. nat.)
der
Mathematisch-Naturwissenschaftlichen Fakultät
der
Rheinischen Friedrich-Wilhelms-Universität Bonn

vorgelegt von

Mark Kerzhner

aus

Winnyzja, Ukraine

Bonn 2018

Angefertigt mit Genehmigung der Mathematisch-Naturwissenschaftlichen Fakultät der
Rheinischen Friedrich-Wilhelms-Universität Bonn

1. Gutachter: Prof. Dr. Michael Famulok
2. Gutachter: Prof. Dr. Olav Schiemann
Tag der Promotion: 25.10.2018
Erscheinungsjahr: 2019

Parts of this thesis have been published in:

- Kerzhner, M.; Abdullin, D.; Więcek, J.; Matsuoka, H.; Hagelueken, G.; Famulok, M.; Schiemann, O., Post-synthetic Spin-Labeling of RNA through Click Chemistry for PELDOR Measurments, *Chem. Eur.J.* **2016**, *22*, 12113 –12121.
- Kerzhner, M.; Matsuoka, H.; Wuebben, C.; Famulok, M.; Schiemann, O., High-Yield Spin Labeling of Long RNAs for Electron Paramagnetic Resonance Spectroscopy, *Biochemistry,* **2018**, *57,* 2923–2931.

Danksagung

An erster Stelle möchte ich Herrn Prof. Dr. Michael Famulok danken, dass er mir die Chance ermöglicht hat, an diesem anspruchsvollen aber hochinteressanten Projekt zu arbeiten. Außerdem bin ich ihm sehr dankbar, dass er mir über die Jahre sein Vertrauen geschenkt hat.

Großer Dank gilt außerdem dem Kooperationspartner Herrn Prof. Dr. Olav Schiemann, ohne dessen Unterstützung die Umsetzung dieses Projektes nicht möglich gewesen wäre. Er und seine Arbeitsgruppe haben entscheidende Beiträge zu den erzielten Ergebnissen dieser Arbeit geleistet.

Allen Mitgliedern meiner Prüfungskommission danke ich für die Begutachtung dieser Dissertation.

Ich danke meinen Kooperationspartnern aus der Arbeitsgruppe von Herrn Prof. Dr. Olav Schiemann. Bei Dr. Dinar Abdullin, Dr. Hideto Matsuoka und Dr. Andreas Meyer bedanke ich mich herzlich für die zahlreichen PELDOR-Messungen sowie Hilfe bei verschiedenen Fragestellungen. Dr. Hideto Matsuoka, Christine Wübben und Jennifer Wiecek danke ich für die Durchführung der cw-EPR Messungen. Bei Dr. Gregor Hagelueken bedanke ich mich für eine Einführung in die von ihm freundlicherweise bereitgestellte Software MtsslWizard.

Den Mitarbeitern der Zentralanalytik danke ich für die gemessenen Massen- und NMR-Spektren.

Bei Dr. Stefanie Kath-Schorr sowie Dr. Seergazhi G. Srivatsan möchte ich mich ganz herzlich für die anregenden Diskussionen bedanken, die mir viele Denkanstöße lieferten.

Dr. Sven Freudenthal, Sandra Ullrich und Gabriele Alonso Rodriguez danke ich für die Unterstützung bei den organisatorischen Fragen.

Für das Korrekturlesen dieser Arbeit bedanke ich mich bei Dr. Dinar Abdullin, Dr. Daniel Matzner, Dr. Yury Lebedev, Dr. Alexandra Lisovskaya, Dr. Silvana Haßel, Franziska Pfeiffer und Shannon Smith.

Jeder erfolgreichen Arbeit ist eine gute Arbeitsatmosphäre vorausgesetzt. In diesem Zusammenhang möchte ich mich bei ausnahmslos allen Mitgliedern der Arbeitsgruppen Famulok, Mayer, Kath-Schorr und Schiemann bedanken.

Meinem Laborpartner und gutem Freund Daniel Matzner danke ich für das großartige Arbeitsklima und die gute Zusammenarbeit.

Laura Lledo Bryant, Ignazio Geraci, Dr. Daniel Matzner, Dr. Fabian Tolle, Sebastian Pilsl, Christian Renzl, Malte Rosenthal, Dr. Silvana Haßel, Dr. Laia Civit, Franziska Pfeiffer, Dr. Anna Schüller, Daniel Keppner, Dr. Julian Valero Moreno, Christof Domnick, Frank Eggert, Laura Eiden und Olga Plückthun danke ich für zahlreiche Freizeitaktivitäten außerhalb des Labors.

Für die finanzielle Unterstützung bedanke ich mich bei dem Sonderforschungsbereich 813 der Deutschen Forschungsgemeinschaft.

Zur guter Letzt gilt mein besonderer Dank meiner Mutter, ohne deren Hilfe diese Arbeit nicht möglich gewesen wäre und die mich all diese Jahre in Höhen und Tiefen unterstützt hat.

Abstract

Due to the conformational variability of riboswitches, their structural analysis is of a great importance. The most frequently used techniques to investigate dynamic processes within the riboswitches are NMR and FRET. EPR spectroscopy in combination with site-directed spin labeling has also been applied for elucidation of structural dynamics of riboswitches, but such studies are not very common. One of the underlying reasons for this is an absence of efficient and inexpensive spin-labeling approaches. The existing spin-labeling methods are quite tedious and time consuming. In addition, the majority of the known riboswitches exceed the size of synthetically accessible RNA. The currently known spin-labeling approaches for long RNAs have low yields and are therefore less attractive. Thus, alternative, more efficient methods for site-directed spin labeling of long riboswitches are required.

Using copper(I)-catalyzed azide-alkyne cycloaddition (click chemistry) and the spin label **dŲ**, two efficient spin labeling approaches for RNA were established.

In the first approach, the click reaction was performed on CPG solid support, on which protected RNA remained after solid phase synthesis. The performance of the **dŲ** label was benchmarked on a self-complementary RNA duplex with Electron-Electron Double Resonance (PELDOR). In addition, this approach was compared with another established method that employs the rigid spin label **Çm** for RNA labeling. The influence of both labels on RNA was analyzed using CD spectroscopy, thermal denaturation measurements, cw-EPR as well as PELDOR. The results obtained by PELDOR measurements demonstrated that both labels **dŲ** and **Çm** provide a set of orientation-selective time traces, yielding information about the inter-label distances and the relative orientations of the labels.

In the second approach, the click reaction was carried out in solution using fully deprotected RNA. In combination with enzymatic ligation, this method provides a highly efficient labeling of complex and long RNAs. Using this approach, aptamer domains of 34 nt long preQ1 riboswitch from *Fusobacterium nucleatum* as well as of 81 nt long TPP riboswitch from *E. coli* were spin labeled. Furthermore, the results presented in this work demonstrated that the conformational exchange within the aptamer domain of preQ1 riboswitch can be monitored using cw-EPR and PELDOR.

In addition, an efficient assembling strategy of the entire TPP riboswitch comprising only one ligation step was elaborated and implemented in this work. This strategy can be used for site-specific spin labeling of the stems P1, P2 and P3 in future studies of TPP riboswitch.

Zusammenfassung

Aufgrund einer großen Vielfalt an möglichen Konformationen von Riboschaltern ist ihre Strukturanalyse von großer Bedeutung. Die Konformationsänderungen sind dort größtenteils dynamischer Natur und werden somit hauptsächlich mit NMR- oder FRET-Spektroskopien analysiert. Da bekannte Spinmarkirungsmethoden kostspielig sowie zeitaufwändig sind, ist die Verwendung von EPR-Spektroskopie in Kombination mit Spinmarkierung deutlich weniger geläufig. Darüber hinaus können die meisten der bekannten Riboschaltern aufgrund Ihrer großen Länge nicht mittels Festphasensynthese hergestellt werden. Die derzeit bekannten Spinmarkierugsmethoden für lange RNA Moleküle sind aufgrund ihrer geringen Ausbeuten wenig effektiv. Um dieser Tatsache entgegen zu wirken sind alternative, effizientere Methoden zur Spinmarkierung langer Riboschalter nötig.

In dieser Arber wurden mithilfe der Kupfer (I) -katalysierten Azid-Alkin-Cycloaddition (Klick-Chemie) und des Spin-Labels **dŲ** zwei neue Spinmarkierungsansätze für RNA etabliert. Im ersten Ansatz wurde die Klick-Reaktion am CPG-Träger durchgeführt. Diese Methode wurde anschließend an einer selbstkomplementären RNA-Duplex mit Hilfe von *Electron-Electron Double Resonance* (PELDOR) verifiziert. Des Weiteren wurde dieser Ansatz mit einem schon etablierten Verfahren verglichen, in welchem das starre Spin-Label **Çm** für die RNA-Markierung verwendet wurde. Der Einfluss beider Spin-Labels auf die RNA wurde mittels CD-Spektroskopie, thermischen Denaturierungsmessungen, cw-EPR sowie PELDOR analysiert. Die PELDOR-Messungen ergaben sowohl für **dŲ** als auch für **Çm** Spin-Labels orientierungsselektive Zeitspuren, aus welchen Informationen über die Abstände und die relativen Orientierungen der Labels gewonnen werden konnten.

Im zweiten Ansatz wurde die Klick-Reaktion an vollständig entschützter RNA in Lösung durchgeführt. Diese Herangehensweise in Kombination mit enzymatischer Ligation lieferte eine hocheffiziente Markierungsmethode für komplexe und lange RNA Moleküle. Die Effizienz des zweiten Ansatzes wurde dann an Aptamerdomänen eines 34 nt langen preQ1 Riboschalters aus *Fusobacterium Nucleatum* sowie eines 81 nt langen TPP Riboschalters aus *E. coli* erfolgreich demonstriert. Außerdem zeigten die Ergebnisse dieser Arbeit, dass der Konformationsaustausch innerhalb der Aptamerdomäne des preQ1 Riboschalters mithilfe von cw-EPR sowie PELDOR nachverfolgt werden kann.

Zu guter Letzt wurde im Rahmen dieser Arbeit eine effiziente Assemblierungsstrategie des gesamten TPP Riboschalters in nur einem Ligationsschritt erarbeitet und implementiert. Diese Strategie kann nun für die Spinmarkierung der Stämme P1, P2 und P3 des TPP-Riboschalters verwendet werden.

Contents

1 Introduction

1.1 Structural aspects of RNA

The discovery of nucleic acids by the Swiss physician Friedrich Miescher in 1868.[1] contributed substantially to our present knowledge about the processes taking place within living organisms. Although both types of nucleic acids, deoxyribonucleic acid (DNA) and ribonucleic acid (RNA), belong to the same class of biomolecules, the functions that they perform in living cells are quite different. DNA is mainly a carrier of the genetic code,[2] whereas RNA can perform a large number of functions, e.g., catalysis of biological reactions, control of gene expression, sensing, and communicating responses to cellular signals. The different biological roles of DNA and RNA are interconnected with their structural differences, which are: 1) In contrast to 2′- deoxyribose of DNA, the sugar moiety of RNA is a ribose. 2) Instead of the nucleobase thymine, which is present in DNA, RNA contains uracil. Both bases share the same pyrimidine core except that uracil lacks the 5’ methyl group. 3) RNA is commonly found as a single strand, whereas DNA usually appears as a double helix. Nevertheless, RNA can also form a double helix e.g. in viruses.[3]. The double stranded regions are usually formed when a single stranded part of RNA folds back to form base-paired segments between two short fragments of complementary sequences. The helical structure of RNA is different from DNA. Compared to DNA, where the double helical structure typically has a B form[4], RNA possesses an A form of a double helix. The reason for that is an additional OH-group in RNA, which locks the ribose moiety into the C3′-endo conformation thereby preventing the formation of B form helices (Figure 1).[5]

The 2’-OH group of ribose sugar also provides an additional hydrogen bond, which results in a greater diversity of secondary structures that RNA can adopt. The most frequently found RNA structure is a hairpin (Figure 2a).[6] It is formed when two complementary strands of the same RNA sequence form a double helix, also called stem region, which ends in a loop consisting of unpaired nucleobases. As a key building block in RNA, it guides RNA folding and plays an essential role in many biologically active RNAs. For example, as a secondary structure element of messenger RNA (mRNA), it protects its structural stability.[7] Moreover, hairpins can serve as a recognition motive for RNA-binding proteins and also act as a substrate for enzymatic reactions.[8] A loop can be formed not only in a hairpin, but also in the middle of double-stranded RNA segments thereby forming a bulge loop (Figure 2b) or an internal loop (Figure 2c). A helical junction or a multi-branched loop can also occur when more than two double helices interact (Figure 2d).

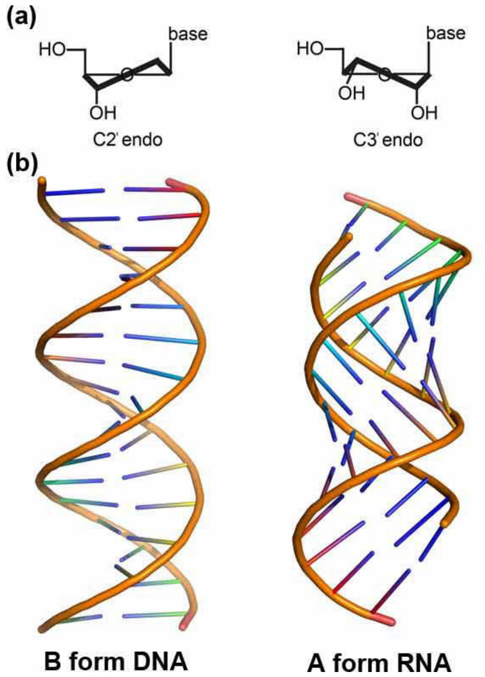

Figure 1: (a) Conformations of sugar moiety in B and A type duplexes. (b) Models of the B form DNA and A form RNA in comparison. Both structures were modelled using PyMOL molecular graphics system.

In salty solutions, RNA form various three dimensional structures, also termed as tertiary structures. Tertiary structures consist of combinations of interactions between secondary structure motifs e.g., the interactions between two helices, two unpaired regions or between an unpaired region and double-stranded helices. The type of interaction can range from weak van der Waals contacts to hydrogen bonds formed by Watson-Crick pairs. For example, in a so-called A-minor motif, adenines bind to the minor groove of neighboring helices through building Watson-Crick pairs to guanines and cytidines.[9]

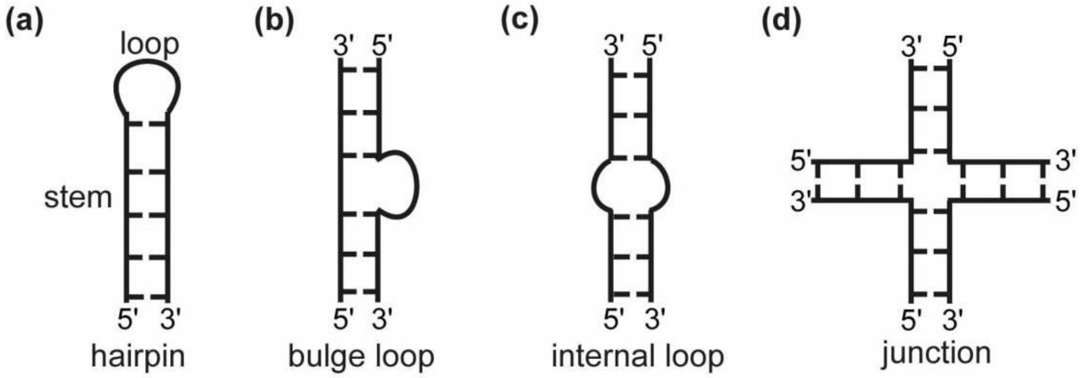

Figure 2: Example secondary structures that RNA molecules can adopt.

Another typical example of tertiary RNA motifs is a pseudoknot, which involves at least two helical elements connected by single stranded regions or a loop(s). First recognized in the turnip yellow mosaic virus,[10] pseudoknots have been shown to play a key role in many biologically active RNAs. For instance, pseudoknots compose the main structural element in the catalytic domain of human telomerase RNA[11-12]. Moreover, for many retroviruses pseudoknots have been shown to promote an efficient frameshifting, which retroviruses use to regulate retroviral gene expression.[13] The best-characterized pseudoknot is depicted schematically in Figure 3. It is formed by the base pairing between the loop and the single stranded region of the hairpin. These and other tertiary interactions define the biological functions of many regulatory RNAs. Thus, to gain a deeper understanding of their biological relevance, tertiary interactions are currently the subject of intense investigations, including methods such as e.g. Nuclear Magnetic Resonance (NMR), X-ray crystallography or Electron Paramagnetic Resonance (EPR).

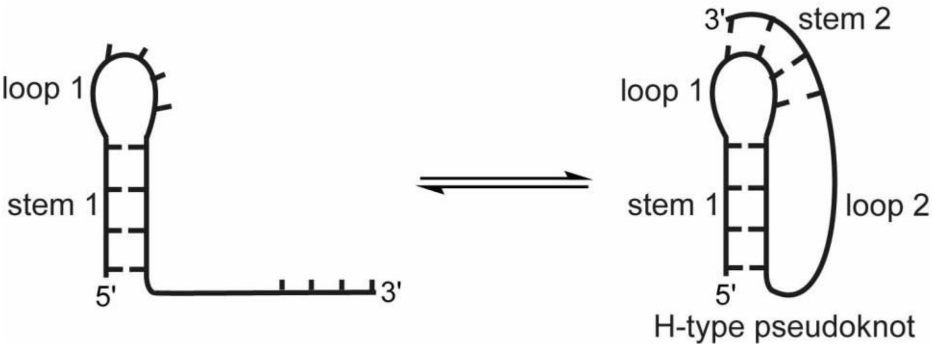

Figure 3: Pseudoknot formation between two non-contiguous complementary RNA sequences.

1.2 Regulatory RNA

It was believed for a long time that RNA only serves as information storage for protein synthesis. For this, RNA was divided into three main classes known as mRNA, transfer RNA (tRNA) and ribosomal RNA (rRNA). The pioneering studies which showed that RNA can perform other functions besides a carrier of information was conducted by Cech[14] and Altman[15] in 1982/83. They demonstrated the catalytic activity of RNA and called this type of RNA with the word “ribozymes”. Furthermore, they also showed that RNA catalysis takes place at the core of RNA splicing[16] and mRNA translation[17] demonstrating thereby the role of RNA as the platform of protein synthesis. However, no evidence was found about the regulatory role of RNA. The starting point of intense investigations on regulatory functions of RNA was the discovery of a small single-stranded non-coding RNA in nematode larvae (*Caenorhabditis elegans*), called microRNA (miRNA). miRNAs have been shown to act as inhibitors of translation processes by binding to the 3´UTRs of target mRNAs with imperfect complementarity.[18] Furthermore, upon the binding to mRNA, miRNAs can accelerate their degradation.[19] Another important example of short non-coding regulatory RNAs is small interfering RNA (siRNA).[20] In contrast to miRNA, siRNA is not endogenous and is transfected into the cells. In addition, it is double-stranded and usually binds to the 3' region of mRNAs by perfect base pairing. This leads to the degradation of the corresponding mRNA. In addition, regulatory functions were also found for long (>200 not) non-coding RNAs, called lncRNA.[21-22] the given examples demonstrate that the identification of various non-coding RNAs and the analysis of their functions are crucial for the understanding of many gene regulation processes.

1.3 Riboswitches

Regulatory RNAs have been also identified in bacteria.[23] They can be classified into two main categories depending on whether they consist of either *trans*-[24] or *cis*-acting RNA elements.[25-26] the former ones are called RNA regulators and the latter ones belong to riboswitches. The following text focuses on riboswitches only.

Riboswitches sense and respond to the level of a certain metabolite in the cell by controlling gene expression either at the transcriptional or translational level without the need of additional protein factors. They are usually located within the 5'-untranslated region of bacterial mRNAs. However, one class of riboswitches has also been identified in plants and fungi.[27-28]

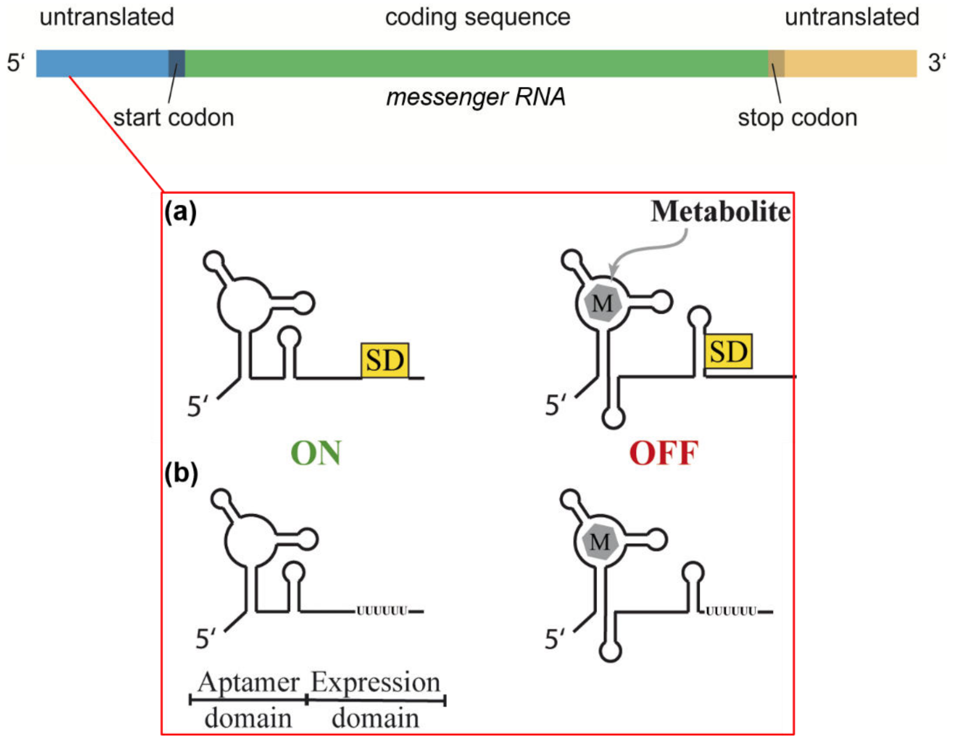

Figure 4: Schematic explanation of the mechanism of riboswitches using examples for an OFF switch.[29] (a) Inhibition of translation initiation by sequestering the Shine-Dalgarno sequence (SD) (b) Termination of transcription by forming a transcriptional terminator hairpin followed by a polyuridine sequence.

As shown in Figure 4, riboswitches are typically composed of two domains.[29] The domain that serves as a molecular sensor for high specific binding of the corresponding metabolite is called aptamer domain. It is highly conserved in sequence and its structure is independent of the bacteria it was identified in. It can vary in length from about 30 nt to around 200 nt.[23] The binding of a metabolite to the aptamer domain induces conformational changes within the second domain, called expression domain, which is adjoined directly downstream. In contrast to the aptamer domain, expression domains can differ in sequence, structure and size between bacterial species. Changes in the secondary structure within the aptamer domain result in a modulation of the expression of genes required for the synthesis or transport of the respective metabolite ligand. The switching from ON to OFF state occurs either through termination of transcription or by inhibition of translation initiation.[30] For the first, changes in the secondary structure of the expression domain lead to the formation of an intrinsic terminator hairpin, followed by several uridines in a row (Figure 4). Consequently, this terminator prevents transcriptional elongation. The inhibition of translation initiation occurs in a similar way, through sequestering the ribosome-binding site, also called Shine-Dalgarno sequence (Figure 4). This, in turn, prevents binding to the ribosome, thereby repressing the expression of the coding region of the mRNA. The mechanism of the riboswitches discussed above is given using examples for an OFF switch. Note that there are also riboswitches, which primarily activate gene expression in the presence of their cognate ligand. The working mechanism of some of the ON switches can be found in several articles.[31-33]

Riboswitches are quite widespread in bacteria. Since the first report by Winkler *et al.*[34] in 2002, about 40 different classes of riboswitches were found (Figure 5). Nevertheless, it is speculated that many thousands of riboswitch classes remain to be discovered.[35]

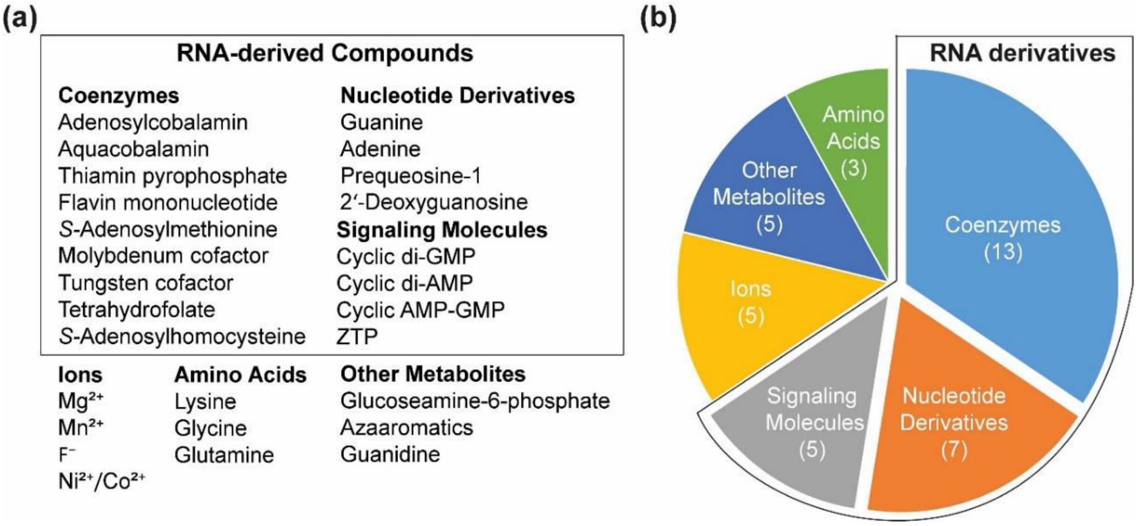

Figure 5: Metabolite ligands for identified riboswitch classes.[36](a) List of the ligands classified by ligand type. (b) Pie chart representation of the numbers of different riboswitch classes that bind the ligand type given in (a). Adapted from Ref.[36]

Riboswitches can respond to the different types of molecules including coenzymes, nucleotide derivatives, signaling molecules, amino acids, ions and other metabolites. The majority of the respective ligands are derived from RNA nucleotides or their precursors (Figure 5). For example, more than a dozen classes of riboswitches respond to nine nucleotide-like coenzymes, of which thiamine pyrophosphate,[34] adenosylcobalamin,[37] S-adenosylmethionine[38] and Flavin mononucleotide are the most frequent.[39] Interestingly, these coenzymes were present during the evolutionary phase, even before proteins appeared.[36, 40] Thus, the study of riboswitches and of RNA-mediated genetic control in general could enhance our understanding of the RNA role in the evolutionary process of living organisms. Moreover, their ability to discriminate between different cognate metabolites with extremely high specificity makes riboswitches a promising tool in the antibacterial drug discovery.[40] Therefore, investigation of riboswitches is of a great interest. One of the important aspects in studying the mechanism and functions of riboswitches is their structural analysis. Due to the great conformational variability of riboswitches, the structural analysis remains to be a rather difficult task. X-ray crystallography and NMR spectroscopy are the most commonly used techniques for this goal. Both provide high-resolution structures of RNA molecules. However, the structural rearrangements of riboswitches usually occur in a highly dynamic fashion, which makes the crystallization of RNA very difficult. Moreover, due to conformational heterogeneity of riboswitches, the obtained crystal structures do not always correspond to the biologically-active conformations of riboswitches.[41] In contrast, NMR spectroscopy can be carried out in solution under biologically relevant conditions. However, it becomes very problematic to use NMR spectroscopy when the size of RNA exceeds 50 kDa, which is the case for the majority of the identified riboswitches.[42]

Due to these limitations, complementary methods for the structural analysis are required. Alternative approaches, which are often used for RNAs in structural biology, include Fluorescence Resonance Energy Transfer (FRET)[43] and EPR spectroscopies.[44] Similar to NMR, both methods can be used to gain information about the structure and dynamics of RNA under biologically relevant conditions. The advantages of these methods as compared to NMR spectroscopy are that they enable the determination of long-range distances and, thus, follow some conformational changes and that considerably smaller amounts of the sample are required.

1.4 Site-directed spin-labeling of RNA

The main requirement for EPR analysis is the presence of paramagnetic centers in the molecule studied. Since most RNAs are diamagnetic, an incorporation of paramagnetic centers into their structures is then needed. One possible approach to introduce paramagnetic species into RNA is to replace its diamagnetic metal co-factors, such as Mg^{2+}, by paramagnetic ions. For example, Mn^{2+} possesses similar ion properties and, therefore, it is quite often used as a substituent for Mg^{2+} to study metal-ion binding sites of RNA.[45-46] However, the most commonly used approach is to incorporate small organic radicals, also called spin labels, into the RNA structure. The spin labels have to fulfill several requirements. First, they have to be stable under biologically relevant conditions. In the last decades, aminoxyl nitroxide prevailed over other paramagnetic species (Figure 6). Their stability is pointed out by four methyl groups and the unpaired electron that is delocalized over nitrogen and oxygen atoms.

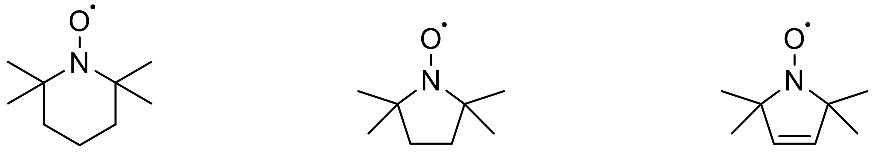

piperidine-based radical pyrrolidine-based radical pyrroline-based radical

Figure 6: Examples of aminoxyl nitroxides

Second, the flexibility of the linker, which bridges the paramagnetic center with the RNA molecule, is of high importance for spectroscopic studies. For example, an EPR spectrum of a spin label that contains a very long flexible linker will partially reflect the dynamics of the linker rather than the dynamics of an RNA to which this spin label is attached. In contrast, using a short, rigid linker for EPR measurements enables exploring the local dynamics of a RNA at the spin-labeled site. In addition, the obtained EPR-measured distances between two short, rigid spin labels can be easier translated into the structural constraints between two RNA sites as compared to the case of two long, flexible spin labels. On the other hand, rigid spin labels may cause local perturbation of the RNA structure at the labeling sites. Another important criterion is the ability of a spin label to be site-specifically attached to a certain position of RNA. Randomly introduced spin labels will not allow selective analysis of RNA dynamics. There are three main approaches to incorporate spin labels into RNA, including spin-labeling during the synthesis of RNA using phosphoramidite chemistry, post-synthetic spin-labeling at the pre-functionalized sites of RNA, and spin-labeling using non-covalent spin labels. These approaches will be discussed in the following in more detail.

It should be noted that even small modifications could crucially affect the biological activity of RNA. Therefore, it is always very important to verify the functionality of RNA upon spin-labeling. In the case of riboswitches, it is their affinity for the cognate metabolites, which has to be persisted upon the spin-labeling procedure. There are several biophysical techniques, such as e.g. microscale thermophoresis (MST)[47] and isothermal titration calorimetry (ITC), which are commonly used for binding studies of riboswitches.[48] Alternatively, thermal denaturation experiments[49] and circular dichroism (CD) spectroscopy[50] can be applied to study whether the attached spin labels influence the stability as well as the secondary structure of RNA.

1.4.1 Phosphoramidite approach

Introduction of spin labels into RNA using phosphoramidite chemistry is one of the most frequently used approaches. This approach requires a synthesis of spin-labeled building blocks, also called phosphoramidites, which are then incorporated stepwise into RNA at pre-determined positions using automated RNA solid phase synthesis.[51] The reactive groups of phosphoramidites have to be protected prior to RNA synthesis. There are several approaches to protect 2'-OH groups of RNA. One of the most commonly used methods makes use of *tert*-butyldimethylsilyl (TBDMS) protecting group.[52] Figure 7 shows a typical synthesis cycle of unmodified RNA using TBDMS chemistry. Here, 5'-OH group is protected by dimethoxytrityl ether, and exocyclic amino groups of nucleobases are protected with benzoyl (for adenine), acetyl (for cytidine) and isobutyryl (for guanine).[53] The synthesis of RNA proceeds in the 3' to 5' direction, starting with a single nucleotide coupled to a solid support (usually using controlled pore glass).

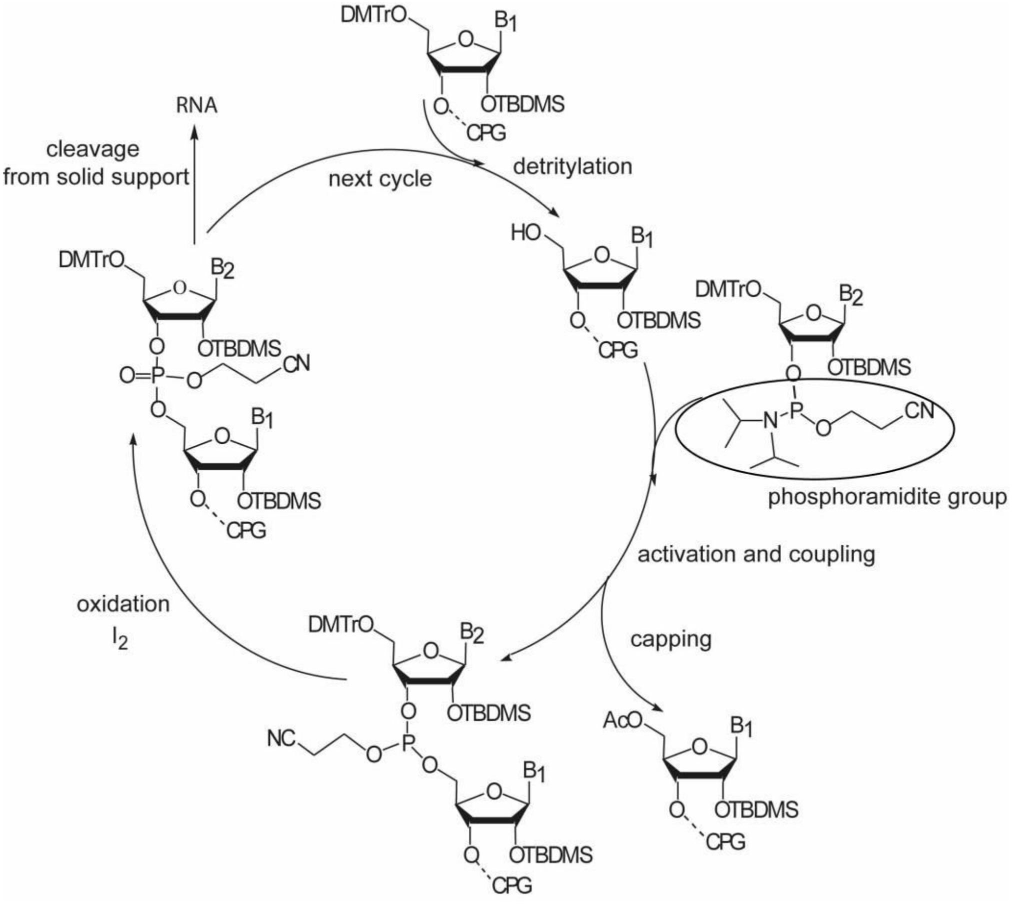

Figure 7: The phosphoramidite RNA synthesis cycle.

One synthesis cycle consists of four steps, which includes detritylation of the first nucleotide, activation and coupling to the phosphoramidite building block, capping of the unreacted 5′-hydroxyl groups and oxidation of P(III) to P(V). The synthesis is stopped once the desired length of RNA is achieved. The RNA is then deprotected and cleaved from the solid support using concentrated ammonia solution. TBDMS protecting group can be easily removed using a fluoride-containing reagent, such as e.g. tetra-n-butyl ammonium fluoride.

Considering the spin-labeled phosphoramidites, it should be ensured that the reaction conditions, which are applied during the solid-phase synthesis, are compatible with the spin label. For example, iodine solution that is commonly used in the oxidation step is a potential reducing agent for spin labels. Trichloroacetic acid used in the detritylation step can lead to disproportionation of the nitroxide. To circumvent this, *tert*-butyl hydroperoxide (TBHP) is used as an alternative oxidant, whereas less acidic dichloroacetic acid can be applied instead of trichloroacetic acid.[54] The most-commonly chosen target of the spin-labeling is nucleobases, in particular the 5th position. The advantage of this position is that it can be easily halogenated and subsequently functionalized by means of a transition-metal-catalyzed coupling reaction, thereby forming a carbon-carbon bond. Originally, the phosphoramidite approach was used for site-specific spin-labeling of DNA. For this purpose, Hopkins and co-workers synthesized spin-labeled phosphoramidite **1** using the palladium-catalyzed Sonogashira cross-coupling reaction of 5-iodouridine with 2,2,5,5-tetramethylpyrrolin-1-yloxy-3-acetylene (TPA) (Figure 8).[55] Spin-labeling by means of the Sonogashira coupling was later adopted to RNA **2**, where the Sonogashira reaction was carried out on the column during the RNA solid phase synthesis.[56] Although this approach does not imply the synthesis of the spin-labeled phosphoramidite, the TPA spin label attached to RNA was further exposed to the chemicals used in the following steps of the RNA synthesis. The same strategy was also applied to RNA **3** and RNA **4,** respectively.[56] However, the conversion of the starting material in this approach is not quantitative, which entails a tedious separation of the spin-labeled RNA from its iodo-modified derivative.

The advantages of TPA label, which is attached to RNA through the Sonogashira approach, are a fairly small size and reduced flexibility, which is preferable for PELDOR spectroscopy. This label is called semi-rigid because only one single bond of its structure can be rotated. Furthermore, several spin labels with fully rigid linkers are known in the literature.[57-58] A prominent example of such labels is the spin label **5**, also called **Çm**.[59]The rigidity in this spin label is caused by the fusion of nitroxide-bearing isoindolin with cytidine. The greatest advantage of this label is that, besides the distance measurements, it can also be used for determination of angular orientation between the labels attached to the same nucleic acid, which allows e.g. the determination of DNA dynamics.[60-61] However, the synthesis of **Çm** is quite laborious and time consuming since it consists of 16 steps.

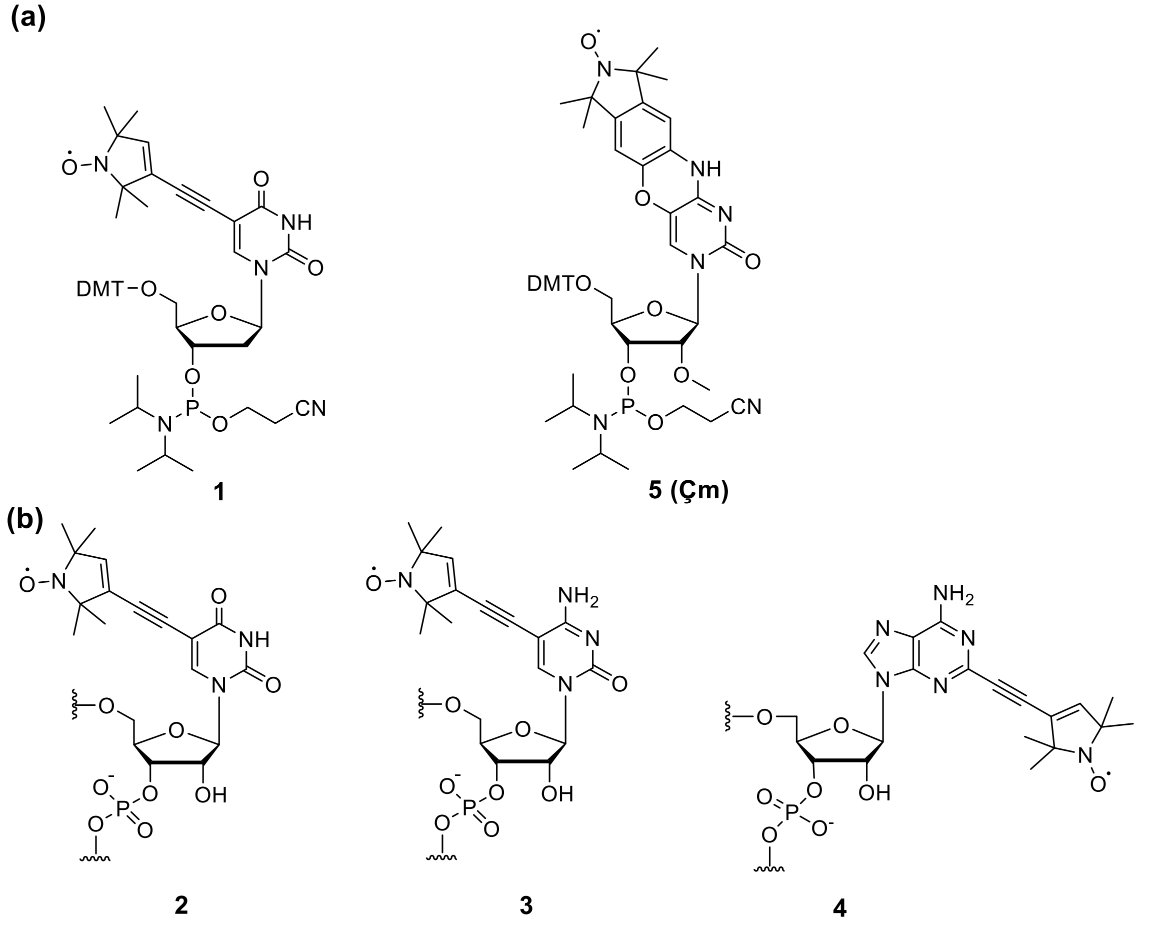

Figure 8: (a) Examples of spin-labeled phosphoramidites, which have been incorporated into nucleic acids using phosphoramidite approach. (b) Nucleotides spin-labeled during RNA solid phase synthesis using on-column Sonogashira reaction.[56]

1.4.2 Post-synthetic approach

The fundamental difference between the phoshporamidite and post-synthetic approaches is that in the latter one spin labels are introduced after the synthesis of RNA at pre-functionalized sites. Due to this fact, the spin labels are not exposed to potentially reducing conditions during the RNA synthesis. Various publications highlighted post-synthetic spin-labeling as the most frequently used approach for RNA. However, particular attention should be paid to the selection of functional groups to be incorporated prior to the labeling, since they have to be more reactive than other functionalities in RNA, such as exocyclic amines of nucleobases or oxygen atoms of phosphodiesters. There is a great number of spin-labeling reagents currently applied in the post-synthetic spin-labeling of RNA, some of which are depicted in Figure 9. One of the first examples of such reagents is compound **6**. Although post-synthetic labeling implies the incorporation of spin labels after RNA synthesis, the spin-labeling reagent **6** was initially applied to several tRNAs from *E. coli*, which naturally contained 4-thiouridines, yielding the spin-labeled nucleotide **10** (Figure 10).[62]

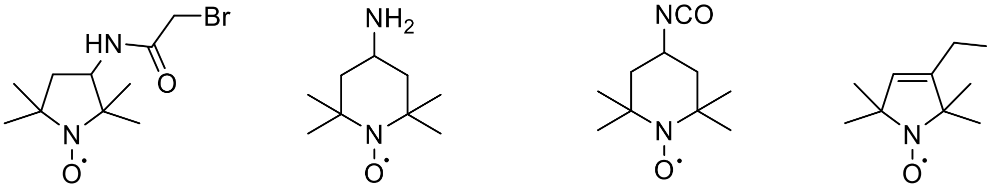

6 **7** **8** **9**

Figure 9: Examples of spin-labeling reagents.

This approach became very widespread for post-synthetic site-specific spin-labeling of RNA, when the chemical synthesis of 4-thiouridine containing RNA was established. However, instead of spin-labeling reagent **6,** its commercially available iodo-derivative is widely used.[63] When using this approach it should be taken into account that the introduced spin label may lead to local structural perturbation in RNA due to the hindrance of hydrogen bonding. Moreover, the linker of the spin label is fairly flexible, which complicates the interpretation of measured inter-label distance distributions in terms of RNA structure. Alternatively, the exocyclic amino groups of nucleobases can also be spin-labeled. Höbartner and co-workers used a convertible nucleoside approach of Verdine[64] to spin label exocyclic amino groups of RNA **11**.[65] This method involves a nucleophilic substitution reaction between an amine functionalized spin label, such as reagent **7,** and the nucleobase that bears a leaving group in place of exocyclic amine. Although this method was shown to preserve the base pairing capability of the amino function, it requires multi-step synthesis of the corresponding phosphoramidites.

Besides the nucleobase of RNA, the sugar moiety and phosphate backbone are also attractive target sites for spin-labeling. In the case of the sugar moiety, all known approaches are associated with the 2' position, which is usually functionalized with an amine moiety. Compared to the exocyclic amines, primary amine is more reactive, which enables spin-labeling at selected positions of RNA.

An efficient way to take advantage of the higher reactivity of the 2' amino group was shown by Sigurdsson and co-workers. They used the 2' amino-modified RNA and 4-isocyanato-TEMPO reagent **8** to obtain RNA **12**.[66] The advantage of the method is that both, amino modified RNA and reagent **8**, are commercially available. However, isocyanates are quite reactive and unstable toward hydrolysis, which impedes the handling of this reagent. Moreover, spin-labeling of long RNAs was shown to be incomplete.

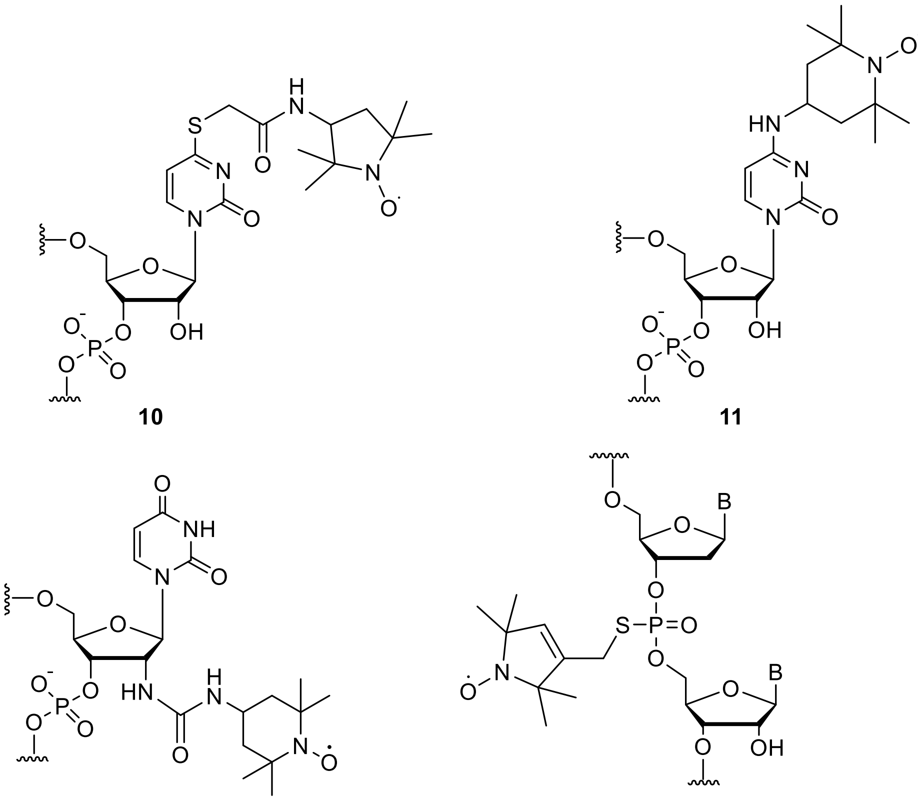

10 **11** **12** **13**

Figure 10: Examples of post-synthetic spin-labeling of nucleobase, sugar moiety and phosphate backbone of RNA.

Spin-labeling of phosphate back bone of RNA was introduced by Qin and co-workers.[67] They treated the thioate modified phosphate backbone of RNA with spin label reagent **9** furnishing RNA **13**. The incorporation of sulfur was achieved by using sulfurizing agent instead of oxidizing reagent in the oxidation step during solid phase synthesis of RNA. Compared to the labeling of nucleobase or sugar, this method has an advantage that the incorporated spin label is placed at the edge of RNA diminishing its influence on duplex formation. However, there are also several blemishes: 1) the negative charge of phosphodiester disappears upon spin-labeling, which may have some influence on the intra- or intermolecular electrostatic interactions of RNA; 2) the target nucleotide for spin-labeling cannot contain the 2' hydroxy group due to the potential intramolecular trans-esterification, which in turn can lead to the strand cleavage: 3) due to the diastereotopic nature of sulfur, a mixture of S_p and R_p diastereomers is formed which are not straightforward to separate.

1.4.3 Non-covalent spin-labeling

Both phosphoramidite and post-synthetic approaches imply covalent attachment of spin labels to RNA. However, it is also possible to attach spin labels to RNA based on van der Waals and hydrogen bonding interactions. This approach refers to the non-covalent spin-labeling. The common example of non-covalent spin-labeling is introduction of abasic sites into a RNA duplex. Spin labels bind to such sites non-covalently.

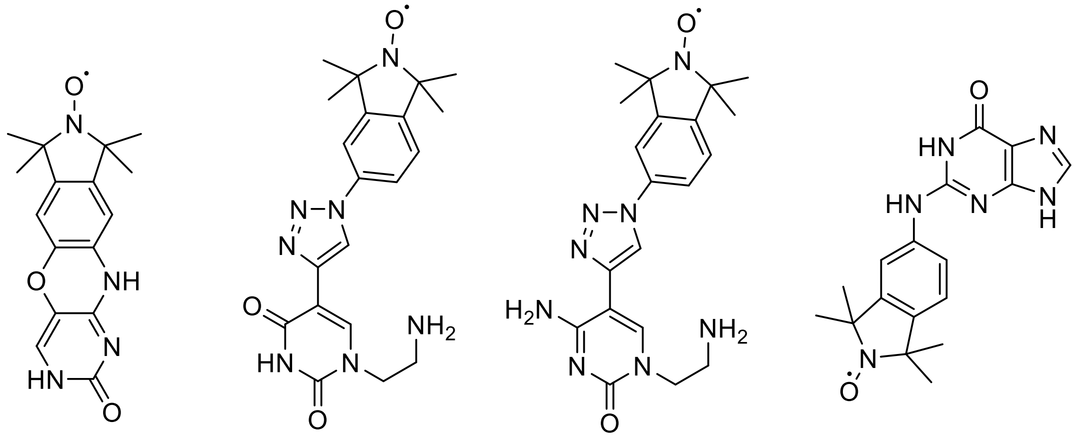

14 **15** **16** **17**

Figure 11: Examples of non-covalent spin labels used to label abasic sites of RNA duplexes.

The compound **14** was used for the non-covalent spin-labeling of DNA (Figure 11).[68] This spin label is structurally similar to the label **Çm**. However, due to its low solubility in aqueous solutions, only 30% was found to bind to the abasic site of the RNA duplex.[69] In contrast, the triazol-linked spin labels **15** and **16** have been shown to nearly completely bind to abasic sites.[70] Nonetheless, the same labels revealed some affinity to unmodified RNAs indicating an extensive non-specific binding. The best results so far have been achieved using spin label **17** that was shown to bind to the abasic site of RNA with high affinity and specificity.[69]

However, the disadvantage of the non-covalent spin-labeling approach is that it requires the presence of a double strand. Due to this fact, it cannot be applied to studies of single stranded RNAs.

1.5 Spin-labeling of long RNA

The majority of the biologically relevant RNAs, such as e.g. riboswitches, exceed the size of RNA that is accessible by solid phase RNA synthesis (approx. 50 nucleotides). Spin-labeling of long RNAs is, however, of particular interest and the development of efficient spin-labeling methods is therefore of great importance. The most frequently used approaches that were proposed in the literature imply the use of enzymes. Enzymatic ligation of two or more RNA fragments using T4 DNA or T4 RNA ligases is one of such methods. Both ligases are adenosine triphosphate (ATP)-dependent enzymes and catalyze the formation of phosphodiester linkage between acceptor RNA with a free 3'-hydroxy group and a donor RNA bearing a 5' monophosphate group. The essential difference between both ligases is that T4 RNA ligase prefers a single stranded RNA, whereas T4 DNA ligase recognizes a double stranded template, which is formed by addition of a splint oligonucleotide (Figure 12).

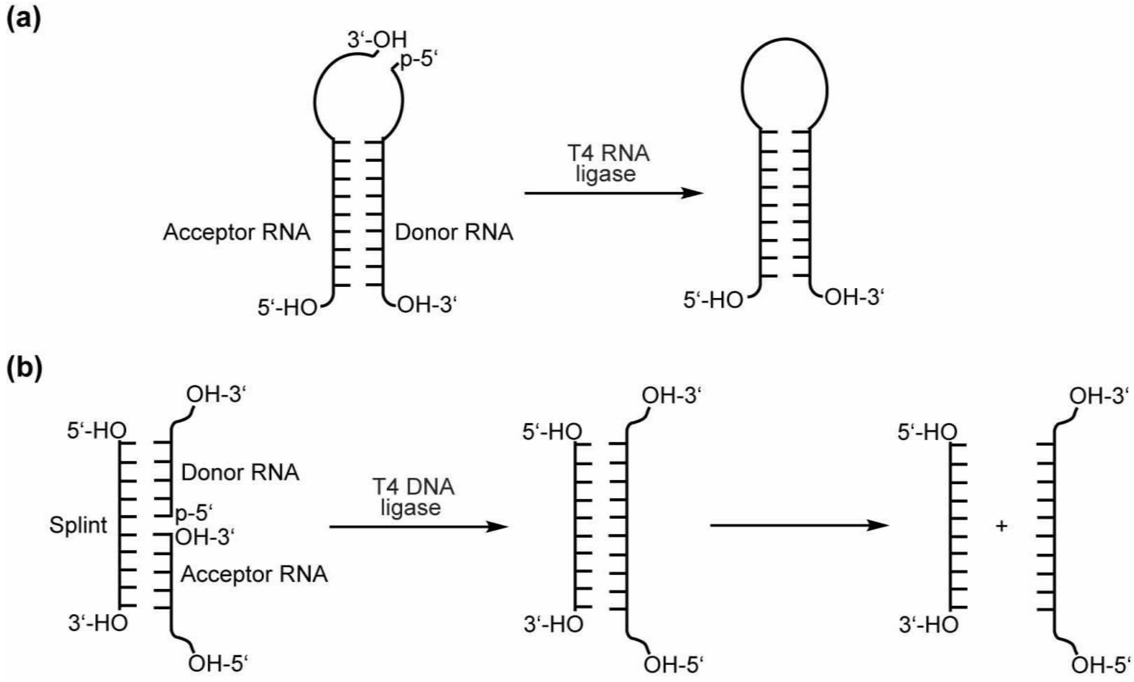

Figure 12: Enzymatic ligation of RNA[71]. Schematic representation of ligation using (a) T4 RNA ligase and (b) T4 DNA ligase.

In the case of T4 RNA ligation, the 5' phosphate group has always to be accessible to the enzyme and as close as possible to the 3' end of acceptor RNA.[72] This is the reason why the ligation of helical regions of RNA is commonly carried out using T4 RNA ligase.

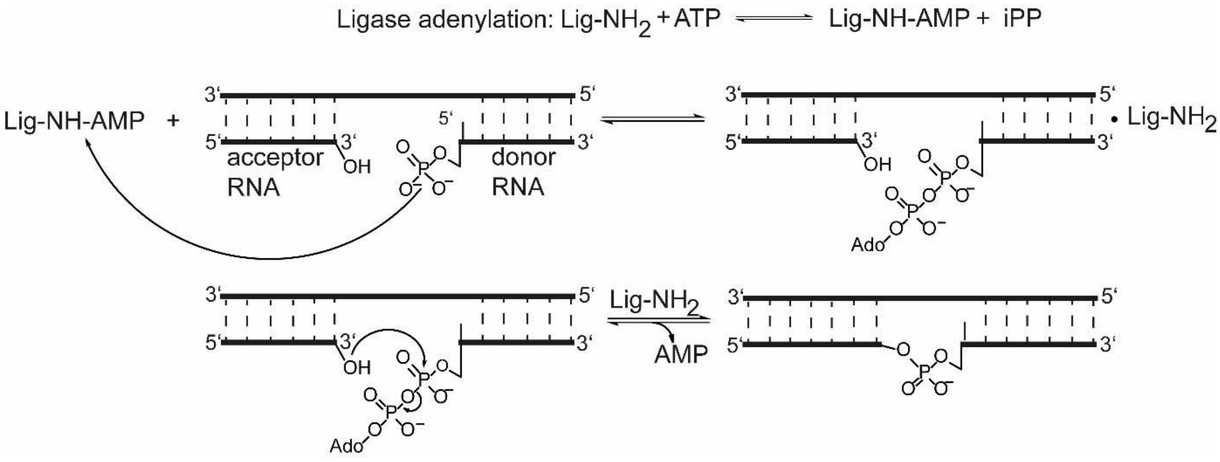

Figure 13: Schematic representation of the reaction mechanism of T4 DNA ligase.

Figure 13 schematically explains the mechanism of the ligation reaction of two RNA strands using the example of T4 DNA ligase. The first step is adenylation of the ligase by ATP. Next, the ligase transfers and adds adenosine monophosphate to the 5' phosphate group of donor RNA. In the final step, a nucleophilic attack of 3'-hydroxy group on the alpha positioned phosphate group takes place resulting in the formation of a covalent bond between the two and the release of AMP. This ligation reaction was often used in literature. For example, Duss *et al.* assembled a 70-kDa protein-RNA complex by spin-labeling two 4-thiouridine modified RNA fragments using 3-(2-iodoacetamido)-PROXYL spin label (IAP) and ligated them to each other by T4 DNA ligase (ligation efficiency of 20-40%).[73] To prevent the reduction of the spin labels they used the ligase without mild reducing agent dithiothreitol (DTT) in the buffer.

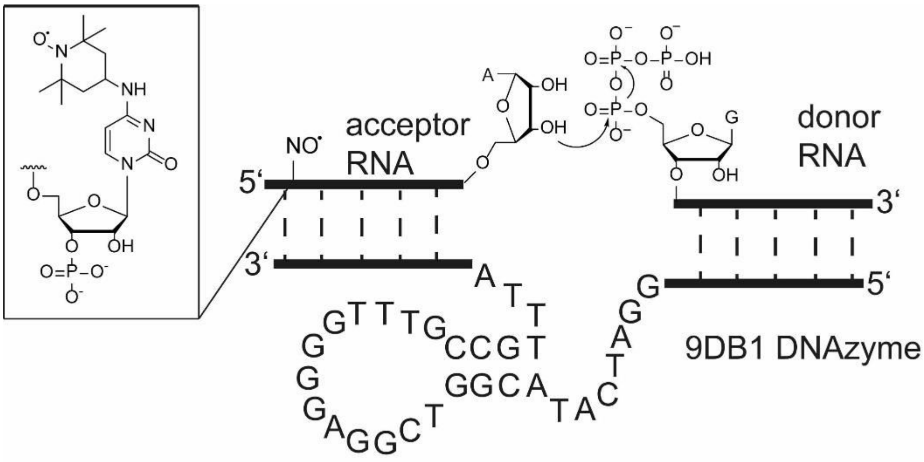

Figure 14: Schematic representation of RNA ligation using 9DB1 DNAzyme.[74] Acceptor strand is labeled by the convertible nucleoside approach.[64]

An alternative way to connect two RNA strands is application of DNAzymes. Höbartner and co-workers used 9DB1 DNAzyme to assemble spin-labeled 118 nt long SAM-I riboswitch.[74]

They labeled the short RNA fragment using the convertible nucleoside approach described above and subsequently ligated it to a long *in vitro* transcribed RNA strand. The working principle of 9DB1 DNAzyme is demonstrated in Figure 14. First, the DNAzyme hybridizes both RNA fragments at their 5' and 3' ends. As in the case of enzymatic ligation, the 3' end of the acceptor RNA bears a hydroxyl group, but the 5' end of the donor RNA holds a triphosphate moiety. Together with the divalent metal ion cofactors, 9DB1 DNAzyme initiates the nucleophilic attack of the 3'-OH group on the 5'-triphosphate resulting in the release of the pyrophosphate group and the formation of a phosphodiester linkage. There are also some sequence related selection rules for the use of 9DB1 DNAzyme, namely: C cannot be at the 3' terminus of the acceptor RNA, and the transcription of the donor RNA should begin with 5'-GA or 5'-AA.[75] Despite the sequence requirements to the ends of RNA sites, the reported yield of the spin-labeled SAM-I riboswitch was only 30%. Moreover, only one spin label has been incorporated so far using this approach and no distance determinations have been reported yet.

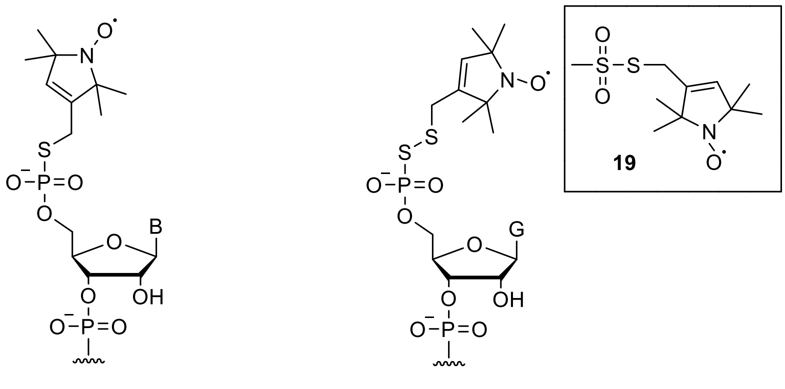

18 **20**

Figure 15: Examples of spin-labeling **5**'-end of RNA.

There are also several publications, which reported on spin-labeling of long RNA using enzymes without the need to link two or more RNA fragments. For example, Qin and co-workers applied T4 polynucleotide kinase to introduce phosphorthioate group at the 5'-end of RNA, which was subsequently treated with the reagent **9** to yield RNA **18** (Figure 15). Alternatively, Shin and co-workers introduced guanosine monophosphorthioate (GMPS) at the 5'-end of RNA using the T7 *in vitro* transcription. The resulting phoshorthioate-labeled RNA was then threated with the reagent **19** to furnish spin-labeled RNA **20**. However, both approaches are restricted to the 5' end of RNA and cannot be used for internal labeling.

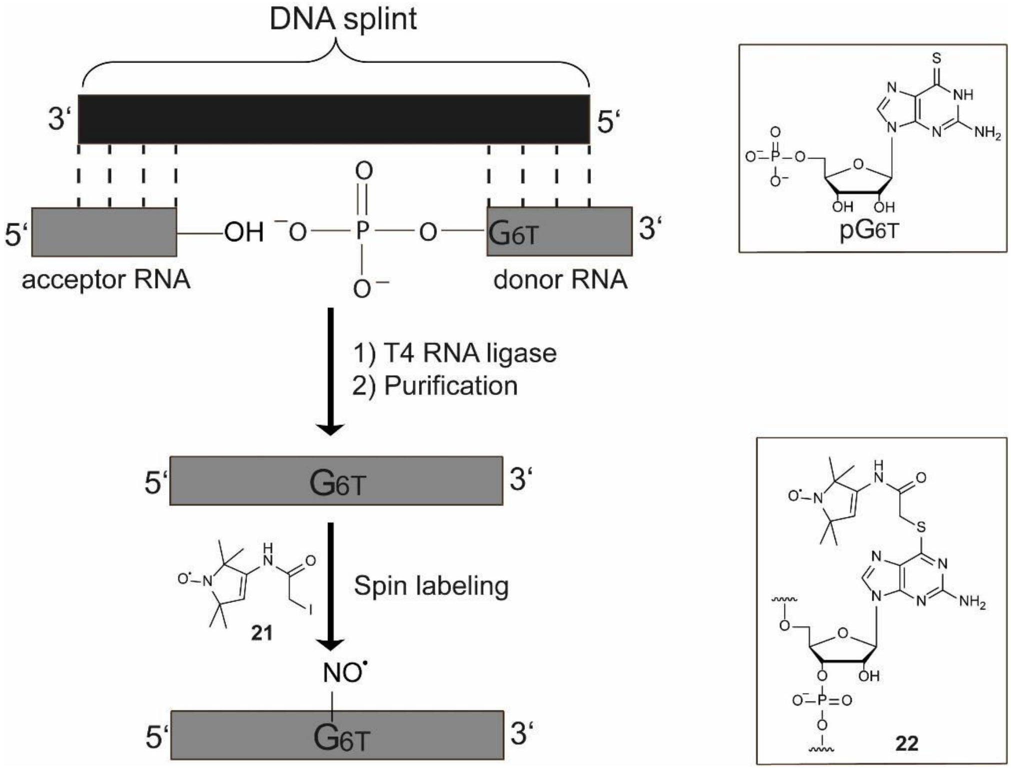

Figure 16: Schematic representation of site-specific spin-labeling of RNA using thioguanosine-5'-O-monophosphate (pG6T).

Another approach, which was reported recently, implies a combination of *in vitro* incorporation of pre-functionalized monophosphate nucleotide with enzymatic ligation and subsequent spin-labeling (Figure 16).[76]

Thioguanosine-5'-O-monophosphate (pG6T) was introduced at the 5'-end of RNA, as described above for guanosine monophosphorthioate, using T7 *in vitro* transcription. In the next step, the transcribed thio-modified RNA fragment was ligated to another RNA strand using a T4 RNA ligase and complementary DNA splint. The resulting thio-modified full-length RNA was subsequently spin-labeled by 3-(2-iodoacetamido)-PROXYL spin label **21** to obtain RNA **22**. Although this approach poses as an efficient way of site-selective spin-labeling of long RNAs, two spin labels have not been incorporated into the same sequence yet.

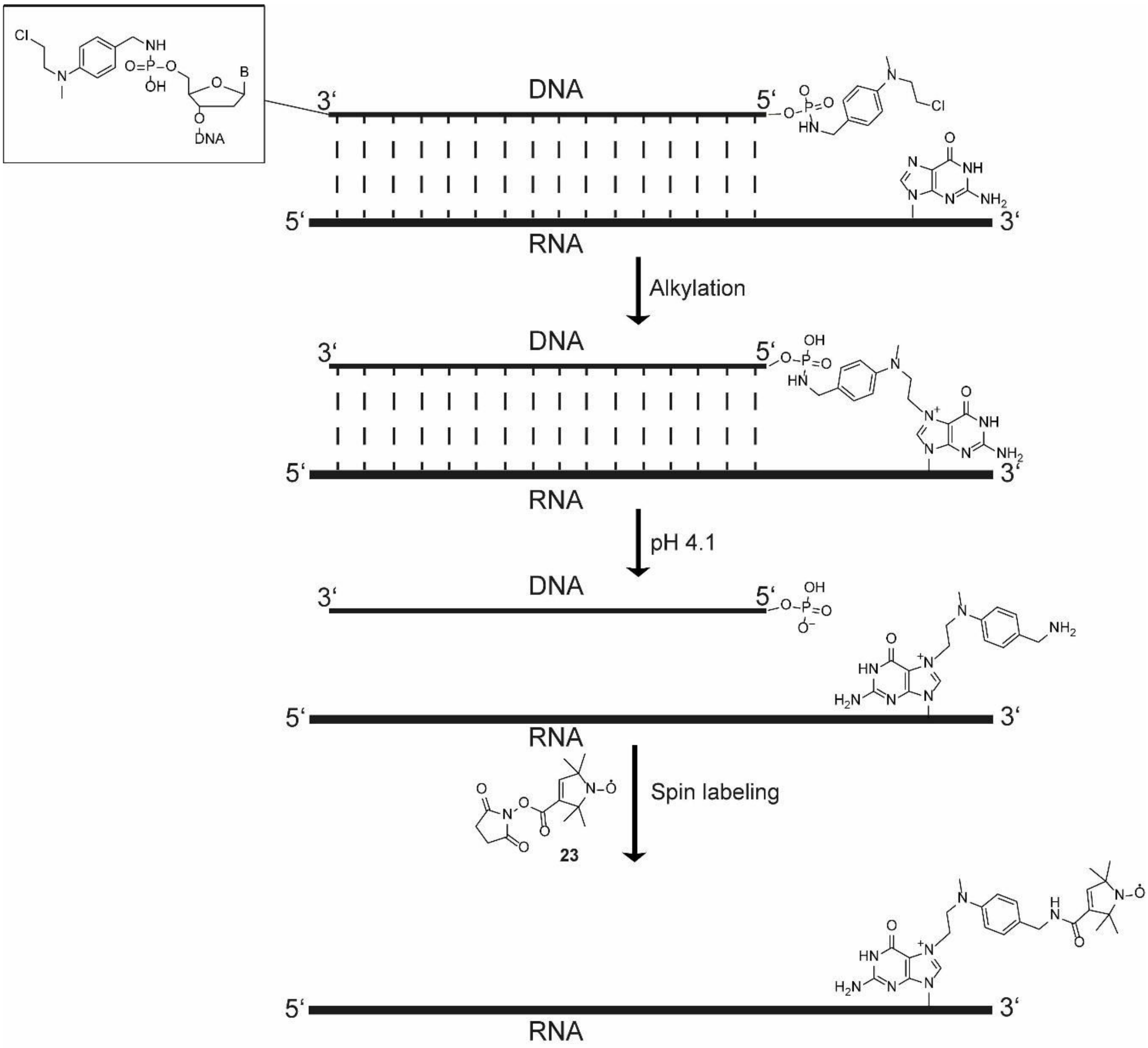

Figure 17: Schematic representation of site-specific spin-labeling of RNA based on the complementary-addressed approach.[77-78]

An elegant way to introduce two spin labels in RNA without enzymes was reported by Bagryanskaya and co-workers (Figure 17).[77] They applied a complementary-addressed site-specific alkylation of RNA using a DNA sequence containing 4-[N-(2-chloroethyl)-N-methylamino]benzylphosphoramide.

This DNA sequence was fully complementary to RNA sequence adjacent to the site of labeling. The 4-[N-(2-chloroethyl)-N-methylamino]benzyl phosphoramide moiety, which is located at the 5' end of DNA, can thus react either with the last 3'-terminal base of DNA/RNA heteroduplex or with the next unpaired RNA base. Figure 17 shows an example of the latter case, the alkylation of N7 of guanine. Note that the same was also demonstrated for adenine and cytidine. Upon alkylation, the phosphoramide bond was hydrolyzed and the aliphatic amino group was released. In the last step, the resulting amino group was coupled to the spin-labeling reagent **23**. Using this method, two spin labels were incorporated into Hepatitis C Virus genomic RNA internal ribosome entry site (IRES) consisting of 350 nucleotides. However, the disadvantages of this approach are a long flexible linker of the spin label and a low labeling efficiency (approx. 20%).

1.6 Spin-labeling of DNA using click chemistry

Cu(I)-catalyzed Azide-Alkyne cycloaddition (CuAAC), also known as click reaction, is a chemical reaction in which an organic azide reacts with a terminal alkyne to afford a 1,3-triazole (Figure 18). First introduced independently by groups of Sharpless[79] and Mendal[80] this type of reaction found various applications in molecular biology, medicinal chemistry or material science.[81] One of the main reasons, which makes click reaction attractive for chemical synthesis is its extremely high selectivity and specificity. Moreover, it usually provides high yields and is wide in scope.

The most frequently used catalytic system is $CuSO_4$/sodium ascorbate as it is cheap and tolerant to many solvents mixtures such as e.g. water/DMSO or water/*t*-BuOH.[82] Here, ascorbate serves as a reducing agent to generate the catalytically active Cu(I) from Cu(II) complex.

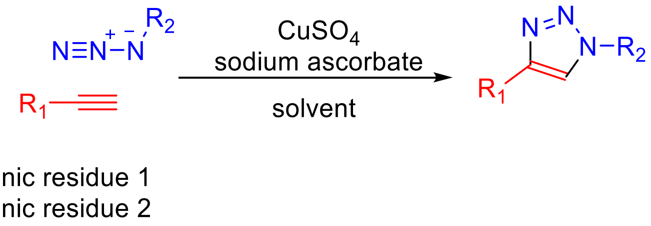

Figure 18: Formation of 1,3-triazole using CuAAC reaction.

Despite the high catalytic activity of Cu (I) /ascorbate system, it also has its disadvantages. In the first instance, the reaction is not fast enough at very low concentrations of reagents. On the other hand, relatively high amount of copper has to be used. This can be overcome by using copper (I) chelating ligands. Especially oligotriazole derivatives, as shown in

Figure 19, were shown to efficiently stabilize the +1 oxidation state of copper catalyst and significantly accelerate the click reaction.[83]

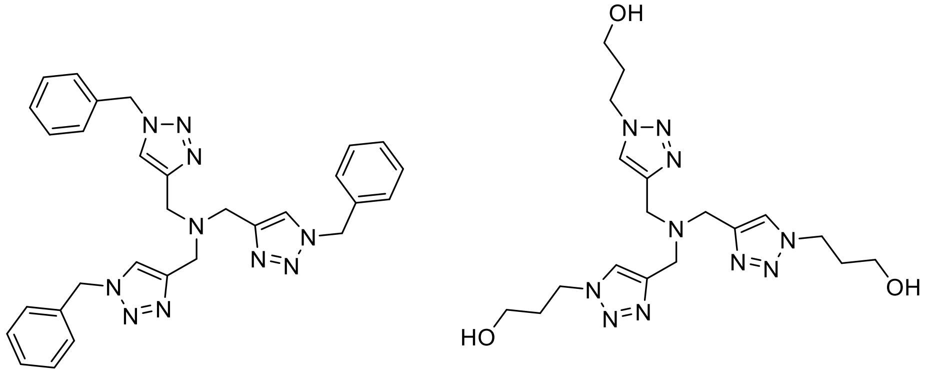

Figure 19: Examples of Cu(I) stabilizing ligands derived from propargylamine core.

The catalytic cycle for CuAAC reaction was proposed by Fokin and coworkers and is depicted in Figure 20.[81] The entire cycle is composed of five steps. In the first step A, a terminal alkyne coordinates to copper/ligand complex **24** forming a copper(I)acetylide **25**.

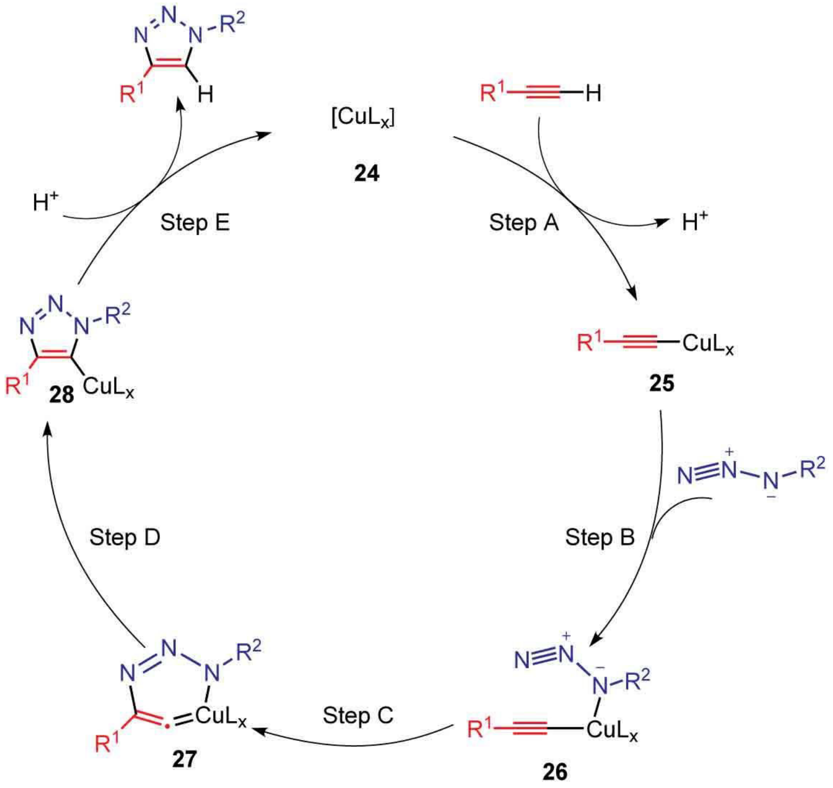

Figure 20: Catalytic cycle for CuAAC reaction. Adapted from Ref.[81]

In the subsequent step B, an azide is activated by linking to copper providing the intermediate **26**. The key step is the formation of the 6-membered copper metallacycle **27** followed by the rearrangement to the energetically more favorable triazolyl-copper derivative **28** (Step C). In the final step E, the triazole product is released upon the proteolysis of **28**.

Being very selective and specific click reaction is also a frequently used method for the conjugation of nucleic acids.[84-85] In this reaction, an ethynyl-functionalized nucleic acid reacts with an azide-modified residue in the presence of Cu(I). In principle, azide functionalized nucleic acid can also be used.[85] However, its synthesis is more challenging since the azide group is less stable than alkyne under reducing conditions of DNA synthesis. Spin-labeling of nucleic acids has also been reported though the existing publications are limited only to DNA. For example, Brown *et. al.* used click chemistry to label 2′-ethynyl-2′-deoxynucleoside modified DNA with different azide functionalized nitroxides, including such examples as **29** and **30** (Figure 21). Here, alkynyl modified DNA was incubated with CuI, THPTA and the corresponding spin label in acetonitrile/water mixture under argon atmosphere for 3h.[86] However, a more common way to introduce spin labels using click chemistry is to use ethynyl-substituted nucleobases. The commercial availability of 5-ethynyl-2’-dU (EdU) modified DNA makes this approach especially widespread. Thus, groups of Sigurdsson and Steinhoff simultaneously reported on spin-labeling of EdU-modified DNA by means of click chemistry.[87-88] In contrast to Steinhoff’s click reaction, which has been carried out in solution, Sigurdsson demonstrated that the reaction is also possible on the solid support to which EdU-modified DNA was covalently attached.

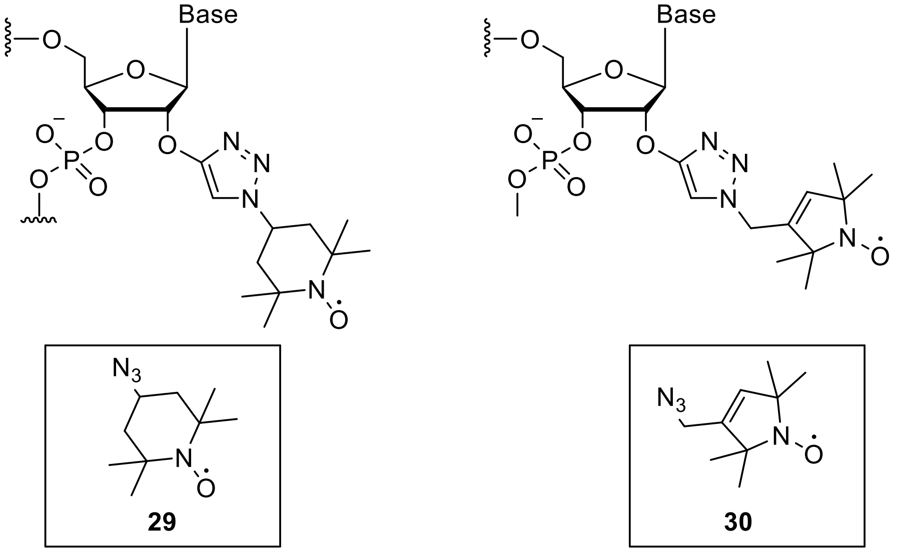

29

30

Figure 21: Spin-labeling 2′-ethynyl-2′-deoxynucleoside modified DNA.

1.7 EPR spectroscopy

Electron paramagnetic resonance (EPR) is a spectroscopic method to study systems with unpaired electrons.[89] The working principle of EPR is very similar to NMR and based on the resonant absorption of microwave (m.w.) radiation by electron spins, which are placed into a constant magnetic field. An important difference of EPR as compared to NMR is the magnetic moment of electron spins which is three orders of magnitude larger than the magnetic moment of protons. Consequently, EPR is more sensitive and allows accessing spin-spin interactions over longer distances. Moreover, the highest EPR time resolution reaches 10 - 100 ns,[90] whereas time scale of NMR spectroscopy is typically in order of milliseconds.

EPR spectroscopy can be applied to various paramagnetic centers, e.g. organic and inorganic radicals, complexes containing paramagnetic ions, and spin-labeled biomacromolecules. The main requirement is the presence of one or more unpaired electrons. Therefore, diamagnetic biomacromolecules, such as e.g. nucleic acids, have to be labeled with paramagnetic species (spin labels) prior EPR studies. The methods of spin-labeling of RNA are discussed in Section 1.4. An attachment of two spin labels to a biomolecule (e.g. RNA) enables one to explore the dipolar coupling between these labels by EPR and, consequently, to determine inter-label distances. This property of EPR is widely used in the structural characterization of proteins and nucleic acids.

EPR spectroscopy can be performed in either continuous or pulsed fashion. In continuous-wave EPR (cw-EPR) experiments, the sample is exposed to a continuous m.w. radiation of a constant frequency while the magnetic field is changed linearly. The pulsed EPR are realized by applying short m.w. pulses to the sample. Depending on the pulse sequence, different types of experiments can be accomplished.[91]

1.7.1 Spin system

When an electron with a spin S = 1/2 is placed into an external magnetic field, its energy levels split into two, which correspond to the magnetic moment of the electron aligned either parallel ($m_s = -\frac{1}{2}$) or antiparallel ($m_s = +\frac{1}{2}$) to the magnetic field. This phenomena was first observed by Zeeman and therefore called Zeeman effect (Figure 22).[90] According to the Zeeman effect, the energy E of an free electron in a static magnetic field of strength B_0 is given by

$$E = g_e \mu_B B_0 m_s \qquad (1)$$

where m_s is the magnetic quantum number, g_e is the g-factor of the free electron, μ_B is the Bohr magneton ($9.274 \cdot 10^{-24}$ J/T). Thus, the energy difference between both energy levels is

$$\Delta E = E_{+\frac{1}{2}} - E_{-\frac{1}{2}} = g_e \mu_B B_0 \qquad (2)$$

As follows from equation (2), the energy difference between two energy levels is proportional to the applied magnetic field. Thus, the resonance condition is given by

$$h\nu_0 = \Delta E = g_e \mu_B B_0 \qquad (3)$$

Here, h is the Plank constant, and ν_0 is the frequency of m.w. radiation. Equation (3) postulates a resonance condition, which has to be fulfilled in order to observe the transition between the two energy levels.

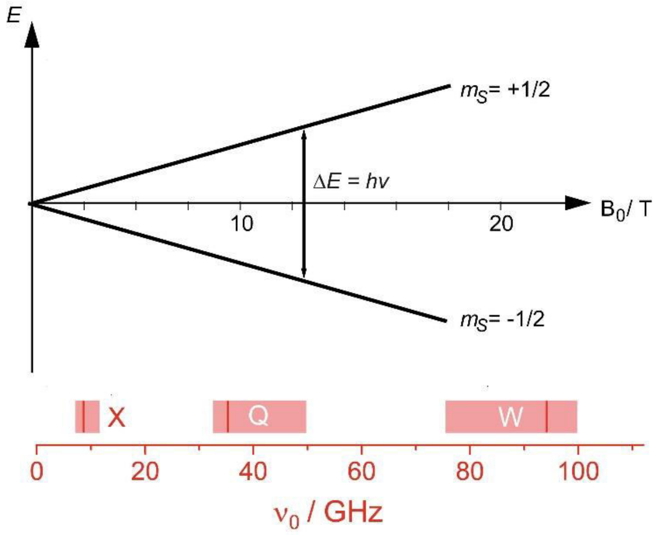

Figure 22: Top: Splitting of energy levels of an electron in an external magnetic field. Bottom: Typical microwave bands.

In accordance with the Boltzmann distribution, the populations of both energy levels can be described as follows:

$$n_2 = n_1 e^{-\frac{\Delta E}{\kappa T}} = n_1 e^{-\frac{g_e \mu_B B_0}{\kappa_B T}} \qquad (4)$$

where n_1 and n_2 are the populations of upper and lower levels respectively and k_B is the Boltzmann constant ($1.381 \cdot 10^{-23}$ J/K). Thus, equation (4) implies that at finite temperatures the population of the lower energy level is higher than the one of the upper level.

1.7.2 cw-EPR

Equations (3) and (4) can be used to explain the working principle of cw-EPR. Let us assume that a sample that contains electron spins is placed into a static magnetic field B_0 and exposed to m.w. radiation of frequency ν_0. In accordance with equation (3), this leads to the spin transitions between the energy levels of the electron spins. The probability of these transitions depends on the population difference between the energy levels (polarization), which is described by equation (4). The cw-EPR experiment is usually performed using a constant m.w. frequency ν_0 and changing magnetic field B_0 linearly. The resulting absorption line is depicted in Figure 23. Due to sensitivity reasons, the cw-

EPR signals are usually acquired in a form of the first derivative of the absorption spectrum. This is obtained by modulation of the external magnetic field.

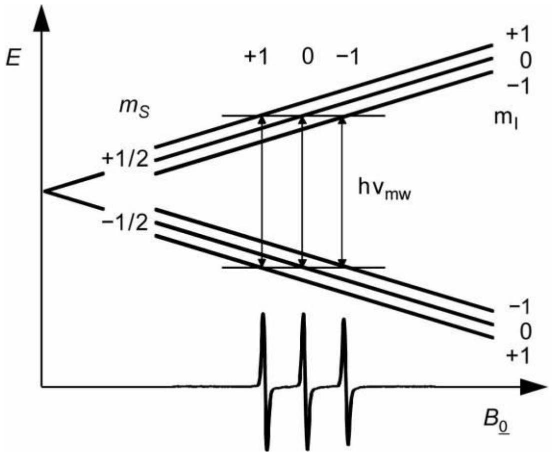

Figure 23: Energy level scheme and EPR spectrum for a spin system S=1/2, I=1. Note that only electron Zeeman and hyperfine interactions are considered. Adapted from Ref.[89]

So far, the cw-EPR experiment was considered for the case of free electrons (Figure 23). When one extends this approach towards the nitroxide, a deviation of the g-value from g_e is obtained due to spin-orbit coupling. Moreover, the additional hyperfine interaction of the electron spin with the nuclear spin of the ^{14}N atom has to be taken into account (Figure 24). The ^{14}N hyperfine coupling is anisotropic and has a largest value along the $2p_z$ orbital. Conversely, the hyperfine interaction constant is small when magnetic field is perpendicular to $2p_z$ orbital (Figure 24).

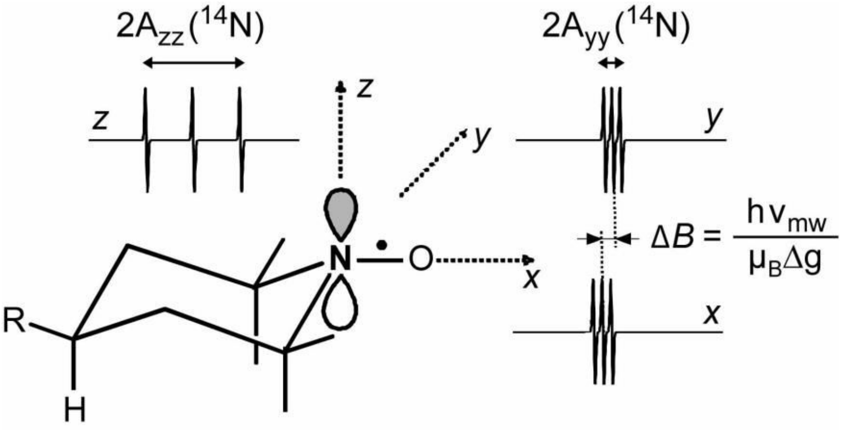

Figure 24: Anisotropic interactions of a nitroxide radical including hyperfine interactions and g-shift. Adapted from Ref.[89]

Importantly, the hyperfine interaction constant of the nitroxide is very sensitive to the environment around the electron spin. For example, a presence of polar solvent molecules near to the nitroxide leads to a shift of the electron density of the nitroxide towards the nitrogen atom, which increases the values of the hyperfine coupling constant. The same holds when the oxygen atom of the nitroxide forms hydrogen bonds with surrounding atoms.

Furthermore, the analysis of the hyperfine interaction of the nitroxide allows determination of the mobility of nitroxides. The common way to analyze the mobility of the nitroxides in solution is to determine their rotational correlation time τ_C. τ_C values defines the time during which the nitroxide maintains its spatial orientation. In the case of very fast rotation, the anisotropic interaction is averaged to zero and the EPR spectrum contains three lines of equal intensity (Figure 25).[89, 92] In contrast, if the motion of nitroxide is slow, the rotation of a spin label does not influence the EPR line shape and, thus, the anisotropic hyperfine interaction dominates the EPR spectrum. In the area between both extrema, the shape of EPR line is strongly dependent on the nitroxide mobility.[89, 93] Analyzing the mobility of nitroxides of spin-labeled biopolymers, such e.g. RNAs, can provide insights into the dynamics of their folding processes. This will be described in more detail in the results and discussion section.

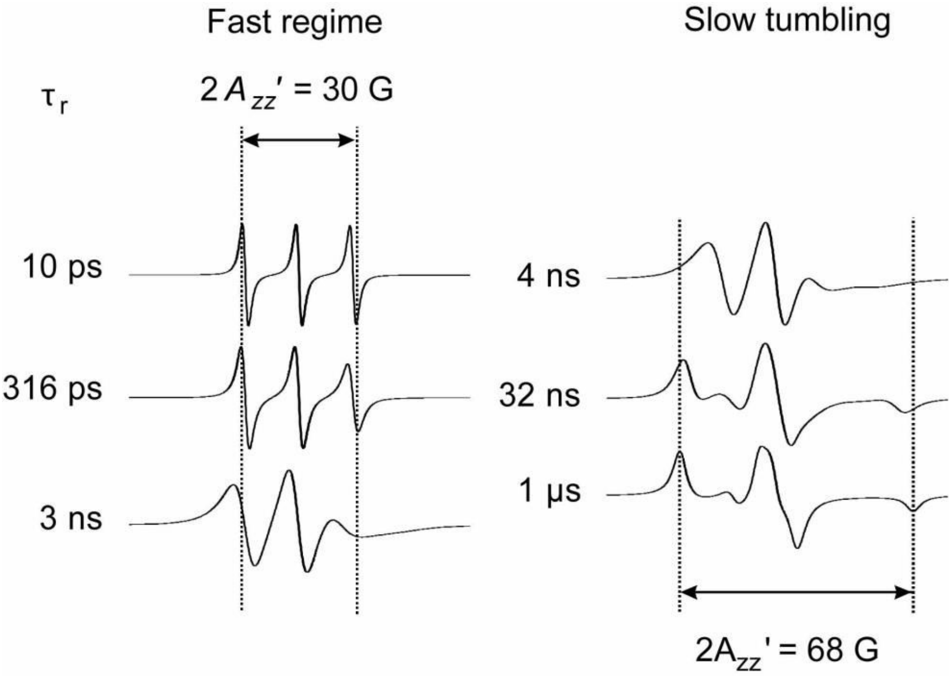

Figure 25: Simulated nitroxide spectra in dependence of rotational correlation time τ_C. In the fast regime ($\tau_C \approx 10$ ps) the outer extrema splitting $2A_{zz}$ approximately corresponds to the double amount of the isotropic hyperfine coupling. In the rigid limit of slow tumbling $2A_{zz}$ value is twice the hyperfine coupling along the z-axis. Adapted from Ref.[89]

cw-EPR spectroscopy can also be used for distance measurements between two electrons based on the dipolar coupling. The distance range, in which this technique can be applied, is between 0.8 and 2.5 nm.[94]

1.7.3 Pulsed EPR

The dipole-dipole coupling above the distances of 2.5 nm is much smaller than inhomogeneous linewidth of EPR spectrum caused by unresolved hyperfine interactions and g anisotropy.[95] Thus, in order to get access to larger inter-spin distances the dipolar coupling has to be separated from the other electron spin interactions. This can be achieved by using pulsed EPR methods, which makes use of microwave pulses of nanosecond duration instead of continuous radiation. One such technique is known as Pulsed Electron-Electron Double Resonance (PELDOR or DEER).[96-97] It allows for the determination of inter-spin distances in the range 1.5-15 nm.[98] In the present work PELDOR was used and will be further explained in the section 1.7.3.2.

1.7.3.1 Basics of pulsed EPR

As it was described above, the energy of two spin states of an unpaired electron in an external magnetic field are split into two sublevels. The higher population of the lower energy level (parallel to the external magnetic field) leads to a net magnetization of electron spins along the z-axis, which is parallel to the external magnetic field. In the pulsed EPR experiment, short m.w. pulses manipulate this magnetization. The notations of m.w. pulses are usually defined by the rotation angles they induce. For example, a $\pi/2$ pulse rotates the magnetization into the x-y plane, whereas a π pulse inverts the magnetization by 180°. Figure 26 illustrates schematically the detection of a Hahn echo by using these two pulses. The first $(\pi/2)_x$ pulse rotates the magnetization in the y-direction thereby shifting it from its thermal equilibrium and establishes phase coherence. Then, the spin packets start to dephase because of inhomogeneous distribution of their Larmor frequencies. Consequently, the transverse magnetization vanishes. Applying the second $(\pi)_x$ pulse after the first free evolution time τ inverts the sign of the spin precession in the x-y plane. Thus, the phases of the spins with different Larmor frequencies are refocused after another evolution time τ, which yields the magnetization in the -y direction. This magnetization is then detected as a signal, which is known as a spin echo.

The return of magnetization to its equilibrium state is due relaxation processes. These processes are characterized by two relaxation time constants T_1 and T_2. Relaxation time T_1, known as spin-lattice or longitudinal relaxation time, shows how fast the magnetization recovers to its equilibrium state along the z-axis. In turn, the relaxation time T_2, also called as transverse relaxation time, characterizes how fast the magnetization dissipates in the x-y plane. Since T_2 is usually shorter than T_1, T_1 determines the repetition rate of spin echo detection.

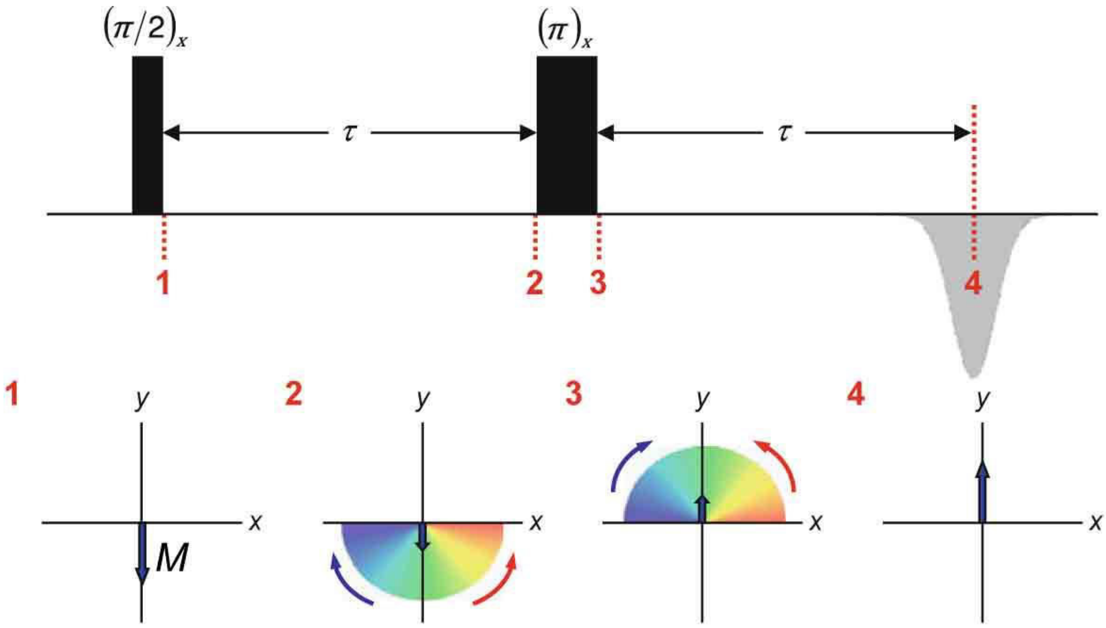

Figure 26: Schematic representation of Hahn echo formation using m.w. pulses. Top: The pulse sequence. Bottom: Orientation of magnetization *M* in the xy plane in dependence on the applied pulse. Adapted from Ref.[99]

1.7.3.2 PELDOR experiment

PELDOR technique is a pulsed EPR method that allows to separate spin-spin interaction from other electron spin interactions. Figure 27a shows the 4-pulse sequence of the PELDOR experiment. This sequence comprises the m.w. pulses at two different frequencies, the observer or detection frequency (ω_A) and the pump frequency (ω_B). The detection frequency is on resonance with the one spin of the spin pair, which is called in the following spin A. In turn, the pump frequency on resonance with the second spin of the spin pair, which is called here spin B.

The first two pulses, π/2 and π, create a spin echo from spins A. Then, the third π pulse is applied at the pump frequency, which flips spins B. The flip of spins B inverts the local magnetic field of spins A due to the dipolar coupling (Figure 27b). This changes the Larmor frequency of the coupled spins A and, consequently, reduces the intensity of the refocused echo from spins A, which is obtained through applying the fourth π pulse at the detection frequency. The frequency difference between spin A and spin B must be high enough in order to prevent the overlapping of excitation profiles. In the case of nitroxides, the anisotropy can be used for selection of appropriate frequencies (Figure 27c).

Since the time position of the pump pulse is varied and the timing of three detection pulses is kept constant, the dipolar frequencies modulate the amplitude of the refocused echo (Figure 28a). The modulation frequency is given by the equation:

$$\omega_{AB} = \frac{52.16}{r^3}(1 - 3cos^2\theta) \quad (6)$$

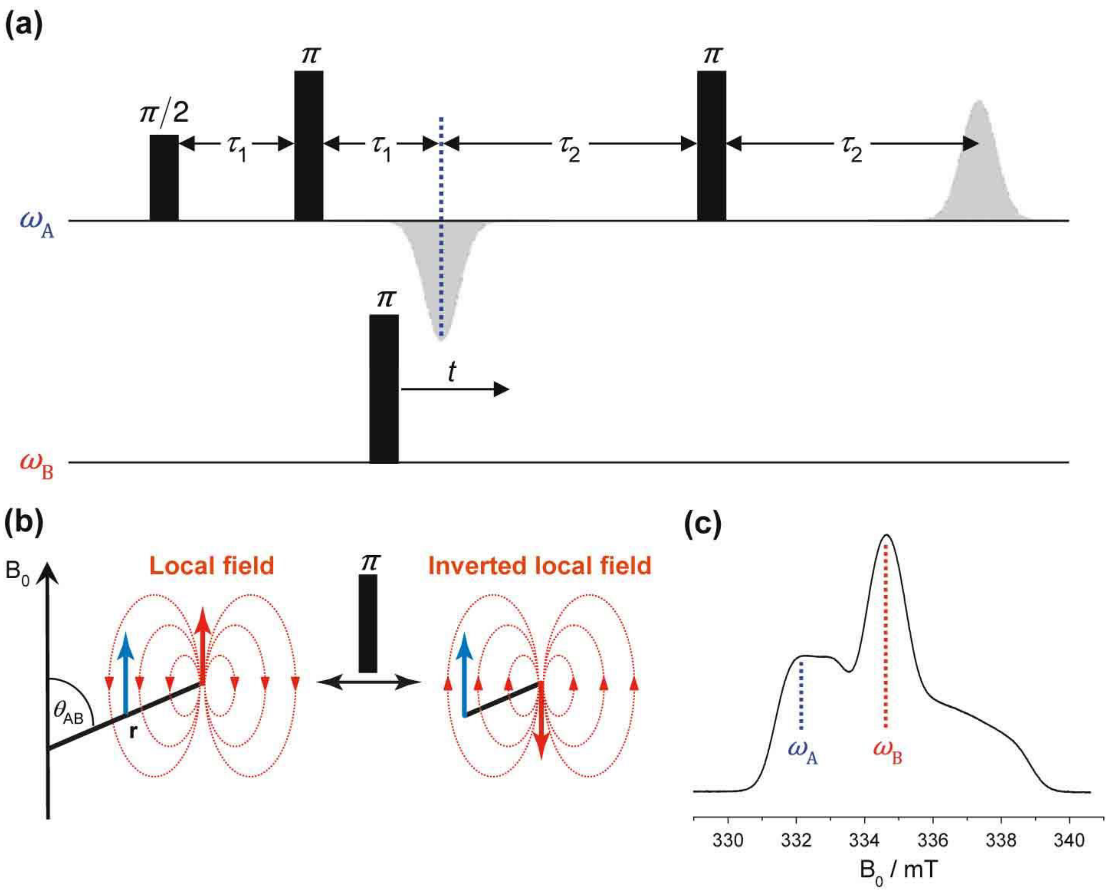

Figure 27: 4-pulsed PELDOR experiment. (a) PELDOR pulse sequence. (b) Representation of the influence of the local filed of spin A by spin B using a π pulse at frequency ω_B. (c) Example of a nitroxide powder spectrum. Positions of detection and pump frequency are depicted as ω_A and ω_B respectively. Adapted from Ref.[99]

where *r* is the inter-spin distance vector, 52.16 [MHz nm^3] is the dipolar splitting constant for nitroxides and θ the angle between *r* and the external magnetic field. The Fourier transform of a PELDOR time trace yields a spectrum of the dipole-dipole interaction between spins A and B, which is known as a Pake pattern (Figure 28b). The inter-spin distance distribution is usually extracted from the PELDOR time trace by using the so-called Tikhonov regularization, which is e.g. implemented in the program DeerAnalysis.[100] Figure 28 illustrates an example of PELDOR data that has no orientation selectivity. The analysis of orientation selective PELDOR data is however more tedious, since it requires recording time traces at different frequencies offsets (ω_A - ω_B) to probe different orientations of spin centers. The analysis of such data can be done by means of the computer program PeldorFit.[101]

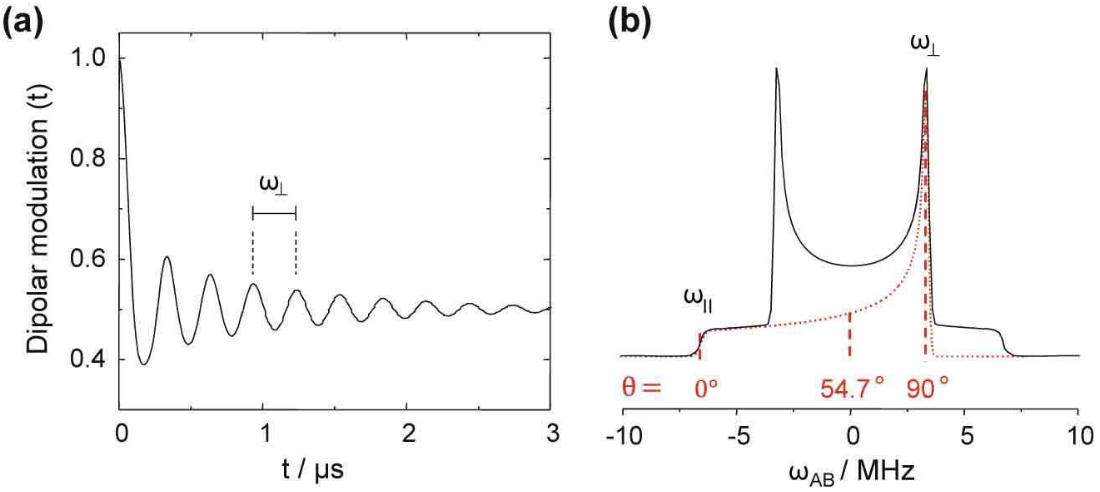

Figure 28: (a) Example of the time domain data for coupling between two nitroxides at X band. (b) Pake pattern obtained by means of Fourier transformation of time domain in a. ω⊥ and ω ∥ are angular frequency contributions. A most probable angle θ between *r* and field B_0 is 90 °. Adapted from Ref.[99]

2 Aim of the study

The aim of this study was to develop a competitive and powerful spin-labeling approach for long RNAs and to analyze its applicability on long riboswitches. Click chemistry is currently frequently used for conjugation of nucleic acids.[84-85] This method in combination with enzymatic ligation provided a basis for this work. Previously, click reaction was successfully applied for site-specific spin-labeling of DNA.[86-88, 102] In particular, two approaches have been demonstrated. In the first approach, DNA was spin-labeled on the solid support, to which it was covalently attached. In the second approach, the click reaction was carried out in solution. Compared to other spin-labeling approaches discussed in the introduction section, both methods have been demonstrated to be more straightforward to carry out, highly selective and extremely specific. Furthermore, they provided high yields. However, spin-labeling using click chemistry has never been done for RNA. One of the possible reasons for this might be an extremely high sensitivity of 2'-OH group of ribose to copper(I) containing salts. Thus, this method had to be adapted and implemented for RNA. Moreover, the effectiveness of click chemistry should be verified by comparing it to another approach that employs the well-established label **Çm** (section 3.2.1).

In addition, the applicability of click-labeling procedure should be demonstrated on the aptamer domains of the preQ1 riboswitch from *Fusobacterium nucleatum (Fsu)* (Figure 29a) as well as of TPP riboswitch from *E. coli* respectively (Figure 29b).

Furthermore, efficient ligation strategies should be elaborated and established for site-specific labeling of the full-length TPP riboswitch.

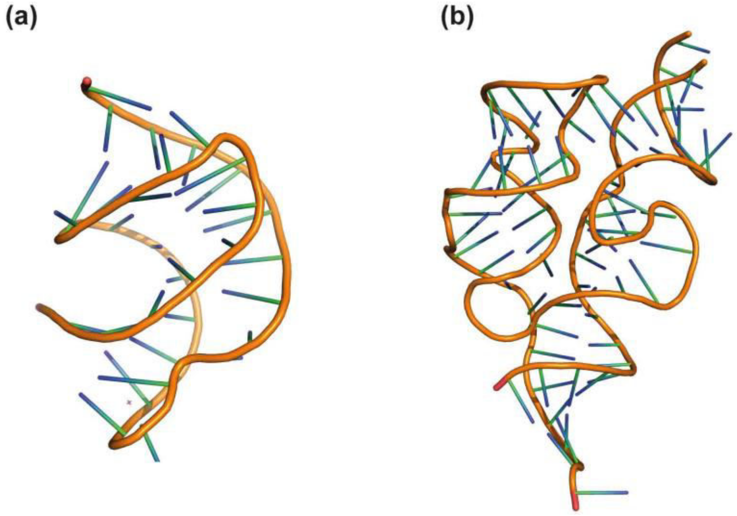

Figure 29: Crystal structures of aptamer domains of (a) preQ1 riboswitch from *Fsu* (3Q50) and (b) TPP riboswitch from *E. coli* (4NYG) in metabolite-bound states. Both structures were generated using PyMOL molecular graphics system.

3 Results and Discussion

The first part of this chapter is focused on test reactions to establish spin-labeling approaches for RNA. Two spin-labeling strategies are highlighted, the first is a post-synthetic spin-labeling via click chemistry and the second is an automated RNA solid phase synthesis using spin-labeled phosphoramidites. Both strategies are compared to each other and the influence of the incorporated spin labels on the RNA is analyzed using UV-Vis, CD and EPR spectroscopies (section 3.3). The second part of this chapter describes an application of the post-synthetic spin-labeling approach to the aptamer domains of the preQ1 and TPP riboswitches, which is then followed by their EPR studies (section 3.4). In addition, ligation strategies for the site-specific spin-labeling of the full-length TPP riboswitch are elaborated (section 3.5).

3.1 Site-directed spin-labeling of RNA using post-synthetic approach

This section describes the use of click chemistry for post-synthetic spin-labeling of RNA. For this purpose, two azide-functionalized nitroxides **43** and **44**, which are introduced in section 3.1.1 (scheme 1), were synthesized and incorporated into commercially available 5-ethynyl-2’-dU (EdU) modified RNA. The click reaction was performed on the RNA that remained on the CPG solid support after solid-phase synthesis (section 3.1.2) as well as on fully deprotected RNA in solution (section 3.1.3). Furthermore, as an alternative to EdU, 5-ethynyl-2‘-O-methylcytidine (**EmC**) phosphoramidite was synthesized and incorporated into RNA. Later the spin label **43** was introduced into EmC-modified RNA via click chemistry (section 3.1.3.2).

3.1.1 Isoindoline derived spin labels 43 and 44

Azide-functionalized nitroxide **43** has been previously synthesized and introduced into DNA by Jakobsen *et. at.*[87] The same synthetic route was applied here to obtain the ethylated derivative **44**. The first step of the synthesis route of **43** and **44** is the reaction of commercially available phthalic acid anhydride **31** with benzyl amine,[103] followed by a Grignard reaction, in which the aliphatic substituents were introduced (Scheme 1). This is the most critical step of the whole synthesis due to anhydrous reaction conditions and the requirement of temperature control over the entire reaction time. Further debenzylation of **33** and **34** provided the corresponding amines **35** and **36** in good yields (94% for **35**, 86% for **36**). The subsequent introduction of the amine group into the aromatic ring required two steps, including aromatic nitration of **35** and **36** and catalytic hydrogenation. The resulting aromatic amines **39** and **40** were then converted into the corresponding azides **41** and **42**. In contrast to the reported procedure, less explosive imidazole-1-sulfonyl azide hydrochloride[104] was used instead of trifluoromethanesulfonyl azide as diazotransfer reagent. The subsequent oxidation of the isoindoline-derived azides **41** and **42** using *m*CPBA resulted in the formation of azide-functionalized nitroxides **43** and **44** in good yields. The purity as well as the paramagnetic nature of the obtained spin labels was verified by LCMS and EPR spectroscopy, respectively.

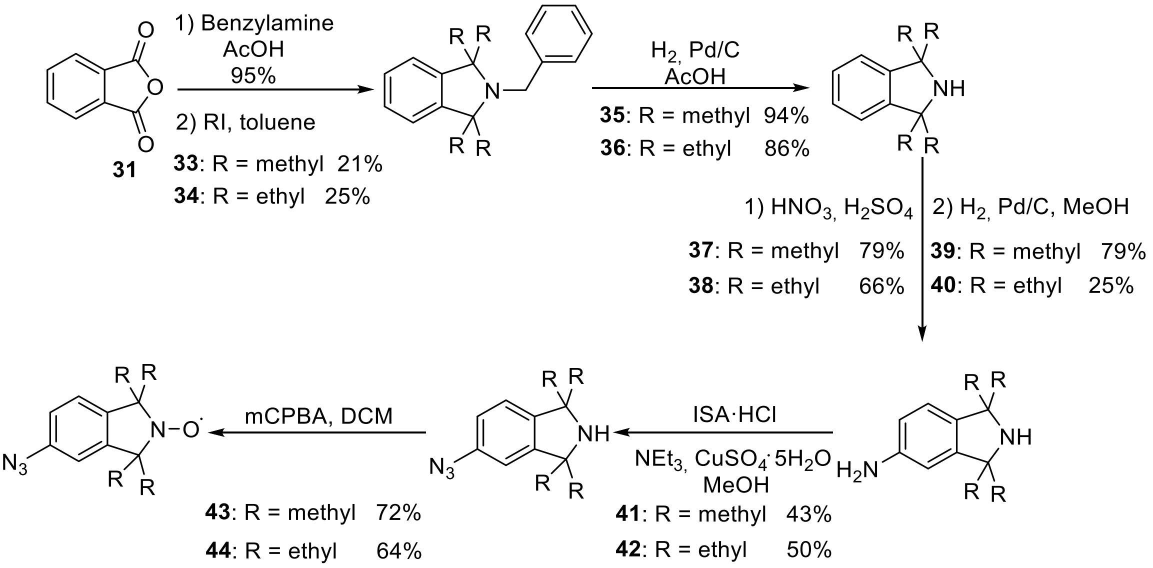

Scheme 1: Synthesis of isoindoline-derived nitroxides **43** and **44**.

3.1.2 Spin-labeling of RNA via click chemistry on solid support

This chapter describes the post synthetic spin-labeling of RNA attached covalently to CPG solid support. Two RNA systems including a self-complementary sequence **45** (section 3.1.2.1) and the aptamer domain of preQ1 riboswitch from *Fsu* (section 3.1.2.2) were tested.

3.1.2.1 Spin-labeling of self-complementary RNA 45

Here, click chemistry was applied to a self-complementary 5-ethynyl-2′-dU modified RNA **45** (Scheme 2a). In this reaction, the RNA was covalently attached to the CPG solid support. The reaction procedure included incubation of **45** on the solid support (200 nmol scale synthesis) with the spin-labeled azide **43** or **44** in the presence of CuI and the Cu(I)-stabilizing ligand tris(3-hydroxypropyltriazylmethyl) amine (THPTA) in DMSO (Scheme 2b). Note that the usual way to generate catalytically-active Cu(I) species is *in situ* reduction of Cu(II) to Cu(I) using a reducing agent, such as ascorbate.[81] However, due to the reducible nature of **43** and **44** (section 3.1.3.1), CuI was used directly.

(a)

5'-CAUCUGAUAUCAGA**X**G-3'
3'-G**X**AGACUAUAGUCUAC-5'
X = EdU
45

(b)

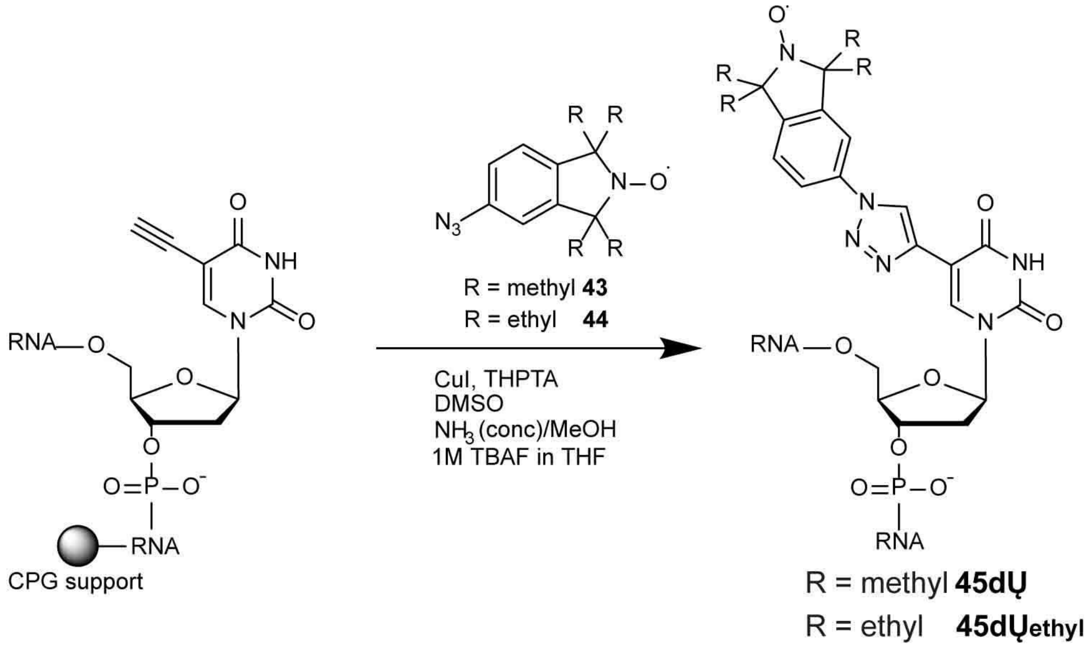

Scheme 2: (a) Self-complementary RNA sequence **45**. EdU modification is indicated by bold **X**. (b) Spin-labeling of RNA **45** with the isoindoline-derived nitroxides **43** and **44** on CPG support using click chemistry.

The click reaction was performed at room temperature for 24 h. Afterwards, the RNA was cleaved from the CPG solid support and its nucleobases were deprotected using the mixture of concentrated ammonia in methanol at room temperature. In order to remove the TBDMS protecting groups from the 2'-OH positions of RNA, it was incubated in the solution of 1M TBAF in THF for 16 h. After desalting the RNA on the NAP10 column (GE Healthcare illustra), the crude reaction mixture was analyzed via LCMS and purified using reverse phase HPLC chromatography (Figure 30).[1] The corresponding spin-labeled RNAs are called **45dŲ** and **45dŲethyl**, respectively. Although the LCMS analysis of the crude samples showed the nearly quantitative conversion of **45** for both labels, the yield of the isolated RNA after the HPLC purification was higher for **45dŲ** (22 nmol) as compared to **45dŲethyl** (12 nmol). One possible explanation can be the loss of **45dŲethyl** during the HPLC purification due to the impediment through small impurities (Figure 30b). Furthermore, no reduced species of either **43** or **44** attached to RNA could be observed,

---

[1] For simplicity, the nitroxides 43 and 44 attached to uridine are called in the following as **dŲ** and **dŲethyl**.

indicating that both spin labels were stable towards the cleavage and deprotection conditions.

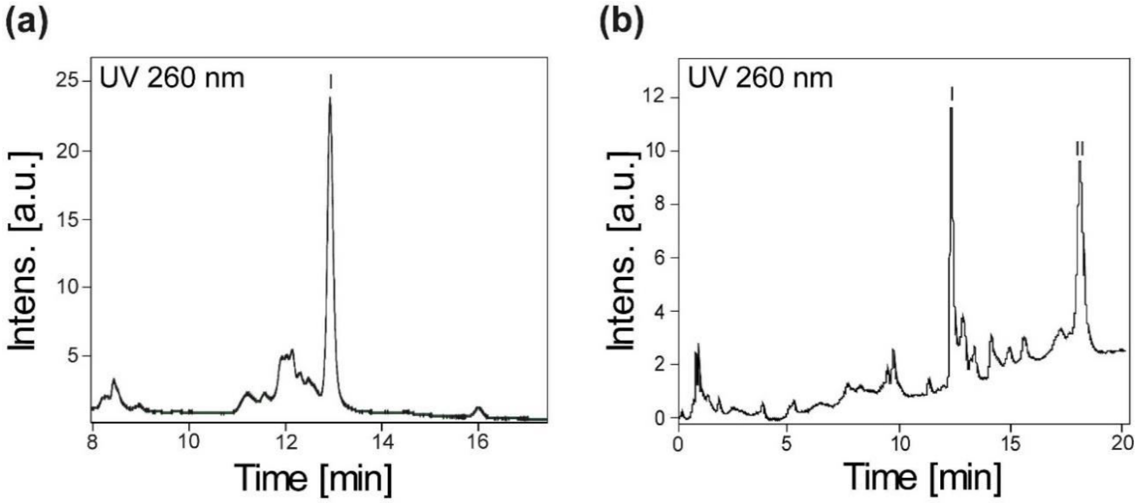

Figure 30: HPLC analysis of the crude reaction mixtures of self-complementary RNA **45** with (a) **43** and (b) **44** using click chemistry approach on solid support. Reaction time - 24 h. UV peaks are assigned as follows: for (a) I = **45dŲ**; for (b) I = **45dŲethyl**, II = **45dŲethyl** + DMT protecting group.

3.1.2.2 Spin-labeling of preQ1 dŲ4-dŲ32 and preQ1 dŲ32

In order to extend the spin-labeling on solid support to long RNA sequences, two mutants of the 34-nucleotide-long preQ1 aptamer domain, containing one (preQ1 **dŲ32**) or two ethynyl moieties (preQ1 **dŲ4-dŲ32**) were chosen. The labeling procedure given in section 3.1.2.1 was slightly modified here. The RNA on solid support (200 nmol scale) was incubated with the spin label **43** and catalyst in DMSO for 4 h. Then, the RNA was washed with acetonitrile, dried under vacuum and again incubated for 4 h in the freshly prepared reaction mixture. The washing and drying steps were repeated 2 times and then the RNA was subjected to the final incubation in the freshly prepared reaction mixture for 16 h. However, even after 24 h of reaction time, the considerably lower conversion of the starting materials (roughly 36% for both mutants) was achieved as compared to the self-complementary sequence **45** (Figure 31). No obvious explanation for such a discrepancy between the two spin-labeling results can be given. Since the present reaction was performed in DMSO, the influence of the secondary structure of RNA on the accessibility of the spin label is unlikely.[105] A more reasonable explanation is the lower concentration of the full-length preQ1 mutant RNA on solid support in the click reaction. It is known, that the solid phase synthesis of RNA becomes less efficient with the increasing length of the RNA.[106] Therefore, it could be that the amount of the ethynyl-modified RNA was higher in the case of **45**. Thus, it should be noted that this approach is currently more efficient for short RNA sequences.

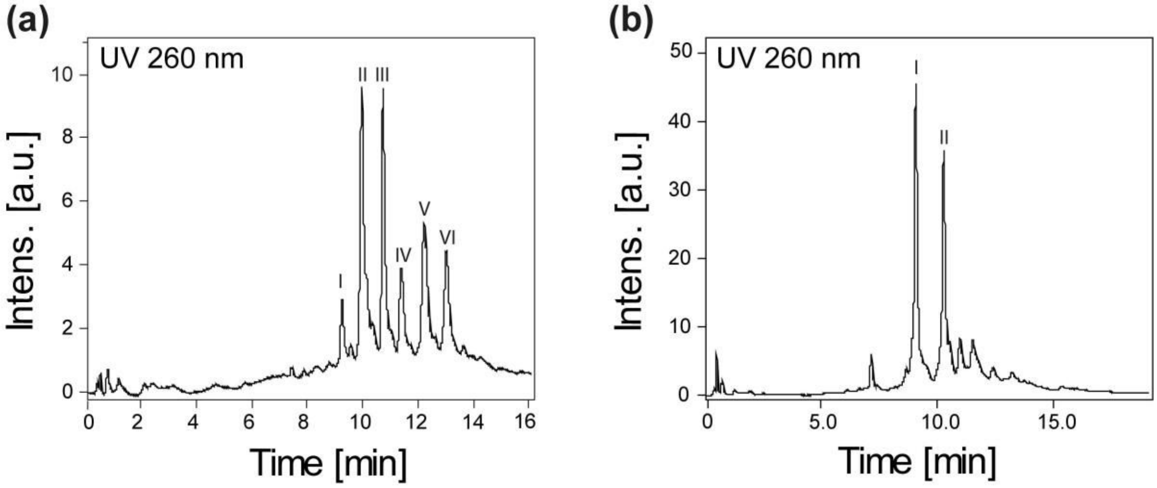

Figure 31: ESI mass spectrometric analysis of the crude reaction mixture of (a) preQ1 **dŲ4-dŲ32** and (b) preQ1 **dŲ32** labeled using click chemistry approach on solid support. Reaction time was 24 h. UV peaks are assigned as follows: In the case of (a) **I** = starting material, **II** = single labeled preQ1 **dŲ4-dŲ32**, **III** = preQ1 **dŲ4-dŲ32**, IV = starting material + DMT protecting group, V = singly labeled preQ1 **dŲ4-dŲ32** + DMT protecting group, VI = preQ1 **dŲ4-dŲ32** +DMT protecting group; In the case of (b) **I** = starting material, **II** = preQ1 **dŲ32**.

3.1.3 Spin-labeling of RNA via click chemistry in solution

The limitations of the labeling-strategy on solid support approach initiated the search for new reaction conditions that would allow spin-labeling of long RNA sequences. In this section, the spin-labeling conditions were changed from RNA on solid support to fully deprotected RNA in solution. Changing the reaction conditions was justified not only by easier and more straightforward handling but also by the possibility of determining the exact RNA concentration prior to the labeling.

3.1.3.1 Spin-labeling of 46

Functionalization of RNA by means of click chemistry in solution has been demonstrated in various publications.[107-108] In most cases the method of choice for generating catalytically active Cu(I) species is an *in situ* reduction of catalytically inactive Cu(II) to Cu(I) using ascorbate as a mild reducing agent. However, considering the reducible nature of the label **43** *in situ* reduction of Cu(II) should be avoided. On the other hand, the 2'-hydroxyl group of RNA is labile toward hydrolysis by Cu(I) or Cu(II) ions, which may impede the use of copper salts. That might be the reason why the spin-labeling of oligonucleotides using click chemistry in solution was done only for DNA so far.

In this work, adopting spin-labeling using click chemistry in solution to RNA started with analysis of Cu(I) generating conditions. For this purpose, two different approaches to generating catalytically active Cu(I) species were tested (Scheme 3).

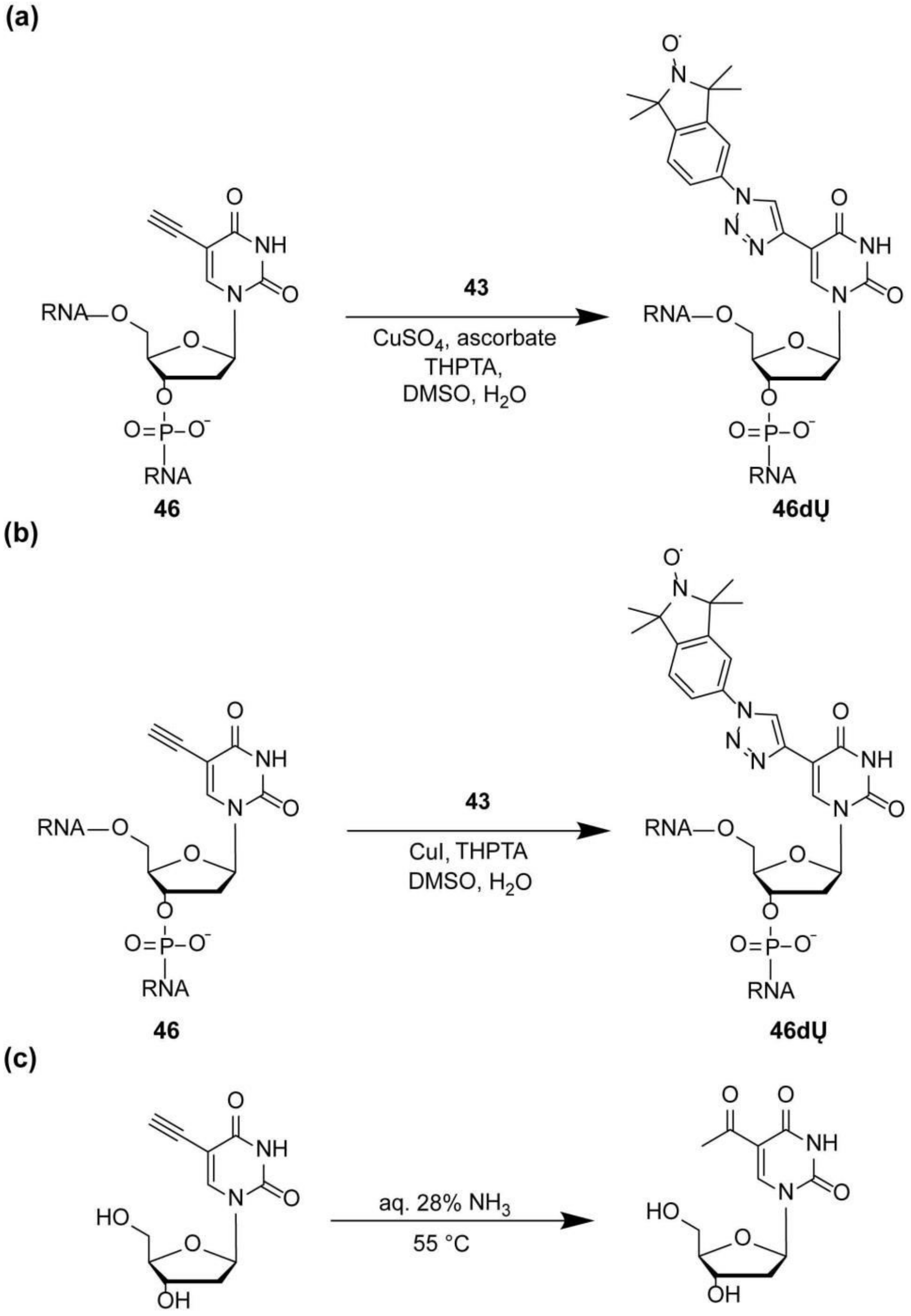

Scheme 3: Spin-labeling of the ethynyl modified RNA **46** (GGUXCGACCUXGCC, X = EdU) using (a) *in situ* Cu (I) generating conditions and (b) CuI. (c) Base-catalyzed hydration of ethynyl modified nucleosides as a side reaction.[109]

In the first approach (Scheme 3a), the catalytically active Cu(I) species were generated *in situ* using ascorbate, whereas Cu(I) was used directly in the form of copper iodide in the second approach (Scheme 3b). Both procedures included the incubation of the RNA **46** (2.5 nmol, 1 eq.) in a solution of **43** (5 eq.) and Cu(II) (16 eq.)/ascorbate (32 eq.) or CuI (16 eq.) and THPTA (32 eq.) in a DMSO/water mixture for 2 h, followed by desalting, LCMS analysis and reverse HPLC purification. Although, the LCMS profiles showed a complete conversion of the starting material after 2 h, the resulting reaction products were different in both cases (Figure 32). Furthermore, LCMS analysis of both reactions revealed that mass found for peak I at 7.8 min corresponded to the calculated mass of a by-product with two ketone functionalities, which are usually formed due to the oxidation of the ethynyl moieties during the alkaline RNA workup after RNA solid phase synthesis (Scheme 3c).[109] However, in case of the *in situ* Cu(I) generating reaction, only the masses of peaks III and IV at 11.4 min and at 11.6 min respectively corresponded to the calculated mass of **46dŲ**.

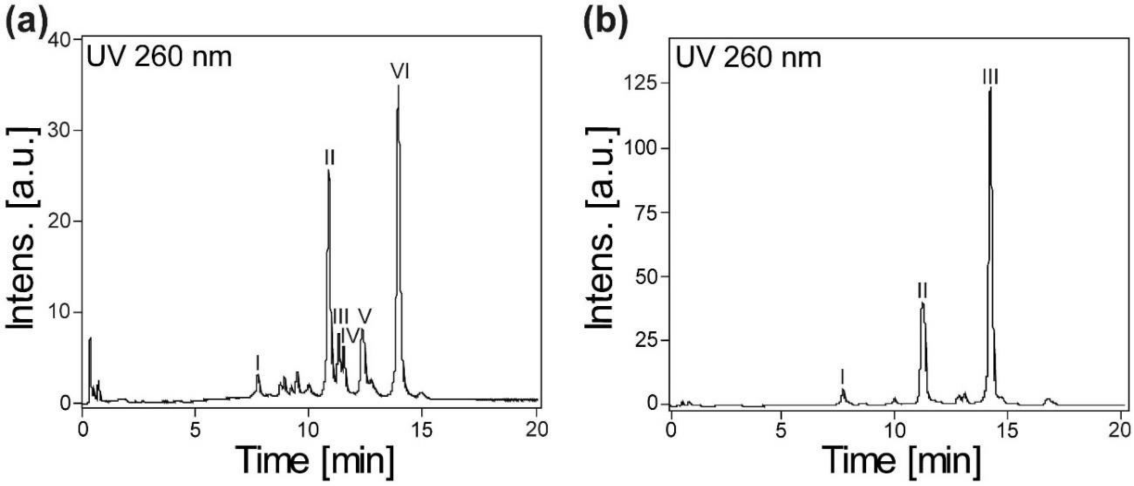

Figure 32: ESI mass spectrometric analysis of the crude reaction mixtures after spin-labeling of **46** using (a) Cu(II)/ascorbate and (b) CuI after desalting. Reaction time: 2 h. UV peaks are assigned as follows: for (a) I = a by-product of **46** containing two ketone groups, III, IV = **46dŲ**; in case of (b) I = a by-product of **46** containing two ketone groups, II = a by-product of **46dŲ** containing one label and one ketone group, III = **46dŲ**.

On the presented spectrum (Figure 32a), the peaks II, V, and VI with retention times of 10.9, 12.4 and 14 min could not be identified. The mass found for peak II was 33 m/z higher than the calculated mass for **46dŲ** containing one label whereas the masses found for peaks V and IV were 16 m/z and 31 m/z higher than the calculated mass for **46dŲ**. Moreover, the obtained sample was found to be EPR-silent. This result indicated that **dŲ** label is not stable towards these reaction conditions. However, the presence of multiple UV peaks containing masses higher than the calculated masses suggests that the side reactions occurring during the click reaction are not related to the reduction by ascorbate, which would provide formation of hydroxylamine with the lower mass.[110-112] Most likely, it suggests an occurrence of some side reactions of nitroxide **43** or its attached version **dŲ** with hydroxyl radicals, which could be generated during a copper-linked oxidation of ascorbate.[113-114] The working principle of the generation of hydroxyl radicals is very similar to the classical Fenton reaction of Fe(II) with hydrogen peroxide.[115] In the case of a copper ascorbate mixture, hydrogen peroxide is produced in the presence of oxygen (equations 1-3). In the following Fenton-like reaction it oxides Cu(I) to Cu(II) producing at the same time hydroxyl radicals (equations 4). Moreover, an additional source of hydroxyl radical can be the direct oxidation of ascorbate by a superoxide anion radical, which is produced during the oxidation of Cu(I) by molecular oxygen (equations 2,5).

$$\mathrm{ASC} + 2\mathrm{Cu}^{2+} \rightarrow 2\mathrm{Cu}^{1+} + \mathrm{DHA} + 2\mathrm{H}^{+} \qquad (1)$$

$$\mathrm{Cu}^{1+} + \mathrm{O}_2 \rightarrow \mathrm{O}_2^{\cdot-} + \mathrm{Cu}^{2+} \qquad (2)$$

$$\mathrm{Cu}^{1+} + \mathrm{O}_2^{\cdot-} + 2\mathrm{H}^{+} \rightarrow \mathrm{Cu}^{2+} + \mathrm{H}_2\mathrm{O}_2 \qquad (3)$$

$$\mathrm{Cu}^{1+} + \mathrm{H}_2\mathrm{O}_2 \rightarrow \mathrm{OH}^{-} + \mathrm{OH}^{\cdot} + \mathrm{Cu}^{2+} \qquad (4)$$

$$\mathrm{O}_2^{\cdot-} + \mathrm{ASC} \rightarrow \mathrm{DHA} + \mathrm{OH}^{-} + \mathrm{OH}^{\cdot} \qquad (5)$$

ASC = ascorbate, DHA = dehydroascorbic acid

These results indicate that, although ascorbate leads to quantitative conversion of the starting material, at the same time it can also modify the paramagnetic spin center. In contrast, according to the LCMS analysis of the crude mixture with CuI, the mass of the major UV peak corresponded to the calculated mass of **46dŲ** (Peak III, Figure 32b) whereas peak II at 11.3 min was correlated with **46** with one spin label and one ketone group attached. In addition, the incorporation of **dŲ** into **46** was also verified by EPR spectroscopy (Appendix). Based on these results a new approach to the click reaction using CuI can be proposed, which will be discussed in the following sections in more details.

3.1.3.2 Spin-labeling of self-complementary RNA 53EmC

Whereas the application of EdU is the method of choice for the conjugation of nucleic acids, the use of the other ethynyl-functionalized nucleobases such as EdC, EdA and EdG is limited. Especially the synthesis of alkyne-modified purines EdA and EdG remains challenging task.[88, 109, 116] In order to verify that spin-labeling proposed in this work, is also applicable to other ethynyl modified nucleobases, the spin-labeled azide **43** or **45** had to be introduced into RNA containing one of the ethynyl functionalized nucleobases mentioned above or their 2'- derivatives. Due to the tedious synthesis routes of EdA and EdG the decision was in favor of EdC, the synthesis of which was introduced by Seela and co-workers.[109] Thus, its derivative 5-ethynyl-2'-O-methylcytidine (**EmC**) was synthesized, incorporated into RNA and spin-labeled with **43**. For this purpose, the corresponding phosphoramidite **EmC** was synthesized according to a slightly changed synthesis route of its 2'-deoxy derivative (Scheme 4).[109]

5-Ethynyl-2'-O-methylcytidine **50** was synthesized from commercially available 2'-O-methylcytidine **47** in three steps. The first step included an oxidative iodination of **47** using iodine, DMF and *m*CPBA.[117] In the second step the ethynyl moiety was introduced into **48** by means of Sonogashira coupling in form of TMS protected acetylene at 5th position of the nucleobase[118] followed by the deprotection of TMS group using potassium carbonate in methanol. Then, in order to avoid any side-reactions during the RNA solid phase synthesis an acetyl-protecting group was added to the exocyclic amino group of **50**. Due to a better reactivity of the primary amine with acetyl compared to primary or secondary alcohols, 1.2 eq. of acetic acid anhydride in DMF was sufficient to convert **50** to the corresponding protected cytidine.

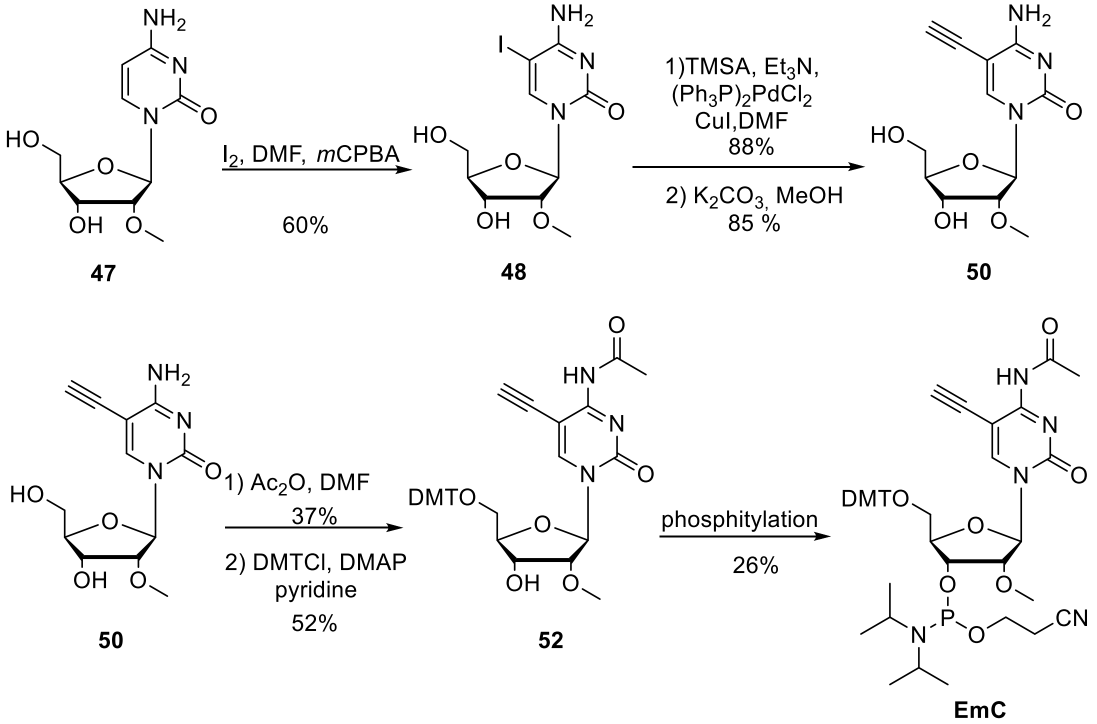

Scheme 4: Synthesis of DMT- protected phosphoramidite **EmC.**

The following DMT protection yielded **52** in sufficient yield (52%). In principle, it is also possible to protect the 5'-OH group of **50** first and then the exocyclic amine group of the nucleobase, as it was proposed by Seela. However, DMT protection of **50** led to very low yield of isolated product (13%) compared to the protection of **51**. In the final step, the phosphoramidite functionality was introduced into 3'-OH group of **52** using 2-cyanoethyl N,N,N′,N′-tetraisopropyldiamidophosphite providing **EmC** in moderate yield.

The resulting **EmC** phosphoramidite was incorporated into a self-complementary RNA sequence **53EmC** by means of solid phase synthesis using previously published coupling conditions for EdU phosphoramidites (Figure 33a)[87]. The coupling efficiency of **EmC** during solid phase synthesis was determined to approximately 30%. After cleavage from the solid support, LCMS analysis of the crude RNA verified a successful incorporation of **EmC** phosphoramidite into RNA **53EmC** (Figure 33b). Peaks I and II were assigned to the single stranded and double stranded **53EmC**, respectively. However, as it is shown in the Figure 33b, in addition to the desired **53EmC** several small unidentified impurities were observed.

The crude **53EmC** was then used in the click reaction without further HPLC purification.[2] After 2h of reaction time, no mass corresponding to the starting material could be found by LCMS analysis. Except small impurities, which have been already observed in the mixture of **53EmC** the main product was assigned to **53Ḉm** (Figure 33c).

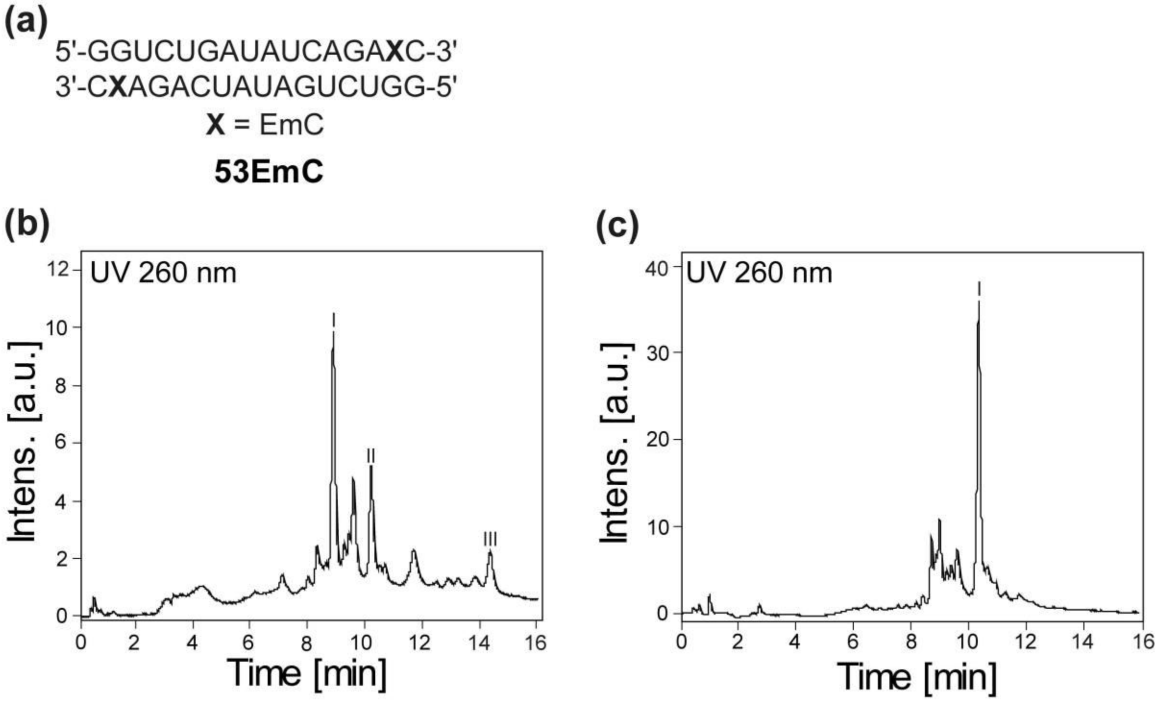

Figure 33: (a) RNA sequence **53EmC**. **EmC** modification is indicated by bold **X**. (b) LCMS analysis of the crude reaction mixture of **EmC** modified self-complementary sequence **53EmC** after RNA synthesis (c) LCMS analysis of the crude reaction mixture of **53Ḉm** using click reaction in solution. Reaction time 2 h. UV peaks are assigned as follows: for (a) **I** = single stranded **53EmC**, **II** = double stranded **53EmC**, **III** = **53EmC** + DMT protecting group; for (b) **I** = **53Ḉm**.

3.1.3.3 Suppressing of RNA degradation during the click reaction

Spin-labeling using click chemistry in solution was also tested on longer EdU modified RNA strands **36nt dŲ68** and **45nt dŲ20** consisting of 36 and 45 nucleotides respectively. Both RNA sequences are fragments of the aptamer domain of TPP riboswitch introduced in the section 3.4. Due to the previously mentioned oxidation of ethynyl moieties during alkaline nucleobase deprotection, commercially available TIPS protected 5-ethynyl-2’-dU phosphoramidites were used in the RNA synthesis of both RNA fragments. The advantage of the TIPS protecting group is that it hinders the oxidation of the ethynyl moieties during the basic nucleobase deprotection and that it can be easily removed in the second deprotection step together with the TBDMS protecting groups.[109]

According to LCMS analysis, the conversion of both EdU modified RNA strands to **45nt dŲ20** and **36nt dŲ68** was quantitative. However, the yields obtained from 5 nmol scale

---

[2] The attached version of 53 to **EmC** is termed here as **Ḉm** for simplicity

reaction after HPLC purification were 0.433 nmol for **45nt dŲ20** and 0.570 nmol for **36nt dŲ68**, which correspond to a relative yield of 9% and 11% respectively. It was assumed that considerable amount of RNA was hydrolyzed by copper ions during the click reaction and then passed through the size exclusion column during desalting procedure. In order to go into the matter of this assumption, reaction mixtures of **45nt dŲ20** and **36nt dŲ68** were directly analyzed by HPLC without prior desalting of the samples. As shown in Figure 34, the presence of two UV peaks of similar size was observed in each HPLC chromatogram (peak I and II).

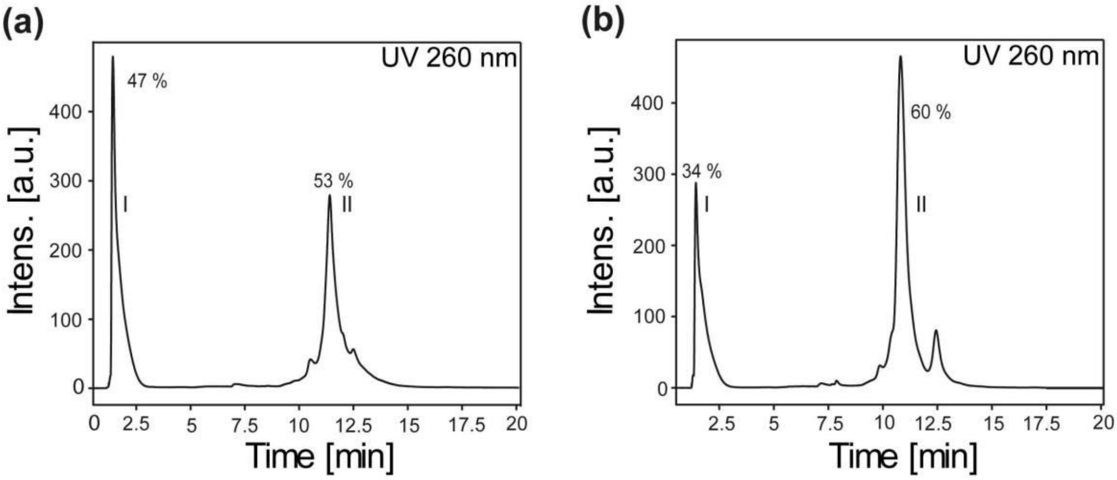

Figure 34: HPLC profiles of reaction mixtures of (a**) 45nt dŲ68** and of (b**) 36nt dŲ68** after 2 h of reaction. UV peaks are assigned as follows: for (a) **I** = The low retention time of peak **I** indicates that this peak could be correlated with hydrolyzed RNA, **II** = **45nt dŲ20**; for (b) **I** = Hydrolyzed RNA, **II** = **36nt dŲ68**.

LCMS analysis of separated UV fractions revealed that in both cases peak II corresponded to the spin-labeled RNA, whereas the mass of peak I could not be identified. Nevertheless, due to the short retention time of peak I, it was assumed that its content could correspond to single nucleotides, which could be generated during RNA degradation. A simple cleavage of RNA would lead to formation of additional UV signals with different retention times corresponding to different RNA sizes. Thus, to increase the yield of spin-labeled RNA click reaction in solution was analyzed in more detail. In order not to waste the high-priced RNA, a short EdU modified DNA sequence **54** (Figure 35a) was used for further analysis of reaction conditions instead of **45nt dŲ68** or **36nt dŲ68**. First, it had to be verified, that the alkyne modified DNA **54** had similar reactivity compared to the alkyne modified RNAs used before. Therefore, **43** was incubated with DNA **54** under the previously described reaction conditions, and resulting reaction mixture was analyzed every 15 min via LCMS (Figure 35b, c). Surprisingly, LCMS analysis revealed quantitative conversion of the starting material already after 15 min. Peak I was associated with DNA containing a ketone functionality, whereas peak II corresponded to the spin-labeled DNA.

(a)

5'-GCACTGT**X**CATTCGCG-3'

X = EdU

54

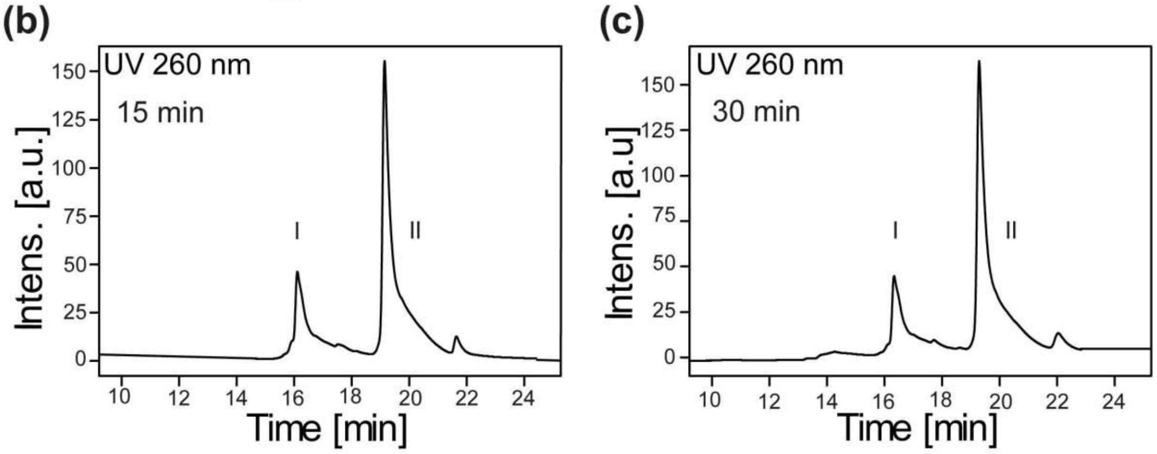

Figure 35: (a) EdU modified DNA sequence **54**. EdU modification is indicated by bold **X**. HPLC reaction time monitoring of spin-labeling of **54** after (b) 15 min and (c) 30 min using click reaction in solution. UV peaks are assigned as follows: **I** = a by-product of **54** containing a ketone functionality, **II** = **54dŲ**.

The final CuI concentration in the click reactions, described in sections 3.1.3.1 and 3.1.3.2 was 4 mM. In the next experiment, an appropriate Cu(I) concentration for click reaction was determined. For this purpose, four click reactions were performed containing 100 µM, 500 µM, 1 mM and 2 mM copper iodide and stopped after 15 min (Figure 36). According to the LCMS analysis of each reaction mixture, only in the case of 100 µM the starting material was not completely consumed (Figure 36).

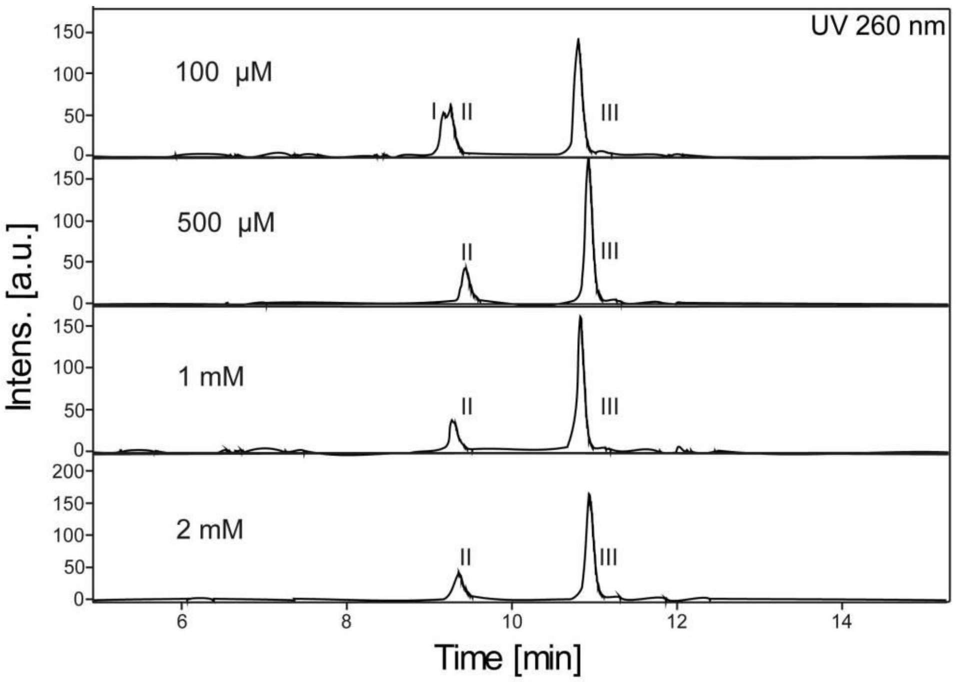

Figure 36: HPLC monitoring of spin-labeling DNA using click chemistry at different CuI concentrations. Reaction time: 15 min. UV peaks are assigned as follows: **I** = **54**, **II** = a by-product of **54** containing a ketone functionality, **III** = **54dỤ**.

This result discloses that already 500 µM CuI is sufficient to convert all of the starting material within 15 min. In order to find out how much RNA would be hydrolyzed under these reaction conditions (500 µM CuI, 15 min reaction time) unmodified RNA **55** (RNA sequence is given in caption 37) was incubated under the same reaction conditions as for the labeling of **54**. Integration of the chromatographic peaks after HPLC purification of **54dỤ** revealed small amounts of presumable RNA degradation (Figure 37a, UV peak at around 1.75 min).

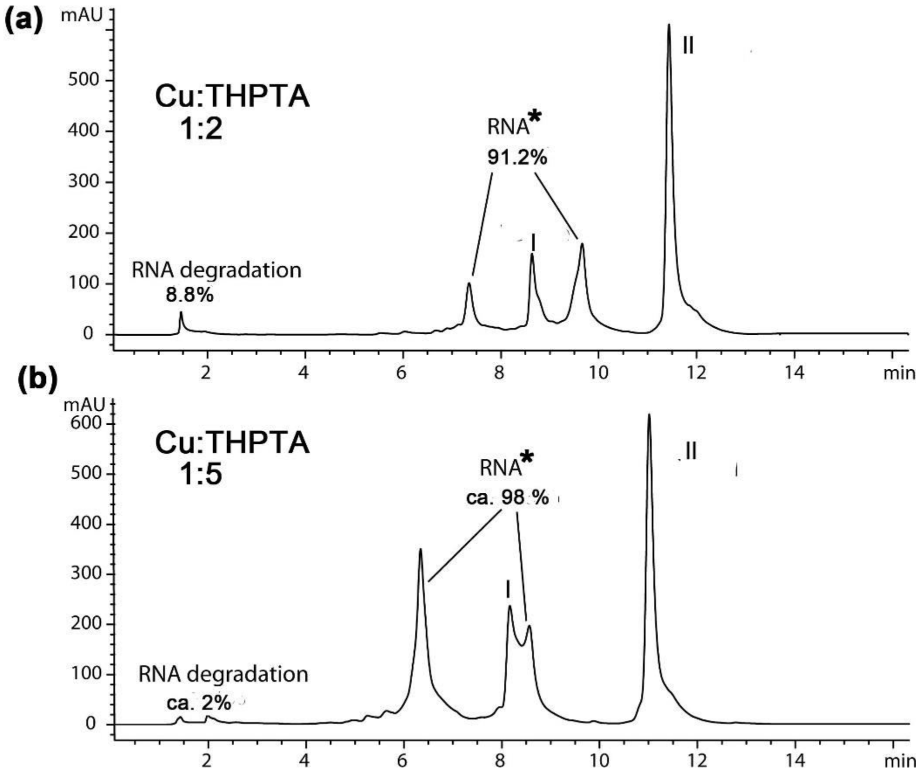

Figure 37: HPLC analysis of spin-labeling DNA **54** using (a) 1:2 Cu:THPTA and (b) 1:5 Cu:THPTA ratios. UV peaks are assigned as follows: **I** =**54** containing a ketone functionality, **II** = **54dŲ**. Black star indicates the unmodified self-complementary RNA **55** (5'-CAUCUGAUAUCAGAUG-3') which has been added in equimolar amount to analyze the level of RNA degradation. Two UV peaks of RNA imply single and double strands.

A possible reason for hydrolyzed RNA still appearing could be insufficient amounts of Cu(I) stabilizing ligand THPTA. Therefore, the ratio of CuI to THPTA was changed from 1 to 2 to 1 to 5 and the resulting reaction mixture analyzed by HPLC (Figure 37b). Indeed, increased amount of THPTA reduced the amount of the peak at 1.75 min from ca 8.8% to ca.2%.

To verify that the improved reaction conditions are also appropriate for alkyne modified RNA, deprotected self-complementary RNA **45** (section 3.1.2.1) was used in the further click reaction as a proof of principle. As it is evident from the HPLC chromatogram in Figure 38a, the conversion of the starting material was quantitative providing the spin-labeled RNA **45dŲ** in excellent yield (95%). In addition, almost no RNA degradation was observed. Interestingly, performing the same reaction for one hour using 4mM CuI, but keeping the ratio of THPTA to Cu(I) 5 to 1 had only minor effect on RNA hydrolysis (Figure 38b). The current data highlight the importance of THPTA as stabilizing ligand for Cu(I) and may serve as an indication that a longer reaction time becomes essential for RNA hydrolysis only in combination with not sufficient amount of THPTA ligand as it was shown in Figure 34 for **36nt dŲ68** and for **45nt dŲ20** respectively.

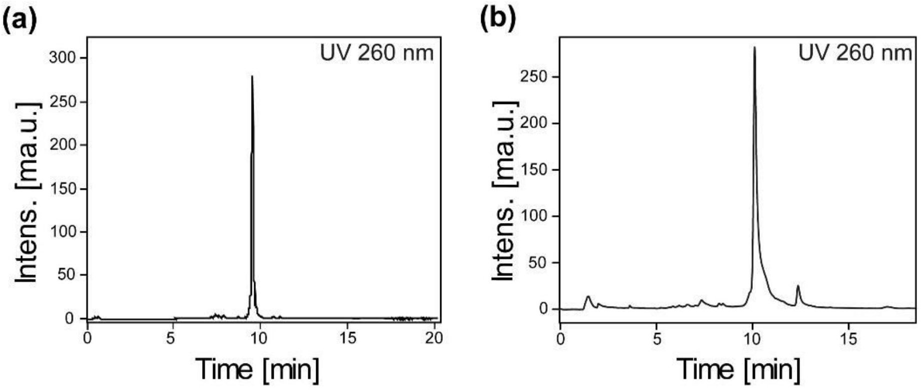

Figure 38: HPLC profiles of the crude reaction of spin-labeling self-complementary sequence **45** via click chemistry in solution for (a) 15 min, 500 µM CuI, 2 mM THPTA, 37°C and (b) 60 min, 4 mM CuI, 20 mM THPTA, 37°C. The major UV signal in each HPLC chromatogram corresponds to the spin-labeled RNA **45dŲ**.

Based on these results, this study showed significant improvements compared to the resent publications related to spin-labeling of DNA by means of click chemistry[86-88]. The reaction time could be drastically reduced from 3h to 15 min, thereby providing a very high efficiency. Moreover, no argon atmosphere was applied and also non-degassed solvents were used, which essentially facilitates the preparation and set-up of the reaction procedure.

3.2 Site-directed spin-labeling of RNA using phosphoramidite approach

One of the most prominent and established examples of spin-labeled phoshoramidites, which have been incorporated into nucleic acids, is the spin label **Ç** and its methylated derivative **Çm** (Figure 39).[59, 119] **Çm** was used in this study for comparison with the **dŲ** label, which has been introduced in previous sections. **Çm** was synthesized and incorporated into a self-complementary RNA **46Çm** according to the literature (section 3.2.3). Then the performance of both labels was analyzed by cw-EPR and PELDOR spectroscopy (sections 3.3.2 and 3.3.3).

In addition, this section also describes an application of click chemistry in the synthesis of the novel spin-labeled phosphoramidites **Ųm** and **Ḉm** (Figure 39).

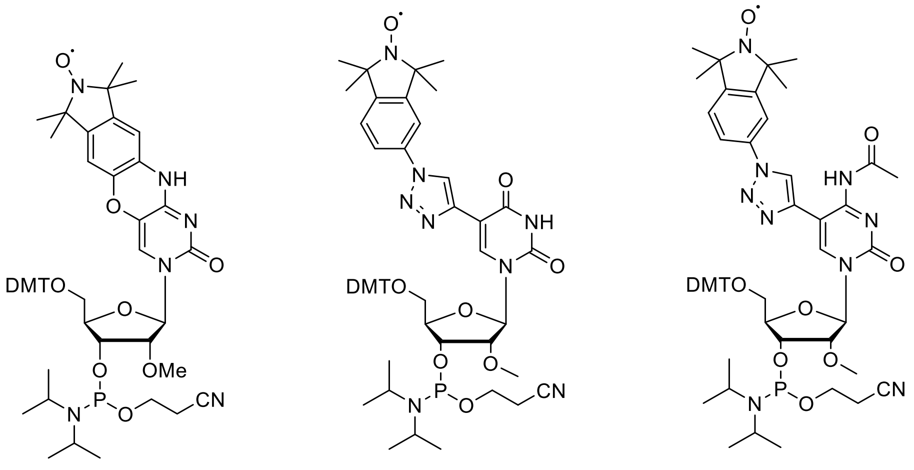

Çm **Ųm** **Ḉm**

Figure 39: Structures of spin-labeled phosphoramidites **Çm**, **Ųm** and **Ḉm**.

3.2.1 Çm label

According to the literature, the synthesis of phoshoramidite **Çm** consists of two synthetic pathways including 16 nonlinear steps (Scheme 5). The first pathway comprises the synthesis of isoindoline-derived moiety **58**.

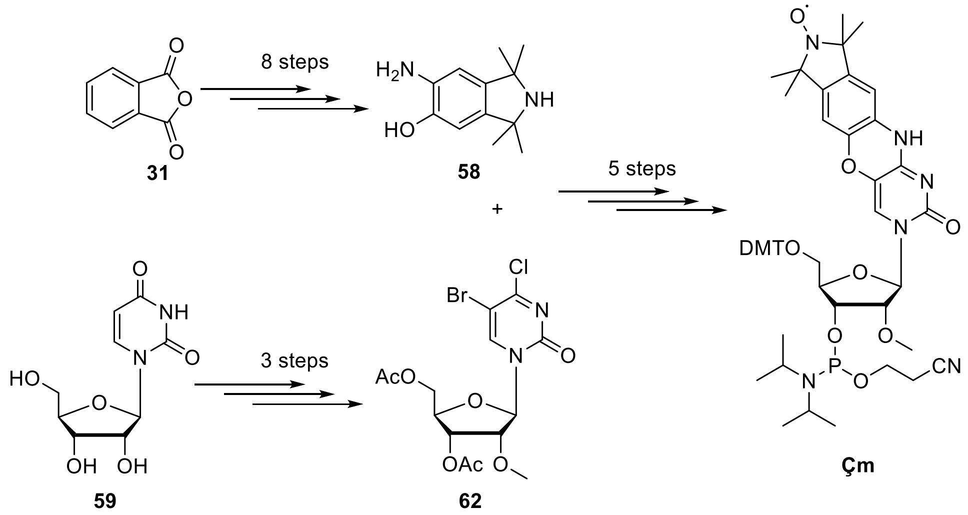

Scheme 5: Overview of the synthesis of phosphoramidite **Çm**.

In the second pathway, **58** is coupled to the activated and protected nucleoside **62** followed by four steps including a cyclization, oxidation, DMT protection and phosphitylation. The starting point of the synthesis of isoindoline derivative **58** is the diazotization reaction in combination with the subsequent hydrolysis of isoindoline-derived amine **39** (Scheme 6), which has been synthesized as a precursor for **43** (Scheme 1).

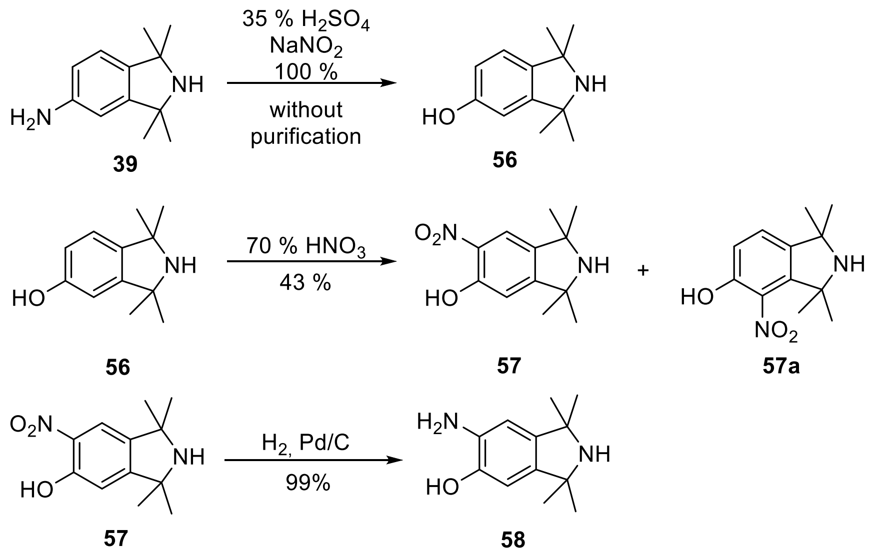

Scheme 6: Synthesis of isoindoline derivative **58**.

The obtained phenol **56**, which was used in the following step without further purification, was converted into a mixture of ortho-nitrated isomers **57** and **57a** by aromatic nitration. Both isomers had similar retention behavior on a SiO_2 column but could be well separated applying dichloromethane as eluent giving the desired isomer **57** in moderate yields. Catalytic hydrogenation of **57** yielded the isoindoline derivative **58**.

In the second pathway, the nucleoside **59** was first brominated at the fifth position of the nucleobase followed by acetyl protection of 3' and 5'-OH groups. The subsequent reaction of **61** with PPh_3 and CCl_4 yielded the corresponding chlorinated and protected nucleoside **62**.

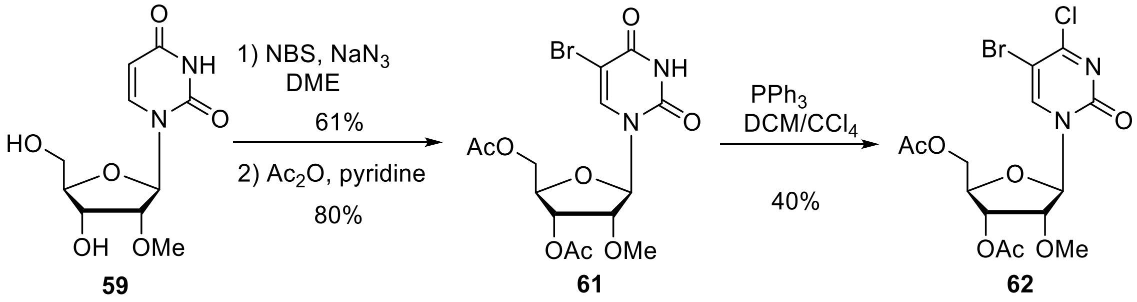

Scheme 7: Synthesis of acetyl protected 4'-chlorinated 5' bromouridine derivative **62**.

The coupling of **58** to **62** was not successful under the reported reaction conditions (Scheme 8). According to the LCMS monitoring, no conversion of the starting material was observed even after 16 h of reaction time. It was assumed that one possible reason could be the low solubility of **58** in DCM that was suggested as a solvent in the reported reaction procedure.[59] Therefore, a solvent mixture of 20% DMF in DCM was applied and the coupling reaction was analyzed by LCMS. Indeed, the starting material was completely converted after 1h of reaction time.

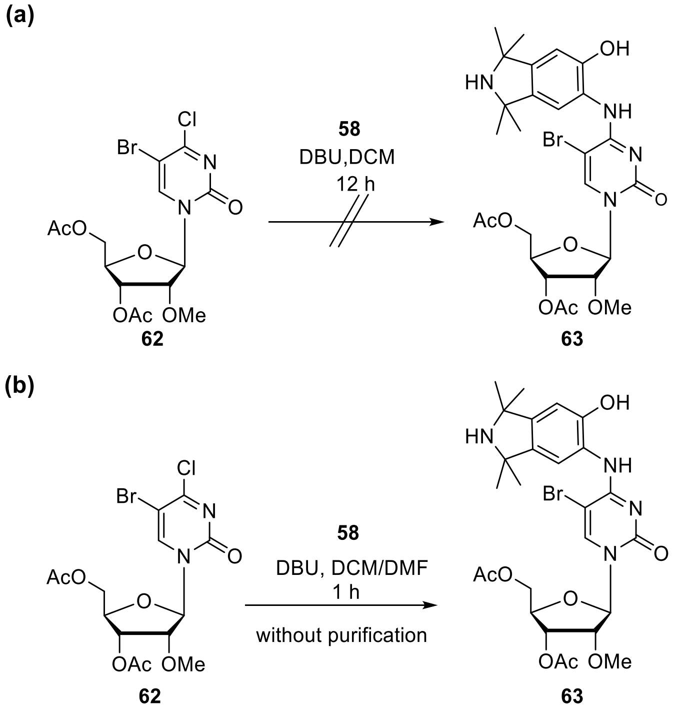

Scheme 8: Coupling of isoindoline-derivative **58** to the dihalogenated nucleoside **62** in (a) DCM and (b) 20% DMF in DCM.

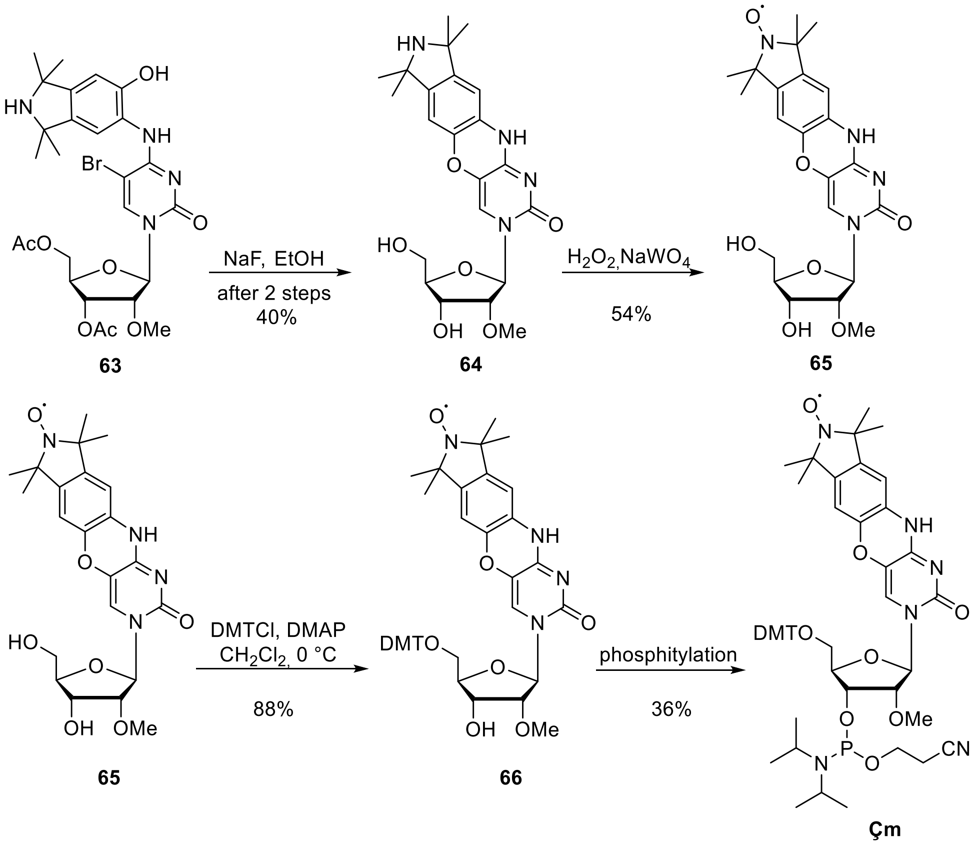

Scheme 9: Synthesis of **Çm**.

The obtained coupling product **63** was used in the following cyclization reaction with NaF in ethanol without purification yielding a phenoxazine derivative **64** in moderate yields (Scheme 9). The oxidation of **64** to its paramagnetic derivative **65** was carried out in methanol in the presence of hydrogen peroxide and sodium tungstate. The generation of the nitroxide spin center was confirmed by EPR spectroscopy. In the next step 5’ hydroxyl group of **65** was protected using 4,4’-dimethoxytriphenylmethyl chloride yielding compound **66** followed by a phosphitylation reaction (Scheme 9). The purification of **Çm** was carried out by means of repeated precipitation in hexane and subsequent SiO_2 column chromatography using neutral silica gel and ethyl acetate as eluent.

3.2.2 Ųm and Ḉm labels

As it was demonstrated in previous sections, click chemistry can be used as an effective method for site-specific spin-labeling of RNA. Moreover, it was also shown that click reaction proceeded with the same efficiency on both ethynyl functionalized uridine and cytidine. However, this approach requires a successful incorporation of the EdU or EmC phorsphoramidites into the corresponding RNA sequence. In principle it should be also possible to introduce **43** or **44** to both ethynyl functionalized uridine and cytidine on the nucleoside level and then convert them to the respective phosphoramidites. As it was shown for cytidine, the introduction of ethynyl moiety to the nucleobase is straightforward and can be accomplished in three steps. Thus, if it can be succeeded to incorporate the corresponding spin-labeled phoshoramidite of uridine or cytidine into RNA with the similar efficiency as post-synthetically this would substantially reduce the entire labeling procedure. For this purpose, synthesis routes of both phoshoramidites, termed here as **Ųm** and **Ḉm** respectively, were elaborated.

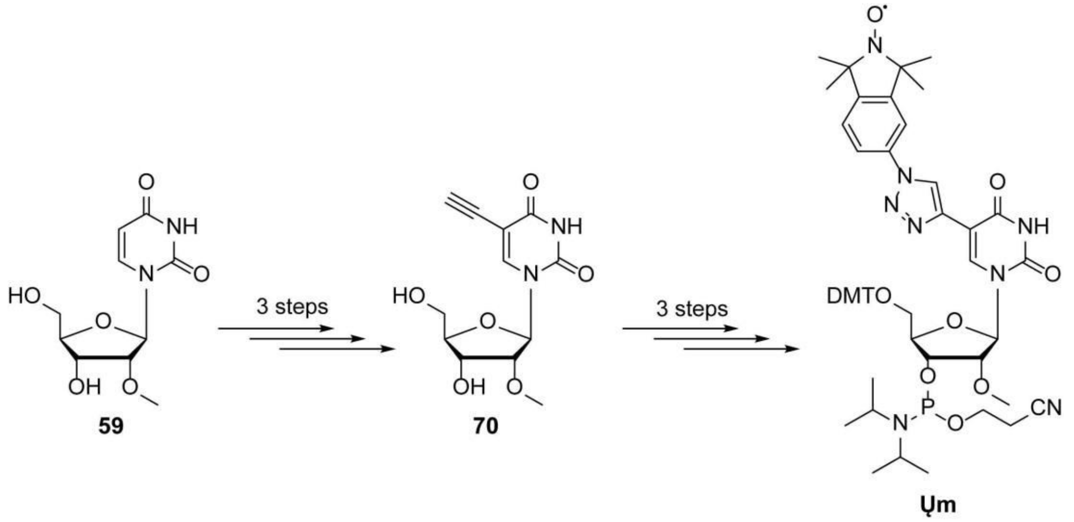

Scheme 10: Overview of the synthesis of phosphoramidite **Ųm**.

The synthesis of the phosphoramidite **Ųm** consists of 6 linear steps and can be divided into two parts (Scheme 10). The first part describes the synthesis of 5-Ethynyl-2‘-O-methyluridine **70**, whereas the second part of synthetic route comprised the spin-labeling of **70** as well as its conversion into the corresponding DMT protected phosphoramidite **Ųm**.

The synthesis route of **Ųm** started with the iodation of the commercially available RNA building block 2‘-O-methyluridine **59** (Scheme 11). For this, the method of Asakura was applied, which implies Ce (IV)-mediated halogenation of uridine at 5th position.[120] This type of halogenation gave **68** in good yield (82%). To introduce the ethynyl moiety into the halogenated uridine **68** palladium catalyzed Sonogashira coupling was used in the next step. This reaction furnished 5-(trimethylsilylethynyl)-2‘-O-methyluridine **69** in a yield of 92 percent. The subsequent deprotection of trimethylsilyl group of **69** using potassium carbonate in methanol yielded the corresponding alkyne modified uridine **70**.

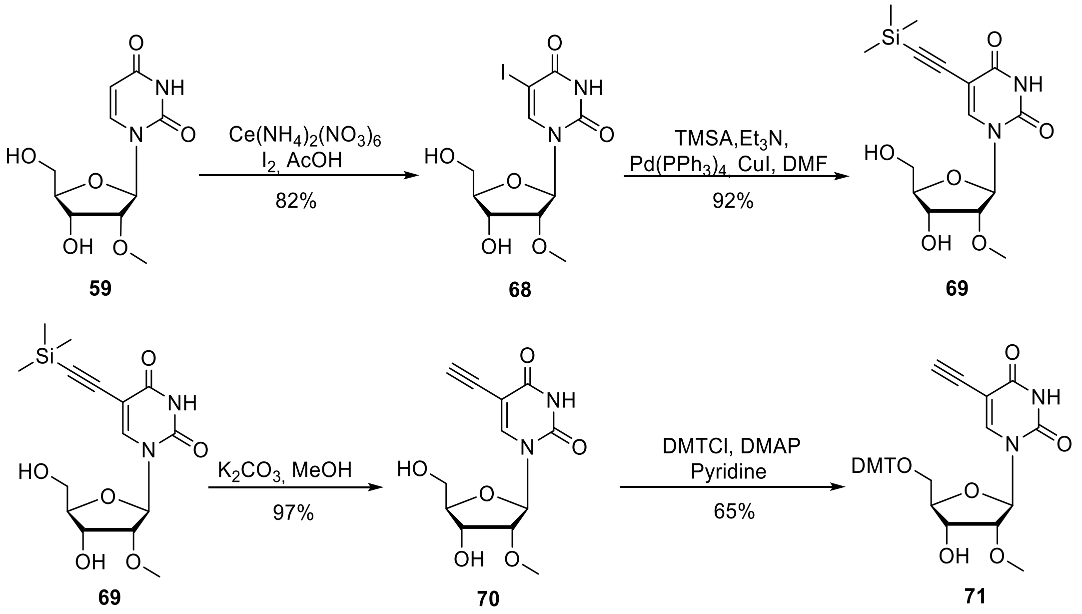

Scheme 11: Synthesis of 5’ DMT-protected alkyne modified uridine **71.**

After the DMT protection of 5’ hydroxy group of **70**, compound **71** was functionalized with spin label **43** by means of click reaction (Scheme 12). This reaction furnished the paramagnetic spin-labeled uridine **72** in excellent yields (93%). In principle, **70** can be first modified with **43** and then protected at 5’-OH group. However, DMT protection and subsequent click reaction provided a slightly higher yield of **72**. The phosphitylation reaction of **72** gave the desired phosphoramidite **Ųm** in sufficient yields (55%) (Scheme 12).

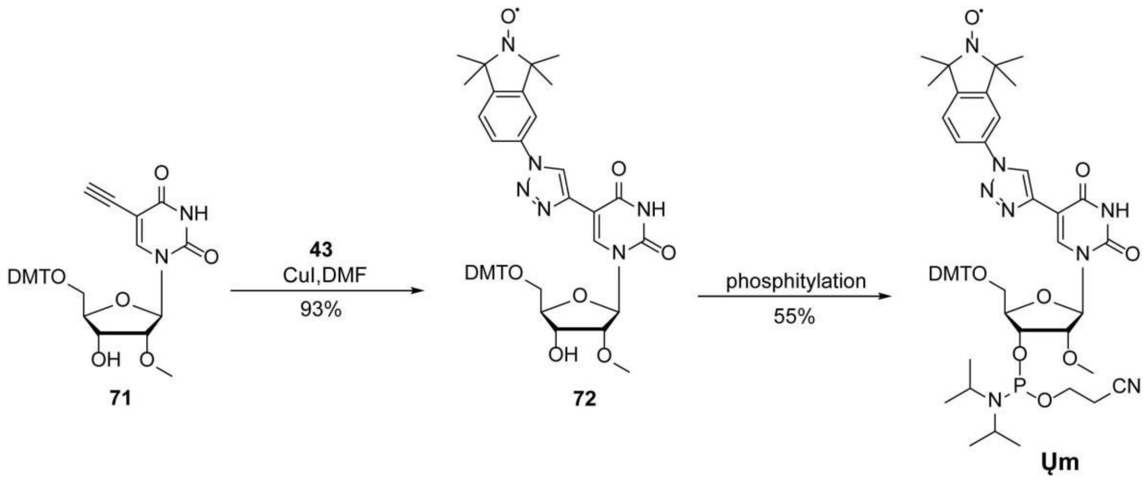

Scheme 12: Synthesis of **Ųm**.

Phosphoramidite **Ḉm** was synthesized applying a similar sequence of reactions as for **Ųm**. The only difference was an additional step, which implied a protection of the exocyclic amine of cytidine with acetyl group as it was shown for the synthesis of **EmC** (section 3.1.3.2). Thus, DMT and acetyl protected cytidine **52** was used in the click reaction to get **74** in good yields (73%). The phosphitylation reaction of **74** provided phosphoramidite **Ḉm** in similar yields as for **Ųm** (Scheme 13).

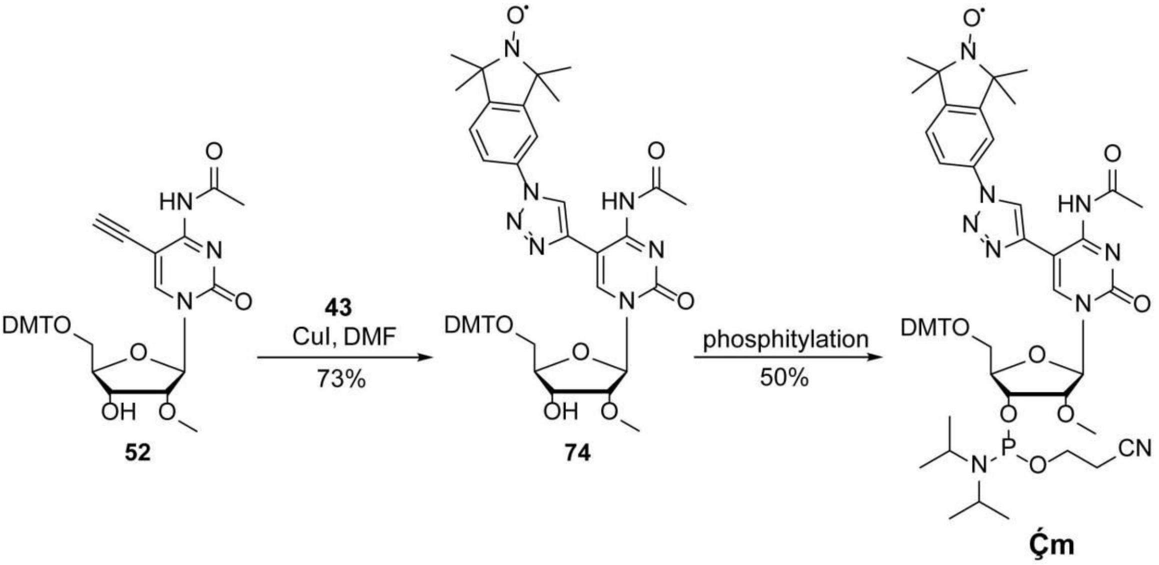

Scheme 13: Synthesis of DMT-protected phosphoramidite **Ḉm**.

3.2.3 Incorporation of Çm, Ųm and Ḉm phosphoramidites in RNA using RNA solid phase synthesis. Comparison to post-synthetic spin-labeling using click chemistry

Synthesized phosphoramidites **Çm** and **Ųm** were incorporated into RNAs **76Çm** and **77Ųm** by means of automated RNA solid phase synthesis (Figure 40a, b). According to the reported synthesis procedures of **Çm** containing RNA, the incorporation of spin-labeled phosphoramidites required modified reaction conditions compared to the conventional RNA synthesis.[59] Due to the sensitive nature of the radicals towards an environment containing reducing agents, great attention should be paid when choosing the chemicals for RNA solid phase synthesis. For instance, iodine, which is commonly used to oxidize P(III) to P(V) during RNA synthesis, can also irreversibly reduce nitroxide of spin-labeled phosphoramidite to its amine.[56, 121] However in the case of **Ç** (analog of **Çm**), it was shown, that the decomposition of **Ç** could be avoided using the milder oxidizing agent 1 M *tert*-butyl hydroperoxide (TBHP) in toluene instead of iodine.[54]

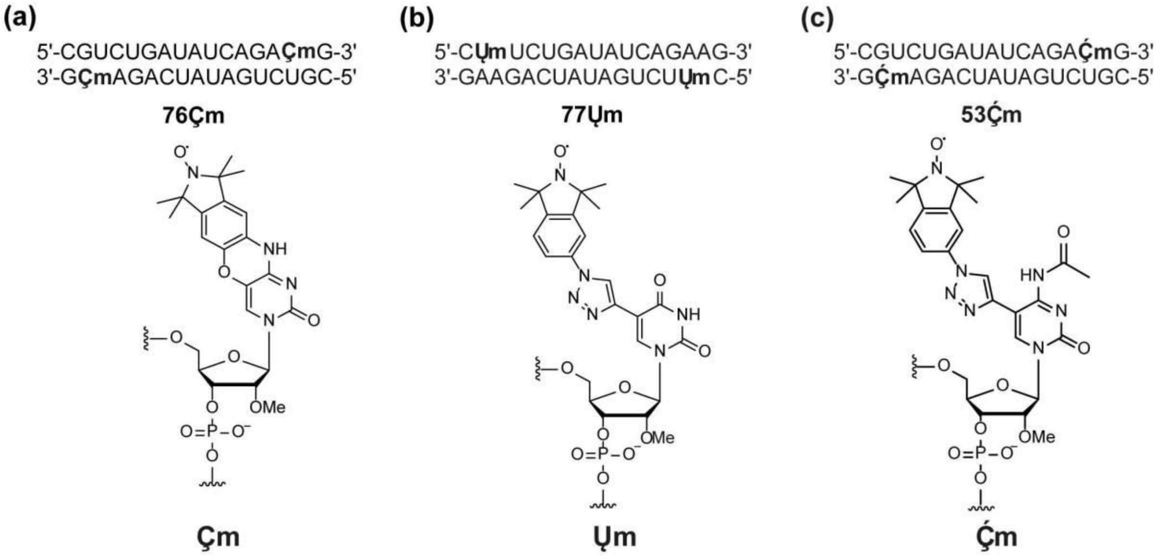

Figure 40: Spin-labeled self-complementary RNA sequences of (a) **Çm** labeled RNA **76Çm**, (b) **Ųm** labeled RNA **77 Ųm** and (c) **Ḉm** labeled RNA **53Ḉm**. The labeling positions are depicted as bold **Çm**, **Ųm** and **Ḉm** respectively. Structures of the incorporated spin-labeled nucleotides are shown below.

Another critical step during the oligonucleotide synthesis using spin-labeled phosphoramidites is the detritylation of the hydroxyl groups. The common reagent for this reaction is 3% trichloroacetic acid (TCA) in dichloromethane. However, according to the literature, incubation of label **Ç** with 3% TCA in DCM demonstrated that under such conditions 5-10% of **Ç** were partially reduced to the corresponding amine after 10 min. Alternative detritylation reagent was found in a milder 3% dichloroacetic acid (DCA) in dichloromethane, which considerably slowed up the reduction of **Ç**.[54] Thus, taking into account the labile nature of nitroxide toward reduction, 1 M TBHP in toluene as well as 3% DCA in DCM were used in the oxidation and detritylation steps respectively during the incorporation of spin-labeled phosphoramidites into the corresponding self-complementary sequences. Moreover, it should be noted that **76Çm** was commercially purchased from Ella Biotech whereas **77Ųm** was synthesized in the laboratory. After the RNA solid phase synthesis both RNA sequences were cleaved from the CPG solid support and their nucleobases were deprotected using standard procedures including a treatment of RNA in a mixture of the concentrated ammonia in methanol and subsequent incubation in 1 M TBAF in THF. The incorporation of spin labels was verified by LCMS. Applying 200 nmol synthesis scale in both cases, the yield of the HPLC purified **76Çm** was amounted to 18 nmol (9%) compared to only 5.2 nmol (3%) for **77Ųm**. It can be assumed that such a discrepancy in the obtained yields might be due to the different RNA synthesizers, which have been used for both, **76Çm** and **77Ųm**. Another reason might be the different coupling efficiency of both phosphoramidites. Nevertheless, both RNA syntheses provided lower yield compared to the introduction of **dŲ** via click chemistry in solution demonstrating again a high efficiency of the novel post-synthetic spin-labeling approach. It should be noted that an attempt was made to introduce label **Ḉm** into **53Ḉm**. However, the RNA synthesis was not successful due to the failed coupling step of **Ḉm** phosphoramidite during the RNA solid phase synthesis.

Comparing the efficiencies of the phosphoramidite approaches discussed above to the efficiency of the post-synthetic labeling of RNA using click chemistry from the section 3.1 clearly highlights the advantages for click-labeling procedure. Whereas click chemistry in solution provided a quantitative conversion of starting material even for RNA containing two ethynyl moieties, the relatively low yield of 16 nt long **76Çm** RNA suggests that the efficiency of the incorporation of two **Çm** labels into RNA of the same size may be even further decreased. The same can be assumed for the long **Çm** containing RNAs.

Incorporation of **Ųm** label into **77Ųm** proceeds with 3% extremely low yield while the introduction of **Ḉm** phosporamidite to **53Ḉm** failed completely. These results indicate that a further thorough analysis of coupling conditions for both **Ųm** and **Ḉm** are required and can be the subject of the future work.

3.3 Influence of spin labels on self-complementary RNA sequences. EPR spectroscopy analysis

3.3.1 CD and thermal denaturation measurements

The influence of **dŲ**, **dŲethyl** **Çm**, **Ųm** and **Ḉm** labels on the secondary structure of RNA duplexes was analyzed by CD spectroscopy (Figure 41). The recorded CD spectra revealed that all duplexes adopt an A-form helix, which is given by the characteristic absorption profile with a minimum at 210 nm and a maximum at 260 nm.[122] However, as it is shown in Figure 41b, both **Çm** and **Ḉm** labels have a noticeable influence on the structure of RNA duplexes. The amplitudes of the extrema in the absorption profiles of both **76Çm** and **53Ḉm** are considerably reduced compared to the non-modified RNA **78**. Similar observations have been made before for **Çm**-labeled RNA.[59] In case of **53Ḉm**, the destabilization effect on RNA seems to be even more pronounced. In contrast, the introduction of **dŲ**, **dŲethyl** and **Ųm** labels in **45dŲ**, **45dŲethyl** and **77Ųm** did not lead to evident changes in the CD spectra showing only very minor effects of the labels on the secondary structures of the respective RNA duplexes.

(a)

5'-CGUCUGAUAUCAGAXG-3'
3'-GXAGACUAUAGUCUGC-5'

78: X = C
76Çm: X = **Çm**
53Ḉm: X = **Ḉm**

5'-CAUCUGAUAUCAGAXG-3'
3'-GXAGACUAUAGUCUAC-5'

55: X = U
45dŲ: X = **dŲ**
45dŲethyl: X = **dŲethyl**

5'-CXUCUGAUAUCAGAAG-3'
3'-GAAGACUAUAGUCUXC-5'

79: X = U
77Ųm: X = **Ųm**

(b)

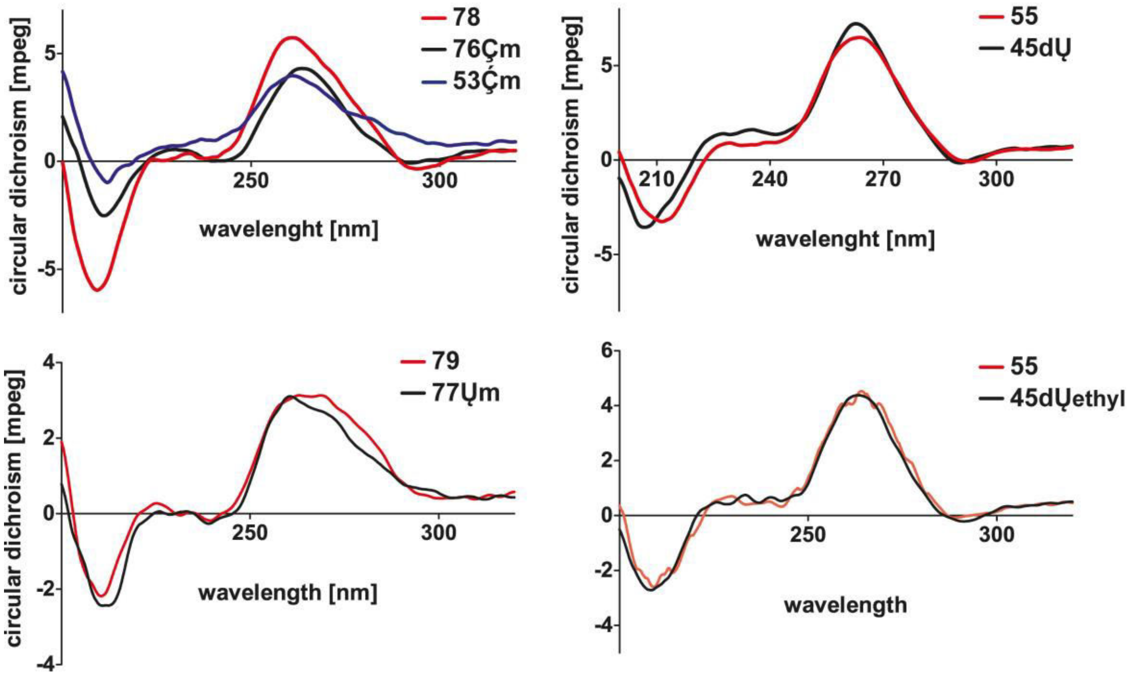

Figure 41: (a) Sequences of non-modified and spin-labeled RNAs. (b) CD spectra of non-modified self-complementary RNAs **55**, **78** ,**79** in comparison to their spin-labeled counterparts **76Çm**, **53Ḉm** **45dŲ**, **45dŲethyl** and **77Ųm**.

In order to investigate the influence of each spin label on the stability of the RNA duplexes, UV melting experiments have been carried out (Table 1). Both labels **dŲ** and **dŲethyl** caused an equal decrease of melting temperature from 66°C for **55** to 58°C for **45dŲ** and **45dŲethyl** respectively. Taking into account a presence of two spin labels in a RNA duplex the decrease of melting temperature caused by each **dŲ(ethyl)** can be amounted to -4 °C. A similar result was obtained before for **dŲ** in DNA.[87] In contrast, the difference between the melting temperatures of **78** (*Tm* = 73°C) and **76Çm** (*Tm* = 72°C) was amounted to only

1 °C. Previously it was shown that the 2’-OMe group of RNA has a positive effect on the overall stability of the 2’-O methylated RNA.[123-124] This effect was attributed to the locking of the ribose moiety in the C3′-endo conformation by the 2’-OMe group.[125]

Table 1 Melting points of spin-labeled RNA duplexes **76Çm**, **53Ḉm**, **45dŲ**, **45dŲethyl**, **77Ųm** as well as of their unlabeled counterparts **78**, **55** and **79.**[a]

Sequence ↓ RNA name→	X = C Tm [°C] **78**	X = **Çm** Tm [°C] **76Çm**	X = **Ḉm** Tm [°C] **53 Ḉm**	X = U Tm [°C] **55**	**79**	X = **dŲ** Tm [°C] **45dŲ**	X = C Tm [°C] **45dŲethyl**	X = **Ųm** Tm [°C] **77Ųm**	ΔT
5‘-CGUCUGAUAUCAGAXG-3‘ 3‘-GXAGACUAUAGUCUGC-5‘	73	72							-1
5‘-CGUCUGAUAUCAGAXG-3‘ 3‘-GXAGACUAUAGUCUGC-5‘	73		62						-11
5‘-CAUCUGAUAUCAGAXG-3‘ 3‘-GXAGACUAUAGUCUAC-5‘				66		58			-8
5‘-CAUCUGAUAUCAGAXG-3‘ 3‘-GXAGACUAUAGUCUAC-5‘				66			58		-8
5‘-CXUCUGAUAUCAGAAG-3‘ 3‘-GAAGACUAUAGUCUXC-5‘					64			68	+4

[a]Tm curves are collected in Appendix.

In case of **53Ḉm**, despite the presence of 2’-OMe protecting group, a decrease of the melting temperature from 73 °C for **78** to 62 °C for **53Ḉm** was observed,. Thus, the destabilizing effect caused by one **Ḉm** label (5.5 °C) is even higher than for **dŲ**. This effect may be assigned to the different stabilities of the corresponding base pairs. CG base pair is more stable than U(T)A[126-127] and, therefore, the hindering of its formation might lead to the greater decrease of the overall thermostability of RNA as compared to the hindered base pair formation between uridine and adenine. In contrast, the melting temperature of **77Ųm** was 4 °C higher than the one of non-modified **79**. Even though, the presence of 2’-OMe group in **Ųm** can contribute to the overall stability of RNA, such an increase of melting temperature of **77Ųm** is quite unexpected. This also contradicts the destabilization effects of **dŲ** and **Ḉm** on RNA duplexes, which share the same nitroxide core with **Ųm** label.

3.3.2 cw-EPR analysis of the dŲ label

Previous cw-EPR measurements on the **dŲ**-modified DNA at room temperature revealed that the label is flexible to some degree.[87] In this section, EPR analysis of the **dŲ**-modified RNA **45dŲ** was carried out at room temperature to analyze the mobility of the label. For comparison, cw-EPR analysis of **76Çm** at room temperature was also performed. As it can be seen from Figure 42, cw-EPR spectra of both RNA duplexes display the typical line pattern of the partially immobilized nitroxide. In order to characterize the nature of the observed nitroxides, both spectra were simulated using the program MultiComponent.[128] According to the simulations, the effective rotational correlation times τ_c were 1.8 and 0.9 ns for **dŲ** in **45dŲ**, whereas in the case of **76Çm** τ_c values for **Çm** were amounted to 7.9 and 0.8 ns respectively. The amount of the spin labels with longer τ_c,

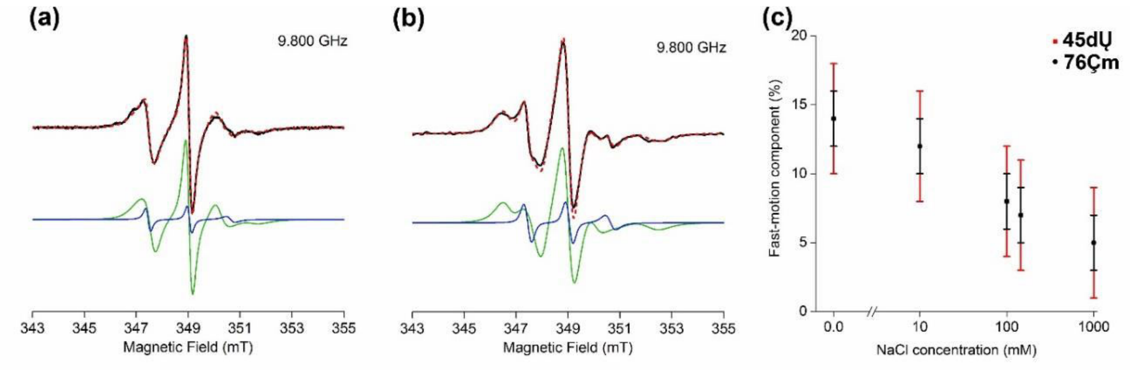

Figure 42: Experimental (black lines) and simulated (red dashes) cw-EPR spectra of (a) **45dŲ** and (b) **76Çm** measured at room temperature. Conditions: 145 mM NaCl, 10 mM $Na_2HPO_4*2H_2O$, 10 mM $Na_2H_2PO_4*2H_2O$, pH 7.0. The simulated spectra of the slow-motion and fast-motion fractions of the spin labels are depicted in green and blue lines, respectively. (c) The amount of the fast-motion fraction of the nitroxides in **45dŲ** and **76Çm** as a function of the NaCl concentration (H. Matsuoka, D. Abdullin).

called here "slow-motion" fraction, is 93% for both cases. The remaining 7% ("fast-motion" fraction) correspond to the spin labels with shorter τ_C. The slow-motion fractions are attributed to spin labels attached to the RNA duplexes, because their rotational correlation times are in the same range as the rotational correlation times of nitroxides introduced into double helices.[59, 87] The appearance of a small fast motion fraction in cw-EPR spectra of **45dŲ** and **76Çm** indicates the presence of single stranded species, which can be due to e.g. RNA duplex dissociation. However, the relatively high melting temperatures of both duplexes contradict this assumption. The presence of free labels in the samples can also be excluded, because the obtained τ_C values are too large for a free label (0.8 for **76Çm** and 0.9 ns for **45dŲ** as compared to ~0.1 ns for the free labels). Another possible explanation of the presence of the small-motion fraction might be a fraying of RNA, in which the ends of RNA duplex go apart creating thereby single stranded ends freely moving in solution. This phenomenon is known to be reduced by increasing salt concentrations.[129] To verify this presumption, the cw-EPR spectra of **45dŲ** and **76Çm** were recorded at different NaCl concentrations and the amount of the "fast motion" fraction was determined for each case. Indeed, increasing the concentration of NaCl from 0 to 1 M lead to a gradual decrease of the fast-motion fraction from 14% to 5% in both RNA duplexes. (Fig. 43c and Table 2).

Comparing the rotational correlation times of the slow-motion fraction in **45dŲ** (τ_C = 1.8 ns) and **76Çm** (τ_C = 7.9 ns) also reveals that **dŲ** label possesses a considerably higher mobility at room temperature as compared to **Çm**. The obtained differences in mobility can be related mainly to the mobility of their linkers, because both RNAs are almost identical in structure.

Table 2 Dependence of slow-motion fraction of **45dŲ** and **76Çm** on different NaCl concentrations (H. Matsuoka, D. Abdullin).

NaCl concentration (mM)	Fast motion Fraction (%)	
	45dŲ	**76Çm**
0	0.14 ± 0.04	0.14 ± 0.04
10	0.12 ± 0.04	0.12 ± 0.04
100	0.08 ± 0.04	0.08 ± 0.04
145	0.07 ± 0.04	0.07 ± 0.04
1000	0.05 ± 0.04	0.05 ± 0.04

3.3.3 PELDOR measurements of 45dŲ and 76Çm

The self-complementarity of **45dŲ** and **76Çm** implies the presence of two spin labels in each RNA duplex. This enables one to apply PELDOR spectroscopy on both RNA duplexes to compare the performance of both spin labels in distance measurements. Previous X- and G-band PELDOR studies of **Ç** or **Çm** containing nucleic acids revealed strong dependence of the corresponding PELDOR time traces on the relative orientation between the labels.[60, 130-132] In this study, the obtained Q-band PELDOR time traces of **76Çm**, were also found to be strongly orientation selective, which is reflected by varying modulation depth and modulation frequencies at different frequencies offsets (Figure 43).

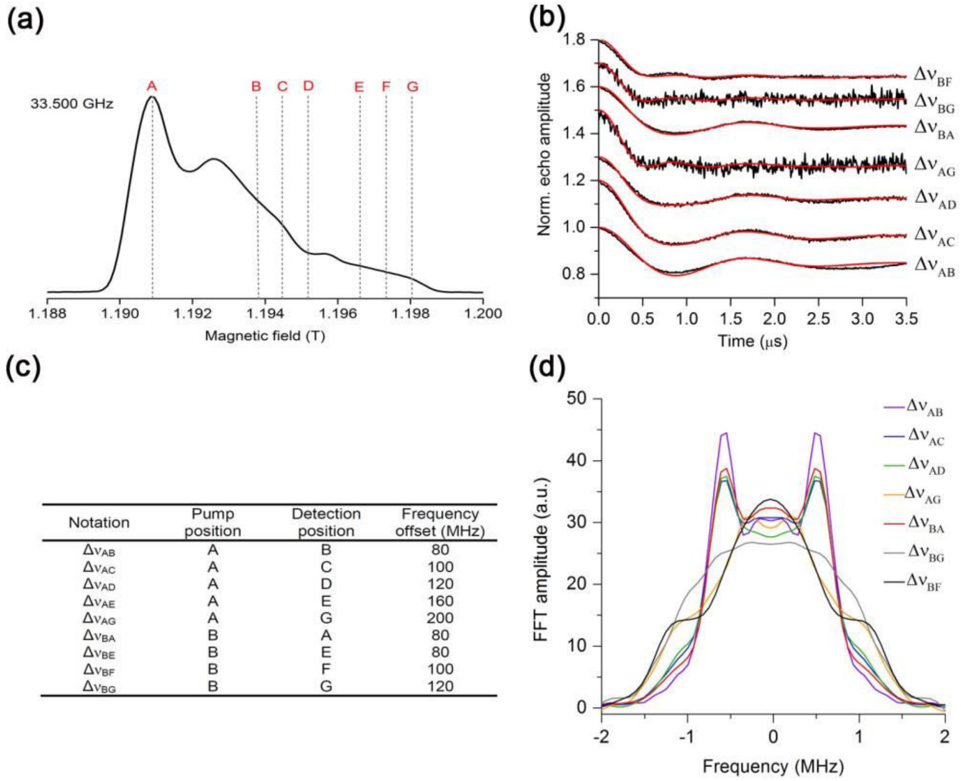

Notation	Pump position	Detection position	Frequency offset (MHz)
$\Delta\nu_{AB}$	A	B	80
$\Delta\nu_{AC}$	A	C	100
$\Delta\nu_{AD}$	A	D	120
$\Delta\nu_{AE}$	A	E	160
$\Delta\nu_{AG}$	A	G	200
$\Delta\nu_{BA}$	B	A	80
$\Delta\nu_{BE}$	B	E	80
$\Delta\nu_{BF}$	B	F	100
$\Delta\nu_{BG}$	B	G	120

Figure 43: (a) Q-band spectrum of the **76Çm**. Different pump/detection positions are shown by dashed lines and labeled by letters. The corresponding notations of different frequency offsets are given in the table in table (c). (b) PELDOR time traces (black) acquired at different frequency offsets are overlaid with their simulations (red) obtained using program PeldorFit[101] for **76Çm**. (d) Fourier transformations of the experimental PELDOR time traces of **76Çm** (H. Matsuoka, D. Abdullin).

Moreover, the PELDOR time traces of **45dŲ** also revealed a strong orientation selectivity (Figure 44). This result was unexpected, since cw-EPR spectra of **45dŲ** disclosed higher flexibility of its nitroxide group as compared to the nitroxide group of **Çm** at room temperature (Figure 42). Experimentally obtained time traces of both **76Çm** and **45dŲ** could be well fitted by using a program PeldorFit.[101, 133] For **76Çm**, PeldorFit yielded the distance distribution with the mean distance of 4.30 nm and the standard deviation of 0.24 nm. In case of **45dŲ**, the determined mean distance as well as the standard deviation were 4.68 nm and 0.24 nm, respectively. A more detailed analysis of the corresponding time traces of **76Çm** and **45dŲ** can be found in Ref.[133]

A similar amount of orientation selectivity as well as the similar widths of the inter-label distance distributions for both RNA duplexes clearly indicate that the mobility of the **dŲ** label in the frozen sample is similar to that of the **Çm** label. To analyze the dynamics of **dŲ** label, DFT calculations of the spin-labeled nucleobase of **dŲ** were performed. The optimized structure obtained by DFT calculations provided an almost planar geometry of the nucleobase of **dŲ** (Figure 45).

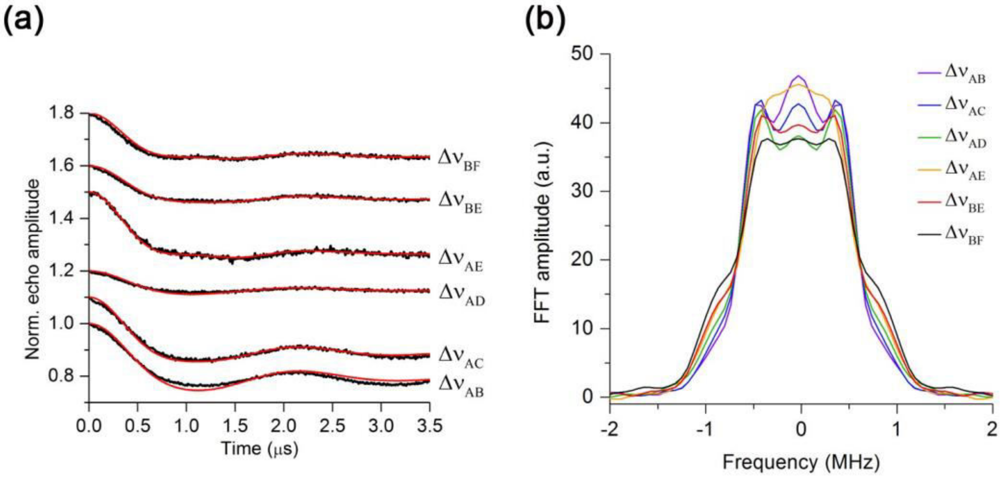

Figure 44: (a) PELDOR time traces (black) acquired at different frequency offsets are overlaid with their simulations (red) for **45dŲ**. The corresponding notations of different frequency offsets are given in the table in Figure 43 (c). (b) Fourier transformations of the experimental PELDOR time traces of **45dŲ** (H. Matsuoka, D. Abdullin).

In order to analyze the motions of both, nitroxide and triazol moiety in more detail, a relaxed scan of the energy profiles for the dihedral angles $\chi 1$ (C1-C2-C3-C4) and $\chi 2$ (C4-N1-C6-C7) was performed (Figure 45). The energy profile of $\chi 1$ yielded an energetic barrier of 50 kJ/mol and a single energy minimum at 0°. This result is in a good agreement with the previous *in silico* calculations obtained for triazole functionalized deoxyuridine.[134] Such a high energetic barrier is presumably caused through the repulsion between the lone pairs of the nitrogen of triazole and the oxygen of uridine. Consequently, it can be assumed, that the rotation of the triazole moiety around the C2-C3 bond is hindered even at the room temperature resulting in the coplanar conformation with uridine. In contrast, an energetic barrier of 14 kJ/mol and 2 energetically equal minima around 0° and 180° were obtained for χ2. Taking into account, that the energy of this barrier is relatively low it is not further surprising to observe higher mobility of **dŲ** compared to the rigid label **Çm** at room temperature.

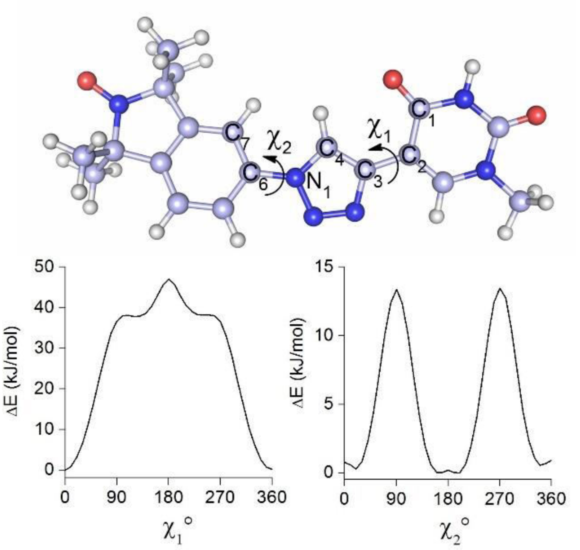

Figure 45: DFT structure of the **dŲ** nucleobase. The carbon, oxygen, nitrogen, and hydrogen atoms are colored light blue, red, blue and grey, respectively. The dihedral angles χ1 (C1-C2-C3-C4) and χ2 (C4-N1-C6-C7) are shown by arrows. Torsional energy profiles for these angles are shown below (D. Abdullin).

The nitroxide moiety can probably overcome this energy barrier at the room temperature, resulting in its rotation around N1-C6 bond. The low energy barriers obtained for χ2 suggest that lowering the temperature to the freezing point of the solvent may stabilize one of the energetically favorable conformations of the N1-C6 bond.

To compare the accuracy of the obtained PELDOR results for **45dŲ** and **76Çm** both structures including the spin labels were modelled. To model the structures of the corresponding A form RNA duplexes program 3DNA was applied.[135] Subsequently, the program MtsslWizard[136-138] was used to introduce the labels to the previously generated RNA structures. For this purpose, label **Ç** was taken from the literature and used as a model for **Çm**, whereas for **dŲ** label the DFT-optimized structure was applied (Figure 46).The predicted distance for the model of **45dŲ** was amounted to 4.78 nm and deviated from the PELDOR-obtained value (4.67) by 0.11 nm only. In contrast, the predicted inter-labeled distance for **76Çm** was 3.71 nm and deviated from the experimentally obtained value (4.30 nm) by 0.59 nm indicating a poor accuracy of the applied model. One possible explanation for the observed deviation for **76Çm** might be a different orientation of the cytidine nucleobase caused by 2' methoxy-group, which is not considered in the model of **Ç** (Figure 47). Therefore, the model **Ç** was substituted by its 2'-methylated version using its crystal structure from the literature.[139] Indeed, using 2’-methylated derivative of **Ç** could decrease the observed deviation from 0.59 nm to 0.3 nm. Nevertheless, remaining 0.3 nm of deviation indicate that **Çm** labels can lead to some changes of the helix structure. Another indication for this assumption was observed before in the reduced extrema in the CD spectrum of **76Çm** as compared to **78** (section 3.3.1).

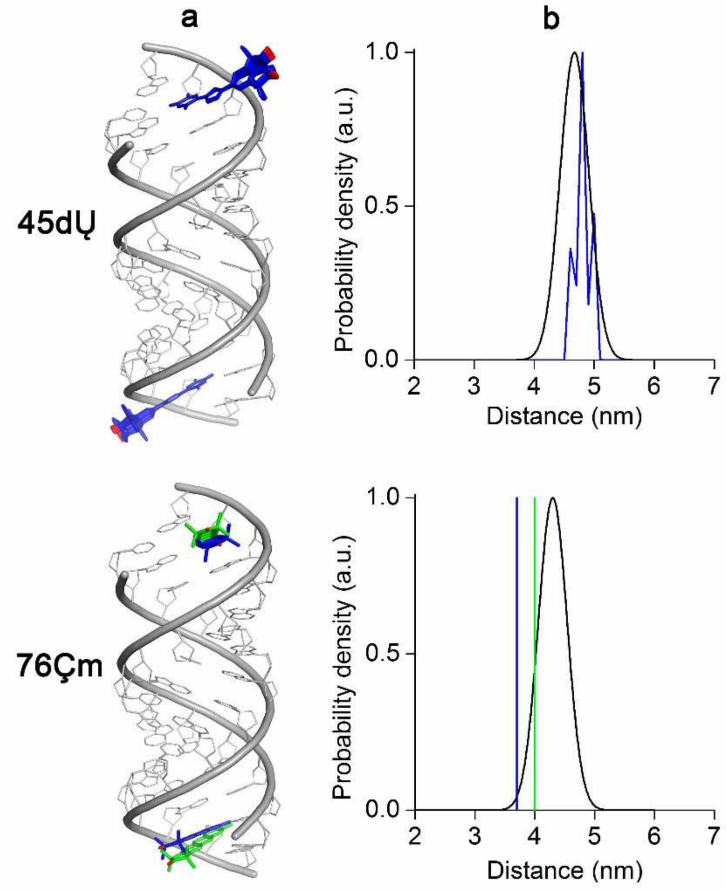

Figure 46: (a) Modelled structures of the spin-labeled RNA duplexes **45dŲ** and **76Çm**. Spin labels are depicted as blue sticks with a red drawn oxygen atom. The methylated version of **Ç** label is shown with green color. (b) Predicted distances (blue) are overlaid with PeldorFit-obtained distances (black). The inter-label distances predicted for the 2’-methylated **Ç** is depicted in green (D. Abdullin).

Based on these results it can be stated that **dŲ** label possesses similar properties at low temperature as the well-established rigid **Çm** label. Moreover, the set of the orientation-selective PELDOR time traces, which has been obtained for **45dŲ** enables one to apply **dŲ** not only for distance determination but also for relative orientations of the labels yielding thereby additional structural information. This is a significant result since it highlights an alternative approach of introducing nitroxide moieties of similar rigidity (in the frozen sample) as **Çm** to RNA. In addition, synthesis and labeling procedure of **dŲ** are substantially easier than of **Çm**, which considerably facilitates an access to RNA containing rigid spin labels.

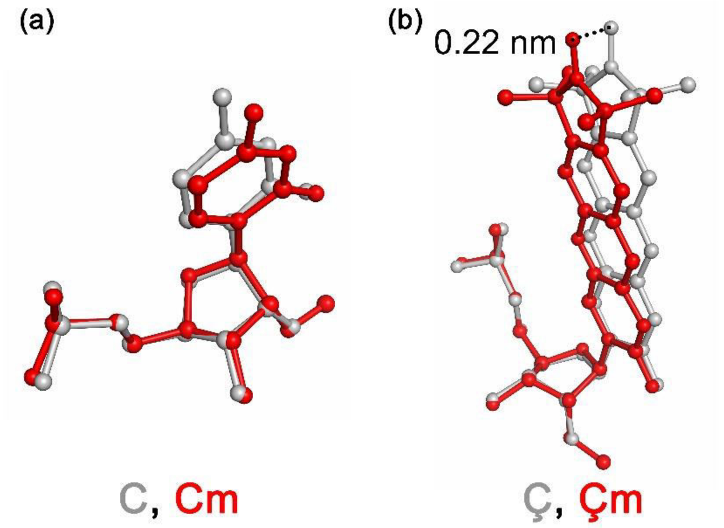

Figure 47: Influence of 2’ methoxy group on the orientation of **Çm**. (a) Structure of cytidine C (grey, generated by the program 3DNA[135]) is overlaid with its 2’-methylated derivative **Cm** (red, adapted from the crystal structure with PDB-ID 310D[139]). (b) The overlaid structures of **Ç** (grey) and **Çm** (red) (D. Abdullin).

3.3.4 Relaxation times T_2 of Çm, dŲ and dŲethyl in comparison

The effect of the alkyl substituent on the T_2 relaxation time was studied for the **Çm**, **dŲ** and **dŲethyl** labels in the self-complementary sequences **76Çm**, **45dŲ** and **45dŲethyl** respectively (Figure 48). The T_2 relaxation curves of the labels **dŲ** and **Çm** decay to 0 in about 5 µs, whereas the T_2 relaxation curve of the **dŲethyl** label reaches 0 after 15 µs. This shows that T_2 relaxation time of the **dŲethyl** label is significantly larger than that of **dŲ** and **Çm**. Thus, the **dŲethyl** label can allow PELDOR measurements at higher temperatures and determination of longer distances.

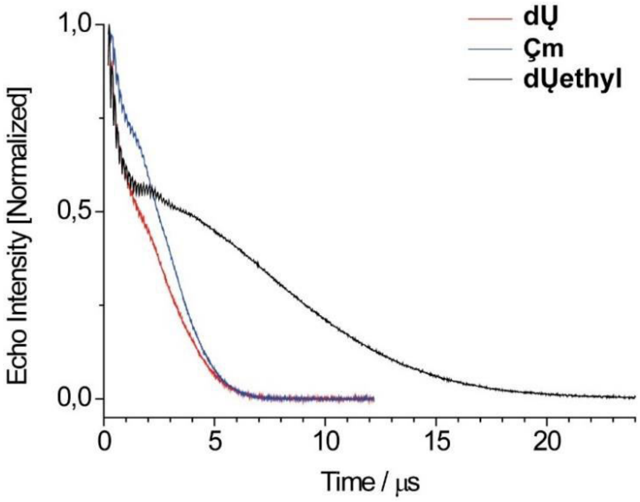

Figure 48: Relaxation times T_2 of **Çm**, **dŲ** and **dŲethyl** labels incorporated in the self-complementary sequences **44Çm**, **45dŲ** and **45dŲethyl** (H. Matsuoka).

3.4 Spin-labeling of Riboswitches through ligation and click chemistry in solution and their EPR analysis

Since the solid phase synthesis is suitable only for relatively short RNAs (roughly 50 nucleotides), site-specific spin-labeling of long RNAs is still a challenging task. The development of the efficient methods for the spin-labeling of long RNAs is therefore of great interest.

This section describes the spin-labeling of long RNAs in solution using click chemistry, the method that was introduced in the section 3.1.3. First, the spin-labeling of the 34 nt long aptamer domain of the preQ1 riboswitch from *Fsu* is described as a proof-of-principle study (Scheme 14a). Second, the applicability of the click chemistry approach to long RNAs was tested on the 81 nt long aptamer domain of TPP riboswitch from *E. coli* (Scheme 14b).

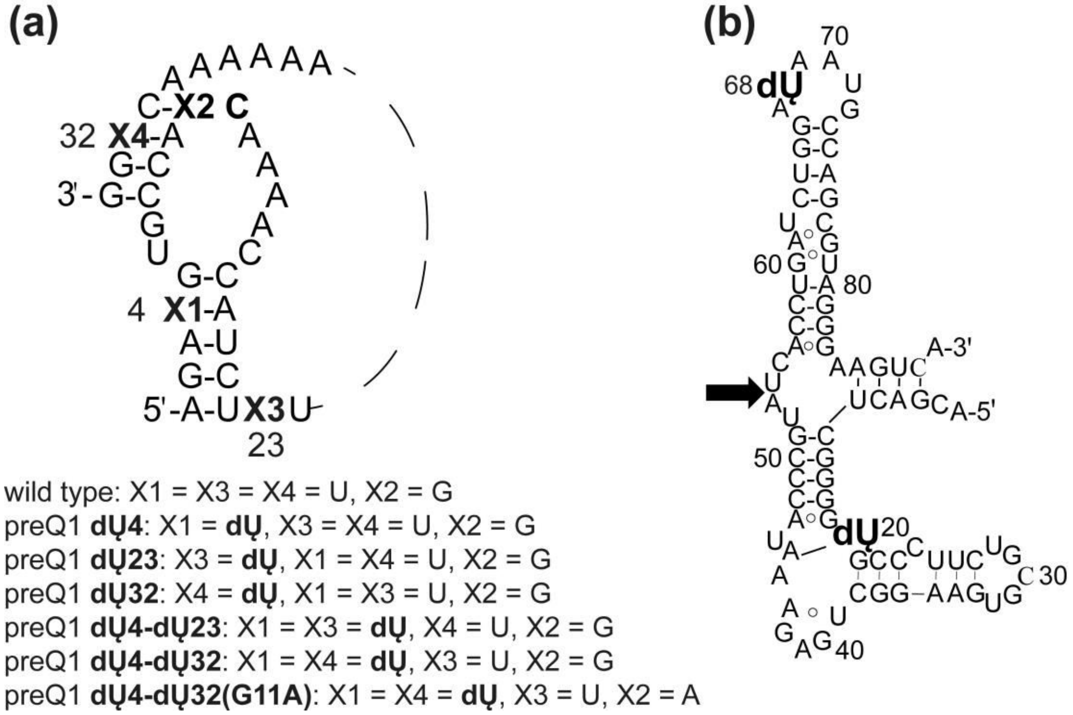

wild type: X1 = X3 = X4 = U, X2 = G
preQ1 **dŲ4**: X1 = **dŲ**, X3 = X4 = U, X2 = G
preQ1 **dŲ23**: X3 = **dŲ**, X1 = X4 = U, X2 = G
preQ1 **dŲ32**: X4 = **dŲ**, X1 = X3 = U, X2 = G
preQ1 **dŲ4-dŲ23**: X1 = X3 = **dŲ**, X4 = U, X2 = G
preQ1 **dŲ4-dŲ32**: X1 = X4 = **dŲ**, X3 = U, X2 = G
preQ1 **dŲ4-dŲ32(G11A)**: X1 = X4 = **dŲ**, X3 = U, X2 = A

Scheme 14: Secondary structure of the (a) preQ1 and (b) TPP aptamer domains in the folded states. For preQ1 aptamer domain spin-labeled and mutated positions are indicated as X1, X2, X3 and X4. For TPP aptamer domain spin-labeled positions are indicated as **dŲ**. The black arrow indicates the ligation site.

Due to the long sequence of the aptamer domain of TPP riboswitch, two separate fragments of this domain were synthesized, spin-labeled and ligated to each other. Both spin-labeled aptamer domains were analyzed by EPR spectroscopy. In addition, the influence of the spin labels on the stability of the RNAs was studied by means of CD spectroscopy and thermal denaturation experiments.

3.4.1 Spin-labeling of the preQ1 aptamer domain

The efficiency of spin-labeling of long RNA in solution via click chemistry was benchmarked on the 34 nt long aptamer domain of the preQ1 riboswitch from *Fsu*. Using the click chemistry approach, three single mutants (preQ1 **dŲ4**, preQ1 **dŲ23**, and preQ1 **dŲ32**) and three double mutants (preQ1 **dŲ4-dŲ32**, preQ1 **dŲ4-dŲ23,** and preQ1 **dŲ4-dŲ32(G11A)**) of the aptamer domain were prepared. Mutant **dŲ4-dŲ32(G11A)** was used as a control since the point mutation G11A leads to a reduced affinity of the aptamer domain to the preQ1 ligand.[140] LCMS monitoring of the reactions revealed that the starting materials were fully converted after 30 min for all six mutants. The quantitative conversion of the starting material was achieved also for the mutants that contain two ethynyl modifications (Figure 49). The identity of the oligos was verified by means of ESI (Table 3). Starting with 2.5 nmol RNA, a yield of 1.8 nmol spin-labeled RNA (72%) was obtained at the end on average.

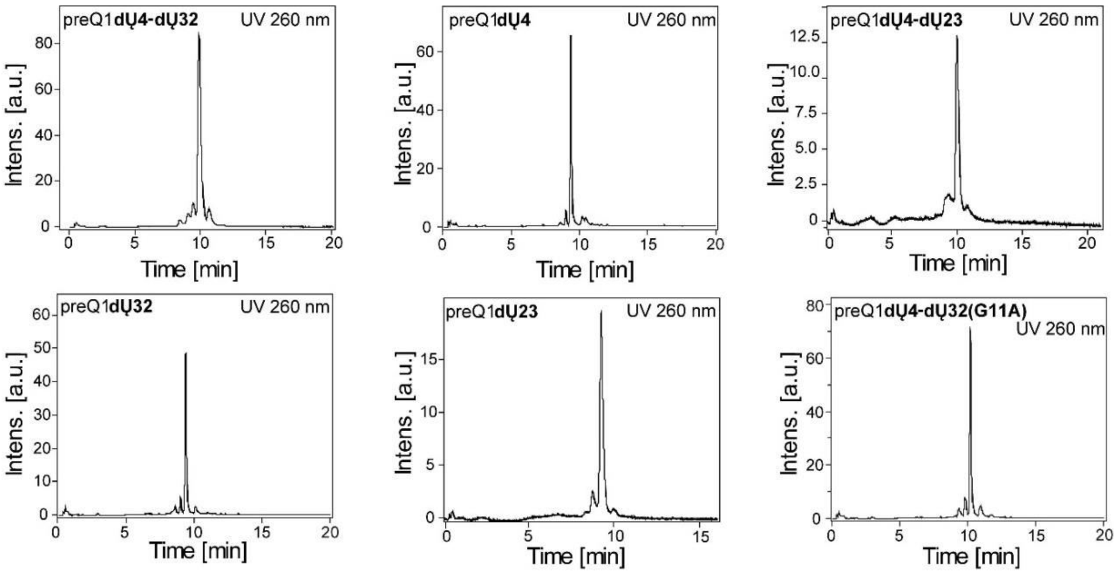

Figure 49: LCMS analysis of the click reactions of preQ1 mutants after 30 min of reaction time. The major UV signal in each chromatogram corresponds to the spin-labeled product.

Table 3 ESI spectroscopic analysis of the most intense UV peak from Figure 49

Spin-labeled constructs	Mass calc. [m/z]	Mass found [m/z]
preQ1 **dŲ4**	11135.66	11137.74
preQ1 **dŲ32**	11135.66	11137.51
preQ1 **dŲ23**	11135.66	11137.09
preQ1 **dŲ4-dŲ32**	11376.78	11376.71
preQ1 **dŲ4-dŲ32(G11A)**	11360.81	11360.96
preQ1 **dŲ4-dŲ23**	11376.78	11376.42

3.4.2 UV-Vis and CD spectroscopy of preQ1 mutants

Previous studies of the preQ1 riboswitch have reported that it adopts a stem-loop structure I with the 3’ overhang (Scheme 15).[141] In addition, Micura proposed the model for the conformation exchange in the riboswitch based on NMR studies. According to this model, the riboswitch is pre-organized in an H-type pseudoknot-like structure II in the presence of Mg^{2+} ions (Scheme 15). This structure is also similar to the ligand-bound conformation III (Scheme 15).[140, 142-143] It is known from the literature that CD spectroscopy allows to follow such a pseudoknot folding process.[50, 144] In particular, the pseudoknot formation leads to an increase of the CD bands at 260 and 210 nm. The CD measurements on the wild-type preQ1 aptamer domain and the mutant preQ1 **dŲ23** after the addition of Mg^{2+} confirmed this. As it is shown on the right side in Figure 50, the amplitudes of the bands at 260 and 210 nm are increased to a similar extent for both wild type and preQ1 **dŲ23** compared to the left side. This indicates that the spin-labeling of the position U23 does not affect the pseudoknot formation. In contrast, the relative increase of the amplitudes of the absorption bands for preQ1 **dŲ4**, preQ1 **dŲ32** and other double mutants is less pronounced. This suggests that **dŲ** labels at these positions have an influence on the pseudoknot formation.

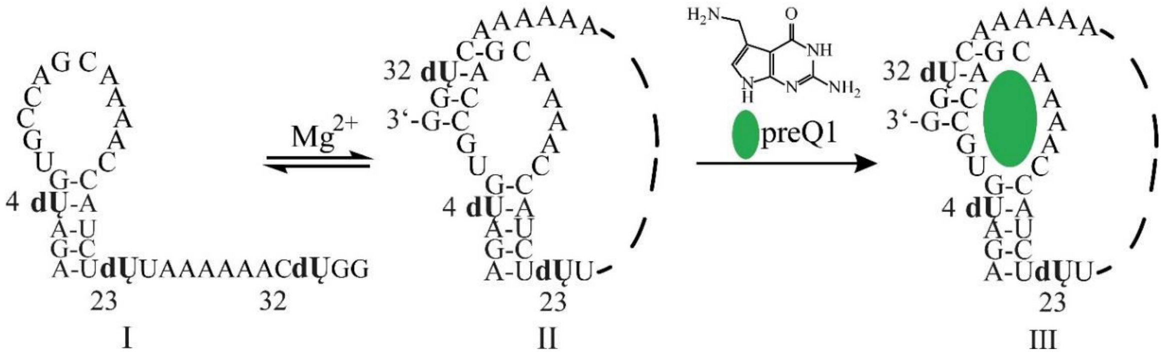

Scheme 15: Schematic representation of the conformational exchange proposed for the aptamer domain of the preQ1 riboswitch.[140-143] Spin-labeled positions are depicted by **dŲ**.

Another evidence of the destabilizing effect of spin label **dŲ4** and **dŲ32** was obtained by measuring the melting curves. In the absence of Mg^{2+}, spin label at position U4 showed with 8 °C the largest decrease in T_m compared to the wild type. A similar effect was also observed for **dŲ** label at position U32 (decrease in T_m of 5 °C). In contrast, the spin-labeling of the position **U23** leads to only a minor decrease in T_m (3 °C) supporting the CD spectra discussed above.

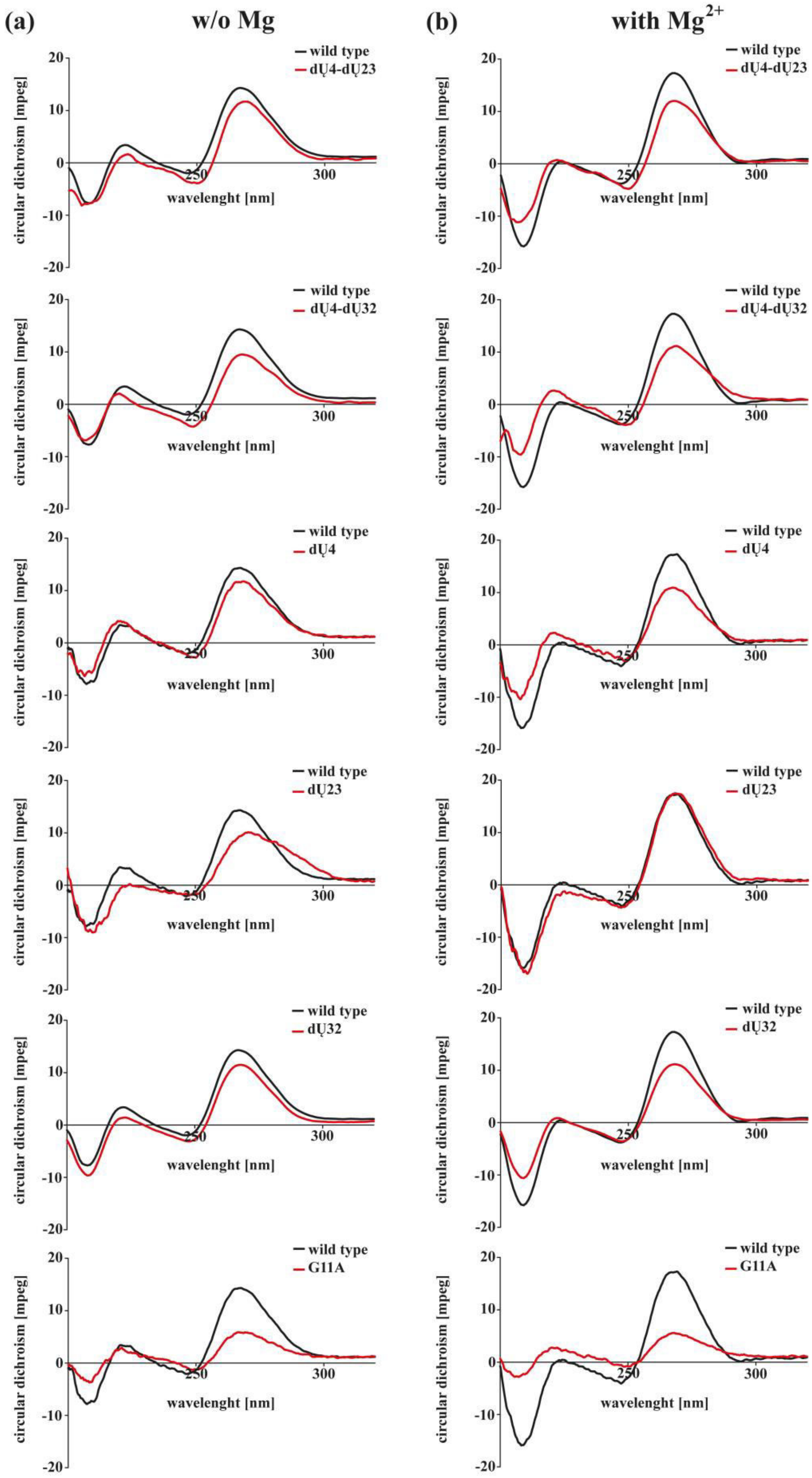

Figure 50: CD spectra of preQ1 mutants (red) compared to preQ1 wild type (black) without Mg^{2+} (a) and with Mg^{2+} (b).

Table 4 Differences in T_m values for the spin-labeled mutants of the preQ1 aptamer domain as compared to the unlabeled ones.[a]

Construct	**ΔT_m [°C]^b w/o Mg^{2+}**	**ΔT_m [°C]^b with Mg^{2+}**
preQ1 **dŲ4**	-8	-4
preQ1 **dŲ23**	-3	+3
preQ1 **dŲ32**	-5	+1
preQ1 **dŲ4-dŲ23**	-2	-2
preQ1 **dŲ4-dŲ32**	-5	-6
preQ1 **dŲ4-dŲ32 (G11A)**	-5	-2

[a] The absolute values as well as the corresponding Tm curves are collected in Appendix.
[b] Values are given per label.

3.4.3 cw-EPR measurements of preQ1 mutants

The incorporation of nitroxide spin labels into the preQ1 mutants was confirmed using X-band cw-EPR spectroscopy. According to the determination of labeling efficiency, spin-labeling of all preQ1 mutants was quantitative (for details see Appendix). In addition, the cw-EPR spectra of preQ1 mutants were recorded after addition of Mg^{2+} ions, as well as after addition of preQ1 metabolite. Figure 51a shows the experimental cw-EPR spectra of preQ1 **dŲ32** at room temperature.

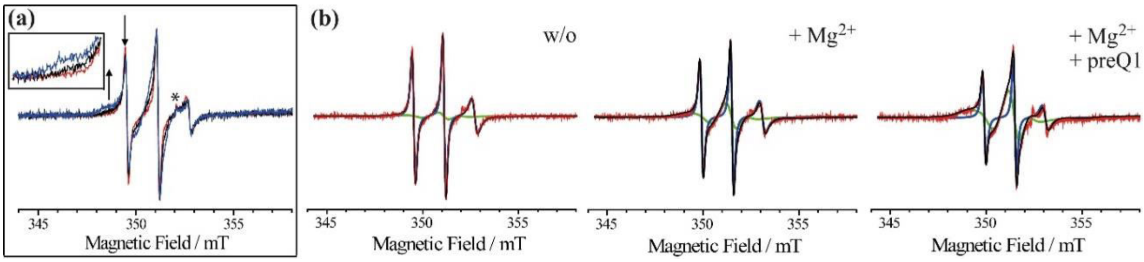

Figure 51: (a) Experimental X-band cw-EPR spectra of preQ1 **dŲ32** in the absence of preQ1 and Mg^{2+} (red), after addition of Mg^{2+} (black) and after addition of preQ1 (blue) at room temperature. The signal intensity was normalized by the signal intensity of the central peak. (b) Experimental (red) and calculated (black) cw-EPR spectra of preQ1 **dŲ32** in the absence of Mg^{2+} and preQ1, after addition of Mg^{2+} and after addition of preQ1 at room temperature. The calculated spectra are composed of two contributions with different mobility: more mobile (blue) and less mobile (green) spin labels). Conditions: C_{RNA} = 100 µM, 10 mM cacodylate buffer; C_{Mg2+} = 2 mM, C_{preQ1} = 1.3 mM. (H. Matsuoka)

Different line shapes of the EPR spectrum can be observed for the samples without and with Mg^{2+} and preQ1. For example, addition of Mg^{2+} and preQ1 changes the intensity of the low-field signal. The obtained spectra were interpreted as a superposition of at least two contributions from nitroxide radicals with different mobility. To evaluate the spectral change quantitatively, computer simulation was performed by using the program EasySpin.[145] Figure 51b shows the obtained fits of the experimental EPR spectra. Independent of the presence of Mg^{2+} and preQ1, the EPR spectra of preQ1 **dŲ32** can be simulated as a superposition of the two contributions: (1) more mobile component with the rotational correlation time of 0.7 ns, (2) less mobile component with the average correlation time of 6.3 ns. Here, the more mobile and less mobile components are called “fast-motion” and “slow-motion” components. The corresponding spectra are depicted by blue and green lines in Figure 51b. In the sample without Mg^{2+}, the weight ratio of the fast-motion and slow-motion components is 71% and 29 %, respectively (Table 5).

Table 5 Quantifications of fast- and slow-motion fractions of spin labels in the cw-EPR spectra for the preQ1 constructs

preQ constructs	**w/o [%][a]**		**Mg^{2+} [%][a]**		**preQ1 [%][a]**	
	I	II+III	I	II+III	I	II+III
dŲ4	71	29	37	63	19	81
dŲ23	12	88	10	90	10	90
dŲ32	71	29	37	63	19	81
dŲ4-dŲ23[b]	71	29	37	63	19	81
	12	88	10	90	10	90
dŲ4-dŲ32[c]	59	41	29	71	17	83
dŲ4-dŲ32 (G11A)[d]	24	76	20	80	15	85

[a] The number in front of the back slash denotes the fraction of the mobile, the number behind the slash, the fraction of the immobile component.
[b] Simulations were done by assuming four components, fast and slow for each label site. The weight ratio was set to 50:50 for the two sites.
[c] In these two cases only one mobile and one immobile component was sufficient to simulate the spectra, because preQ1 **dŲ4** as well as preQ1 **dŲ32** have identical τ_c values.
[d] Simulations were done by assuming only two components, fast and slow.

After the addition of Mg^{2+}, the fast-motion fraction is decreased to 37%. It is reduced even further to 19% in the presence of preQ1. Thus, the slow-motion fraction increased to 63% and 81% in presence of Mg^{2+} and the ligand, respectively. The obtained data is in a good agreement with the model of conformational exchange, which was proposed by Micura (Scheme 15). In the conformation I, the spin label **dŲ32** is located in the single-stranded region, which is fairly dynamic. Consequently, the fast-motion fraction dominates the corresponding EPR spectrum. The addition of Mg^{2+} initiates the conformational change during which **dŲ32** forms new stem region, in which its motion is restricted. Thus, the slow motion fraction of the spin labels in this conformation is increased. Note that the presence of conformation III after addition of Mg^{2+} cannot be excluded due to the spectral overlapping. Previous smFRET studies on preQ1 riboswitches from *Bacillus subtilis (Bsu)* and *Thermoanaerobacter tengcongensis (Tte)* disclosed the conformation III even in the absence of ligand.[146-147] Addition of the preQ1 ligand has only a slight influence on the pseudoknot-like structure, which leads to a minor increase of the slow-motion fraction. Thus, the present EPR results can be well correlated with the NMR studies, in which the slow-motion and fast-motion fractions were related to the folded (II and III) and unfolded (I) structures, respectively. According to the NMR studies, the formation of II occurs only in the presence of magnesium ions at room temperature.[142] However, the obtained results indicate that preQ1 riboswitch may pre-organize into II even without magnesium at the ambient temperature. Similar observations have been made for *Bsu* and *Tte* riboswitches by smFRET.[146]

Interestingly, the EPR spectrum of preQ1 **dŲ4** was found identical to that of preQ1 **dŲ32** (Figure 52a, c). As in the case of preQ1 **dŲ32**, spectrum of preQ1 **dŲ4** is also dominated by the fast-motion component in the absence of Mg^{2+}. This result is surprising, because the stem region, in which **dŲ4** is located, should restrict the movement of **dŲ4** label, as compared to **dŲ32,** which is supposed to be a part of the single stranded 3' overhang of the preQ1 aptamer domain (scheme 15). However, as revealed by thermal denaturation experiments, destabilization and local disruption of the stem region caused by the spin label can be a possible reason for the presence of such a high population of the fast motion fraction in the spectrum of preQ1 **dŲ4**.

In contrast, the cw-EPR spectrum of preQ1 **dŲ23** is dominated by slow-motion component, even in the absence of Mg^{2+} (Figure 52b, d). The weight ratio of the slow- and fast-motion fractions for **dŲ23** in the absence of Mg^{2+} was evaluated to be 88% and 12%, respectively. It was almost constant after addition of Mg^{2+} and preQ1 (90% and 10%), which indicates that the position U23 is insensitive to the conformational change.

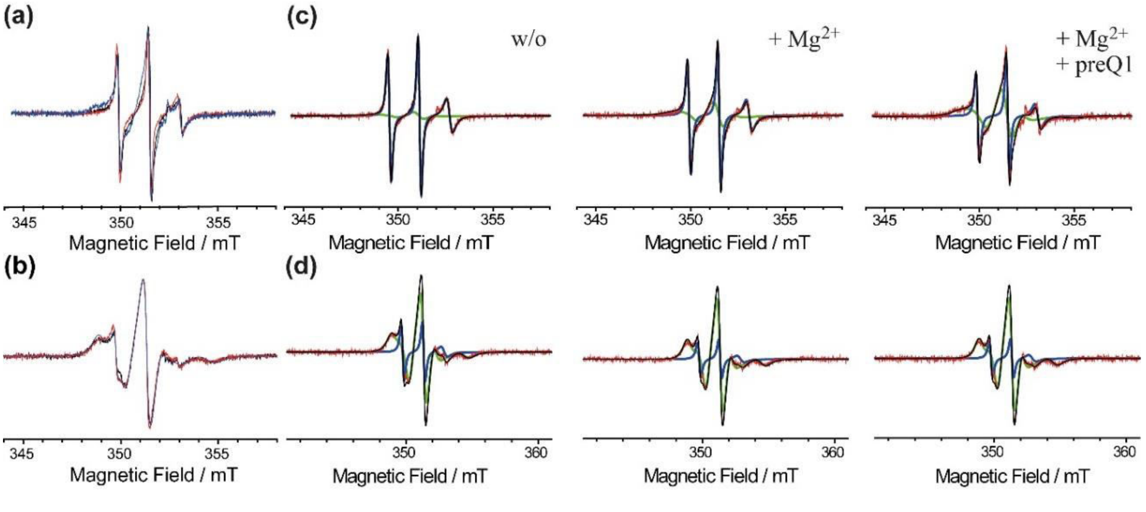

Figure 52: Experimental X-band cw-EPR spectra of (a) preQ1 **dŲ4** and (b) preQ1 **dŲ23** in the absence of preQ1 and Mg^{2+} (red), after addition of Mg^{2+} (black) and after addition of preQ1 (blue) at room temperature. The signal intensity was normalized by the signal intensity of the central peak. Experimental (red) and calculated (black) cw-EPR spectra of (c) preQ1 **dŲ4** and (d) preQ **dŲ23** in the absence of preQ1 and Mg^{2+}, after addition of Mg^{2+} and after addition of preQ1 at room temperature. The calculated spectra are composed of two contributions with different mobility: more mobile (blue) and less mobile (green) spin labels. Conditions: C_{RNA} = 100 µM, 10 mM cacodylate buffer; C_{Mg2+} = 2 mM, C_{preQ1} = 1.3 mM. (H. Matsuoka).

The EPR spectra of the double-labeled mutant preQ1 **dŲ4-dŲ32** in the absence of Mg^{2+}, after addition of Mg^{2+} and in presence of both Mg^{2+} and preQ1 ligand are shown in Figure

53a. The experimental spectra could be reproduced by taking into account the spectra of the corresponding single-labeled mutants preQ1 **dŲ4** and preQ1 **dŲ32**.

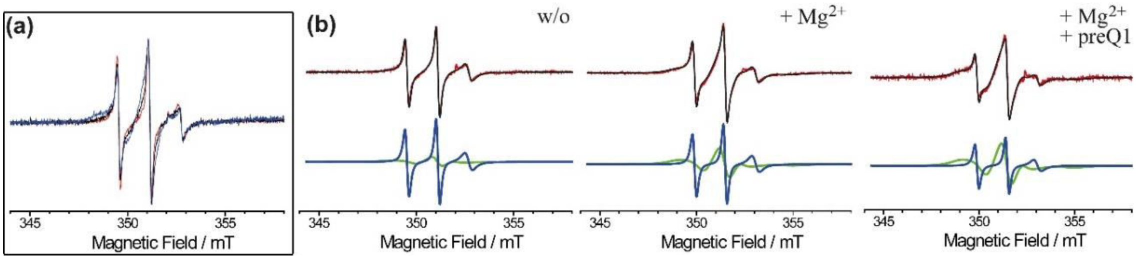

Figure 53: (a) Experimental X-band cw-EPR spectra of preQ1 **dŲ4-dŲ32** in the absence of preQ1 and Mg^{2+} (red), after addition of Mg^{2+} (black) and after addition of preQ1 (blue) at room temperature. The signal intensity was normalized by the signal intensity of the central peak. (b) Experimental (red) and calculated (black) cw-EPR spectra of preQ1 **dŲ32** in the absence of Mg^{2+} and preQ1, after addition of Mg^{2+} and after addition of preQ1 at room temperature. The calculated spectra are composed of two contributions with different mobility: more mobile (blue) and less mobile (green) spin labels. Conditions: C_{RNA} = 50 µM, 10 mM cacodylate buffer; C_{Mg2+} = 2 mM, C_{preQ1} = 1.3 mM. (H. Matsuoka).

In a similar way, it could be shown that the cw-EPR spectrum of the double-labeled preQ1 **dŲ4-dŲ23** can be interpreted as a superposition of the spectra of preQ1 **dŲ4** and preQ1 **dŲ23** (Figure 54).

To confirm that the observed spectral changes after addition of Mg^{2+} and preQ1 are related to the conformational changes, cw-EPR measurements were also performed on the preQ1 **dŲ4-dŲ32(G11A)** mutant. The cw-EPR spectrum of this mutant was only slightly changed after addition of Mg^{2+} and preQ1, as can be seen in Figure 55. It should be noted that the spin-labeling positions of this mutant are the same as that of preQ1 **dŲ4-dŲ32**. This result demonstrates that the observed spectral change in Figure 53 correlates with the conformational change inhibited by a single nucleobase mutation.

In contrast, simulations of the preQ1 **dŲ4-dŲ32(G11A)** revealed 24% of the fast-motion fraction in the absence of Mg^{2+}, which is decreased to 20% upon the addition of Mg^{2+} and further decreased to 15% in the presence of preQ1. Such a low population of the fast-motion fraction, even in the absence of Mg^{2+}, indicates that the G11A mutation leads to a different initial conformation of riboswitch, which is barely affected by Mg^{2+} or the preQ1 ligand. Since the secondary structure of preQ1 **dŲ4-dŲ32(G11A)** is not clear, no straightforward explanation of the cw-EPR results can be given for this case.

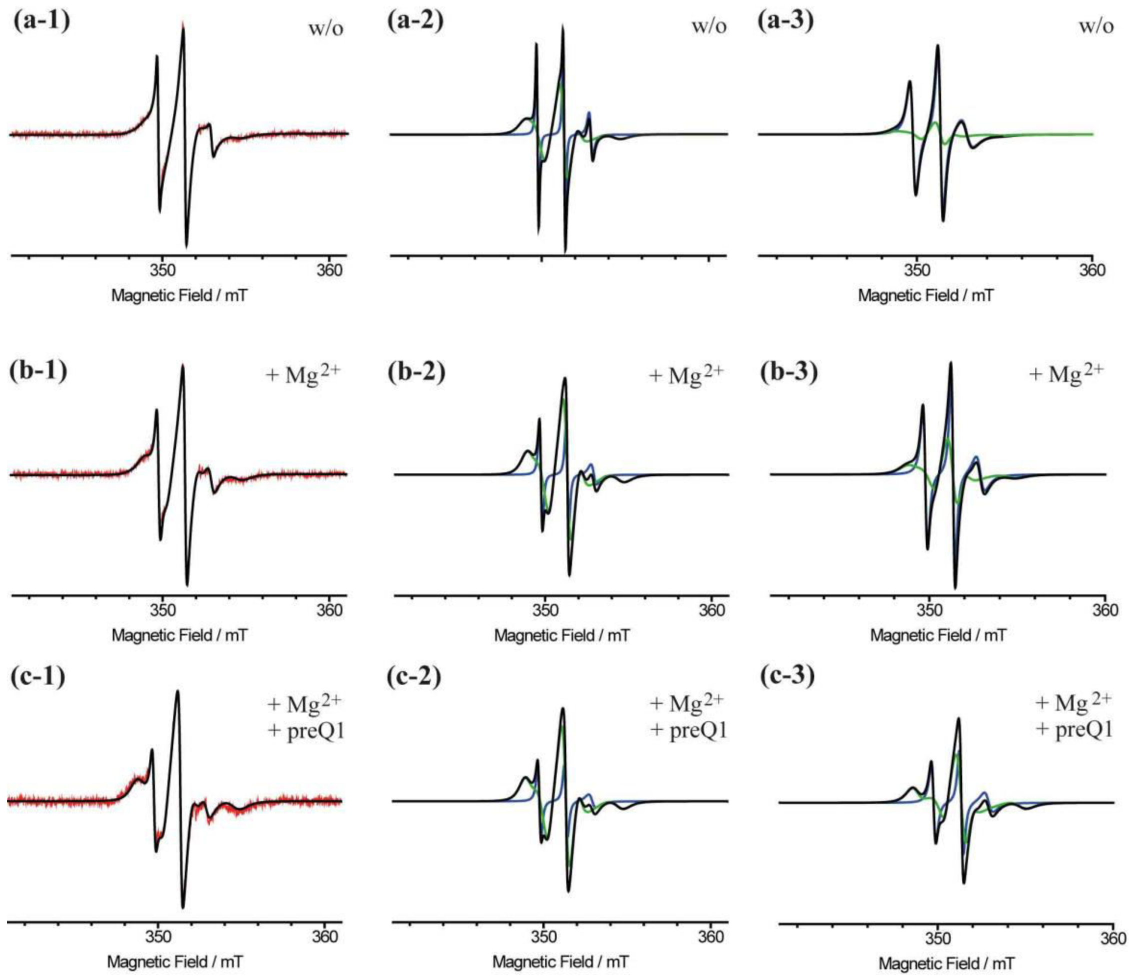

Figure 54: (a,b,c-1) Experimental (red) and calculated (black) cw-EPR spectra of preQ1 **dŲ4-dŲ23** in the absence of preQ1 and Mg^{2+}(a-1), after addition of Mg^{2+} (b-1) and after addition of preQ1 at room temperature (c-1). The calculated spectra are composed of four contributions with different mobility, two of which are the more mobile (blue) and less mobile (green) spin labels for preQ1 **dŲ23** (a,b,c-2) and the other two of which are for preQ1 **dŲ4** (a,b,c-3). Conditions: C_{RNA} = 50 µM, 10 mM cacodylate buffer; C_{Mg2+} = 2 mM, C_{preQ1} = 1.3 mM. (H. Matsuoka).

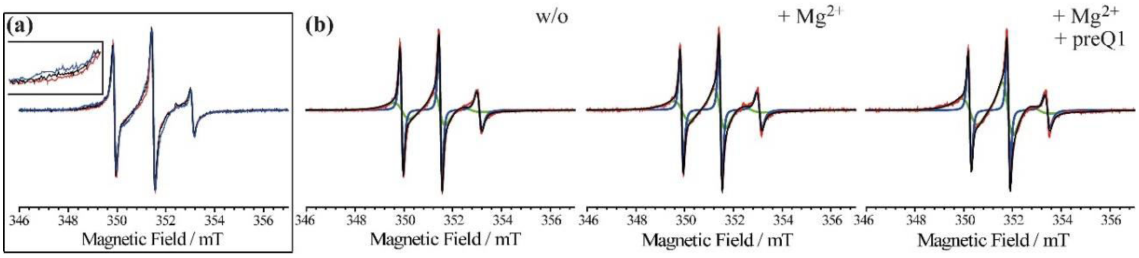

Figure 55: (a) Experimental X-band cw-EPR spectra of preQ1 **dŲ4-dŲ32(G11A)** in the absence of preQ1 and Mg^{2+} (red), after addition of Mg^{2+} (black) and after addition of preQ1 (blue) at room temperature. The signal intensity was normalized by the signal intensity of the central peak. (b) Experimental (red) and calculated (black) cw-EPR spectra of preQ1 **dŲ4- dŲ32(G11A)** in the absence of preQ1 and Mg^{2+}, after addition of Mg^{2+} and after addition of preQ1 at room temperature. The calculated spectra are composed of two contributions with different mobility: more mobile (blue) and less mobile (green) spin labels. Conditions: C_{RNA} = 50 µM, 10 mM cacodylate buffer; C_{Mg2+} = 2 mM, C_{preQ1} = 1.3 mM. (H. Matsuoka).

3.4.4 PELDOR measurements of double labeled preQ1 mutants.

The conformational change within the preQ1 aptamer domain was also observed by means of the PELDOR technique. In analogy to the experiments described in the section 3.3.3, PELDOR measurements were conducted for preQ1 **dŲ4-dŲ32**. The obtained PELDOR signals revealed however only slight orientation selectivity (for details see Appendix). This enabled the use of the common Tikhonov regularization procedure for the determination of distance distributions. Figure 56 shows the dependence of inter-label distance distribution in preQ1 **dŲ4-dŲ32** on the presence of Mg^{2+} and preQ1. The obtained distance distributions were deconvoluted into two Gaussians, which are illustrated by gray and green dashed lines in Figure 56. The Gaussians are centered at 1.9 and 2.8 nm. In the sample without Mg^{2+} and preQ1, the relative weights of the longer and shorter distance peaks are 59% and 41%, respectively (Table 6).

In order to identify the pseudoknot-like conformation, crystal structures for ligand-free and ligand-bound states of preQ1 riboswitch from *T. tengcongensis*[148] were labeled *in silico* with **dŲ** at positions U4 and U32 by the computer program MtsslWizard (Figure 56).[136] The derived mean inter-label distance equals 2.7 nm for conformations III, which is in a good agreement with the experimentally determined distance peak at 2.8 nm. On the other hand, *in silico* labeling of conformation II revealed that the position U32 is fairly occluded in this conformation and that the incorporation of **dŲ** label at this site might induce some structural changes. Consequently, mtsslWizard yielded a mean distance of 1.7 nm for conformation II. This result fits nicely to the experimental distance of 1.9 nm.

Upon addition of Mg^{2+}, the relative weight of the two Gaussians changed only marginally, being 53% and 47% for longer and shorter distance peaks respectively. These results indicate that a similar amount of the pseudoknot-like conformation is stabilized with lowering the temperature independently on the presence of Mg^{2+}. Interestingly, the previous NMR study also showed that the pseudoknot-like structure II of the preQ1 aptamer domain can occur at lower temperatures even without Mg^{2+}.[142] Indeed, the tendency of RNA to form pseudoknots at lower temperatures is known in the literature. For example, the CD spectroscopic studies of the synthetic RNA PK5 revealed that both lowering the temperature and the addition of Mg^{2+} lead to the pseudoknot formation.[50]

The addition of preQ1 to preQ1 **dŲ4-dŲ32** increased the weight of the longer distance component from 41% to 79% (Figure 56c). This result is again in agreement with the NMR data, which demonstrated that conformation III is predominantly populated in the presence of both Mg^{2+} and the ligand.

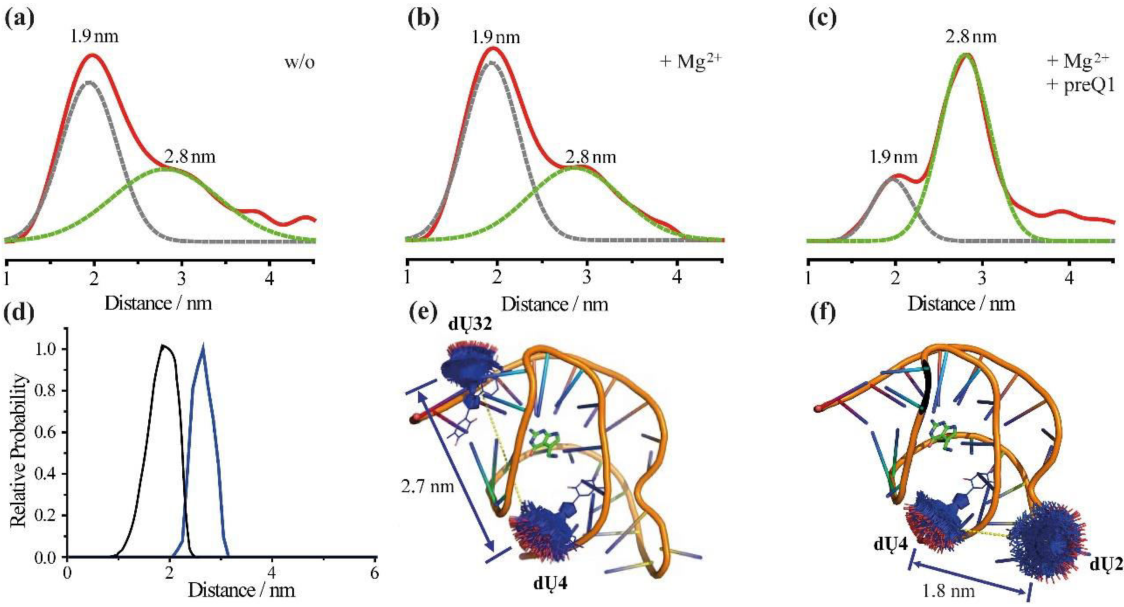

Figure 56: Top: The derived distance distributions (red lines) for doubly labeled preQ1 **dŲ4-dŲ32** (a) without Mg^{2+} and preQ1, (b) in presence of Mg^{2+} and (c) after addition of preQ1. Each distance distribution was deconvoluted by two Gaussian components (gray and green dashed lines). (d) MtsslWizard distance distributions for preQ1-bound states of preQ1 **dŲ4-dŲ23** (black) and preQ1 **dŲ4-dŲ32** (blue). Next are shown the crystal structures of the preQ1 riboswitch for (e) preQ1 **dŲ4-dŲ32** and (f) preQ1 **dŲ4-dŲ23** in the preQ1-bound state(PDB 3Q50), where the spin labels have been attached by means of the program mtsslWizard, are drawn as blue sticks with a red-coloured oxygen atom. Conditions: 20% deuterated ethylene glycol/buffer (10 mM cacodylate buffer), c_{RNA} = 50 µM, C_{Mg2+}= 2 mM, c_{preQ1} = 1.2 mM. (H. Matsuoka)

To verify the reliability of the assignment of the two distance components, PELDOR measurements were also performed on the preQ1 **dŲ4-dŲ32(G11A)** mutant. As shown in Figure 57a, no drastic change in the distance distribution was observed after the addition of preQ1. The peak shift was only by 0.2 nm. Thus, two distance peaks at 1.9 and 2.8 nm in Figure 57 can be related to the conformational change of preQ1 between the states II and III.

Table 6 Deconvolutions of the distance distributions for doubly labeled preQ1 mutants w/o Mg^{2+}, with Mg^{2+} only and with Mg^{2+} and preQ1.

preQ constructs	w/o [nm]	w/o [%]	Mg [nm]	Mg [%]	preQ1 [nm]	preQ1 [%]
dŲ4-dŲ23	1.9	100	1.9	100	1.9	100
dŲ4-dŲ32	1.9	59	1.9	53	1.9	21
	2.7	41	2.7	47	2.7	79
dŲ4-dŲ32	1.9	61	1.9	70	1.9	89
(G11A)	3	39	3	30	3	11

PELDOR measurements were also performed on the preQ1 **dŲ4-dŲ23** mutant, which was shown to be insensitive to the pseudoknot formation by using cw-EPR. Regardless of the presence or absence of Mg^{2+} and preQ1, the inter-label distance peak were observed at around 1.94 ± 0.3 nm (Figures 56, 57b). This result clearly correlates with the cw-EPR results of preQ1 **dŲ4-dŲ23** and preQ1 **dŲ23**, revealing that position U23 is not involved in the pseudoknot formation.

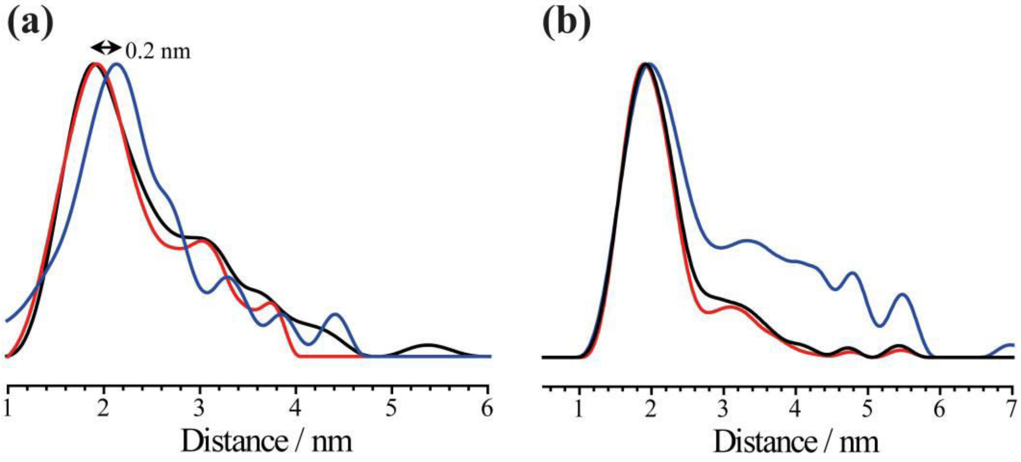

Figure 57: Distance distributions derived from the PELDOR time traces for (a) preQ1 **dŲ4-dŲ32(G11A)** and (b) preQ1 **dŲ4-dŲ23** in the absence of preQ1 and Mg^{2+} (red), after addition of Mg^{2+} (black) and after addition of preQ1 (blue) (H. Matsuoka).

3.4.5 Spin-labeling of TPP aptamer domain

The TPP aptamer domain from *E. coli* was used here as a further model system for testing the click chemistry as a novel spin-labeling approach for long RNA. In contrast to the 34 nt long preQ1 aptamer domain, the aptamer domain of TPP riboswitch consists of 81 nucleotides and thus cannot be synthesized using RNA solid phase synthesis in good yields. In order to overcome this limitation, the spin-labeling via click chemistry was used here in combination with splinted T4 DNA ligation strategy. Positions U20 and U68 were chosen for the spin-labeling. Being the parts of two sensor arms of TPP riboswitch, these positions could provide an insight into the dynamic processes taking place within the aptamer domain. For this purpose, 2 ethynyl pre-functionalized RNA fragments of the TPP aptamer domain, consisting of 45 nucleotides (**45nt dŲ20**) and 36 nucleotides (**36nt dŲ68**) were spin-labeled by means of click chemistry in solution. Similar to the preQ1 aptamer domain, the spin-labeling of **45nt dŲ20** as well as of **36nt dŲ68** sequences was quantitative and with only minimal RNA degradation (Figure 58a, b). The identity of spin-labeled constructs was confirmed by ESI (Table 7).

Subsequently, the double-labeled TPP aptamer domain was assembled by means of splinted enzymatic T4 DNA ligation, which was performed in analogy to the previously published protocols.[71, 149-150] The ligation reaction was monitored by agarose gel electrophoresis and was stopped after 3.5 h (Figure 59a). Afterwards, the spin-labeled full-length TPP aptamer domain was separated from unreacted RNA fragments at 80 °C by means of anion-exchange HPLC.

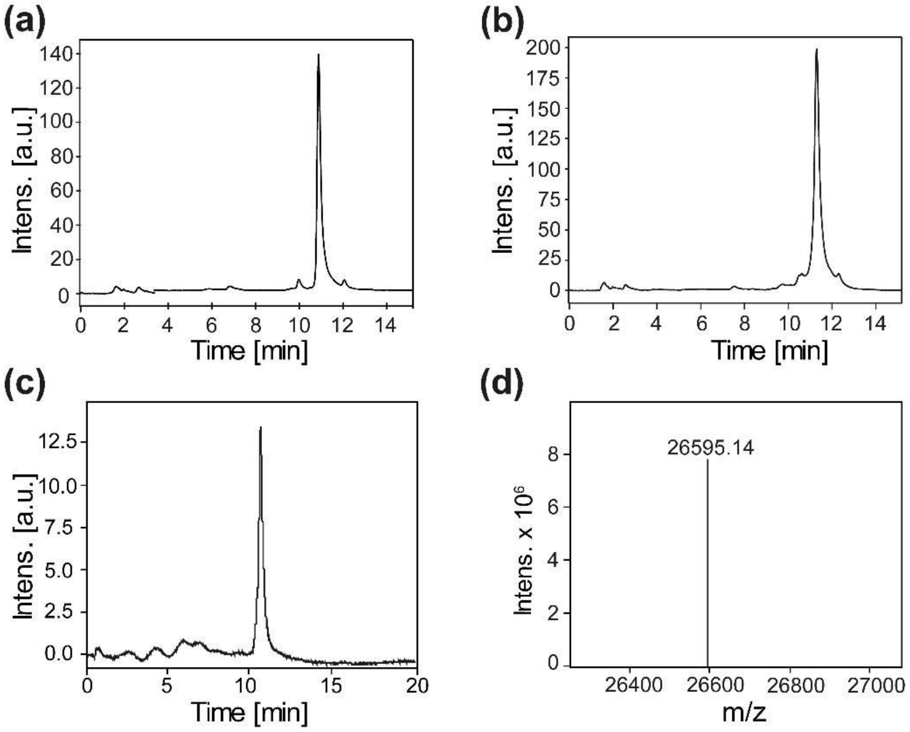

Figure 58: LCMS analysis of the click reactions of (a) **36nt dŲ68** and (b) **45nt dŲ20** after 30 min of reaction time. (c) HPLC profile of TPP **dŲ20-dŲ68** after purification. The major UV signal in each chromatogram correspond to the spin-labeled product. (d) ESI mass spectrometric analysis of TPP **dŲ20-dŲ68**. M_{calcd}(TPP **dŲ20-dŲ68**) = 26596.17 m/z and M_{found}(TPP **dŲ20-dŲ68**) = 26595.14 m/z.

Table 7 ESI spectroscopic analysis of major UV peaks from the Figure 58.

Spin-labeled constructs	Mass calc. [m/z]	Mass found [m/z]
45nt dŲ20	14713.06	14712.56
36nt dŲ68	11892.12	11891.45
TPP **dŲ20-dŲ68**	26596.17	26595.14
TPP **dŲ20**	26360.59	26358.57
TPP **dŲ68**	26360.59	26360.22

Performing the ligation on a 5 nmol scale, 2.5 nmol of the double-labeled TPP aptamer domain were obtained after the purification. The ligation yield was amounted to 50% and is in agreement with the literature values (50%).[71] The purity of the final double-labeled product was verified by the ESI spectroscopic analysis (Figure 58c, d). Surprisingly, the presence of dithiothreitol (DTT) in the ligation buffer did not affect the spin labels, demonstrating the high stability of the **dŲ** label towards reduction. The single-labeled TPP mutants TPP **dŲ20** and TPP **dŲ68** were also synthesized through ligation of non-modified sequences to their spin-labeled counterparts **36nt dŲ68** and **45nt dŲ20,** respectively (Figure 59b).

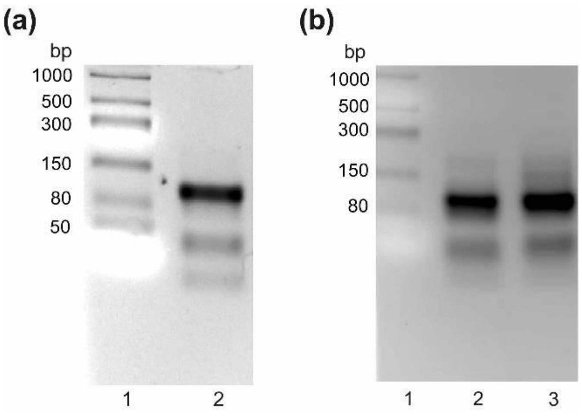

Figure 59: Agarose gel of the ligation mixtures of (a) double labeled TPP mutant TPP **dŲ20-dŲ68** and (b) single labeled TPP mutants TPP **dŲ20** (line 2) and TPP **dŲ68** (line 3) after 3.5 h of reaction time. Line 1 on both agarose gels implies a low range RNA ladder as a reference. The most pronounced bands at the length of 80 base pairs correspond to the ligation products.

3.4.6 UV-vis of TPP mutants

UV-Vis revealed only marginal influence of the **dŲ** labels on the stability of the TPP aptamer domain (see Appendix). The decrease of the melting temperature of TPP **dŲ20** relative to the wild-type was only 2 °C.

3.4.7 cw-EPR measurements of TPP mutants

The incorporation of the spin labels into the TPP aptamer domain was verified by means of cw-EPR spectroscopy (Figure 60). The cw-EPR spectrum of TPP **dŲ20-dŲ68** exhibited the typical line pattern of partially immobilized nitroxide radicals, confirming a successful incorporation of the spin labels into the TPP riboswitch. Computer simulations of TPP **dŲ20-dŲ68** showed that the spectrum is composed of at least two contributions with different mobility.

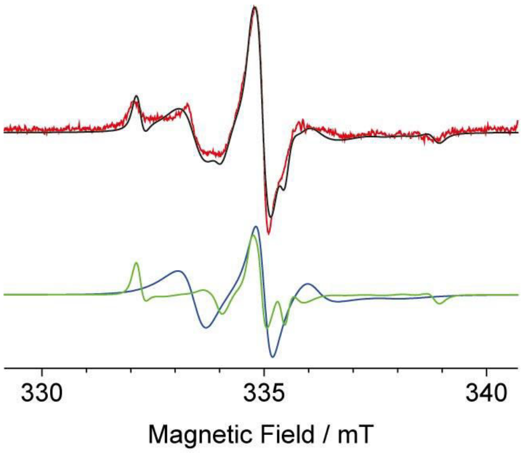

Figure 60: Experimental (red) and calculated (black) cw-EPR spectra of the TPP **dŲ20-dŲ68** in the absence of TPP and Mg^{2+} at room temperature. The calculated spectra composed of two contributions with different mobility: more mobile (blue) and less mobile (green) spin labels (H. Matsuoka).

The cw-EPR spectra of TPP **dŲ20-dŲ68** were recorded without and in the presence of Mg^{2+} and the TPP metabolite (Figure 61a). No difference in the spectrum was observed after the addition of Mg^{2+}. However, the addition of the TPP metabolite led to a measurable change of the low-field component of the EPR spectrum. On the other hand, no difference in the cw-EPR spectra of single-labeled TPP **dŲ68** was observed, neither in the presence of Mg^{2+} nor after the addition of the TPP metabolite (Figure 61b). This result is in a good agreement with the crystal structure of the aptamer domain[151] and with previous enzymatic studies of the secondary structure of the entire TPP riboswitch.[152]

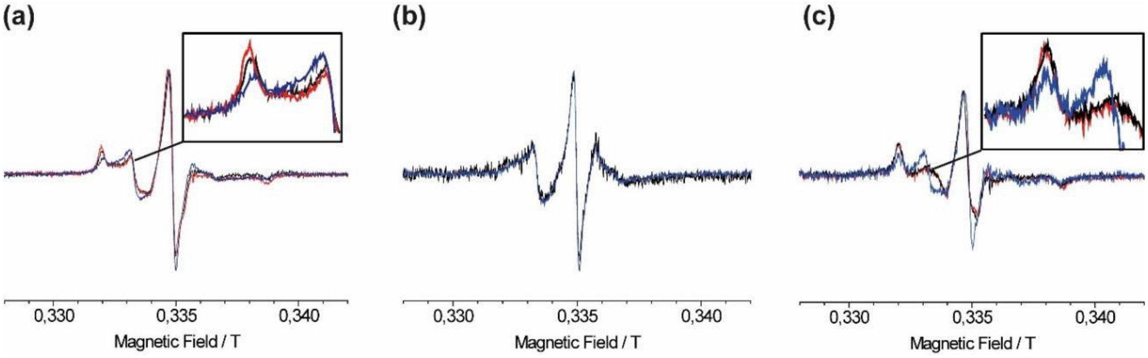

Figure 61: cw-EPR spectra of (a) TPP **dŲ20-dŲ68** (b) TPP **dŲ68** and (c) TPP **dŲ20** in the absence of Mg^{2+} and TPP (red), after addition of Mg^{2+} (black) and after addition of TPP (blue) at room temperature (H. Matsuoka).

Thus, it can be assumed that, being a part of the loop, the label **dŲ68** can freely move in solution independently on the presence of Mg^{2+} or the TPP metabolite. In contrast, the EPR spectra of TPP **dŲ20** mutant revealed similar behavior to the EPR spectra of TPP **dŲ20-dŲ68** (Figure 61c). That suggests that the spectral change observed for TPP **dŲ20-dŲ68** mutant in the presence of the TPP ligand can be assigned to the spin label at position **dŲ20**. Moreover, the full width of the spectra remains similar independently on the Mg^{2+} or TPP presence. Thus, it can be assumed that the obtained result is due to at least two conformations of TPP **dŲ20**, in which the **dŲ** label possesses the same mobility. However, a more detail analysis of these spectra is required, which is the object of future work.

3.4.8 PELDOR measurements on TPP dŲ20-dŲ68

The PELDOR measurements on the double-labeled TPP **dŲ20-dŲ68** mutant were performed without Mg^{2+}, with Mg^{2+} and with Mg^{2+} and TPP. Figure 62 shows the corresponding time trace of TPP **dŲ20-dŲ68** mutant without Mg^{2+}. The maximal evolution time of this PELDOR measurement was 12 μs, which allowed reliably measured distances up to 8 nm. Two peaks were observed in the obtained distance distributions, at 5.1 and 7.2 nm, indicating that there exist at least two conformations in the absence of Mg^{2+}(Figure 62a, inset). Conformational changes of the TPP riboswitch were investigated before by single-molecule FRET (smFRET).[149] For this purpose, TPP aptamer domain was labeled at positions U24 and U68, which are comparable with positions used in this study. In the respective smFRET histogram, a bimodal distribution was observed in the absence of Mg^{2+} including a highly populated low-FRET (0.2) and weakly populated intermediate-FRET (0.45) states (Figure 63a).

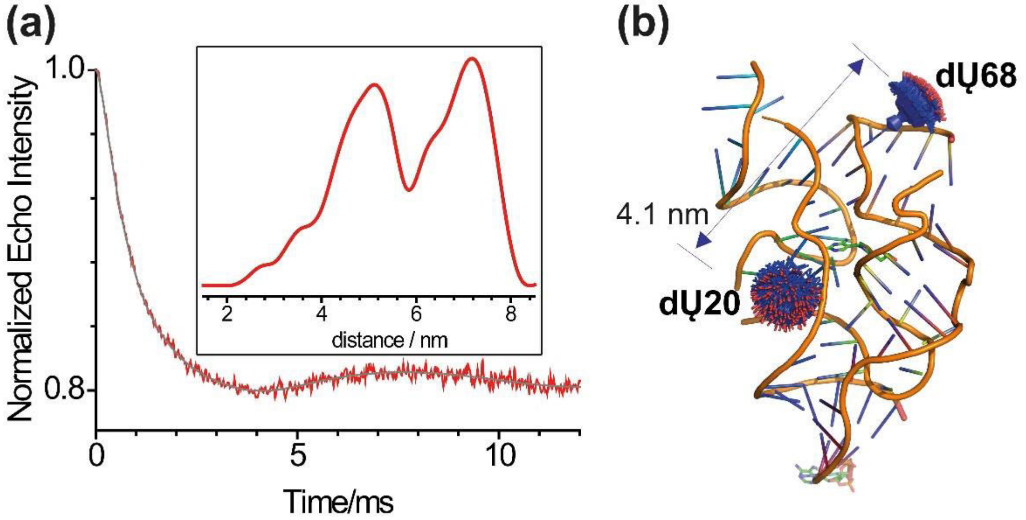

Figure 62: (a) Baseline-corrected Q-band PELDOR time trace of the doubly-labeled TPP **dŲ20-dŲ68** in the absence of TPP and Mg^{2+}as shown by the red line. The calculated time trace (gray) was obtained by the Tikhonov analysis of the experimental data using DeerAnalysis. Inset shows the distance distributions derived by the Tikhonov analysis of the PELDOR time traces. (b) The crystal structure of the aptamer domain of TPP riboswitch in the TPP-bound state (PDB 4NYG),[151] where the spin labels are drawn as blue sticks with a red-colored oxygen atom. (H. Matsuoka).

The distance between the two labels was not evaluated in the literature. Assuming a random orientation and Förster radius R_0 = 6 nm for the dye molecules, the distance is estimated to be 4.8 and 5.8 nm for the low- and intermediate-FRET states. The distances between U24 and U68 are proximal to the PELDOR-derived distances between U20 and U68. However, the appearance of the PELDOR derived peak at 5.1 nm indicates that the conformational equilibrium in the absence of Mg^{2+} is shifted with lowering temperature to metabolite-bound state, in which the predicted distance was amounted to 4.1 nm. These results are similar to the PELDOR results of preQ1 riboswitch mentioned above, indicating that both riboswitches preorganize into RNA states, similar to the metabolite-bond one, in a temperature dependent manner.

On the other hand, upon addition of Mg^{2+}, the relaxation time measured for TPP **dŲ20-dŲ68** dropped to almost 0 at 10 µs (Figure 64a).

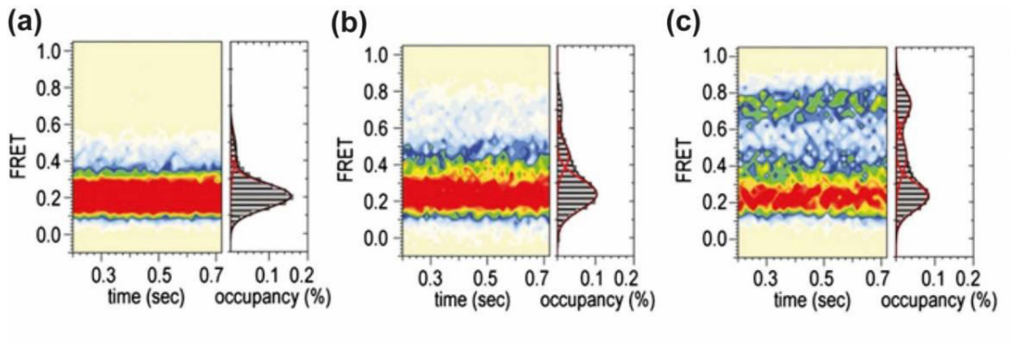

Figure 63: Population smFRET histograms of TPP aptamer domain labeled at positions C24 and U68 in the absence of Mg^{2+} and TPP ligand (a), in the presence of Mg^{2+} (b) and in the presence of Mg^{2+} and TPP (c).Adapted from Ref.[149]

Consequently, the evolution time of the corresponding PEDLOR measurement decreased from 12 µs to roughly 6 µs thereby reducing the distance accessible by PELDOR experiment as shown in Figure 64b. Thus, the obtained time trace provided reliable distance information only for 6 nm (Figure 64c). A similar result was also observed for the sample with Mg^{2+} and TPP, although the relaxation time slightly increased upon addition of TPP metabolite (Figure 64a). No obvious explanation for such a drop of relaxation time of **dŲ** can be given. However, one can assume a great number of conformations of TPP **dŲ20-dŲ68** in the presence of Mg^{2+}, which in turn might diminish the relaxation time of **dŲ** labels.

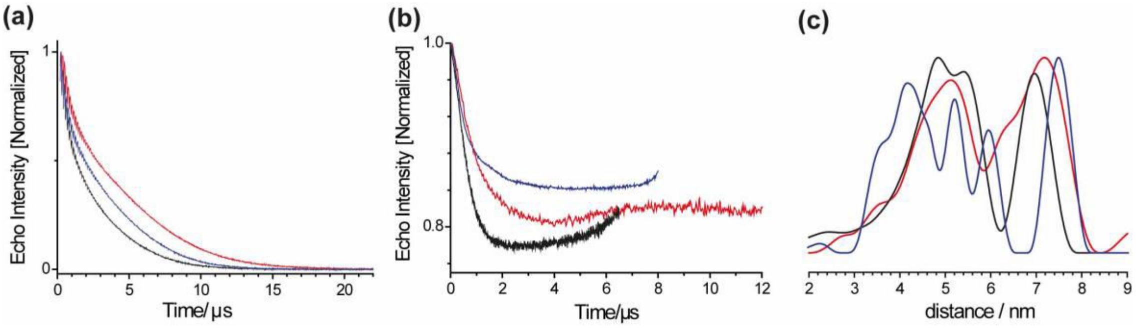

Figure 64: (a) Relaxation time of TPP **dŲ20-dŲ68** in the absence of TPP and Mg^{2+} (red), presence of Mg^{2+} (black) and with Mg^{2+} and TPP (blue). (b) Baseline-corrected Q-band PELDOR time traces of the doubly-labeled TPP **dŲ20-dŲ68** in the absence of TPP and Mg^{2+} (red), the presence of Mg^{2+} (black) and with Mg^{2+} and TPP (blue). (c) Distance distributions derived from the PELDOR time traces for TPP **dŲ20-dŲ68** in the absence of TPP and Mg^{2+} (red), after addition of Mg^{2+} (black) and after addition of TPP (blue) (H. Matsuoka).

The results obtained by FRET analysis of the TPP aptamer domain support the assumption of many RNA conformations in presence of Mg^{2+}. According to the FRET histogram of TPP aptamer domain with Mg^{2+}, the intermediate state is slightly increased compared to the sample without Mg^{2+} (Figure 63b).[149] In addition, a transiently occurring high-FRET state (0.75) could also be observed, a population of which substantially increased upon addition of TPP ligand (Figure 63c). Such broad FRET range indicates that both sensor arms pose a highly dynamic system even in presence of RNA stabilizing Mg^{2+} and TPP ligand. Thus, assuming a great conformational heterogeneity of TPP aptamer domain in the presence of only Mg^{2+} or Mg^{2+} and TPP ligand it can be speculated that anisotropic hyperfine interactions of the nitroxide spin centers of **dŲ** label with the surroundings becomes significant leading thereby to the drop of the relaxation time T_2. Thus, based on these results it should be considered applying different azide-functionalized nitroxides possessing longer relaxation time T_2 for further EPR analysis of TPP riboswitch. Some potential candidates for that are given in the section 4.4. Even though the PELDOR measurements could not be evaluated completely upon addition of Mg^{2+}, the applied spin-labeling strategy has shown a great potential for the structural elucidations of large RNA systems, especially due to the yields obtained for both click reaction and ligation.

3.5 Assembling of full-length TPP riboswitch for site-selective spin-labeling of the stems P1, P2 and P3

The results presented in the section 3.4.5 are related to the spin-labeling of only the aptamer domain of TPP riboswitch. However, the total length of the TPP riboswitch aptamer plus expression domain is 165 nucleotides. Due to the limitations of RNA solid phase synthesis mentioned above, site-specific spin-labeling of the full-length TPP riboswitch is an even greater challenge compared to aptamer domain only. Micura and co-workers constructed full-length TPP riboswitch from *E. coli* by applying three enzymatic ligations.[71] In particular, they assembled the aptamer and expression domains in two separate ligation reactions, and then subsequently ligated both domains to each other. Using relatively short RNA fragments (28-45 nt), this approach allows site-specific modifications for both domains. However, starting with 60-90 nmol of RNA precursors, they obtained only roughly 7 nmol of full-length riboswitch at the end, which corresponds to a total yield of 8-11%. High costs of synthetic RNA and the relatively low yield of the final ligation product make this ligation strategy for site-specific spin-labeling of TPP riboswitch less convenient. Nevertheless, it can be assumed that a decrease in the number of ligation steps could increase the yield of the final ligation product. Thus, attention is paid in this section to obtaining an effective way to an efficient ligation strategy for site-selective spin-labeling of the entire TPP riboswitch. In particular, the results presented here are related to spin-labeling of the stems P1, P2 and P3 (Figure 65).

Applying site-specific spin-labeling via ligation, several important requirements should be taken into account. On the one hand, the size of the RNA strand containing modifications has to be as small as possible due to the low RNA yield during the solid phase synthesis. On the other hand, the size of the strand without modifications is less critical, because it can be prepared *in vitro* using conventional enzymatic methods. In addition, considerable attention should be paid to the absence of DTT in the ligation buffer if using sulfurous spin labels. Taking into account these requirements, two ligations strategies for TPP riboswitch were worked out (Figure 65).

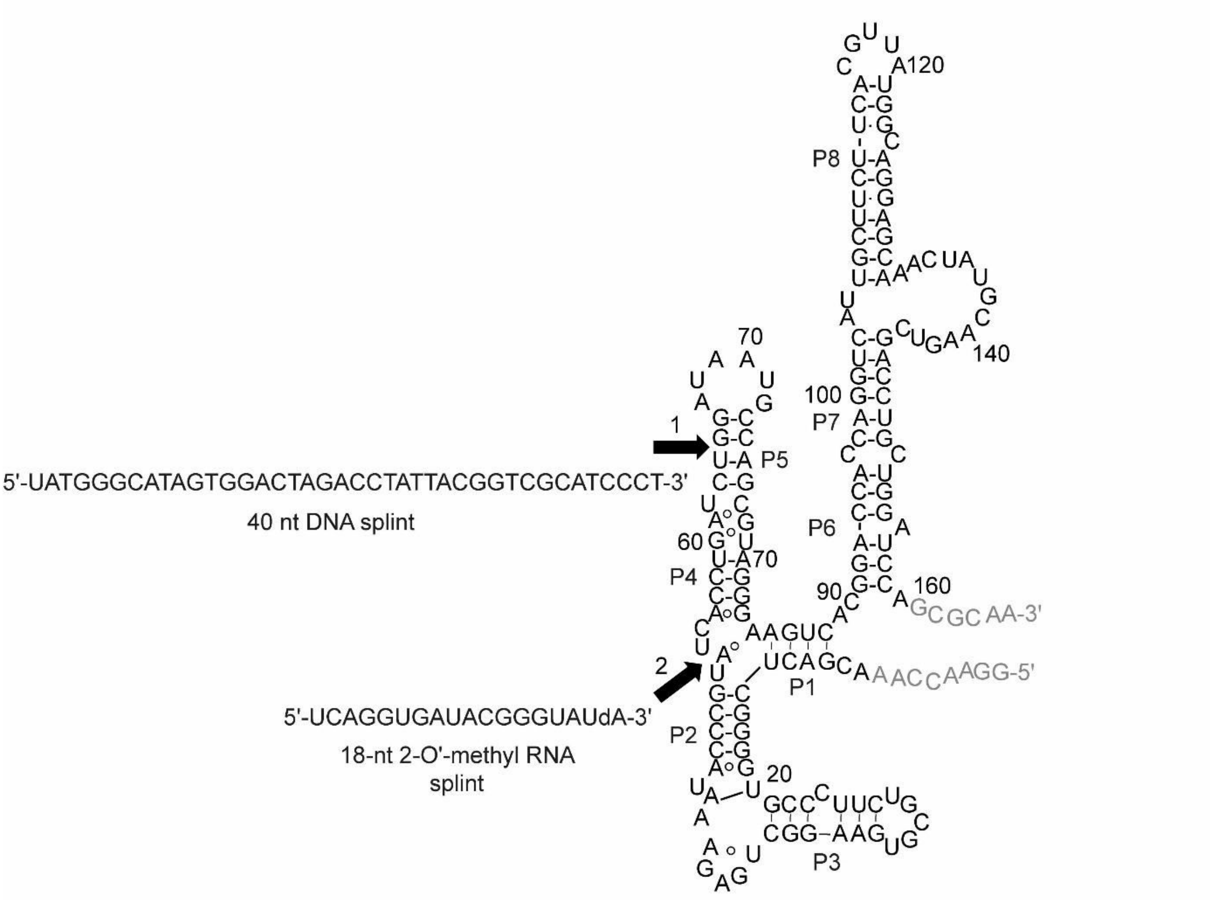

Figure 65: Secondary structure of TPP riboswitch in the metabolite-bound state. Black arrows 1 and 2 indicate the ligation sites. Nucleotides, which do not participate in Watson base pairs upon metabolite binding, are depicted in grey. Sequences of 40 nt DNA as well as 18 nt 2-O'-methyl RNA splints are shown next to the RNA structure.

Both strategies imply ligation of two RNA strands. In the first approach, the acceptor strand consists of 64 nucleotides and the donor strand of 101 nucleotides, whereas the RNA lengths in the second approach are 53 nucleotides of the acceptor and 112 of the donor respectively. Note, that the numbers of nucleotides are reduced for the longer RNA strand in the first strategy (from 101 nt to 95 nt) and for the shorter RNA strand in the second strategy (from 53 nt to 45 nt, Figure 65, grey colored nucleotides). These nucleotides were shown not to be essential for base pairing formation upon metabolite binding.[152] In principle, the length of 64 nt acceptor strand used in the first strategy can also be reduced to 54 nucleotides for the same reason. However, 64 nt RNA strand was used as a proof of the method because of its facile *in vitro* synthesis.

In the first approach, the ligation site was selected in accordance with the requirements of T7 RNA polymerase, one of which implements the presence of one or two guanines at the start of RNA sequence to initiate the transcription.[153] In order to *in vitro* synthesize RNA strands required for ligation, a plasmid containing the riboswitch sequence was isolated from *E. coli* bacteria and subsequently PCR-amplified resulting in 165 nt DNA precursor of TPP riboswitch (Figure 66a, b). In the next step, the obtained 165 nt DNA construct served as a template for another PCR to get 115 nt and 84 nt DNA sequences containing T7 promoter sequence required for RNA polymerase (Figure 66c).

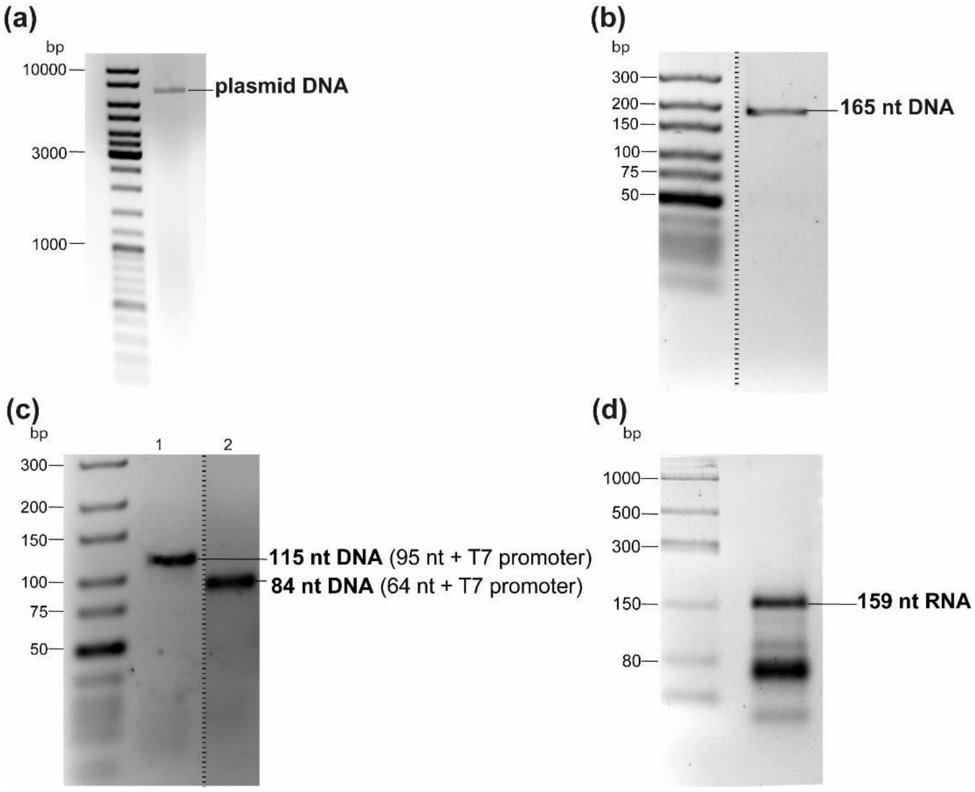

Figure 66: *In vitro* assembling of 159 nt TPP riboswitch. Agarose gel analysis of (a) isolated plasmid from *E. coli*, (b) PCR amplification of 165 nt DNA, (c) PCR amplification of 115 nt and 84 nt DNA sequences containing T7 promoters and (d) T4 DNA ligation of 159 nt TPP riboswitch. The dashed lines indicate that the lines not related to the results were cut out from the gel.

After transcription, the triphosphate group of the obtained 95 nt RNA strand was removed using alkaline phosphatase, which catalyzes hydrolysis of phosphates and the resulting 5'-OH group of RNA was phosphorylated by T4 polynucleotide kinase. In the last step, both *in vitro* obtained RNA strands consisting of 95 nucleotides and 64 nucleotides were ligated to each other using splinted enzymatic T4 DNA ligation, in which 40 nt DNA sequence was used as a splint oligonucleotide to form a double-helical structure with both RNA sequences (Figure 65, 66d). According to the concentration measurements, the yield of the obtained ligation product after the ion exchange HPLC purification and desalting was about 10%.

The second strategy included the ligation of two RNA strands consisting of 112 and 45 nucleotides respectively. The ligation site was adapted from the section 3.4.5, applying 18 nt 2'-O-methyl RNA oligonucleotide as a splint. However, the longer 112 nt RNA strand could not be *in vitro* synthesized from the DNA template using T7 RNA polymerase due to the absence of guanine at the beginning of the corresponding DNA sequence. To overcome this, *cis*-acting hammerhead ribozyme was incorporated into the DNA sequence. Placed upstream the corresponding DNA sequence of this ribozyme it is known to release desired RNA with defined 5'-OH terminus by self-cleavage during transcription.[154-156]

For this purpose, a DNA template consisting of 182 nucleotides (112 nt + Hammerhead ribozyme sequence) was constructed first. 2 DNA sequences consisting of 80 nucleotides each and one DNA sequence containing 68 nucleotides were used as DNA templates in a PCR reaction (Material & Methods). To find the most appropriate annealing temperature, a temperature gradient from 55 °C to 65 °C was applied (Figure 67a). According to the agarose gel analysis, multiple band formation was observed at every applied temperature. Nevertheless, a band at the high of 182 base pairs was observed at all temperatures, indicating the PCR product, even though the corresponding band at 65 °C is less pronounced. Thus, this band was cut out from the gel and agarose gel extraction was carried out. The obtained DNA was again PCR amplified using corresponding forward and revers primers (Figure 67b, Material & Methods). During the following transcription of the 182 nt DNA, hammerhead ribozyme was released by RNA cleavage providing the desired 112 RNA strand (Figure 67c). One of the additional advantages of hammerhead ribozyme is that after the transesterification reaction induced by the ribozyme, the released RNA already contains 5'-OH group accessible for phosphorylation. Thus, the isolated 112 nt RNA strand was subsequently phosphorylated using T4 polynucleotide kinase. The corresponding ligation to the 45 nt RNA strand occurred with a similar efficiency compared to the ligation of **36nt dŲ68** to **45nt dŲ20**, providing the ligation product in 48% after ion exchange HPLC purification (Figure 67d).

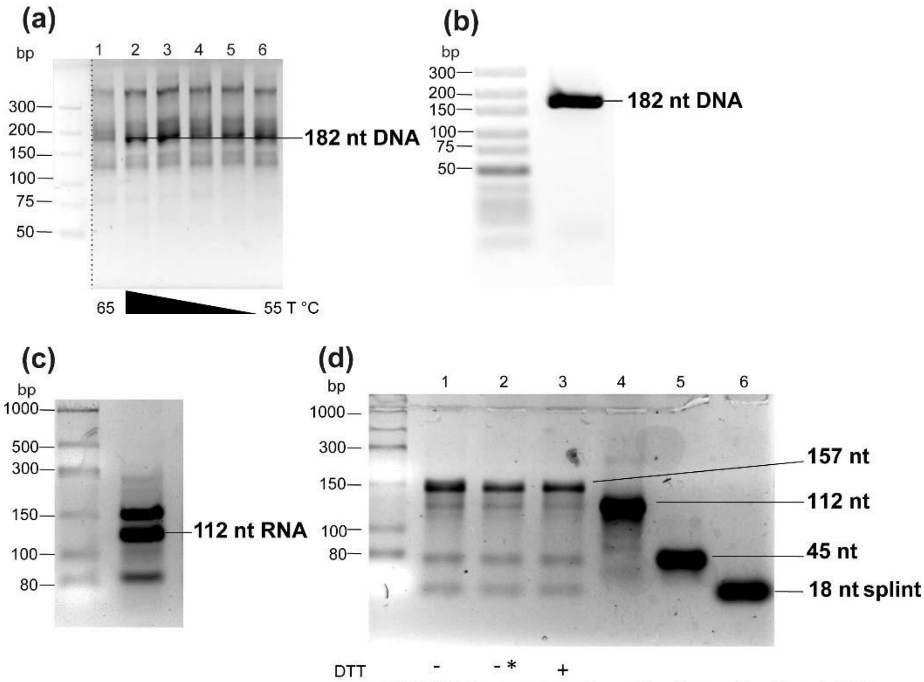

* T4 DNA ligase was stored for 6 month without DTT in its storage buffer

Figure 67: Agarose gel of (a) PCR amplification of 182 nt DNA containing hammerhead ribozyme sequence at different temperatures, (b) PCR amplification of 182 nt DNA template after agarose gel extraction (c) RNA transcription of 112 nt RNA and (d) the ligation reaction of the 157 nt TPP riboswitch using T4 DNA ligase with and without DTT. The band in (d) at 150 nt in lanes 1-3 indicates the ligation product. No difference in ligase activity was observed for reaction buffers with (+) and without DTT (-). *T4 DNA ligase is unaffected by storage without DTT for at least 6 months. The yield of ligation product is around 48% based on concentration calculations. The dashed line indicates that the lines not related to the results were cut out from the gel.

The obtained results demonstrate that the length of the RNA donor strand (phosphorylated RNA) is not essential for the ligation efficiency of TPP riboswitch. Compared to the first ligation strategy, the second one provides substantially higher yield and can be therefore considered for site-specific spin-labeling of stems P1, P2 and P3 of TPP riboswitch. It is interesting to note that the use of the same ligation reaction without reducing agent dithiothreitol (DTT) in the ligation buffer did not lead to a decrease in ligation efficiency. Even using T4 DNA ligase, which has been stored without DTT for six months, did not affect the ligation reaction, as shown in Figure 67d. The results obtained may be of great interest for the potential site-selective spin-labeling of long RNAs using less stable spin labels such as e.g. MTSL, which can be affected by DTT during ligation.

4 Conclusion and Outlook

4.1 Spin-labeling of RNA using click chemistry on solid support

Section 3.1.2.1 demonstrated a successful incorporation of **dŲ** and **dŲethyl** labels into self-complementary sequence **45dŲ** and **45dŲethyl** respectively using click chemistry on a solid support. This approach proved to be more effective than the well-established synthesis of **Çm** modified RNA using the corresponding spin-labeled phoshoramidite **Çm**, because it has a simpler process of synthesis and labeling procedure. Moreover, **dŲ** label was found to possess similar conformational heterogeneity to **Çm** label at the freezing temperature of the solvent. This fact enables one performing orientation selective PELDOR measurements, providing not only the inter-spin distance, but also the relative orientation between the labels. However, applying this labeling approach for long RNA, such as preQ1 aptamer domain, resulted in lower conversion compared to the self-complementary RNA **45dŲ**. Therefore, improved reaction conditions are required to maintain the high efficiency of this method even for long RNAs. It is assumed that the reason for the lower conversion of long RNA is the unknown RNA concentration on the solid support. In addition, Cu(I) ions can undergo redox and disproportionation reactions if they are not properly linked to stabilizing ligand. It has been shown before that appropriate concentration of Cu(I) ions is essential for efficient click reaction.[81] Therefore, it can be assumed that at low concentrations of ethynyl modified RNA, disproportionation of Cu(I) occurs faster than the click reaction, even when a sufficient amount of THPTA ligand is added. Thus, it can be considered to determine the approximate RNA concentration by deprotecting of a tiny amount of RNA from solid support before click reaction and evaluating it to the total amount of solid support. This would enable one to estimate roughly the concentration of the applied RNA on solid support in the following click reaction. An approximate RNA concentration of 250 µM can be suggested as a good starting point, as it was shown to be sufficient for quantitative spin-labeling for the same reaction in solution.

4.2 Spin-labeling preQ1 riboswitch

The spin-labeling of preQ1 riboswitch was accomplished with high efficiency by click chemistry in solution. The new spin-labeling strategy provides a much faster reaction time compared to the same reaction on solid support and higher yield for long RNAs. Moreover, it was demonstrated that addition of an appropriate amount of Cu(I) stabilizing THPTA ligand suppresses RNA degradation during the spin-labeling procedure.

PreQ1 aptamer domain was successfully labeled at different positions using in solution approach. Furthermore, the conformational equilibrium and pseudoknot formation of preQ1 aptamer domain could be monitored by cw-EPR measurements, illustrating a great potential of **dŲ** label for elucidations of dynamic processes within an RNA molecule. The conformation of the preQ1 riboswitch and its dynamics after addition of Mg^{2+} and preQ1 were also observed by the distance measurements based on the PELDOR technique. The correlation between the conformational change of the preQ1 riboswitch and EPR/PELDOR results were confirmed by the EPR and PELDOR measurements of the preQ1 **dŲ4-dŲ32(G11A)** mutant.

Thus, the data obtained in this study confirm a high potential of **dŲ** label as well as its spin-labeling strategy for further applications in biologically relevant RNA systems such as preQ1 riboswitch. However, obtained results must be confirmed due to the destabilization of RNA caused by the **dŲ** label at positions U4 and U32, as shown in the CD spectra and in the thermal denaturation experiments of preQ1 mutants. Therefore, in order to verify the obtained EPR results, an additional position e.g. U6 can be considered for spin-labeling. Being a part of the loop U6 should not have a destabilizing effect at this position on the preQ1 aptamer domain. On the other hand, incorporation of **Ḉm** label using click chemistry in solution would allow spin-labeling of available cytidines of preQ1 aptamer domain that could provide additional information about the folding mechanism.

4.3 Spin-labeling TPP riboswitch

The spin-labeling strategy using click chemistry was applied to the TPP aptamer domain containing 81 nucleotides. It was shown that access to the spin-labeled RNA systems of this size can be gained by combining click chemistry in solution with the enzymatic ligation. The distance measurement of TPP **dŲ20-dŲ68** in the absence of Mg^{2+} showed that there exist at least two stable conformations for the TPP riboswitch, even in the metabolite-free state. However, it was shown that upon addition of Mg^{2+} the relaxation time of **dŲ** labels drastically dropped leading to a reduced evolution time of the corresponding PELDOR experiment. Consequently, distances beyond roughly 6 nm could not be precisely determined. Thus, to investigate TPP aptamer domain, PELDOR experiments have to be performed, which would provide measurements of longer distances. As it has already been proposed in the section 3.4.8, one possible way to overcome this hindrance can be the application of azide-functionalized nitroxides with longer relaxation times. For example, **dŲethyl** label was shown to possess a considerably longer relaxation time compared e.g. to **dŲ** or **Çm,** as shown in Figure 48, and thus, it is a good candidate for further spin-labeling of TPP riboswitch.

In addition, successfully performed ligation of the entire riboswitch allows for EPR analysis of stems P1, P2 and P3 of the full-length construct. In the future, it can be also considered to establish further ligations, which would provide site-specific spin-labeling of the remaining stems of the TPP riboswitch. For instance, in order to label stems P6, P7 or P8 one can consider ligation between 117 nt RNA and 42 nt RNA strands (Figure 68). This ligation site was successfully used to assemble the expression domain of TPP riboswitch and therefore, it is a promising candidate for ligation of a full length riboswitch.[71]

The RNA element containing 117 nt can be easily synthesized *in vitro* using T7 RNA polymerase while 42 nt RNA should be accessible by RNA solid phase synthesis. Combining the ligation strategies for site-specific spin-labeling of stems P1, P2, P3 and P6, P7, P8 would provide some insights into the three dimensional structure of the entire riboswitch. In addition, it would allow for elucidation of the dynamics between the aptamer and expression domains.

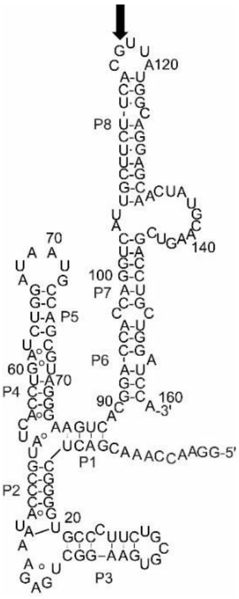

Figure 68: Secondary structure of TPP riboswitch in the metabolite-bound state. Black arrow indicates the potential ligation site.

4.4 Incorporation of different spin label azides

Spin-labeling approaches presented in this work are not limited to the spin label azides **43** and **44**. Therefore, a wide range of azide-functionalized nitroxides can be considered for spin-labeling. Potential candidates for this have been already successfully incorporated using click chemistry into alkyne modified DNA (Figure 69).[86]

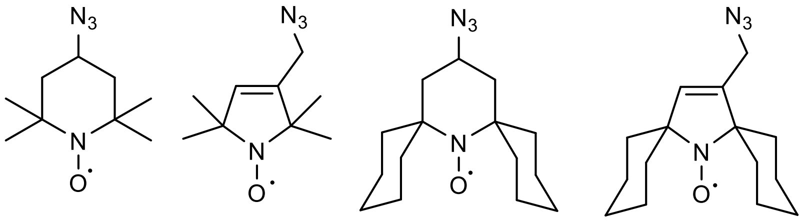

6-Me **5-Me** **6-sp** **5-sp**

Figure 69: Azide-functionalized nitroxide spin labels, which can serve for site-specific spin-labeling of RNA using click chemistry.

Furthermore, similar to **dŲethyl** label **6-sp** and **5-sp** have been shown to possess longer relaxation times T_2 compared to the methylated spin labels. This property allows measuring longer inter-spin distances, and enables one to perform PELDOR experiments at higher temperatures.[77, 157-158] Further modifications of the present spin labels are still required to allow the room temperature PELDOR-based distance measurements, which is one of the hot topics in the scientific community. Another important aim of the future studies will be PELDOR studies of spin-labeled RNA in cell.

5 Material & Methods

5.1 Chemical synthesis

5.1.1 Methods used in chemical synthesis

5.1.1.1 NMR-spectroscopy:

^{1}H-, ^{13}C- and ^{31}P-NMR-spectra were recorded on nuclear magnetic resonance spectrometers AM300 (^{1}H = 300 MHz; ^{13}C = 75.4 MHz; ^{31}P = 121.4 MHz), AM400 (^{1}H = 400 MHz; ^{13}C = 100.6 MHz; ^{31}P = 162 MHz), AM500 (^{1}H = 500 MHz; ^{13}C = 126.0 MHz; ^{31}P = 202.4 MHz) and AM600 (^{1}H = 600 MHz; ^{13}C = 151.0 MHz; ^{31}P = 242.9 MHz) from *BRUKER,* Karlsruhe. $CDCl_3$, MeOH-d_4, D_2O and DMSO-d_6 were used as solvents. The chemical shifts in NMR spectra were given as δ-values in ppm. For 1H and 13C spectra they were determined via calibration of the deuterated solvents signals with the values known from the literature.[159] They are δ ($CDCl_3$) = 7.26 ppm, δ (MeOH-d_4) = 3.31 ppm, δ (D_2O) = 4.79 ppm, δ (DMSO-d6) = 2.5 ppm for ^{1}H-spectra and δ ($CDCl_3$) = 77 ppm, δ (MeOH-d_4) = 49 ppm, δ (DMSO-d6) = 39.5 ppm for ^{13}C-spectra. The experimentally obtained NMR-spectra were analyzed by *MestReNova v8.0.0-10524*. The obtained multiplicities were abbreviated as follows: s = singlet, d = doublet, dd = doublet of doublets, t = triplet, q = quartet and m = multiplet. The coupling constants (*J*) were given in Hz.

5.1.1.2 Mass spectrometry

ESI-Mass spectra were recorded either on LCMS consisting of a micrOTOF-Q flight time spectrometer from *Bruker Daltonics* and *Agilent* 1200 Series HPLC or on LCMS including Esquire HCT Ion Trap mass spectrometer from *Bruker Daltonics* and HPLC system 1100 series from *Agilent*. EI spectra were measured with a MAT-95XL from *Thermo Finnigan*.

5.1.1.3 Flash chromatography

Column chromatography was performed on a PuriFlash 430 from *Interchim* using pre-packed silica gel columns.

5.1.1.4 Thin Layer Chromatography (TLC):

Merck silica gel 60 F_{254} plates were used for analytical TLC. The visualization of TLC plates was carried out by means of ether UV light (254nm) or a staining reagent.

5.1.1.5 Iodometric titration

Glacial acetic acid (2 ml) and isopropanol (25 ml) were placed in a 250 ml Erlenmeyer flask and mixed. Freshly prepared iodide-isopropanol solution (preparation: refluxing a mixture of NaI (22 g) in isopropanol (100 ml), followed by cooling down to room temperature and filtration) was added. An accurately determined amount of TBHP solution was added to the solution and the mixture was refluxed for approx. 1 min. The solution was diluted with de-ionized water (100 ml) and immediately titrated with 0.1 M sodium thiosulfate until the yellow colour disappeared. Indicator starch solution was used for a better visualization of the endpoint of titration.

The concentration was calculated according the following equation:

$$C(\text{TBHP}) = \frac{\text{S x M}}{\text{2 x (ml of sample)}},$$

where S is the volume of thiosulfate used for titration and M molarity of thiosulfate.

5.1.1.6 TLC staining

Staining reagent 1: 10 ml p-anisaldehyde, 2 ml acetic acid, 180 ml ethanol, 10 ml conc. sulfuric acid.

Staining reagent 2: (*Seebach*): 2.5 g Cerium(IV) sulfate tetrahydrate, 6.25 g ammonium heptamolybdate tetrahydrate, 225 ml water, 25 ml conc. sulfuric acid.

5.1.1.7 Solvents

Dry solvents were purchased from *Acros, Sigma Aldrich* and *ABCR* or dried using standard procedures known from the literature.[160]

5.1.2 Compounds

2-Benzylisoindoline-1,3-dione (32)[103]

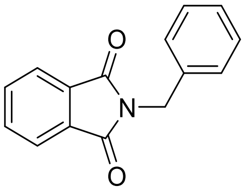

Phthalic anhydride (50 g, 337.6 mmol) was dissolved in glacial acetic acid (1500 ml). Benzyl amine (36.17 ml, 337.6 mmol) was added and the solution was refluxed for 5 h. When the reaction was complete (TLC, cyclohexane/EtOAC 50:50) the reaction mixture was poured into cold water. White precipitate was filtered and washed with cold water. The purification was achieved by the recrystallization in ethanol to give **32** as white crystals (72 g, 90%).

R_f = 0.45 (cyclohexane/EtOAc 1:1);**^{1}H-NMR (500 MHz, $CDCl_3$):** δ = 4.85 (s, 2H, C*H*$_2$), 7.25-7.33 (m, 3H, Ar*H*), 7.43-7.44 (m, 2H, Ar*H*), 6.69-7.70 (m, 2H, Ar*H*), 7.83-7.85 (m, 2H, Ar*H*) ppm;**^{13}C-NMR (126 MHz, $CDCl_3$):** δ = 41.6, 123.3, 127.8, 128.6, 128.6, 132.1, 133.9, 136.3, 168.0 ppm; **MS (ESI (+), 8 eV) m/z:** Calc. for $C_{15}H_{11}NO_2$ $(M+H)^+$ 238.08, found 238.32.

2-Benzyl-1,1,3,3-tetramethylisoindoline (33)[58]

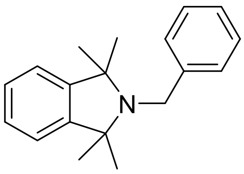

A flame dried 2 L three naked round bottom flask was flashed with argon. Magnesium chips (50 g, 1320 mmol) were added and subsequently covered with dry Et_2O (50 ml). A solution of MeI (78 ml, 1260 mmol) in dry Et_2O (510 ml) was added dropwise and the reaction mixture was stirred for 30 min. The reaction mixture was then concentrated by slow distillation of diethyl ether until the temperature inside the flask reached 80 °C. The reaction temperature was then decreased to 60 °C and a solution of N-benzylphtalimide **32** (50 g, 210 mmol) in dry toluene (350 ml) was added dropwise. The reaction mixture was further concentrated by slow distillation until the internal temperature of 110 °C was reached. The residue was refluxed for 4 h at 110 °C and the reaction volume was then again decreased by further distillation. The reaction mixture was cooled down to 22 °C and diluted with hexane (200 ml). The resulting purple residue was then filtered through celite and concentrated *in vacuo*. The residue was purified on silica gel by flash chromatography eluting with cyclohexane to give **33** as a white solid (12 g, 21%).

R_f = 0.86 (cyclohexane); **^{1}H-NMR (400 MHz, $CDCl_3$):** δ = 1.31(s, 12H, 4 x C*H_3*), 4.00 (s, 2H, C*H_2*), 7.11-7.16 (m, 2H, Ar*H*), 7.19–7.31 (m, 5 H, Ar*H*), 7.43–7.48 (m, 2H, Ar*H*) ppm; **^{13}C-NMR (75.4 MHz, $CDCl_3$):** δ = 28.0, 45.9, 64.8, 120.9, 126.0, 126.4, 127.5, 127.9, 144.0, 147.5 ppm; **MS (ESI (+), 8 eV) m/z:** Calc. for $C_{19}H_{23}N$ $(M+H)^+$ 266.18, found 266.12.

2-Benzyl-1,1,3,3-tetraethylisoindoline (34)

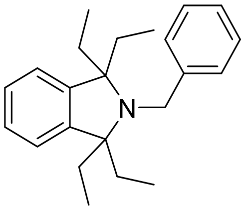

A flame dried 2 L three naked round bottom flask was flashed with argon. Magnesium chips (50 g, 1320 mmol) were added and subsequently covered with dry Et_2O (50 ml). A solution of EtI (78 ml, 1260 mmol) in dry Et_2O (500 ml) was added dropwise and the reaction mixture was stirred for 30 min. The reaction mixture was then concentrated by slow distillation of diethyl ether until the temperature inside the flask reached 80 °C. The reaction temperature was then decreased to 60 °C and a solution of N-benzylphtalimide **32** (50 g, 210 mmol) in dry toluene (350 ml) was added dropwise. The reaction mixture was further concentrated by slow distillation until the internal temperature of 110 °C was reached. The residue was refluxed for 4 h at 110 °C and the reaction volume was then again decreased by further distillation. The reaction mixture was cooled down to 22 °C and diluted with hexane (200 ml). The resulting purple residue was then filtered through celite and concentrated under reduced pressure. The residue was purified on silica gel by flash chromatography eluting with cyclohexane to give **34** as a white solid (17 g, 25%).

R_f = 0.86 (cyclohexane); **^{1}H-NMR (500 MHz, $CDCl_3$):** δ = 0.84 (t, *J* = 7.4 Hz, 12H, CH2C*H3*), 1.61 (dd, *J* = 14.0, 7.3 Hz, 4H, CH_aH_bCH3), 1.99 (dd, *J* = 14.0, 7.3 Hz, 4H, CH_aH_bCH3), 4.07 (s, 2H, NCH_2), 7.12 (dd, *J* = 5.6, 3.2 Hz, 2H), 7.26-7.38 (m, 5H, Ar*H*), 7.55 – 7.49 (m, 2H) ppm.
^{13}C-NMR (126 MHz, $CDCl_3$): δ = 9.6, 30.3, 46.7, 71.3, 123.4, 125.6, 126.5, 127.7, 129.6, 142.4, 144.5 ppm; **MS (ESI (+), 8 eV) m/z:** Calc. for $C_{23}H_{31}N$ $(M+H)^+$ 322.25 found 322.25.

1,1,3,3-Tetramethylisoindoline (35)[58]

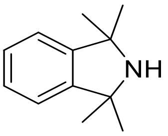

In a 250 ml round bottom flask **33** (9 g, 33.9 mmol) was dissolved in glacial acetic acid (164 ml). The solution was bubbled with argon for 5 min and 10% Pd/C (0.9 g) was added. The reaction flask was sealed with a septum and an air balloon filled with hydrogen connected to a syringe with a needle was attached to the septum. The reaction mixture was stirred for 4 h at 22 °C. The reaction was monitored by TLC (cyclohexane/EtOAc 95:5). When the reaction appeared complete, the reaction mixture was filtered through celite and the solvent was removed in under reduced pressure. The residue was then diluted with water (20 ml) and neutralized with NaOH. The resulting milky solution was extracted with Et_2O (3 x 50 ml). The organic phase was dried over $MgSO_4$ and concentrated to dryness *in vacuo* to give **35** as a white solid (5.6 g, 94%).

R_f = 0.35 (cyclohexane/EtOAc 19:1); **^{1}H-NMR (400 MHz, $CDCl_3$):** δ = 1.46 (s, 12H, 4 x CH_3), 1.93 (br s, 1H, N*H*), 7.10-7.15 (m, 2H, Ar*H*), 7.22-7.27 (m, 2H, Ar*H*) ppm: **^{13}C-NMR (75.4 MHz, $CDCl_3$):** δ = 30.1, 64.3, 121.0, 127.5, 146.7 ppm.

1,1,3,3-Tetraethylisoindoline (36)

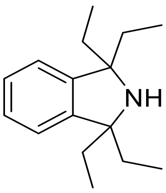

In a 500 ml round bottom flask **35** (17 g, 52.96 mmol) was dissolved in glacial acetic acid (307 ml). The solution was bubbled with argon for 5 min and 10% Pd/C (1.7 g) was added. The reaction flask was sealed with a septum and an air balloon filled with hydrogen connected to a syringe with a needle was attached to the septum. The reaction mixture was stirred for 4 h at 22 °C. The reaction was monitored by TLC (cyclohexane/EtOAc 19:1). When the reaction appeared complete, the reaction mixture was filtered through celite and the solvent was removed *in vacuo*. The residue was then diluted with water (40 ml) and neutralized with NaOH. The resulting milky solution was extracted with Et_2O (3 x 100 ml). The organic phase was dried over $MgSO_4$ and concentrated to dryness under reduced pressure to give **36** as a yellow oil (10.5 g, 85.8%).

R_f = 0.35 (cyclohexane/EtOAc 19:1); **^{1}H-NMR (500 MHz, $CDCl_3$):** δ = 0.87 (t, *J* = 7.4 Hz, 12H, 4 × CH_2CH_3), 1.71 (dd, *J* = 23.4, 7.3 Hz, 9H, 4 × CH_2CH_3, N*H*), 7.07 (dd, *J* = 5.6, 3.1 Hz, 2H, Ar*H*), 7.22 (dd, *J* = 5.6, 3.1 Hz, 2H, Ar*H*); **^{13}C-NMR (126 MHz, $CDCl_3$):** δ = 9.0, 33.7, 68.3, 122.5, 126.5, 147.4; **MS (ESI (+), 8 eV) m/z:** Calc. for $C_{16}H_{25}N$ $(M+H)^+$ 232.20 found 232.20.

5-nitro-1,1,3,3-tetramethylisoindoline (37)[58]

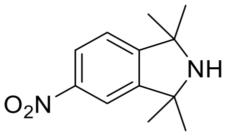

A 250 ml round bottom flask containing **5** (4.5 g, 25.6 mmol) was cooled down to 0 °C. Conc. H_2SO_4 (45 ml) was added dropwise and the dark-red solution was stirred for 15 min at 60 °C. The reaction solution was then cooled to 0 °C and a precooled conc. HNO_3 (2.9 ml, 69.6 mmol) was added dropwise. The reaction mixture was stirred for 2h at 0 °C (the reaction was monitored by TLC (cyclohexane/EtOAc 3:1) and subsequently heated for 10 min at 100 °C. To neutralize the reaction solution an ice cooled 2.5 M NaOH (100 ml) was added and the aqueous solution was extracted with Et_2O (3 x 100 ml). The organic phase was dried over $MgSO_4$ and concentrated to dryness *in vacuo* to give **37** as a yellow powder (4.45 g, 78.6%).

R_f = 0.40 (cyclohexane/EtOAc 3:1); **^{1}H-NMR (400 MHz, $CDCl_3$):** δ = 1.52 (s, 6H, 2 x CH_3), 1.53 (s, 6H, 2 x CH_3), 1.97 (br s, 1H, N*H*), 8.30 (d, 1H, ^3J = 8.3 Hz, Ar*H*), 8.00 (d, 1H, ^4J

= 2.1 Hz, Ar*H*), 8.17 (dd, 1H, ^3J = 8.3 Hz, ^4J = 2.1, Hz, Ar*H*) ppm; **^{13}C-NMR (75.4 MHz, $CDCl_3$):** δ = 31.2, 31.3, 62.3, 62.3, 116.7, 121.8, 122.8, 147.6, 150.2, 155.6 ppm; **MS (ESI (+), 8 eV) m/z:** Calc. for $C_{12}H_{16}N_2O_2$ $(M+H)^+$ 221.12, found 221.18.

5-nitro-1,1,3,3-tetraethylisoindoline (38)

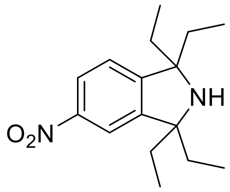

A 250 ml round bottom flask containing **36** (10.5 g, 45.3 mmol) was cooled down to 0 °C. Conc. H_2S0_4 (100 ml) was added dropwise and the dark-red solution was stirred for 15 min at 60 °C. The reaction solution was then cooled to 0 °C and a precooled conc. HNO_3 (6.9 ml, 165.35 mmol) was added dropwise. The reaction mixture was stirred for 2h at 0 °C (the reaction was monitored by TLC (cyclohexane/EtOAc 3:1) and subsequently heated for 10 min at 100 °C. To neutralize the reaction solution an ice cooled 2.5 M NaOH (200 ml) was added and the aqueous solution was extracted with Et_2O (3 x 100 ml). The organic phase was dried over $MgSO_4$ and concentrated to dryness under reduced pressure to give **38** as a yellow powder (8.56 g, 68.5%).

R_f = 0.35 (cyclohexane/EtOAc 3:1); **^{1}H-NMR (500 MHz, $CDCl_3$):** δ = 0.97 – 0.82 (m, 12H, 4 × CH_2CH_3), 1.85 – 1.59 (m, 9H, 4 × CH_2CH_3, N*H*), 7.19 (d, *J* = 8.3 Hz, 1H, Ar*H*), 7.91 (s, 1H, Ar*H*), 8.12 (d, *J* = 8.4 Hz, 1H) ppm; **^{13}C-NMR (126 MHz, $CDCl_3$):** δ = 8.8, 33.5, 66.8, 68.6, 117.9, 119.3, 122.7, 123.0, 147.7 ppm; **MS (ESI (+), 8 eV) m/z:** Calc. for $C_{16}H_{24}N_2O_2$ $(M+H)^+$ 277.18, found 277.19.

5-Amino-1,1,3,3-tetramethylisoindoline (39)[58]

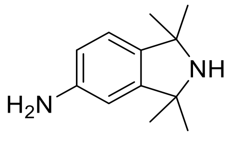

Compound **7** (3g, 13.6 mmol) was dissolved in MeOH (150 ml) in a 250 ml round bottom flask. A yellow solution was bubbled with argon for 5 min and 10% Pd/C (0.3 g) was added. The reaction flask was sealed with a septum and an air balloon filled with hydrogen was attached to the septum. The reaction mixture was stirred for 4 h at 22 °C. The reaction was monitored by TLC (DCM/MeOH 9:1). When the reaction appeared complete, the reaction mixture was filtered through celite and the solvent was removed under reduced pressure. The residue was purified on silica gel by flash chromatography using DCM/MeOH 100:0 to DCM/MeOH 90:10 as a gradient to give **39** as a red-brown solid (2.7 g, 96.1%).

R$_f$ = 0.3 (DCM/MeOH 9:1); **^{1}H-NMR (300 MHz, CDCl$_3$):** δ = 1.52 (s, 6H, 2 x C*H$_3$*), 1.53 (s, 6H, 2 x C*H$_3$*), 5.50 (br s, 2H, N*H$_2$*), 6.40 (dd, 1H, ^4J = 2.2 Hz, ^5J = 0.6 Hz, Ar*H*), 6.60 (dd, 1H, ^3J = 8.1 Hz, ^4J = 2.2 Hz, Ar*H*), 6.88 (dd, 1H, ^3J = 8.1 Hz, ^5J = 0.6 Hz, Ar*H*) ppm; **^{13}C-NMR (75.4 MHz, MeOH-d4):** δ = 27.1, 27.5, 66.6, 66.7, 106.9, 115.5, 121.2, 130.1, 124.7, 148.7 ppm; **MS (ESI (+), 8 eV) m/z:** Calc. for $C_{12}H_{18}N_2$ $(M+H)^+$ 191.15, found 191.06.

5-Amino-1,1,3,3-tetraethylisoindoline (40)

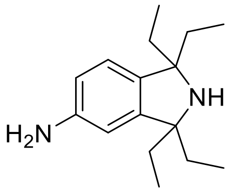

Compound **39** (8.56 g, 31 mmol) was dissolved in MeOH (428 ml) in a 500 ml round bottom flask. A yellow solution was bubbled with argon for 5 min and 10% Pd/C (856 mg) was added. The reaction flask was sealed with a septum and an air balloon filled with hydrogen was attached to the septum. The reaction mixture was stirred for 4 h at 22 °C. The reaction was monitored by TLC (DCM/MeOH 9:1). When the reaction appeared complete, the reaction mixture was filtered through celite and the solvent was removed *in vacuo*. The residue was purified on silica gel by flash chromatography using DCM/MeOH 100:0 to DCM/MeOH 90:10 as a gradient to give **40** as a brown solid (1.9 g, 25.0%).

R$_f$ = 0.3 (DCM/MeOH 9:1); **^{1}H-NMR (500 MHz, MeOH-d4):** δ = 0.86 (td, *J* = 7.3 Hz, 12H, 4 × CH$_2$C*H$_3$*), 1.68 (m, 9H, 4 × C*H$_2$*CH$_3$, N*H*), 6.49 (d, *J* = 2.1 Hz, 1H, Ar*H*), 6.63 (dd, *J* = 8.1, 2.1 Hz, 1H, Ar*H*), 6.83 (d, *J* = 8.1 Hz, 1H, Ar*H*) ppm; **^{13}C-NMR (126 MHz, MeOH-d4):** δ = 7.8, 7.8, 33.0, 33.2, 67.9, 68.3, 109.5, 114.6, 122.6, 133.9, 146.0, 147.8 ppm; **MS (ESI (+), 8 eV) m/z:** Calc. for $C_{12}H_{18}N_2$ $(M+H)^+$ 247.21, found 247.21.

5-azido-1,1,3,3-tetramethylisoindoline (41)[87]

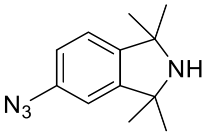

Triethylamine (1 ml, 7.2 mmol), CuSO$_4$*5H$_2$O (24 mg, 0.096 mmol) and imidazole-1-sulfonyl azide (500 mg, 2.89 mmol) were added to a solution of **39** (457 mg, 2.4 mmol) in methanol (20 ml). The resulting reaction mixture was stirred in the dark for 16 h at 22 °C. The reaction was monitored by TLC (DCM/MeOH 9:1). The reaction mixture was poured into saturated aqueous NaHCO$_3$ and extracted with DCM (3 x 20 ml). The combined organic phases were dried over MgSO$_4$ and solvent was removed *in vacuo*.

The residue was chromatographically purified on silica gel using DCM/MeOH 100:0 to DCM/MeOH 90:10 as a gradient to give **41** as a brown liquid (221 mg, 42.5%).

R$_f$ = 0.43 (DCM/MeOH 9:1); **^{1}H-NMR (300 MHz, CDCl$_3$):** δ = 1.44 (s, 6H, 2 x C*H$_3$*), 1.45 (s, 6H, 2 x C*H$_3$*), 2.31 (br s, 1H, N*H*), 6.75 (dd, ^4J = 2.1Hz, ^5J = 0.6 Hz, 1H, Ar*H*), 6.90 (dd, ^3J = 8.1Hz, ^4J = 2.1 Hz, 1H, Ar*H*), 7.08 (dd, ^3J = 8.1Hz, ^5J = 0.6 Hz, 1H, Ar*H*) ppm; **^{13}C-NMR (75.4 MHz, CDCl$_3$):**
δ = 31.7, 31.8, 62.7, 62.8, 112.0, 118.1, 122.6, 139.0, 145.6, 150.7 ppm; **MS (ESI (+), 8 eV) m/z:** Calc. for $C_{12}H_{16}N_4$ $(M+H)^+$ 217.14 found 217.20.

5-azido-1,1,3,3-tetraethylisoindoline (42)

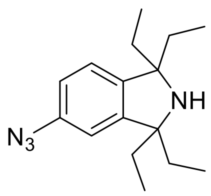

Triethylamine (1.6 ml, 10.8 mmol), $CuSO_4{*}5H_2O$ (35.6 mg, 0.14 mmol) and imidazole-1-sulfonyl azide (747 mg, 4.32 mmol) were added to a solution of **40** (879 mg, 3.6 mmol) in methanol (44 ml). The resulting reaction mixture was stirred in the dark for 16 h at 22 °C. The reaction was monitored by TLC (DCM/MeOH 9:1). The reaction mixture was poured into saturated aqueous $NaHCO_3$ and extracted with DCM (3 x 30). The combined organic phases were dried over $MgSO_4$ and solvent was removed *in vacuo*. The residue was chromatographically purified on silica gel using DCM/MeOH 100:0 to DCM/MeOH 90:10 as a gradient to give **42** as a brown liquid (485 mg, 50.0%).

R$_f$ = 0.43 (DCM/MeOH 9:1); **^{1}H-NMR (500 MHz, CDCl$_3$):** δ = 0.87 (m, 12H, 4 x C*H$_3$*), 1.56 (br s, 1H, N*H*), 1.78 – 1.57 (m, 8H, 4 × C*H$_2$*CH$_3$), 6.69 (d, *J* = 2.1 Hz, 1H, Ar*H*), 6.89 (dd, *J* = 8.1, 2.1 Hz, 1H, Ar*H*), 7.03 (d, *J* = 8.0 Hz, 1H, Ar*H*) ppm; **^{13}C-NMR (126 MHz, CDCl$_3$):** 8.8, 8.8, 33.7, 33.7, 113.0, 117.5, 123.5, 138.4, 144.6, 149.7 ppm; **MS (ESI (+), 8 eV) m/z:** Calc. for $C_{12}H_{16}N_4$ $(M+H)^+$ 273.20 found 273.20.

5-azido-1,1,3,3-tetramethylisoindolin-1-yloxyl (43)[87]

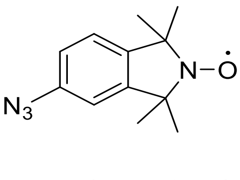

To a solution of **41** (221 mg, 1.023 mmol) in DCM (2 ml) a solution of *m*CPBA (353.13 mg, 2.05 mmol) in DCM (2.6 ml) was added dropwise at 0 °C. The resulting reaction mixture was stirred for 3 h. The progress of the reaction was controlled by TLC (DCM/MeOH 9:1). The reaction mixture was diluted with H_2O (5 ml) and the aqueous phase was extracted with DCM (3 x 5 ml). The combined organic phases were washed with saturated aqueous $NaHCO_3$ (5 mL) and the corresponding aqueous phase extracted with DCM (3 x 5 ml). The solvent was removed *in vacuo* and the residue purified on silica gel by flash chromatography using petroleum ether/EtOAc 100:0 to petroleum ether/EtOAc 95:5 as a gradient to yield **43** as a yellow solid (170 mg, 72.3%).

R_f = 0.9 (DCM/MeOH 9:1); **^{1}H-NMR (300 MHz, $CDCl_3$):** δ = 0.9 (br s), 1.47 (br s), 5.18 (br s), 8.83 (br s) ppm: **MS (ESI (+), 8 eV) m/z:** Calc. for $C_{12}H_{15}N_4O$• $(M+H)^+$ 232.12 found 232.12.

5-azido-1,1,3,3-tetraethylisoindolin-1-yloxyl (44)

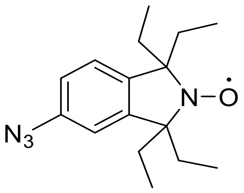

To a solution of **42** (485 mg, 1.78 mmol) in DCM (2.8 ml) a solution of *m*CPBA (615 mg, 3.56 mmol) in DCM (3.00 ml) was added dropwise at 0 °C. The resulting reaction mixture was stirred for 3 h. The progress of the reaction was controlled by TLC (DCM/MeOH 9:1). The reaction mixture was diluted with H_2O (5 ml) and the aqueous phase was extracted with DCM (3 x 5 ml). The combined organic phases were washed with saturated aqueous $NaHCO_3$ (5 mL) and the corresponding aqueous phase extracted with DCM (3 x 5 ml). The solvent was removed *in vacuo* and the residue purified on silica gel by flash chromatography using petroleum ether/EtOAc 100:0 to petroleum ether/EtOAc 95:5 as a gradient to yield **44** as a yellow solid (328 mg, 64.0%).

R_f = 0.9 (DCM/MeOH 9:1); **^{1}H-NMR (500 MHz, $CDCl_3$):** δ = 1.12-1.21 (br m), 1.34 (br s), 5.47 (br s), 9.35 (br s) ppm; **MS (EI, m/z):** Calc. for $C_{16}H_{23}N_4O$• $(M+H)^+$ 287.19 found 287.2.

5-Iodo-2‘-O-methylcytidine (48)[117]

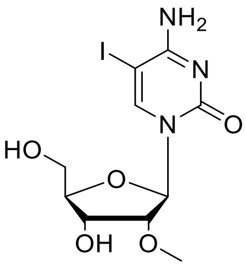

In a flame dried 50 ml round bottom flask **47** (1.0 g, 3.8 mmol) was dissolved in anhydrous DMF (13 ml) under argon atmosphere. Iodine (578 mg, 4.5 mmol) and *m*CPBA (689 g, 4.0 mmol) were added to a solution the reaction mixture was stirred for 4 h at 22 °C. The solvent was removed under reduced pressure and the resulting crude product was purified on silica gel using column chromatography (DCM/MeOH 100:0 to 90:10) to yield **48** as orange powder (900 mg, 60.3%).

R_f = 0.35 (DCM/MeOH 9:1); **^{1}H-NMR (400 MHz, MeOH-d4):** δ = 3.59 (s, 3H, OC*H*$_3$), 3.72 – 3.84 (m, 2H, C-5'H), 4.05 – 3.94 (m, 2H, C-2'H, C-4'H), 4.21 (dd, *J* = 7.9, 5.0 Hz, 1H, C-3'H), 5.87 (d, *J* = 1.9 Hz, 1H, C-1'H), 8.71 (s, 1H, C-6H) ppm; **^{13}C-NMR (100.6 MHz, MeOH-d4):** δ = 58.5, 60.1, 68.4, 84.9, 85.1, 89.5, 148.9, 156.6, 165.4 ppm; **MS (ESI (+), 8 eV) m/z:** Calc. for $C_{10}H_{14}IN_3O_5$ $(M+H)^+$ 384.00 found 384.00.

5-(Trimethylsilylethynyl)-2'-O-methylcytidine (49)

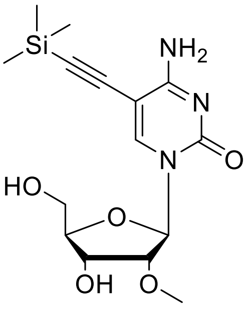

In a flame-dried 50 ml round bottom flask **48** (800 mg, 2.1 mmol) was dissolved in anhydrous DMF (16 ml) under argon atmosphere. CuI (40 mg, 0.21 mmol), $(Ph_3P)_2PdCl_2$ (147 mg, 0.21 mmol) and trimethylsilylacetylene (2.3 ml, 16.7 mmol) were added successively. The resulting reaction mixture was stirred for 1.5 h at 22 °C. The progress of the reaction was controlled by TLC (DCM/MeOH 9:1).The solvent was removed *in vacuo* and the crude residue purified on silica gel by means of flash chromatography using DCM/MeOH 100:0 to DCM/MeOH 80:20 as a gradient to give **49** as a white powder (650 mg, 88%).

R_f = 0.54 (DCM/MeOH 9:1); **^{1}H-NMR (400 MHz, DMSO-d$_6$):** δ = 0.2 (s, 9H, $Si(CH_3)_3$), 3.4 (s, 3H, OC*H*$_3$), 3.55 – 3.73 (m, 3H, C-5'H, C-2'H), 3.82 (dd, *J* = 6.3, 2.9 Hz, 1H, C-4'H), 4.11 (q, *J* = 6.0 Hz, 1H, C-3'H), 5.03 (d, *J* = 6.5 Hz, 1H, O*H*), 5.21 (t, *J* = 4.7 Hz, 1H, O*H*), 5.82 (d, *J* = 3.3 Hz, 1H, C-1'H), 6.64 (br s, N*H*), 7.78 (br s, N*H*) 8.37 (s, 1H, C-6H), 8.85 (s, 1H, N*H*) ppm. **^{13}C-NMR (100.6 MHz, DMSO-d$_6$):** δ = 0.0, 8.7, 45.8, 57.1, 59.5, 67.6, 83.4, 84.2, 87.3, 89.9, 96.9, 97.9, 99.7, 145.5, 153.5, 164.0 ppm; **MS (ESI (+), 8 eV) m/z:** Calc. for $C_{10}H_{13}IN_2O_6$ $(M+Na)^+$ 354.14 found 354.15.

5-Ethynyl-2‘-O-methylcytidine (50)

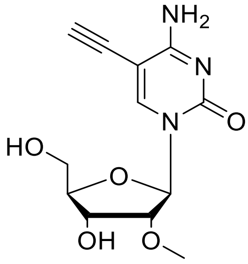

K_2CO_3 (4.0 g, 29.04 mmol) was added to a solution of **49** (5 g, 14.16 mmol) in methanol (700 ml) and the reaction mixture was stirred for 5 h at 22 °C. The monitoring of the reaction progress was carried out using TLC (DCM/MeOH 9:1). The solvent was removed under reduced pressure and the crude residue was purified by column chromatography using DCM/MeOH 100:0 to DCM/MeOH 90:10 as a gradient to yield **50** as a yellow powder (3.4 g, 85%).

R_f = 0.20 (DCM/MeOH 9:1); **^{1}H-NMR (400 MHz, DMSO-d$_6$):** δ = 3.16 (s, 1H, C_{alkyne}*H*), 3.42 (s, 3H, OC*H*$_3$), 3.56 - 3.75 (m, 2H, C-5'H, C-2'H), 3.84 (dt, *J* = 6.7, 2.5 Hz, 1H, C-4'H), 4.07 (dd, *J* = 6.7, 5.0 Hz, 1H, C-3'H), 4.35 (s, 1H, C_{alkyne}*H*), 5.04 (s, 1H, O*H*), 5.26 (s, 1H, O*H*), 5.81 (d, *J* = 3.0 Hz, 1H, C-1'H), 7.00 (br s, 1H, N*H*), 7.83 (br s, 1H, N*H*), 8.45 (s, 1H, C-6H) ppm; **^{13}C-NMR (100.6 MHz, DMSO-d$_6$):** δ = 48.6, 57.6, 59.3, 67.5, 75.6, 83.5, 84.0, 86.0, 87.3, 89.0, 145.72 152.9, 163.9 ppm; **MS (ESI (+), 8 eV) m/z:** Calc. for $C_{12}H_{15}N_3O_5$ $(2M+Na)^+$ 585.19 found 585.19.

N$_4$-Acetyl-5-Ethynyl-2‘-O-methylcytidine (51)

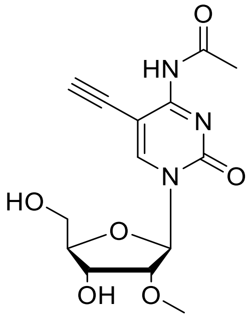

Compound **50** (500 mg, 1.78 mmol) was dissolved in DMF (9.9 ml) and Ac_2O (190 µl, 1.96 mmol) was added. The resulting reaction mixture was stirred for 24 h at 22 °C. The progress of the reaction was controlled by TLC (DCM/MeOH 9:1). The solvent was removed under reduced pressure and the crude residue purified on silica gel by column chromatography using DCM/MeOH 100:0 to DCM/MeOH 90:10 as a gradient to yield **51** as a white foam (3.4 g, 37.4%).

R_f = 0.33 (DCM/MeOH 9:1); **^{1}H-NMR (500 MHz, DMSO-d$_6$):** δ = 2.30 (s, 3H, CH_3), 3.47 (s, 3H, OC*H*$_3$), 3.56 - 3.84 (m, 2H, C-5'H, C-2'H), 3.89 (dt, *J* = 7.9, 2.2 Hz, 1H, C-4'H), 4.08 (td, *J* = 7.3, 4.8 Hz, 1H, C-3'H), 4.48 (s, 1H, C$_{alkyne}$*H*), 5.11 (d, *J* = 7.0 Hz, 1H, O*H*), 5.39 (t, *J* = 4.6 Hz, 1H, O*H*), 5.80 (d, *J* = 1.9 Hz, 1H, C-1'H), 8.45 (s, 1H, C-6H), 9.40 (s, 1H, N*H*) ppm; **^{13}C-NMR (126 MHz, DMSO-d$_6$):** δ = 25.4, 46.2, 55.3, 58.3, 59.1, 67.4, 75.5, 83.9, 84.4, 87.5, 88.7, 92.98, 148.8, 151.9, 161.9, 170.4 ppm; **MS (ESI (+), 8 eV) m/z:** Calc. for $C_{14}H_{17}N_3O_6$ (M+Na)$^+$ 346.10 found 346.10

5'-O-Dimethoxytrityl-N$_4$-Acetyl-5-ethinyl-2'-O-methylcytidine (52)

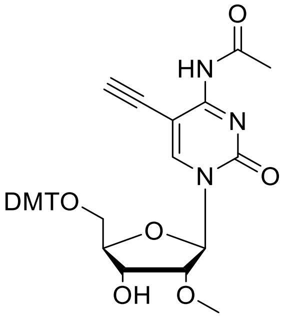

51 (200 mg, 0.62 mmol), DMTCl (272.7 mg, 0.80 mmol) and DMAP (7.6 mg, 0.06 mmol) were dried kept under vacuum for 16 h. Anhydrous pyridine (6 ml) was added and the reaction mixture was stirred for 5 h at 22 °C. The reaction was controlled by TLC (DCM/MeOH 9:1). The solvent was removed by co-evaporation with toluene. The resulting residue was purified on silica gel by flash chromatography (Et_3N/CH_2Cl_2/MeOH 1:99:0 to 1:95:4) to yield **52** as a white foam (200 g, 51.6%).

R$_f$ = 0.55 (DCM/MeOH 9:1).

^{1}H-NMR (500 MHz, CDCl$_3$): δ = 2.70 (s, 3H, CH_3), 2.99 (s, 1H, C$_{alkyne}$*H*), 3.47 - 3.60 (m, 2H, C-5'H), 3.77 (s, 3H, OC*H$_3$*), 3.90 (d, *J* = 5.3 Hz, 1H, C-2'H), 4.03 - 4.09 (m, 1H, C-4'H), 4.44-4.51 (m, 1H, C-3'H), 5.89 (s,1H, C-1'H), 6.801 - 6.87 (m, 4H, Ar*H*), 7.16 - 7.39 (m, 9H, Ar*H*), 8.06 (br s,1H, N*H*,), 8.47 (s, 1H, C-6H) ppm; **^{13}C-NMR (126 MHz, CDCl$_3$):** δ = 26.5, 55.2, 55.2, 59.0, 60.7, 67.9, 72.9, 83.3, 83.5, 86.0, 86.8, 88.8, 91.3, 123.7, 126.9, 135.3, 135.6, 135.9, 144.4, 146.5, 149.8, 158.5, 160.1, 172.0 ppm; **MS (ESI (+), 8 eV) m/z:** Calc. for $C_{35}H_{35}N_3O_8$ (M+Na)$^+$ 648.23 found 648.23.

3’-O-[(2-Cyanoethyl)(N,N-diisopropylamino)phosphinyl]-5’-O-dimethoxytrityl-5-ethinyl -2’-O-methylcytidine (EmC)

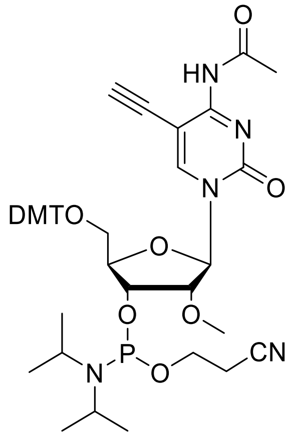

52 (323 mg, 0.25 mmol) was dried under vacuum for 16 h. The residue was dissolved in anhydrous DCM (2.5 ml) and DIPEA (48 µl, 0.28 mmol) was added. The solution was stirred for 5 min and 2-cyanoethyl N,N-diisopropylchlorophosphoramidite (61.4 µL, 0.28 mmol) was added dropwise. The resulting yellow solution was stirred for 3 h at 22 °C. The progress of the reaction monitored by TLC (Cy/EtOAc/Et_3N 47:50:3). The reaction mixture was diluted with DCM (10 ml), washed with saturated aqueous $NaHCO_3$ (3 × 15 mL) and saturated aqueous NaCl (3 × 15 mL). The organic phase was dried over $MgSO_4$ and the solvent concentrated under reduced pressure. The crude product was purified on silica gel by means of column chromatography (Cy/EtOEt/Et_3N 47:50:3) to yield **EmC** as a white foam (110 mg, 26%).

R_f = 0.62 (cyclohexane/EtOAc/Et_3N 47:50:3); **^{1}H-NMR (500 MHz, $CDCl_3$):** δ = 1.07-1.24 (m, 14H), 1.42 (s,1H), 2.42 (t, *J* = 6.2 Hz, 1H), 2.62 (t, *J* = 6.1 Hz, 1H), 2.70 (s, 3H, CH_3), 3.28 -3.6 (m, 6H) 3.68 (s, 3H, OCH_3), 3.89 (m, 1H), 4.00 (dd, *J* = 4.9, 1.4 Hz, 1H), 4.07 (d, *J* = 4.8 Hz, 1H), 4.28 (m, 1H), 4.48 (m, 1H), 4.64 (m, 1H), 5.87-5.92 (s,1H, C-1'H), 6.77 - 6.85 (m, 4H, Ar*H*), 7.16 - 7.39 (m, 9H, Ar*H*), 8.02 (br s,1H, N*H*,), 8.47 (s, 1H, C-6H) ppm.

^{13}C-NMR (126 MHz, $CDCl_3$): 20.5, 24.5, 24.6, 26.9, 43.2, 43.3, 55.2, 55.2, 83.0, 113.2, 117.5, 126.9, 128.0, 128.2, 130.2, 130.2, 130.2, 135.5, 144.4, 158.5, 158.6 ppm; **^{31}P-NMR (202.4 MHz, $CDCl_3$):** δ = 150.1, 151.5 ppm; **MS (ESI (+), 8 eV) m/z:** Calc. for $C_{44}H_{52}N_5O_9P$ $(M+K)^+$ 864.44 found 864.32.

5-Hydroxy-1,1,3,3-tetramethylisoindoline (56)[58]

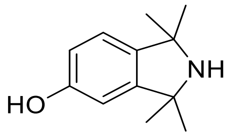

A solution of **39** (3.8 g, 19.98 mmol) in cons. H_2SO_4 (35% w/v,10 ml) was cooled to -10 °C and an ice-cooled solution of $NaNO_2$ (1.65 g, 23.98 mmol) in water (16.5 ml) was added. The resulting reaction mixture was stirred for 3h at -10 °C. The reaction was monitored by ^{1}H NMR in D_2O. When the reaction appeared complete urea (0.24 g, 4.0 mmol) was added and it was stirred at -10 °C for other 15 min. The reaction mixture was then allowed to warm to 22 °C and subsequently refluxed for 4 h. To neutralize the reaction mixture NaOH (30% w/v) was added at -5 °C. The salts were filtered and the filtrate was concentrated *in vacuo* to give a red powder. **56** was in the next step without further purification (3.8 g, 100%).

In-situ **^{1}H-NMR (400 MHz, D_2O):** δ = 1.86-187 (m, 12H, 4 x C*H_3*), 7.93 - 7.96 (m, 1H, Ar*H*), 8.64 - 8.66 (m, 1H, Ar*H*) ppm.

5-Hydroxy-6-nitro-1,1,3,3-tetramethylisoindoline (57)[58]

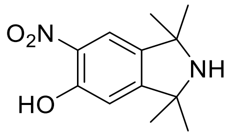

An ice cooled conc. HNO_3 (65%, 16mL) was added to **56** (3.8 g, 19.8 mmol) and the reaction mixture was stirred at -5 °C for 3 h. The reaction was monitored by ^{1}H NMR in D_2O and by TLC (DCM/MeOH, 9:1). When the reaction was complete a solution of NaOH (40% w/v) was added and pH was adjusted to 7. The salts were filtered and the filtrate was concentrated under reduced pressure. The residue was purified on silica gel by flash chromatography using DCM as eluent to yield **57** as yellow powder (2.0 g, 43%).

R_f = 0.81 (DCM/MeOH 9:1); **^{1}H-NMR (400 MHz, $CDCl_3$):** δ = 1.50 (s, 12H, 4 x C*H_3*), 6.87 (s, 1H, Ar*H*), 7.83 (s, 1H, Ar*H*) ppm; **^{13}C-NMR (126 MHz, $CDCl_3$):** δ = 31.3, 31.9, 62.3, 62.9, 112.2, 112, 2, 117.9, 133.1, 141.8, 155.4, 160.2 ppm; **MS (ESI (+), 8 eV) m/z:** Calc. for $C_{12}H_{16}N_2O_3$ $(M+H)^+$ 237.12, found 237.05.

5-Hydroxy-6-amino-1,1,3,3-tetramethylisoindoline (58)[58]

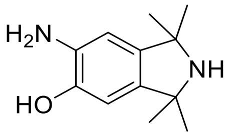

57 (1 g, 4.2 mmol) was dissolved in MeOH (50 ml) and a yellow solution was bubbled with argon for 5 min. 10% Pd/C (0.1 g) was added and an air balloon filled with hydrogen was attached. The reaction mixture was stirred for 3 h at 22 °C. The reaction was monitored by TLC (DCM/MeOH 9:1). After completion of reaction, the reaction mixture was filtered through celite and the solvent was removed *in vacuo* to give **58** as a dark violet solid (0.92 g, 98.5%).

R$_f$ = 0.15 (DCM/MeOH 9:1); **^{1}H-NMR (400 MHz, MeOH-d4):** δ = 1.65 (s, 6H, 2 x C*H$_3$*), 1.66 (s, 6H, 2 x C*H$_3$*), 6.52 (s, 1H, Ar*H*), 6.57 (s, 1H, Ar*H*) ppm; **^{13}C-NMR (75.4 MHz, DMSO-d$_6$):** δ = 29.7, 29.7, 65.6, 65.7, 106.9, 106.9, 134.6, 137.4, 144.6 ppm; **MS (ESI (+), 8 eV) m/z:** Calc. for $C_{12}H_{18}N_2O$ (M+H)$^+$ 207.14, found 207.06.

5-Bromo-2'-O-methyluridine (60)[59]

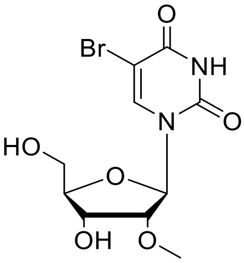

A solution of NaN_3 (6.29 g, 96.8 mmol) in water (20 mL) was added to a suspension of 2'-O-methyluridine **59** (5.0 g, 19.36 mmol) in 1,2-dimethoxyethane (107 ml). After stirring for 15 min at 22 °C N-bromosuccinimide (4.48 g, 25.2 mmol) was added to the reaction mixture and it was stirred for 24 h at 22 °C. Monitoring of the reaction progress was done by TLC (DCM/MeOH 9:1). When the reaction appeared complete the solvent was removed *in vacuo* and the residue was purified on silica gel by flash chromatography using DCM/MeOH 100:0 to DCM/MeOH 90:10 as a gradient to yield **60** as a white solid (4 g, 61.2%).

R$_f$ = 0.54 (DCM/MeOH 9:1); **^{1}H-NMR (400 MHz, DMSO-d$_6$):** δ = 3.39 (s, 3H, OC*H$_3$*), 3.57–3.60 (m, 1H, C-5'Ha), 3.69–3.72 (m, 1H, C-5'Hb), 3.80 (t, *J* = 4.9 Hz, 3.8 Hz, 1H, C-2'H), 3.86–3.87 (m, 1H, C-4'H), 4.12 (q, *J* = 5.3 Hz, 1H,C-3'H), 5.12 (d, *J* = 6.3 Hz, 1H, C-3'O*H*), 5.31-5.34 (m, 1H, C-5'O*H*), 5.80 (d, *J* = 3.8 Hz, 1H,C-1'H), 8.52 (s, 1H, C-6H) ppm; **^{13}C-NMR (75.4 MHz, DMSO-d$_6$):** 57.6, 59.7, 67.7, 83.0, 84.8, 86.7, 95.8, 140.1, 149.8, 159.3; **MS (ESI (+), 8 eV) m/z:** Calc. for $C_{10}H_{13}BrN_2O_6$ (M+H)$^+$ 337.00, found 337.68.

3′,5′-Diacetyl-5-bromo-2′-O-methyluridine (61)[59]

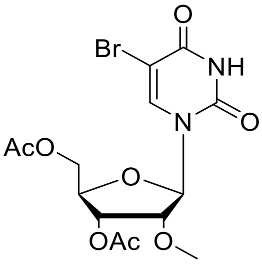

60 (6 g, 17.8 mmol) was dissolved in pyridine (15 ml) and acetic anhydride (11ml, 107.1 mmol) was added at 0 °C and the reaction mixture was stirred for 16 h at 22 °C. The progress of the reaction was monitored by TLC (cyclohexane/EtOAc 1:1). The solvent was removed under reduced pressure and the residue was dissolved in DCM (100 ml) and washed with water (3 x 100 ml). The organic phase was then dried over $MgSO_4$, the solvent concentrated under reduced pressure and the residue purified by column chromatography (cyclohexane/EtOAc 1:1) to give **61** as a white solid (6 g, 80.0%).

R$_f$ = 0.35 (cyclohexane/EtOAc 1:1); **^{1}H-NMR (400 MHz, CDCl$_3$):** δ = 2.15 (s, 3H, C*H*$_3$CO), 2.23 (s, 3H, C*H*$_3$CO), 3.51 (s, 3H, OC*H*$_3$), 4.05 (dd, *J* = 2.5 Hz, 5.1 Hz, 1H, C-2'H), 4.38-4.43 (m, 3H, C-4'H, C-5'H), 4.94 (dd, *J* = 7.1, 5.2 Hz, 1H, C-3'H), 5.93 (d, *J* = 2.6 Hz, 1H, C-1'H), 7.97 (s, 1H, C-6H), 9.29 (br s, 1H, N*H*) ppm; **^{13}C-NMR (75.4 MHz, CDCl$_3$):** δ =20.2, 20.6, 58.7, 61.4, 68.97, 78.9, 81.5, 88.4, 96.8, 138.1, 149.0, 158.4, 169.7, 169.8 ppm; **MS (ESI (+), 8 eV) m/z:** Calc. for $C_{14}H_{17}BrN_2O_8$ $(M+H)^+$ 421.02, found 420.90.

3′,5′-Diacetyl-5-bromo-4-chloro-2′-O-methyluridine (62)[59]

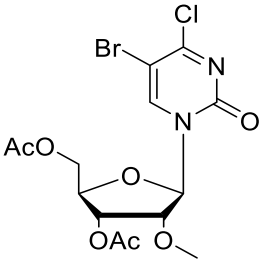

61 (1.2 g, 2.85 mmol) was dissolved in a mixture of DCM/CCl_4 (1:1, 34 ml). A colorless solution was stirred for 15 min at 22 °C and PPh_3 (1.87 g, 7.125) was added. A yellow solution was refluxed for 3 h, thereby the reaction temperature should not exceed 45 °C. The reaction was monitored by TLC (DCM/MeOH 9:1). The solvent was removed and the residue was purified by column chromatography using DCM as an eluent to give **62** as a white solid (0.5 g, 40.0%).

R$_f$ = 0.75 (DCM/MeOH 9:1); **^{1}H-NMR (300 MHz, CDCl$_3$):** δ = 2.14 (s, 3H, C*H*$_3$CO), 2.22 (s, 3H, C*H*$_3$CO), 3.63 (s, 3H, OC*H*$_3$), 4.11-4.13 (m, 1H, C-2'H), 4.41-4.55 (m, 3H, C-4'H, C-5'H), 4.76 (dd, *J* = 9.5, 4.9 Hz, 1H, C-3'H), 5.89 (s, 1H, C-1'H), 8.39 (s, 1H, C-6H) ppm.

3´,5´-Diacetyl-5-bromo-N$_4$-(6-hydroxy-1,1,3,3-tetramethylisoindolinyl)-2´-O-methylcytidine (63)[59]

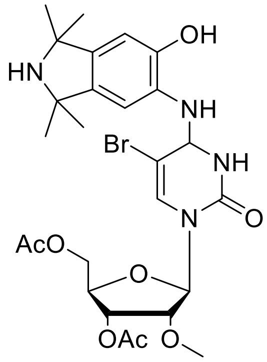

To a solution of **62** (0.64 g, 1.45 mmol) in DCM (28 ml) a solution of **58** (0.25 g, 1.21 mmol) in DMF (8 ml) was added. The reaction mixture was stirred for 5 min at 22 °C and DBU (0.24 ml) was added. A black solution was stirred for 16 h and the solvent was removed *in vacuo* to give a green brown oil. The reaction progress was monitored by LCMS. The crude product was used in the next step without further purification.

***In-situ* MS (ESI (+), 8 eV) m/z:** Calc. for $C_{26}H_{33}BrN_4O_8$ $(M+H)^+$ 609.15, found 609.60.

Phenoxazine derived nucleoside (64)[59]

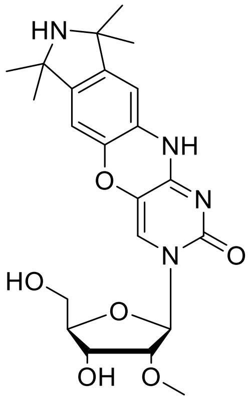

63 (0.73 g, 1.64 mmol) was dissolved in Ethanol (100 ml) and NaF (0.65 g, 15.48 mmol) was added. The yellow reaction solution was refluxed for 3 days, thereby the progress of the reaction was controlled by TLC (DCM/MeOH 90:10). The reaction mixture was filtered and the solvent was removed *in vacuo*. The residue was purified on silica gel by flash chromatography using DCM/MeOH 100:0 to DCM/MeOH 65:35 as a gradient to yield **64** as a yellow solid (0.5 g, 40.0%).

R$_f$ = 0.23 (DCM/MeOH 9:1); **^{1}H-NMR (500 MHz, MeOH-d4):** δ = 1.52 (m, 12H, 4 x C*H$_3$*), 3.58 (s, 3H, OC*H$_3$*), 3.77-3.80 (m, 2H, C-5'H), 3.91-3.97 (m, 2H, C-2'H, C-4'H), 4.23 (dd, *J* = 7.3, 5.0 Hz, 1H, C-3'H), 5.87 (d, *J* = 2.4 Hz, 1H, C-1'H), 6.6 (s, 1H, Ar*H*), 6.9 (s, 1H, Ar*H*), 7.88 (s, 1H, C-6H) ppm; **^{13}C-NMR (126 MHz, MeOH-d4):** δ = 28.9, 29.1, 57.5, 59.6, 64.7, 67.8, 84.0, 84.0, 88.1, 106.2, 109.5, 122.4, 127.0, 128.0, 143.0, 154.4, 154.7; **MS (ESI (+), 8 eV) m/z:** Calc. for $C_{22}H_{28}N_4O_6$ $(M+H)^+$ 445.20, found 445.30.

Spin-labeled nucleoside Çm (65)[59]

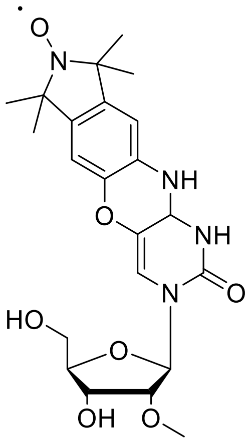

64 (204 mg, 0.46 mmol) was dissolved in methanol (13 ml) and $NaHCO_3$ (39 mg, 0.46 mmol) was added. H_2O_2 (45% w/v, 0.222 ml) was added dropwise and the yellow suspension was stirred for 5 min at 22°C. Na_2WO_4 (23 mg, 0.07 mmol) was added and the resulting reaction mixture was stirred for 30 h at 22 °C. The progress of the reaction was controlled by TLC (DCM/MeOH 9:1). The salts were filtered and the filtrate was concentrated under reduced pressure. The resulting residue was purified by silica flash chromatography to give **65** as a bright yellow powder (0.114 g, 54.0%).

R_f = 0.46 (DCM/MeOH 9:1); **^{1}H-NMR (500 MHz, DMSO-d$_6$):** δ = 3.40 (br s, 3H), 3.60-3.70 (m, 3H), 3.83 (br s, 1H), 4.13 (br s, 1H), 5.10 (br s, 1H), 5.27 (br s, 1H), 5.87 (br s, 1H),), 7.48 (br s, 1H), 10.35 (br s, 1H) ppm; **MS (ESI (+), 8 eV) m/z:** Calc. for $C_{22}H_{27}N_4O_7$• $(M+H)^+$ 460.19, found 460.21.

5'-Dimethoxytritylated, spin-labeled nucleoside Çm (66)[59]

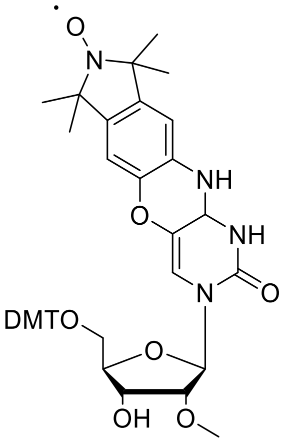

65 (57 mg, 0.12 mmol), DMTCl (51 mg, 0.15 mmol) and DMAP (1.5 mg, 0.013 mmol) were dried kept under vacuum for 16 h. Anhydrous pyridine (2.6 ml) was added and the reaction mixture was stirred for 5 h at 22 °C. The reaction was controlled by TLC (DCM/MeOH 9:1). The solvent was removed by co-evaporation with toluene. The resulting residue was purified on silica gel by flash chromatography ($Et_3N/CH_2Cl_2/MeOH$ 1:99:0 to 1:95:4) to yield **66** as yellow solid (83 mg, 88.0%).

R_f = 0.55 (DCM/MeOH 9:1); **^{1}H-NMR (500 MHz, DMSO-d_6):** δ = 3.46 (br s, 3H, OC*H*$_3$), 3.74 (br s), 3.97 (br s, 1H), 4.26 (br s, 1H), 5.20 (br s, 1H), 5.84 (br s, 1H), 6.53 (br s, 1H), 6.93 (br s, 4H), 7.33 - 7.45 (br s, 9H), 8.10 (br s, 1H), 10.53 (br s, 1H) ppm; **MS (ESI (+), 8 eV) m/z:** Calc. for $C_{43}H_{45}N_4O_9$• $(M+H)^+$ 762.32, found 762.66.

Spin-labeled phosphoramidite Çm[59]

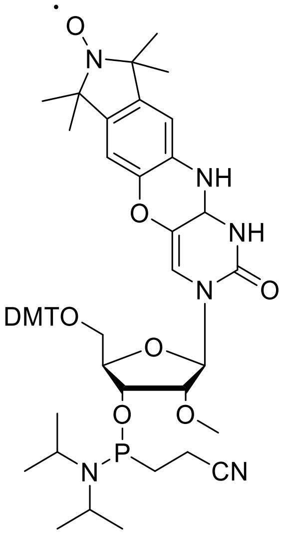

66(100 mg, 0.131 mmol) and diisopropyl ammonium tetrazolide (52 mg, 0.31 mmol) were dissolved in pyridine (1 ml). Pyridone was removed *in vacuo* and the mixture was dried under vacuum for 16 h. The residue was dissolved in anhydrous DCM (5.6 ml) and 2-cyanoethyl N,N,N′,N′-tetraisopropyldiamidophosphite (162 µL, 0.39 mmol) was added dropwise. The resulting yellow solution was stirred for 5 h at 22 °C. The progress of the reaction was monitored by TLC (DCM/MeOH 9:1). The reaction mixture was diluted with DCM (10 ml), washed with saturated aqueous $NaHCO_3$ (3 × 15 mL) and saturated aqueous NaCl (3 × 15 mL). The organic phase was dried over $MgSO_4$ and the solvent concentrated under reduced pressure. In a 50 ml falcon tube the residue was dissolved in diethyl ether (10 ml) and n-hexane (40 ml) was slowly added. A white precipitate was centrifuged and the remaining solvent discarded. The precipitation procedure was repeated three times and the resulting white precipitate was purified by column chromatography using neutral silica gel and EtOAc as an eluent to yield **Çm** as a white solid (46 mg, 36.3%).

R_f = 0.62 (DCM/MeOH 9:1); **^{1}H-NMR (400 MHz, DMSO-d_6):** δ = 1.23-1.42 (br m), 2.46 (br m), 2.64-2.80 (br m), 3.00 (br m), 3.33 (br s), 3.50-3.80 (br m), 4.26 (br s), 4.51 (br s), 4.71 (br s), 6.09 (br s), 6.88 (br s), 7.41 (br s) ppm; **^{31}P-NMR (162 MHz, $CDCl_3$):** δ =

151.0, 152.3 ppm; **MS (ESI (+), 8 eV) m/z:** Calc. for $C_{52}H_{62}N_6O_{10}P$• $(M+Na)^+$ 984.43 found 984.40.

5-Iodo-2'-O-methyluridine (68)[120]

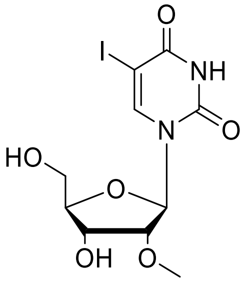

Iodine (4.9 g, 38.8 mmol) and ceric ammonium nitrate (4.9 g, 8.9 mmol) were added to a solution of **59** (5 g, 19.4 mmol) in AcOH (25 ml) and the reaction mixture was stirred for 1 h at 80 °C. The solvent was removed by co-evaporation with water and the resulting residue was crystallized from ethanol to yield **68** as white crystals (6.0 g, 82.2%).

R_f = 0.28 (DCM/MeOH 9:1); **^{1}H-NMR (500 MHz, DMSO-d$_6$):** δ = 3.38 (s, 3H, OC*H$_3$*), 3.57 - 3.70 (m, 2H, C-5'H), 3.79 (dd, *J* = 4.5 Hz, 1H, C-2'H), 3.83 – 3.88 (m, 1H, C-4'H), 4.11 (s, 1H, C-3'H), 5.14 (s, 1H, O*H*), 5.32 (s, 1H, O*H*), 5.78 (d, *J* = 3.8 Hz, 1H, C-1'H), 8.53 (s, 1H, C-6H), 11.70 (s, 1H, NH) ppm; **^{13}C-NMR (126 MHz, DMSO-d$_6$):** δ = 58.0, 60.0, 68.2, 69.8, 83.5, 85.21, 87.0, 145.3, 150.5, 160.9 ppm; **MS (ESI (+), 8 eV) m/z:** Calc. for $C_{10}H_{13}IN_2O_6$ $(M+H)^+$ 384.98 found 384.98.

5-(Trimethylsilylethynyl)-2'-O-methyluridine (69)

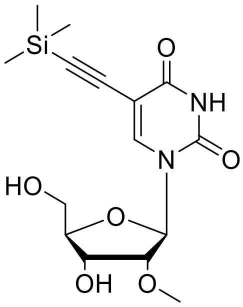

In a flame dried 100 ml round bottom flask **68** (1.5 g, 3.9 mmol) was dissolved in mixture of ACN/NMe_3 1:1 (97 ml) under argon atmosphere. CuI (37.1 mg, 0.2 mmol), $(Ph_3P)_2PdCl_2$ (547 mg, 0.78 mmol) and trimethylsilylacetylene (2.22 ml, 15.6 mmol) were added successively. The resulting reaction mixture was stirred for 3 h at 50 °C. The progress of the reaction was controlled by TLC (DCM:MeOH, 9:1).The solvent was removed *in vacuo* and the crude residue purified on silica gel by means of flash chromatography using DCM:MeOH (100:0) to DCM:MeOH (95:5) as a gradient to give **69** as a yellow powder (1.27 g, 91.8%).

R_f = 0.55 (DCM/MeOH 9:1); **^{1}H-NMR (400 MHz, DMSO-d$_6$):** δ = 0.18 (s, 9H, Si(CH$_3$)$_3$), 3.38 (s, 3H, OC*H$_3$*), 3.56 - 3.73 (m, 2H, C-5'H), 3.81 (dd, *J* = 5.0, 3.9 Hz, 1H, C-2'H), 3.85 (dt, *J* = 5.6, 2.7 Hz, 1H, C-4'H), 4.11 (q, *J* = 5.7 Hz, 1H, C-3'H), 5.12 (d, *J* = 6.3 Hz, 1H, O*H*), 5.25 (t, *J* = 4.7 Hz, 1H, O*H*), 5.80 (d, *J* = 3.9 Hz, 1H, C-1'H), 8.40 (s, 1H, C-6H), 11.66 (s, 1H, N*H*) ppm; **^{13}C-NMR (100.6 MHz, DMSO-d$_6$):** δ = 0.0, 8.7, 45.8, 57.6, 59.7, 67.7, 82.9, 84.8, 86.7, 97.1, 97.9, 98.3, 144.6, 149.4, 161.4 ppm; **MS (ESI (+), 8 eV) m/z:** Calc. for $C_{10}H_{13}IN_2O_6$ $(M+Na)^+$ 377.11 found 377.11.

5-Ethynyl-2‘-O-methyluridine (70)

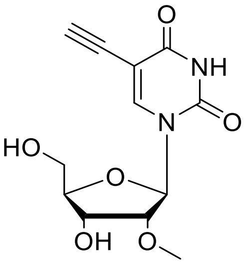

K_2CO_3 (1.00 g, 7.3 mmol) was added to a solution of **69** (1.27 g, 3.58 mmol), in methanol (179 ml) and the reaction mixture was stirred for 5 h at 22 °C. The monitoring of the reaction progress was carried out using TLC (DCM:MeOH, 9:1). The solvent was removed under reduced pressure and the crude residue was purified by column chromatography using DCM:MeOH (100:0) to DCM:MeOH (90:10) as a gradient to yield **70** a yellow powder (1.12 g, 97%).

R_f = 0.35 (DCM/MeOH 9:1); **^{1}H-NMR (500 MHz, DMSO-d$_6$):** δ = 3.38 (s, 3H, OC*H$_3$*), 3.56 - 3.71 (m, 2H, C-5'H), 3.80 (t, *J* = 4.4 Hz, 1H, C-2'H), 3.85 (dt, *J* = 5.6, 2.6 Hz, 1H, C-4'H), 4.11 (s,1H, C-3'H), 5.14 (d, *J* = 6.3 Hz, 1H, O*H*), 5.29 (t, *J* = 4.7 Hz, 1H, O*H*), 5.80 (d, *J* = 3.7 Hz, 1H, C-1'H), 8.43 (s, 1H, C-6H), 11.67 (s, 1H, N*H*) ppm; **^{13}C-NMR (126 MHz, DMSO-d$_6$):** δ = 58.0, 60.1, 68.2, 76.7, 83.4, 84.1, 85.2, 87.0, 98.1, 144.8, 149.9, 162.1 ppm; **MS (ESI (+), 8 eV) m/z:** Calc. for $C_{12}H_{14}N_2O_6$ $(2M+Na)^+$ 587.16 found 587.16.

5’-O-Dimethoxytrityl-5-ethinyl-2’-O-methyluridine (71)

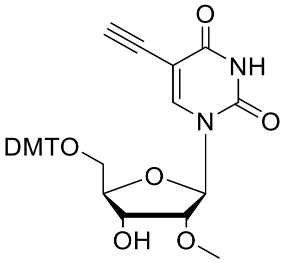

70 (500 mg, 1.77 mmol), DMTCl (780 mg, 2.3 mmol) and DMAP (21.6 mg, 0.18 mmol) were dried under vacuum for 16 h. Anhydrous pyridine (20 ml) was added and the reaction mixture was stirred for 5 h at 22 °C. The reaction was controlled by TLC (DCM:MeOH, 9:1). The solvent was removed by co-evaporation with toluene. The resulting residue was purified on silica gel by flash chromatography ($Et_3N/CH_2Cl_2/MeOH$; 1:99:0 to 1:95:4) to yield **71** as white foam (0.56 g, 65%).

R$_f$ = 0.52 (DCM/MeOH 9:1); **^{1}H-NMR (500 MHz, DMSO-d$_6$):** δ = 2.75 (s, 1H, C$_{alkyne}$*H*), 3.41 – 3.54 (m, 2H, C-5'H), 3.64 (s, 3H, OC*H$_3$*), 3.87 – 3.96 (m, 1H, C-2'H), 4.03 – 4.10 (m, 1H, C-4'H), 4.47 (dd, *J* = 6.9, 5.2 Hz, 1H, C-3'H), 5.93 (d, *J* = 2.5 Hz, 1H, C-1'H), 6.81 – 6.86 (m, 4H, Ar*H*), 7.13-7.36 (m, 9H, Ar*H*), 8.12 (s, 1H, C-6H), 9.15 (br s, 1H, N*H*) ppm; **^{13}C-NMR (126 MHz, DMSO-d$_6$):** δ = 55.2, 58.9, 68.2, 73.7, 82.1, 83.6, 83.8, 87.0, 87.4, 99.4, 113.3, 124.3, 126.9, 126.9, 127.9, 135.2, 135.5, 143.1, 144.4, 149.1, 158.6, 161.3, ppm; **MS (ESI (+), 8 eV) m/z:** Calc. for $C_{33}H_{32}N_2O_8$ $(M+Na)^+$ 607.20 found 607.20.

5’-O-Dimethoxytrityl-5-(1,1,3,3-tetramethyl-5-(4H-1,2,3-triazol-4-yl)-isoindolin-1-yloxyl)-2’-O-methyluridine (72)

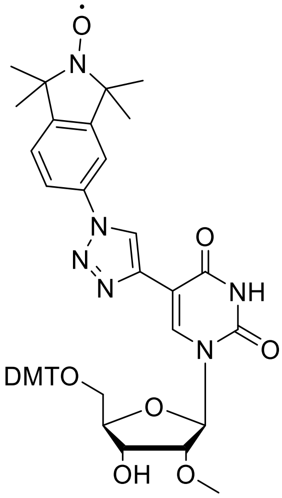

A solution of **71** (331 mg, 0.56 mmol), nitroxide **43** (105 mg, 0.45 mmol) and CuI (21 mg,0.11 mmol) in DMF (3 mL) was stirred for 16 h at 22 °C. The progress of the reaction was controlled by TLC (DCM/MeOH 9:1). The solvent was removed *in vacuo* and the product purified on silica gel by means of flash chromatography using DCM/MeOH 100:0 to DCM/MeOH 90:10 as a gradient to give **72** as a yellow powder (430 mg, 93%).

R$_f$ = 0.67 (DCM/MeOH 9:1); **^{1}H-NMR (500 MHz, CDCl$_3$):** δ = 3.53 – 3.56 (br m), 3.64 (br s), 4.03 (br s), 4.13 (br s), 4.40 (br s), 6.03 (br s), 6.81 – 6.87 (br m), 719-7.51 (br m), 8.12 (s, 1H, C-6H), 8.12 (br s, 1H), 9.08 (br s) ppm; **^{13}C-NMR (126 MHz, CDCl$_3$):** δ = 31.5, 36.6, 55.3, 55.3, 59.0, 62.7, 69.3, 81.3, 83.6, 86.7, 88.6, 106.0, 113.2, 126.7, 127.8, 128.1, 129.2, 130.0, 130.1, 135.8, 136.0, 136.8, 139.5, 147.6, 149.3, 158.4, 158.6, 161.0,162.6 ppm; **MS (ESI (+), 8 eV) m/z:** Calc. for $C_{33}H_{32}N_2O_8$ $(M+Na)^+$ 838.33 found 838.33.

3’-O-[(2-Cyanoethyl)(N,N-diisopropylamino)phosphinyl]-5’-O-dimethoxytrityl-5-(1,1,3,3-tetramethyl-5-(4H-1,2,3-triazol-4-yl)-isoindolin-1-yloxyl)-2’-O-methyluridine (Ųm)

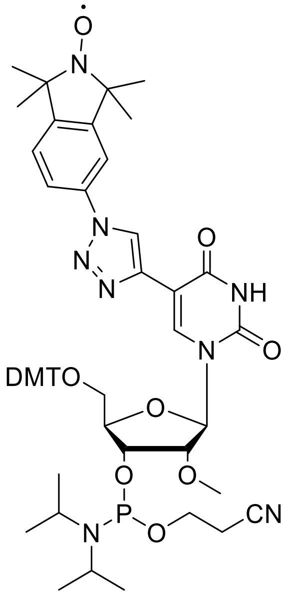

72 (200 mg, 0.24 mmol) and diisopropyl ammonium tetrazolide (67 mg, 0.39 mmol) were dissolved in pyridine (1 ml). Pyridone was removed *in vacuo* and the mixture was dried under vacuum for 16 h. The residue was dissolved in anhydrous DCM (10 ml) and 2-cyanoethyl N,N,N′,N′-tetraisopropyldiamidophosphite (230 µL, 0.72 mmol) was added dropwise. The resulting yellow solution was stirred for 5 h at 22 °C. The progress of the reaction was monitored by TLC (DCM:MeOH, 9:1). The reaction mixture was diluted with DCM (10 ml), washed with saturated aqueous $NaHCO_3$ (3 × 15 mL) and saturated aqueous NaCl (3 × 15 mL). The organic phase was dried over $MgSO_4$ and the solvent concentrated under reduced pressure. In a 50 ml falcon tube the residue was dissolved in diethyl ether (10 ml) and n-hexane (40 ml) was slowly added. A white precipitate was centrifuged and the remaining solvent discarded. The precipitation procedure was repeated three times to yield **Ųm** as white solid (137 mg, 55%).

R_f = 0.74 (DCM/MeOH 9:1); **^{1}H-NMR (400 MHz, $CDCl_3$):** δ = 0.91-0.34 (br m), 2.44 (br s), 2.70 (br s), 3.58-3.84 (br m), 4.12-4.22 (br m), 4.34-4.39 (br m), 6.05-6.013 (br m), 7.19-7.33 (br m) ppm; **^{31}P-NMR (162 MHz, $CDCl_3$):** δ = 151.0, 151.4 ppm; **MS (ESI (+), 8 eV) m/z:** Calc. for $C_{54}H_{64}N_8O_{10}P$• $(M+Na)^+$ 1038.44 found 1038.44.

5’-O-Dimethoxytrityl-N_4-Acetyl-5-(1,1,3,3-tetramethyl-5-(4H-1,2,3-triazol-4-yl)-isoindolin-1-yloxyl)-2’-O-methylcytidine (74)

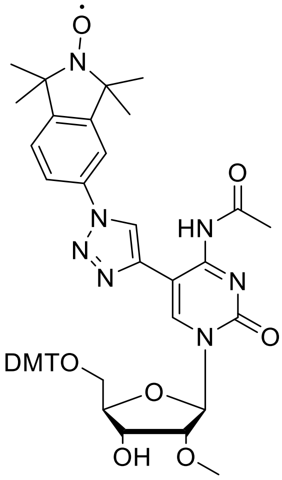

A solution of **52** (260 mg, 0.42 mmol), nitroxide **43** (96 mg, 0.42 mmol) and CuI (24 mg, 0.12 mmol) in DMF (3 mL) was stirred for 16 h at 22 °C. The progress of the reaction was controlled by TLC (DCM/MeOH 9:1). The solvent was removed *in vacuo* and the product purified on silica gel by means of flash chromatography using DCM/MeOH 100:0 to DCM/MeOH 90:10 as a gradient to give **74** as a yellow powder (260 mg, 73%).

R_f = 0.32 (DCM/MeOH 9:1); **^{1}H-NMR (500 MHz, $CDCl_3$):** δ = 1.25 (s, 12H, CH_3), 2.75 (s, 3H, CH_3), 3.2 (d, *J* = 10 Hz, 1H), 3.86 (s, 3H, OC*H_3*), 3.99 (br s, 1H), 4.8 (d, *J* = 8.7 Hz, 1H), 4.5 (br s, 1H), 6.12 (s, 1H), 6.57 - 6.69 (m, 4H, Ar*H*),7.18 - 7.49 (m, 9H, Ar*H*), 8.03 (br s,1H), 8.81 (br s, 1H), 11.10 (br s, 1H, N*H*) ppm; **MS (ESI (+), 8 eV) m/z:** Calc. for $C_{33}H_{32}N_2O_8$ $(M+H)^+$ 857.37 found 857.37.

3’-O-[(2-Cyanoethyl)(N,N-diisopropylamino)phosphinyl]-5’-O-dimethoxytrityl-N_4-Acetyl-5-(1,1,3,3-tetramethyl-5-(4H-1,2,3-triazol-4-yl)-isoindolin-1-yloxyl)-2’-O-methylcytidine (Ḉm)

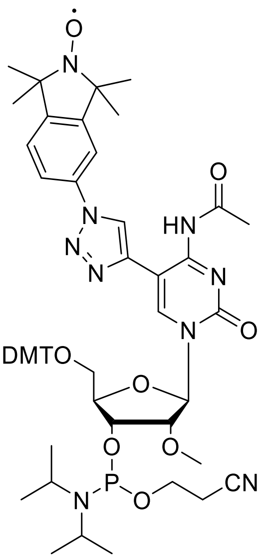

74 (200 mg, 0.24 mmol) and diisopropyl ammonium tetrazolide (67 mg, 0.39 mmol) were dissolved in pyridine (1 ml). Pyridine was removed *in vacuo* and the mixture was dried under vacuum for 16 h. The residue was dissolved in anhydrous DCM (10 ml) and 2-cyanoethyl N,N,N′,N′-tetraisopropyldiamidophosphite (230 µL, 0.72 mmol) was added dropwise. The resulting yellow solution was stirred for 5 h at 22 °C. The progress of the reaction was monitored by TLC (DCM/MeOH, 9:1). The reaction mixture was diluted with DCM (10 ml), washed with saturated aqueous $NaHCO_3$ (3 × 15 mL) and saturated aqueous NaCl (3 × 15 mL). The organic phase was dried over $MgSO_4$ and the solvent concentrated under reduced pressure. In a 50 ml falcon tube the residue was dissolved in diethyl ether (10 ml) and n-hexane (40 ml) was slowly added. A white precipitate was centrifuged and the remaining solvent discarded. The precipitation procedure was repeated three times to yield **Ḉm** as a white solid (123 mg, 50%).

R_f = 0.49 (DCM/MeOH 9:1); **^{1}H-NMR (500 MHz, $CDCl_3$):** δ = 1.07 – 1.13 (br m), 1.41 (br s), 1.64 (br s), 2.34 – 2.36 (br m), 2.62 – 2.65 (br m), 2.75 – 2.76 (br m), 3.13 – 3.15 (br m), 3.24 (br s), 3.48 - 3.50 (br m), 3.79 – 3.80 (br m), 3.99 – 4.10 (br m), 4.30 – 4.40 (br m), 4.56 – 4.56 (br m), 6.11 (d, *J* = 6.9 Hz, 1H, C-1'H), 6.56 – 6.70 (br m, Ar*H*), 7.24 – 7.50 (br m, Ar*H*), 8.8 (s, 1H, C-6H), 11.17 (s, 1H, N*H*) ppm; **^{31}P-NMR (202.4 MHz, $CDCl_3$):** δ = 150.3, 150.6 ppm; **MS (ESI (+), 8 eV) m/z:** Calc. for $C_{54}H_{64}N_8O_{10}P$• $(M+Na)^+$ 1079.46 found 1079.46.

N-Isopropyl-2-propanaminium tetrazol-1-ide[161]

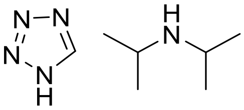

1-H-tetrazole (608 mg, 8.7 mmol) was dissolved in anhydrous acetonitrile (8ml) and diisopropylamine (2ml, 14.2 mmol) was added dropwise. A white precipitate was formed immediately and the solvent was removed under reduced pressure. A white crystalline powder was subsequently dried in high vacuum overnight (1.47 g, 99%).

^{1}H-NMR (600 MHz, CD_2Cl_2): δ = 1.38 (d, *J* = 6.3 Hz, 12H, 4xC*H*$_3$), 3.57 – 3.55 (m, 2H, 2xC*H*), 8.42 (s, 1H, C*H*$_{tetrazole}$) ppm; **^{13}C-NMR (151 MHz, CD_2Cl_2):** δ = 18.9, 46.9, 148. 9 ppm.

Imidazole-1-sulfonyl azide[104]

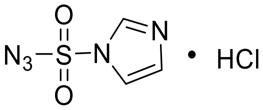

Sulfuryl chrolide (8.5 ml, 100 mmol) was added dropwise to a solution of sodium azide (6.5 g, 100 mmol) in cold ACN (100 ml). The resulting reaction mixture was stirred for 16 h at 22 °C. After 16 h imidazol (13 g, 189 mmol) was added portion-wise at 0 °C and the resulting slurry stirred for 3 h at 22 °C. Ethanol (200 ml) was added and the reaction mixture was washed with water (2 x 200) and saturated $NaHCO_3$ (2 x 200) followed by drying over $MgSO_4$. A solution of 4 M HCl in dioxane (25 ml, 100 mmol) was added dropwise at 0 °C. A white precipitate occurred, which was subsequently washed with EtOAc (3 x 100 ml) to yield imidazole-1-sulfonyl azide as a white crystalline powder (13.89 mg, 42%).

^{1}H-NMR (400 MHz, D_2O): δ = 7.75 (dd, *J* = 2.1, 1.1 Hz, 1H), 7.96 - 7.98 (m, 1H), 9.17 (t, *J* = 1.3 Hz, 1H) ppm; **^{13}C-NMR (100.6 MHz, D_2O):** δ = 121.8, 127.3, 139. 9 ppm.

Anhydrous *tert*-butyl hydroperoxide in toluene[162]

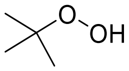

TBHP (81.25 ml, 70% TBHP, 30% H_2O) and toluene (100 ml) were added to a separatory funnel and the resulting solution carefully swirled several times. The aqueous layer (21 ml) was removed and organic phase was transferred in a two-neck flask equipped with Dean-Stark apparatus, a reflux condenser and a thermometer. Water started to accumulate at the pot temperature of 84 °C and was collected as long as no further visible water accumulation could be observed (ca. 1 h, 10 ml water, pot temperature 107 °C). To protect the system from the atmospheric moisture a drying tub filled with Drierite was connected to the reflux condenser and ca.10 ml of distillate removed through the side arm. The solution was allowed to warm to the room temperature and transferred into a brown bottle over 4 Å sieves. The molarity of TBHP was determined by means of iodometric titration.

5.2 Working with oligonucleotides

5.2.1 RNA solid phase synthesis

RNA solid phase syntheses were carried out in 0.2 µmol scale on DNA synthesizer 3400 from *Applied Biosystems (ABI)*. Controlled pore glass (CPG, 500Å pore size) was used as a solid support. Pre-packed columns including the corresponding phosporamidites from *Glenresearch* were applied.

5.2.1.1 Solid phase synthesis of spin-labeled RNA

Deblocking mix: 3% DCA/DCM

Activator: 250 mM 5-(Benzylthio)-1H-tetrazole (BTT), coupling time 3 min for unmodified phosphoramidites and 15 min for modified phosphoramidites.

CAP A: THF/Pyridine/Ac_2O (*Glenresearch*)

CAP B: 16% MeIm in THF (*Glenresearch*)

Oxidizer: 1 M *tert*-butyl hydroperoxide (TBHP) in toluene

RNA bases: Pac-A-CE, Ac-C-CE, *iPr*-Pac-G-CE, U-CE phosphoramidites (*Glenresearch*)

Modified RNA base: **Çm**, **Ųm** and **Ḉm** phosphoramidites were synthesized in the laboratory.

5.2.1.2 Solid phase synthesis of alkyne modified RNA

Deblocking mix: 3% TCA/DCM

Activator: 250 mM 5-(Benzylthio)-1H-tetrazole (BTT), coupling time 3 min for unmodified phosphoramidites and 15 min for **EmC**

CAP A: THF/Pyridine/Ac_2O (*Glenresearch*)

CAP B: 16% MeIm in THF (*Glenresearch*)

Oxidizer: 0.02 M I_2 in THF/Pyridine/H2O

RNA bases: Pac-A-CE, Ac-C-CE, iPr-Pac-G-CE, U-CE phosphoramidites (*Glenresearch*).

Modified RNA base: **EmC** phosphoramidite was synthesized in the laboratory.

5.2.2 Spin-labeling of RNA using click chemistry

5.2.2.1 Spin-labeling of 45dŲ on CPG solid support via click chemistry

5-ethynyl-2′-dU modified RNA **45** (purchased from *Ella Biotech*) on CPG support (0.2 µmol synthesis) was placed into a 1.5 ml reaction tube and dried under vacuum overnight. CuI (0.5 mg), THPTA (5.0 mg) and spin label **43** (5.0 mg) were placed in a small glass reaction vial with a magnetic stir bar. This vial was placed in a 10 ml Schlenk flask and dried under vacuum overnight. Next, 100 µl of DMSO, which was degassed three times using the freeze-pump-thaw method, were poured into the reaction vial under argon atmosphere. The obtained solution was stirred for 2 min. The reaction mixture was poured into the reaction tube with RNA attached to the CPG support. The reaction tube was filled with argon and sealed using a parafilm and then incubated in a thermomixer (350 rpm) at room temperature for 24 hours. Subsequently, the solid support was washed with CH_3CN (3 x 100 µL). The RNA was cleaved from the CPG support and the amino groups were deprotected by adding 2 ml of a mixture of NH_3 (32%) and MeOH in a ratio of 3:1 (v/v) and overnight incubation at ambient temperature. The reaction mixture was filtered and the NH_3 removed in a speed vac. The TBDMS groups were cleaved with 1M TBAF in THF over 16 h at room temperature. After desalting through the NAP-10 column (GE Healthcare) the RNA strands were purified via reverse phase HPLC.

5.2.2.2 Spin-labeling of preQ1 dŲ4-dŲ32 and preQ1 dŲ32 on CPG solid support via click chemistry

The nitroxide-functionalized azide **43** was synthesized according to the synthesis introduced by Jakobsen *et. al.*[87] The 5-ethynyl-2′-dU modified RNA on CPG support was purchased from Ella Biotech. RNA on solid support (0.2 µmol synthesis) was placed into a 1.5 ml reaction tube and dried under vacuum overnight. CuI (1 eq., 0.5 mg, 2.6 µmol), THPTA (4.4 eq., 5.0 mg, 11.5 µmol) and spin label **43** (8.3 eq., 5.0 mg, 21.6 µmol) were placed in a small glass reaction vial with a magnetic stir bar. This vial was placed in a 10 ml Schlenk flask and dried under vacuum overnight. Next, 100 µl of DMSO, which was degassed three times using the freeze-pump-thaw method, were poured into the reaction vial under argon atmosphere. The obtained solution was stirred for 2 min. The reaction mixture was poured into the reaction tube with RNA attached to the CPG support. The reaction tube was filled with argon and sealed using a parafilm and then incubated in a thermomixer (350 rpm) at room temperature for 4 h. Subsequently, the solid support was washed with CH_3CN (3 x 100 µL), dried and then incubated in the freshly prepared reaction mixture of **43** (8.3 eq., 5.0 mg, 21.6 µmol), CuI (1 eq., 0.5 mg, 2.6 µmol) and THPTA (4.4 eq., 5.0 mg, 11.5 µmol) in DMSO for another 4 h. The solid support was then again washed with CH_3CN (3 x 100 µL), dried and incubated for 16 h in the freshly prepared reaction mixture of **43** (8.3 eq., 5.0 mg, 21.6 µmol), CuI (1 eq., 0.5 mg, 2.6 µmol) and THPTA (4.4 eq., 5.0 mg, 11.5 µmol) in DMSO. After the total reaction time of 24 h the RNA was cleaved from the CPG support and the amino groups were deprotected by adding 2 ml of a mixture of NH_3 (32%) and MeOH in a ratio of 3:1 (v/v) and overnight incubation at ambient temperature. The reaction mixture was filtered and the NH_3 removed in a speed vac. The TBDMS groups were cleaved with 1M TBAF in THF over 16 h at room temperature. After desalting through the NAP-10 column (GE Healthcare) the RNA strands were purified via reverse phase HPLC.

5.2.2.3 Spin-labeling of 45dŲ and 54dŲ in solution via click chemistry.

The non-modified RNA strands as well as their 5-ethynyl-2′-dU modified counterparts were purchased from Metabion. 0.8 µl 250 mM THPTA solution in DMSO were mixed with 0.8 µl 50 mM CuI solution in DMSO. 2 µl DMSO were added and the catalytic solution was mixed well and incubated for 5 min at the room temperature. Catalytic solution was placed into a 1.5 ml Eppendorf tube containing a mixture of 5-ethynyl-2′-dU modified RNA (**45** or **54** 2.5 nmol) dissolved in 4.4 µl DEPC water and 2 µl 100 mM spin label **43** solution in DMSO. The resulting reaction mixture was mixed and incubated in a water bath at 37 °C for 15 min. After desalting through the Amicon column (3K) the RNA was purified via reverse phase HPLC. Note that Cu salts should be removed from the reaction mixture once the reaction is stopped to avoid RNA degradation.

5.2.2.4 Spin-labeling of preQ1 mutants and TPP20dŲ and TPP68dŲ in solution via click chemistry.

The non-modified RNA strands as well as their 5-ethynyl-2′-dU modified counterparts were purchased from Metabion. 0.8 µl 250 mM THPTA solution in DMSO were mixed with 0.8 µl 50 mM CuI solution in DMSO. 2 µl DMSO were added and the catalytic solution was mixed well and incubated for 5 min at the room temperature. Catalytic solution was placed into a 1.5 ml Eppendorf tube containing a mixture of 5-ethynyl-2′-dU modified RNA (2.5 nmol) dissolved in 4.4 µl DEPC water and 2 µl 100 mM spin label **43** solution in DMSO. The resulting reaction mixture was mixed and incubated in a water bath at 37 °C for 30 min. After desalting through the Amicon centrifugal filter (3K) the RNA was purified via reverse phase HPLC.

5.2.3 Enzymatic reactions with nucleic acids

5.2.3.1 Preparation of DEPC water

Diethylopyrocarbonate (DEPC) was dissolved in ddH_2O in a ratio of 1:500 (v/v). The resulting solution was vigorously mixed for 2 min and incubated over night at room temperature. After incubation, it was autoclaved at 121 °C for 60 min.

5.2.3.2 Pfu PCR

DNA sequences were amplified using Pfu polymerase (homemade) (Table 8). Reaction conditions as shown in Table 9 were applied. NucleoSpin column (NucleoSpin Extract II) by Macherey & Nagel was applied to purify PCR product.

Table 8 Pipetting scheme Pfu PCR

Reagent	Amount	Stock	Resultant
Pfu PCR buffer	10 µl	10 x	1 x
$MgCl_2$	8 µl	25 mM	2 mM
5’Primer	1 µl	100 µM	1 µM
3’Primer	1 µl	100 µM	1 µM
dNTP	0.8 µl	25 mM	0.2 mM
DNA template	1 µl		1-10 nM
Pfu DNA polymerase	1 µl	2.5 mM	
water	77.2 µl		

Table 9 PCR reaction condition

	Temperature	Time
Denaturing	95 °C	60 s
Annealing	60 °C	60 s
Extension	72 °C	90 s

5.2.3.3 *In vitro* transcription

In vitro transcription of DNA template containing a T7 promotor at its 5’ end was carried out by means of T7 RNA polymerase. Due to a higher T7 RNA polymerase affinity to guanine than to other nucleotides the DNA sequence was designed to contain 2 guanines at its 5’ end. The *in vitro* transcription reaction was applied using the standard pipetting protocol as shown in Table 10. The reaction mixture was incubated at 37 °C overnight.

Table 10: Pipetting scheme of *in vitro* transcription.

Reagent	Amount	Stock	Resultant
HEPES pH 7.9	20 µl	200 mM	40 mM
$MgCl_2$	25 µl	100 mM	25 mM
DTT	5 µl	100 mM	5 mM
NTP mix	10 µl	25 mM	2.5 mM
RNasin	1.24 µl	40 U/µl	0.5 U/µl
IPP	0.2 µl	2 U/µl	0.02 U/µl
ds DNA template	10 µl	150-300 pmol	1.5-3 µM
T7 RNA polymerase	5 µl	50 U/µl	0.5 U/µl
DEPC water	22.8 µl		

5.2.3.4 Dephosphorylation

Calf intestinal alkaline phosphatase (CIAP) was used to hydrolyze phosphate groups from RNA at its 5'end after *in vitro* transcription. The reaction mixture as shown in Table 11 was incubated at 37 °C for 15 min and 0.43 µl CIAP were added. The mixture was incubated for other 15 min at 55 °C before 0.5 µl 0.5 M EDTA were added. After a further incubation at 75 °C for 10 min 150 µl DEPC water were added followed by phenol/chloroform purification and RNA precipitation.

Table 11 Pipetting scheme of dephosphorylation.

Reagent	Amount	Stock	Resultant
CIAP buffer	5 µl	10 x	1 x
BSA	5 µl	10 x	1 x
RNA template		75 pmol	
CIAP	0.85 µl	20 U/µl	17U
RNasin	0.5 µl	40 U/µl	20U
DEPC water	Add 150 µl		

5.2.3.5 Phosphorylation

After dephosphorylating with CIAP RNA was phosphorylated using the T4 polynucleotide kinase (PNK) and ATP. The reaction mixture as shown in Table 12 was incubated at 37°C for 30 min followed by phenol/chloroform.

Table 12 Pipetting scheme of phosphorylation

Reagent	Amount	Stock	Resultant
T4 PNK buffer	2 µl	10 x	1 x
CIAP RNA 45 pmol	3 µl	15 µM	2.25 µM
ATP	2 µl	10 mM	1 mM
T4 PNK	2 µl	10 U/µl	20U
RNasin	0.3 µl	40 U/µl	12U
DEPC water	9.7 µl		

5.2.3.6 Enzymatic ligation using T4 DNA ligase

RNA molecules, which could not be obtained by means of RNA solid phase synthesis, were enzymatically synthesized using a T4 DNA ligase. The annealing mix as shown in Table 13 was heated to 95 °C for 2 min and then allowed to cool to room temperature over 15 min. The reaction mixture as shown in Table 14 was prepared and incubated at 35 °C for 3.5 h. The reaction product was purified via phenol/chloroform extraction and ion exchange HPLC.

Table 13 Pipetting scheme of the annealing mix prior ligation reaction.

Reagent	Amount	Stock	Resultant
RNA acceptor strand	50 µl	100 µl	14.2 µM
RNA donor strand	50 µl	100 µl	14.2 µM
Splint oligonucleotide	50 µl	100 µl	14.2 µM
Water (DEPC)	200 µl	100 µl	

Table 14 Pipetting scheme of ligation reaction.

Reagent	Amount	Stock	Resultant
Annealing mix	350 µl		10 µM
T4 DNA Ligase buffer	50 µl	10 x	1 x
PEG 4000	50 µl		
T4 DNA ligase	50 µl	5 U $µl^{-1}$	250 U

5.2.4 RNA work up and purification

5.2.4.1 Phenol-chloroform extraction

Phenol-chloroform extraction was performed to remove enzymes from nucleic acids after an enzymatic reaction. One volume of phenol was added to one volume of sample and the resulting mixture was vigorously vortexed and centrifuged at 14000 g for 3 min. The upper (aqueous) phase was separated and mixed with four volumes of chloroform. The resulting mixture was vortexed again and centrifuged 14000 g for 3 min. The aqueous phase was separated and transferred into a 2 ml microcentrifuge tube and 1/10 volume 3M NaOAc, 1 µl glycogen and three volumes of EtOH abs. were added. The resulting solution was mixed and incubated at -80°C for 20 min. After incubation, the sample was centrifuged at maximum speed for 30 min. The supernatant was discarded, the pellet washed with 100 µl 70% EtOH. The supernatant was removed again and RNA was dissolved in DEPC water.

5.2.4.2 Polyacrylamide gel electrophoresis PAGE

Polyacrylamide gel electrophoresis was applied for both preparative and quantitative purposes. In this work only 10% gels were prepared according to the protocols given in Tables 15 and 16 respectively. The polymerization process was initiated upon addition of ammonium persulfate solution (APS) and tetramethylethylenediamine (TEMED). The running process was carried out in running chamber containing 1 x TBE buffer. Before loading samples gels were always pre-run for 30 min and pockets were rinsed with the running buffer. The power supply settings were selected as follows: 15 W per gel and 370-600 V. The run time was adjusted depending on the separation issue.

Table 15 Solutions applied for PAGE preparation

Solutions for PAGE	Content
Solution B	8.3 M Urea in 10x TBE
Solution C	Rotiphorese
Solution D	8.3 M Urea

Table 16 Preparation of a 10% PAGE gel

Solutions for PAGE	Amount [ml]			
	100	70	50	30
B	10	7	5	3
C	40	28	20	12
D	50	35	25	15
APS 10%	0.8	0.56	0.4	0.24
TEMED	0.04	0.028	0.02	0.012

5.2.4.3 Reverse phase HPLC

Reverse phase HPLC 1100 series with a column Hypersil ODS (5 µm, 4.6 x 100) from *Agilent* was applied to separate RNA with different functionalities, e.g. spin-labeled from alkyne modified RNA. Two different buffer systems were used including either TEAA buffer or HIFP/ Et_3N in water.

Eluent A: 0.1 M TEEAc in water or 100 mM HIFP/10 mM Et_3N in water

Eluent B: ACN

5.2.4.4 Desalting of RNA using NAP 10 column

NAP-10 columns require only gravity to run. They were equilibrated with 15 ml DEPC water. RNA, taken up in 1 ml DEPC water, was applied to the column and 1.5 ml DEPC water was added. The drops were collected in a 2 ml microcentrifuge tube.

5.2.4.5 Desalting of RNA using Amicon centrifugal filters

Amicon centrifugal filter was placed in the filtrate collection tube followed by adding 500 µl RNA sample. The RNA sample was centrifuged for 30 min at 14000 x g at room temperature. The filtrated was discarded and 450 µl DEPC water was added to the filter. The sample was again centrifuged for 30 min at room temperature and the filtrate was discarded. The whole procedure was repeated three times in total. The filter was then removed and placed upside down in a clean microcentrifuge tube. The sample was spun for 2 min at 1000 x g.

5.2.4.6 Anion-exchange HPLC

To separate RNA strands of different sizes, anion-exchange chromatography was applied using the *Dionex DNAPac PA-100* (9 x 250 mm^2) column.

Eluent A: urea (360 g, 6 mol) and 100 ml 250 mM Tris–HCl buffer, pH 8.0 were dissolved in 1000 ml nanofiltered water. The solution was filtered through a cellulose acetate filter (0.2-mm pore size) and stored at room temperature.

Eluent B: urea (360 g, 6 mol), sodium perchlorate monohydrate (70.2 g, 500 mmol) and 100 ml of 250 mM Tris–HCl buffer, pH 8.0 were dissolved in 1000 ml nanofiltered water. The solution was filtered through a cellulose acetate filter (0.2-mm pore size) and stored at room temperature.

5.2.5 Analytical methods for Oligonucleotides

5.2.5.1 Concentration measurements

The concentration of the oligonucleotides was determined using a spectrophotometer Nanodrop 2000c from *Thermo Scientific*. To calculate the observed concentration Lambert-Beer law was applied:

$$A = \varepsilon l c,$$

where ε is the absorption coefficient, l length of the light (1 mm) path and c the concentration of solution.

5.2.5.2 Agarose gel electrophoresis

Agarose gel electrophoresis was applied to analyze the oligonucleotides of different sizes and PCR products. The agarose gel was prepared in dependence of the length of the DNA or RNA fragments 0.5-4% (w/v). For this purpose, an appropriate amount of agarose was suspended in 1 x TBE buffer (50 ml) and carefully heated in a microwave. For visualization of the sample, ethidium bromide (5 µl) was added to the agarose TBE buffer solution. The obtained mixture was well mixed and poured into a running chamber for 30 min. The samples were mixed with the appropriate loading buffer (DNA or RNA loading buffer) and loaded on the gel. A corresponding DNA or RNA ladder was used a molecular-weight size marker. The voltage, current and the run time were adjusted in the electrophoresis power supply depending on the percentage of the agarose gel. The gel documentation system GenoPlex from *VWR* including an UV transilluminator was applied to visualize the fluorescent bands.

5.2.5.3 LCMS

The mass spectrometry analysis of oligonucleotides was carried out on LCMS including Esquire HCT Ion Trap mass spectrometer from *Bruker Daltonics* and HPLC system 1100 series from *Agilent*. The LCMS data were evaluated using a data analysis program HyStar 3.2 from *Bruker Daltonics*.

Eluent A: 100 mM HIFP (LCMS grade)/10 mM $\mathrm{Et_3N}$ (LCMS grade) in water

Eluent B: ACN (LCMS grade)

5.2.5.4 CD spectroscopy

CD spectra were recorded on a Jasco J-810 spectrophotometer. The measurements were performed on 10 µM RNA samples in phosphate buffer (145 mM NaCl, 10 mM $\mathrm{Na_2HPO_4}$*2$\mathrm{H_2O}$, 10 mM $\mathrm{Na_2H_2PO_4}$*2$\mathrm{H_2O}$, pH 7.0). The spectra were recorded with 100 nm/min scanning speed and three averages.

5.2.5.5 UV measurements

UV melting curves were recorded by means of Jasco V-630 UV-VIS spectrophotometer. Temperature-dependent UV absorbance was measured at 260 nm, with a heating and cooling rate of 1 °C/min. Two full heating and cooling cycles were performed.

5.2.5.6 cw-EPR

All EPR measurements as well as molecular modelling were carried out and evaluated in the laboratory of Prof. Dr. O. Schiemann.

a. 45dŲ and 76Çm

The cw X-band EPR spectra were recorded on a cw X-Band EPR spectrometer EMXmicro (Bruker) equipped with the standard resonator (4119HS). All EPR spectra were collected at room temperature with a microwave power of 2 mW, a modulation frequency of 100 kHz, a modulation amplitude of 1 G, and a time constant of 82 ms. (H. Matsuoka, D. Abdullin)

b. preQ1 mutants, 45nt dŲ20, 36nt dŲ68 and TPP dŲ20- dŲ68

Spin-labeling efficiency was determined by means of a Bruker EMXnano spectrometer. The X-band cw-EPR spectra were recorded on a Bruker EMX-micro EPR spectrometer equipped with EMX standard resonator (4119HS). The EPR spectra were collected at room temperature with a microwave power of 5.65 mW, a modulation frequency of 100 kHz, a modulation amplitude of 1.0 G, a microwave frequency of 9.857 GHz, and 1500 points in the field interval 344.3 mT – 359.3 mT. (H. Matsuoka, C.Wübben)

5.2.5.7 Simulations of cw EPR spectra

a. 45dŲ and 76Çm

The simulation of cw-EPR spectra was performed by means of the program MultiComponent,[128] which uses a model of microscopic ordering with macroscopic disorder (MOMD)[163] to simulate an anisotropic motion of a nitroxide. The spectra of **45dŲ** and **46Çm** were simulated with two components. All parameters of the simulations are given in Appendix. (D. Abdullin)

b. preQ1 mutants, TPP dŲ20- dŲ68

The observed spectra were fitted by using the chili algorithm of EasySpin.[145] The best-fit parameters were found by using a MATLAB (MathWorks Inc., Natick, MA) code for nonlinear least squares. Firstly, the experimental spectra observed for the single-labeled preQ1 were simulated. In the fitting procedures, the principal values of g and A tensors were initially fixed at the values previously determined[1]: $g_x = 2.0086$, $g_y = 2.0064$, $g_z = 2.0026$, $A_x = 0.58$ mT, $A_y = 0.58$ mT, $A_z = 3.67$ mT. The axial diffusion tensor with principal values $R_{//}$ and $R_{\perp}$ as well as the weighting coefficients α for the fast (more mobile) and slow (less mobile) components was considered as the fitting parameters. In each calculation, the double integral of the spectra calculated for the two components was normalized to unity, and the two normalized spectra were summed up as given by

$$S = \alpha S_{fast}^{norm} + (1 - \alpha) S_{slow}^{norm}$$

Here, S_{fast}^{norm} and S_{slow}^{norm} are the normalized spectra for the fast and slow components. The obtained spectrum S was compared with the experimental one in the fitting procedure. After getting the initial guess of $R_{//}$, $R_{\perp}$, and α, the least squares fitting was repeated. In the second fitting, the g and A values were also taken as the fitting parameters. Also for the double-labeled preQ1 mutants, the least-squares method was employed, but g and A were fixed at the values obtained for the single-labeled preQ1 mutants (H. Matsuoka).

5.2.5.8 Pulsed Electron-Electron Double Resonance (PELDOR)

PELDOR measurements were carried out on a Bruker ELEXSYS E580 spectrometer using a Flexline probe head with a Q-band resonator (Bruker, ER5106QT-2). All microwave pulses were amplified via a 150 W TWT amplifier (model 187Ka). To obtain low temperatures, a continuous flow helium cryostat (Oxford Instruments, CF935) and a temperature control system (Oxford Instruments, ITC 503S) were employed. The PELDOR experiments were performed with the standard four-pulse sequence. The frequency of the pumping pulse was set at the maximum intensity of the nitroxide absorption (33.500 GHz). The offset between pump and detection frequencies was 80 MHz. The π/2 and π pulses of the detection sequence had lengths of 12 and 24 ns, respectively, and the pump pulse was 14 ns long. For the π/2 pulse a two-step phase cycle was used. The PELDOR signal was recorded at 50 K with a repetition time of 1 ms. To achieve an acceptable SNR, the signal was averaged for 4 to 24 h depending on the samples. (H. Matsuoka, D. Abdullin)

5.2.5.9 Data Analysis

Computer simulation of cw-EPR spectra was performed with the EasySpin2 Package 5.0.22 based on MATLAB (MathWorks Inc., Natick, MA). The chili algorithm of EasySpin was used to reproduce the EPR spectral shape, in which slow-tumbling model of motion was assumed. PELDOR time traces were analyzed by using DeerAnalysis[164] 2015 software. Distance distributions were obtained with the Tikhonov regularization algorithm implemented in the DeerAnalysis software. (H. Matsuoka, D. Abdullin)

5.2.5.10 Molecular modelling

DFT calculations on the nucleobase of **dỤ** were performed by means of the Orca[165] software using the B3LYP functional, the def2-TZVP basis set, unrestricted spin-wave functions, and D3 dispersion corrections. The vibrational frequencies for the geometry-optimized structure were all positive, indicating that the structure represents an energy minimum. Torsional energy profiles for the dihedral angles χ1 and χ2 of **dỤ** (Figure 45) were obtained by a relaxed scan. The structural models of the RNA duplexes **45dỤ** and **76Çm** were obtained by means of the program 3DNA[135] using the mode “fiber”. To introduce **dỤ** or **Çm** into these models, the program mtsslWizard[136] was employed. The DFT optimized geometry of **dỤ** was used by mtsslWizard as a starting structure of the spin-labeled nucleotide, which was aligned to the uracil base of the initial RNA structure during the *in silico* labeling. Additionally, the dihedral angles χ1 and χ2 of **dỤ** (Figure 45) were allowed to deviate by ±10° from their optimized values of 0° and 0°/180°, respectively. (D. Abdullin)

5.2.5.11 Distance Modelling

a. 45dỤ and 76Çm

The structural models of the RNA duplexes 2 and 3 were obtained by means of the program 3DNA[135] using the mode “fiber”. To introduce **dỤ** or **Çm** into these models, the program mtsslWizard[136-138] was employed. The DFT optimized geometry of **dỤ** was used by mtsslWizard as a starting structure of the spin-labeled nucleotide, which was aligned to the uracil base of the initial RNA structure during the *in silico* labeling. Additionally, the dihedral angles χ1 and χ2 of **dỤ** were allowed to deviate by ±10° from their optimized values of 0° and 0°/180°, respectively.

b. preQ1 mutants

Due to the missing crystal structures for the preQ1 aptamer domain of *Fusobacterium nucleatum*, the X-ray crystal structures for conformation II (3Q51) and III (3Q50) of preQ1 aptamer domain of the *Thermoanaerobacter tengcongensis* were used for distance modelling. The labeling positions A23 and A32 were mutated to U23 and U32 respectively by means of macromolecular model building tool WinCoot.

The distances between the spin labels were quantitatively estimated by the computer program MtsslWizard,4-6 which operates as a plugin for the PyMOL molecular graphics system. It should be mentioned that in the structure 3Q51 position U32 required an increase of the clashes to 10 to allow for labeling this site within mtsslWizard. That the width of the distance distribution U4-U32 for this structure is broader than for the structure 3Q50 is attributed to slightly different orientation of both labels with respect to each other.

5.2.5.12 Oligonucleotide sequences

Name	Sequence (5’ to 3’)
45	CAU CUG AUA UCA GA**EdU** G
45dŲ	CAU CUG AUA UCA GA**dŲ** G
45dŲethyl	CAU CUG AUA UCA GA**dŲethyl** G
46	GGU **EdU**CG ACC U**EdU**G CC
46dŲ	GGU **dŲ**CG ACC U**dŲ** GCC
53EmC	CGU CUG AUA UCA GA**EmC** G
53Ḉm	CGU CUG AUA UCA GA**Ḉm** G
54	GCA CTG T**EdU**C ATT CGC G
55	CAU CUG AUA UCA GAU G
76Çm	CGU CUG AUA UCA GA**Çm** G
77Ųm	C**Ųm**U CUG AUA UCA GAA G
78	CGU CUG AUA UCA GAC G
79	CUU CUG AUA UCA GAA G
preQ1 **dŲ4**	A GA**dŲ** GUG CCA GCA AAA CCA UCU UUA AAA AAC UGG
preQ1 **dŲ23**	A GAU GUG CCA GCA AAA CCA UCU **dŲ**UA AAA AAC UGG
preQ1 **dŲ32**	A GAU GUG CCA GCA AAA CCA UCU UUA AAA AAC **dŲ**GG
preQ1 **dŲ4-dŲ32**	A GA**dŲ** GUG CCA GCA AAA CCA UCU UUA AAA AAC **dŲ**GG
preQ1 **dŲ4-dŲ23**	A GA**dŲ** GUG CCA GCA AAA CCA UCU **dŲ**UA AAA AAC UGG
preQ1 **dŲ4-dŲ32(G11A)**	A GA**dŲ** GUG CCA ACA AAA CCA UCU UUA AAA AAC **dŲ**GG
preQ1 wild type	A GAU GUG CCA GCA AAA CCA UCU UUA AAA AAC UGG
45nt dŲ20	ACG ACU CGG GG**dŲ** GCC CUU CUG CGU GAA GGC UGA GAA AUA CCC GUA
36nt dŲ68	p-UCA CCU GAU CUG GA**dŲ** AAU GCC AGC GUA GGG AAG UCA
TPP **dŲ20-dŲ68**	ACG ACU CGG GG**dŲ** GCC CUU CUG CGU GAA GGC UGA GAA AUA CCC GUA UCA CCU GAU CUG GA**dŲ** AAU GCC AGC GUA GGG AAG UCA
45nt unmod	ACG ACU CGG GGU GCC CUU CUG CGU GAA GGC UGA GAA AUA CCC GUA
36nt unmod	p-UCA CCU GAU CUG GAU AAU GCC AGC GUA GGG AAG UCA

TPP **dŲ20**	ACG ACU CGG GG**dŲ** GCC CUU CUG CGU GAA GGC UGA GAA AUA CCC GUA UCA CCU GAU CUG GAU AAU GCC AGC GUA GGG AAG UCA
TPP **dŲ68**	ACG ACU CGG GGU GCC CUU CUG CGU GAA GGC UGA GAA AUA CCC GUA UCA CCU GAU CUG GA**dŲ** AAU GCC AGC GUA GGG AAG UCA
18-nt 2-O'-methyl RNA	UCA GGU GAU ACG GGU AUdA
165 nt DNA	GGA ACC AAA CGA CTC GGG GTG CCC TTC TGC GTG AAG GCT GAG AAA TAC CCG TAT CAC CTG ATC TGG ATA ATG CCA GCG TAG GGA AGT CAC GGA CCA CCA GGT CAT TGC TTC TTC ACG TTA TGG CAG GAG CAA ACT ATG CAA GTC GAC CTG CTG GAT CCA GCG CAA
5’ Primer 165 nt	TCG TAA TAC GAC TCA CTA TAG GAA CCA AAC GAC TCG
3’ Primer 165 nt	TTG CGC TGG ATC CAG CAG GTC GA
115 nt DNA	TCG TAA TAC GAC TCA CTA TAG GAT AAT GCC AGC GTA GGG AAG TCA CGG ACC ACC AGG TCA TTG CTT CTT CAC GTT ATG GCA GGA GCA AAC TAT GCA AGT CGA CCT G CT GGA TCC A

6 Appendix

6.1 NMR

2-Benzylisoindoline-1,3-dione (32)

^{1}H-NMR (500 MHz, CDCl$_3$):

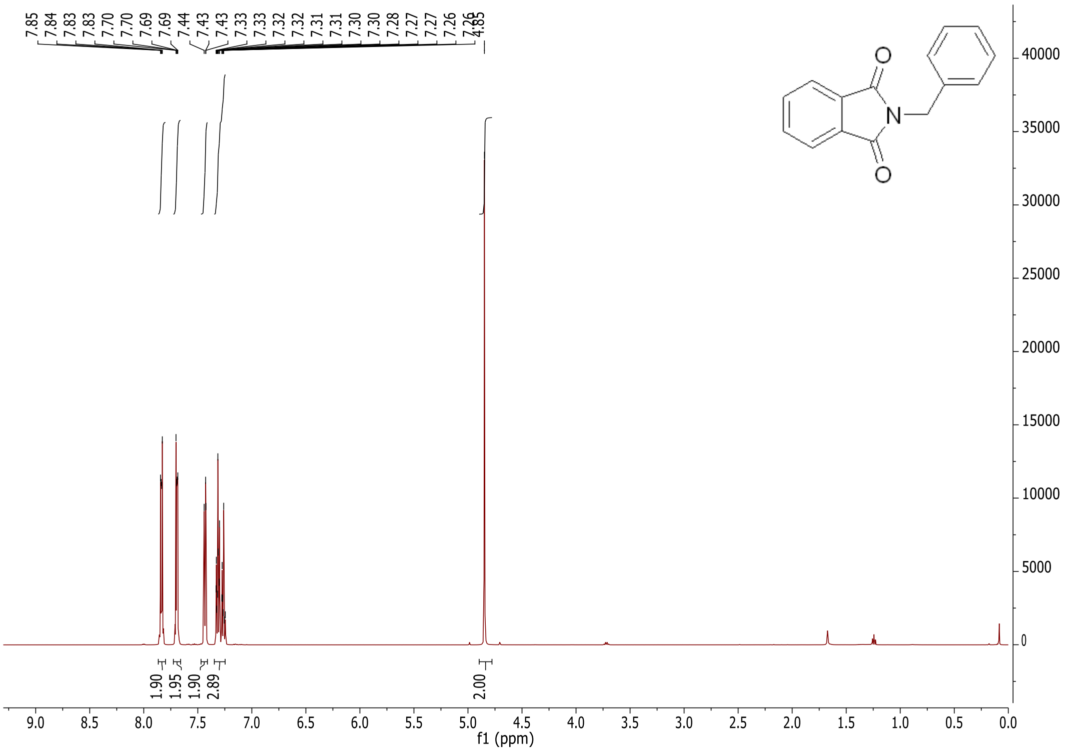

^{13}C-NMR (126 MHz, CDCl$_3$):

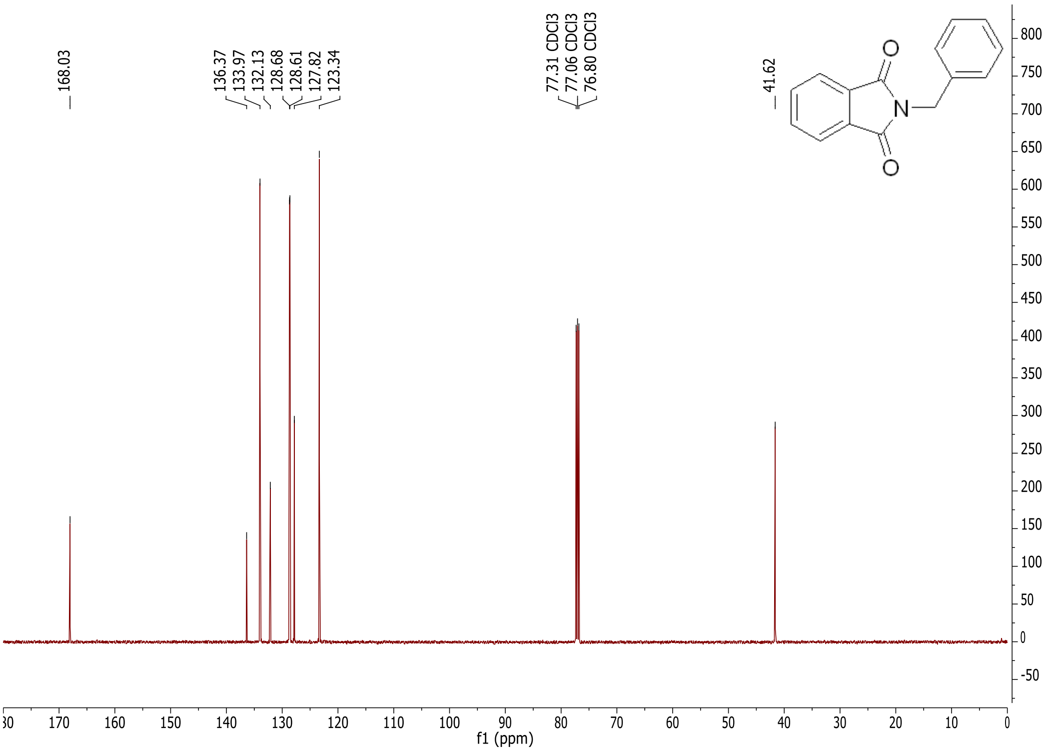

2-Benzyl-1,1,3,3-tetramethylisoindoline (33)

^{1}H-NMR (400 MHz, $CDCl_3$):

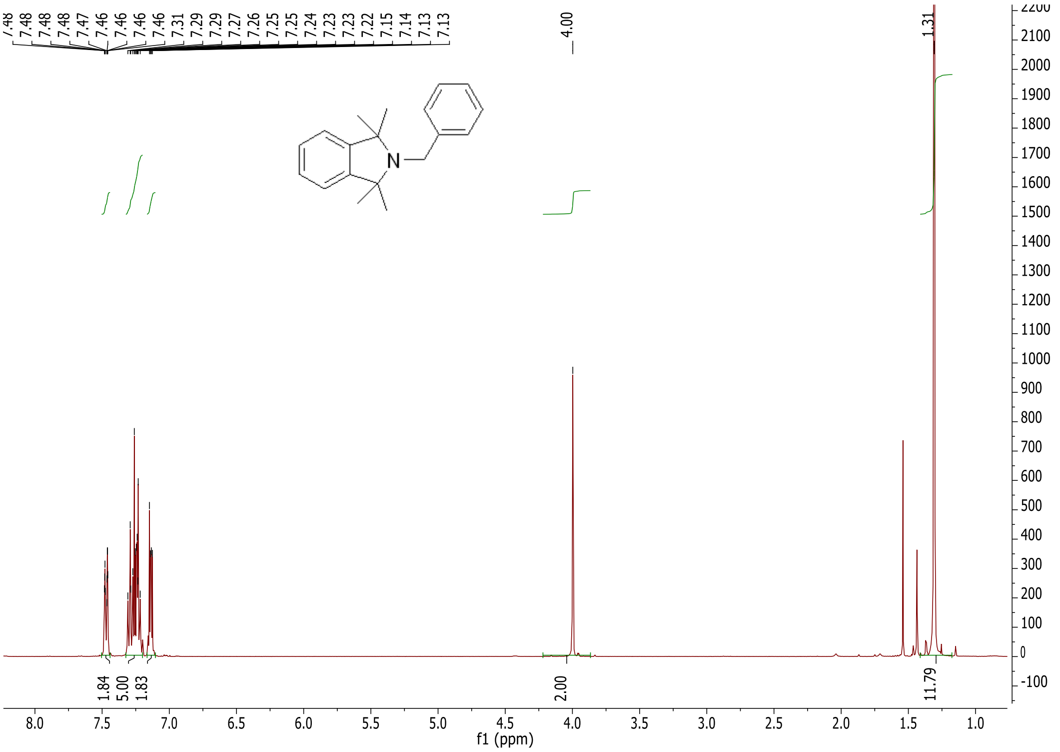

^{13}C-NMR (75.4 MHz, $CDCl_3$):

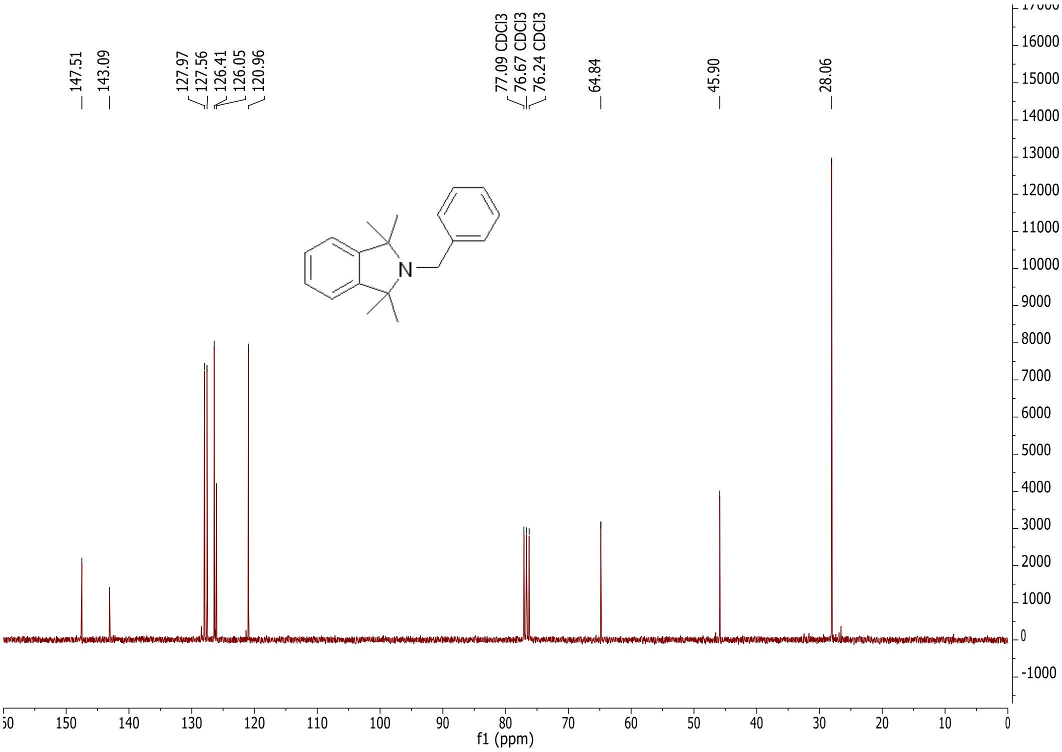

2-Benzyl-1,1,3,3-tetraethylisoindoline (34)

^{1}H-NMR (500 MHz, $CDCl_3$):

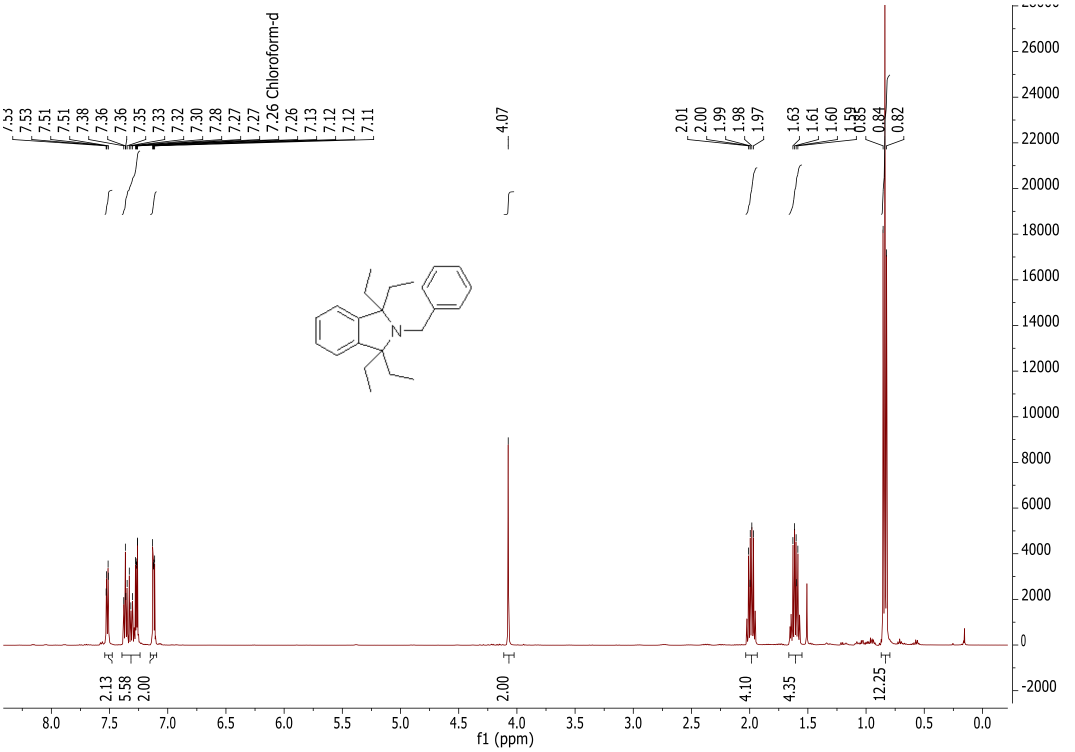

^{13}C-NMR (126 MHz, $CDCl_3$):

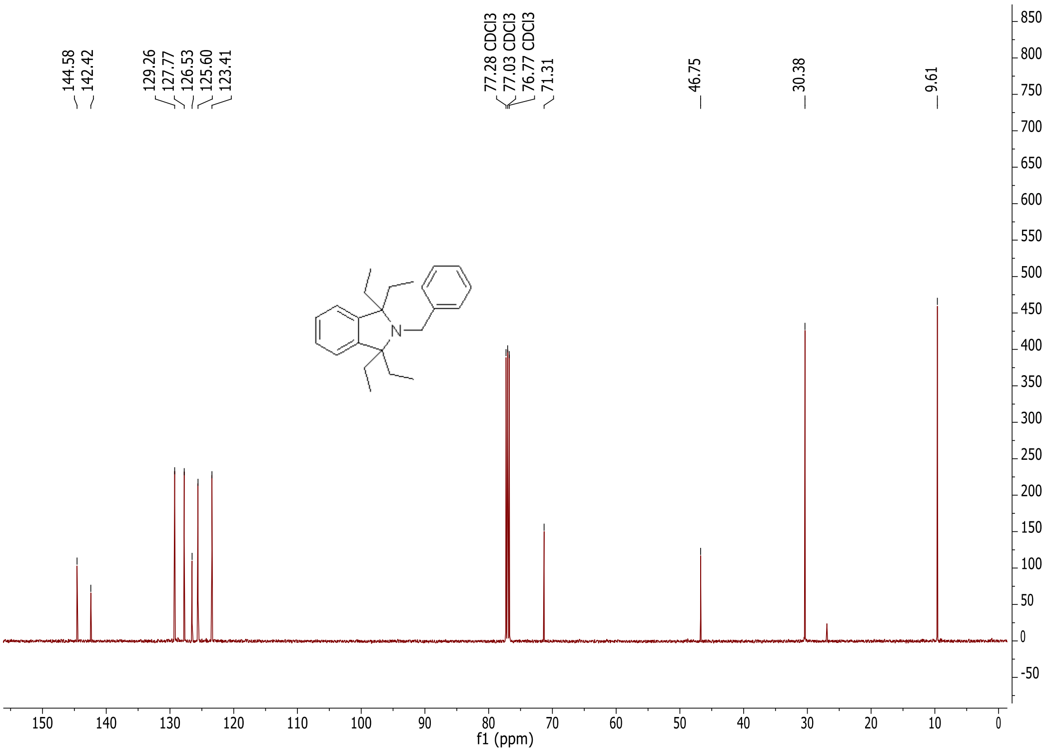

1,1,3,3-Tetramethylisoindoline (35)

^{1}H-NMR (400 MHz, CDCl$_3$):

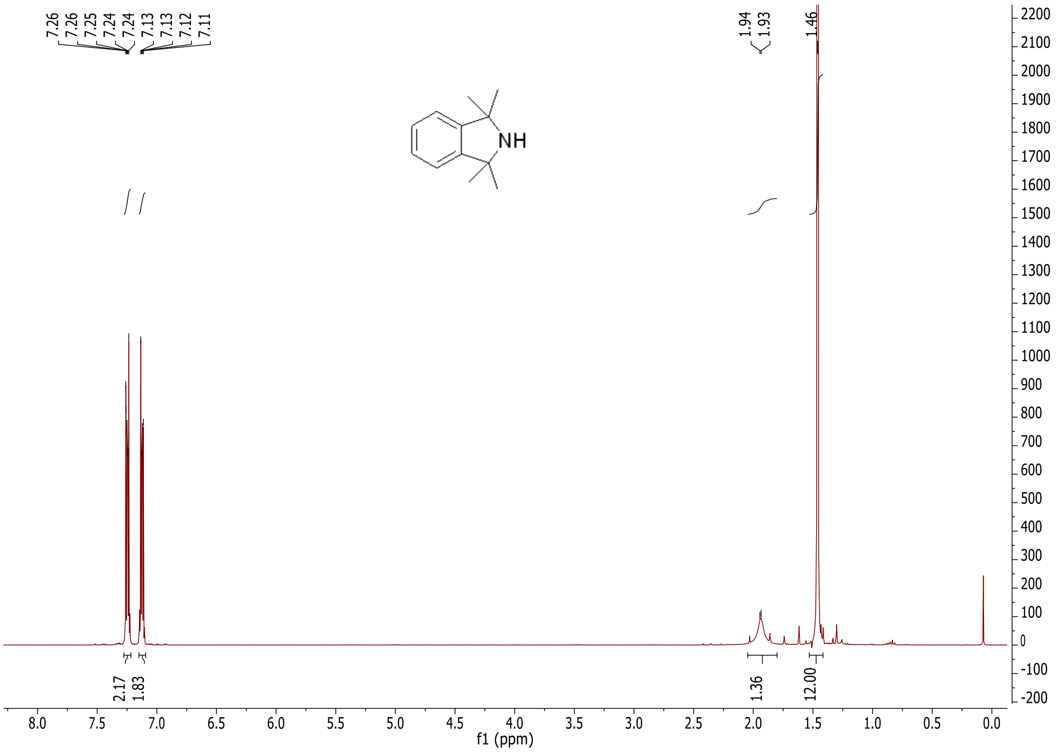

^{13}C-NMR (75.4 MHz, CDCl$_3$):

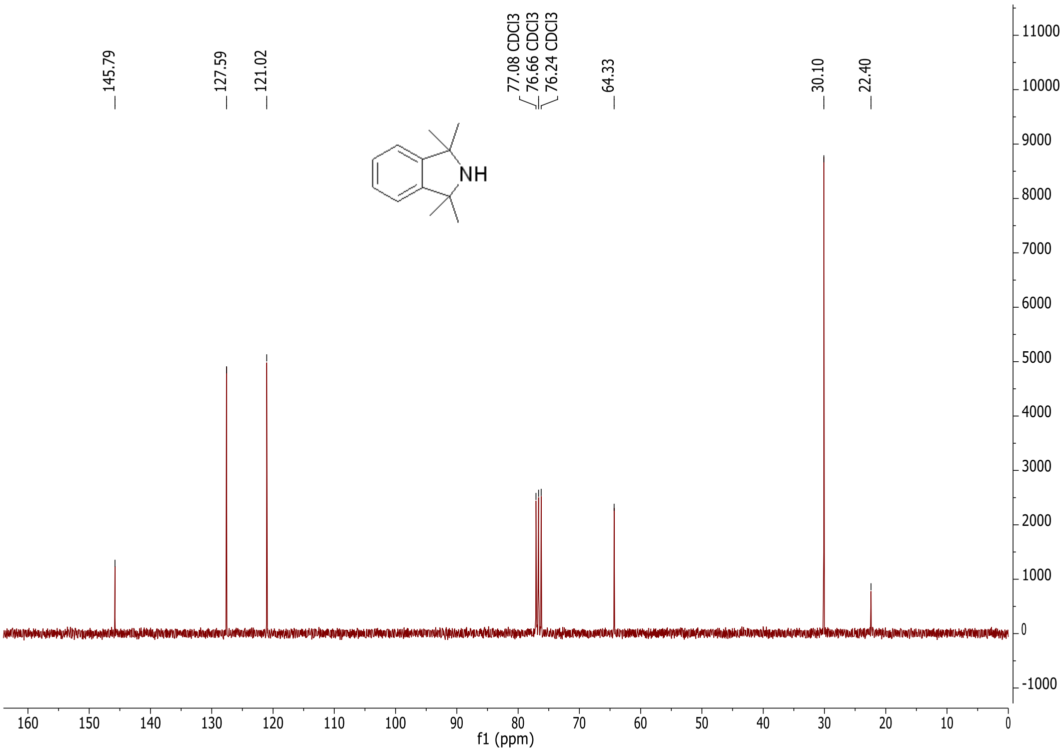

1,1,3,3-Tetraethylisoindoline (36)

^{1}H-NMR (500 MHz, CDCl$_3$):

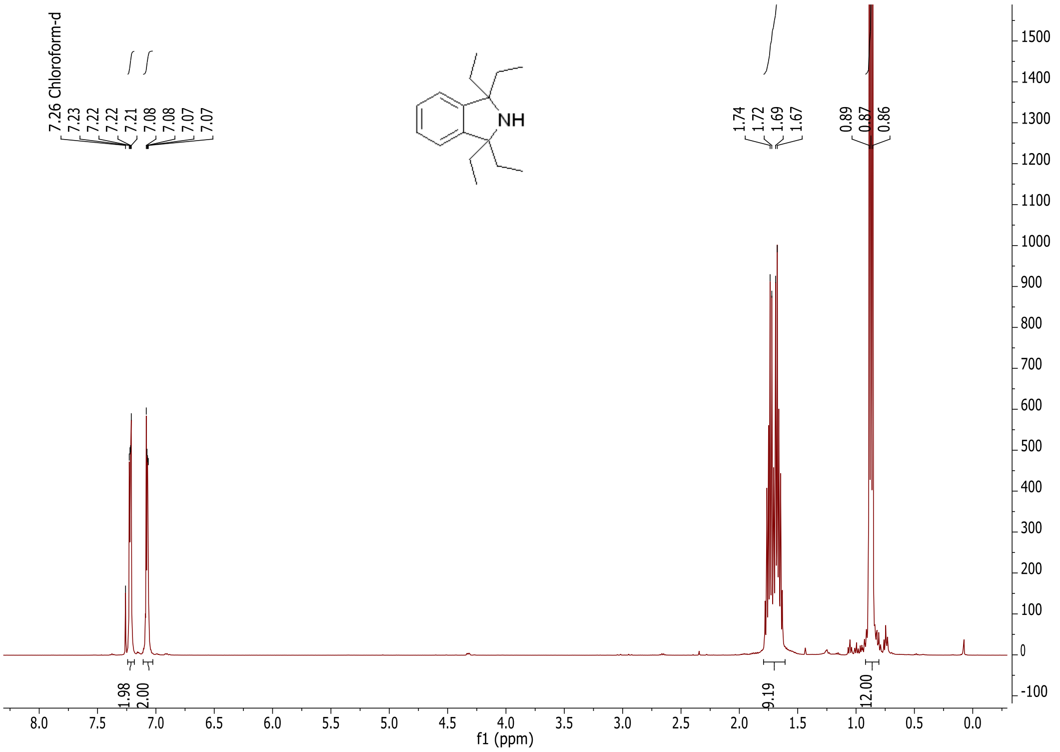

^{13}C-NMR (400 MHz, CDCl$_3$):

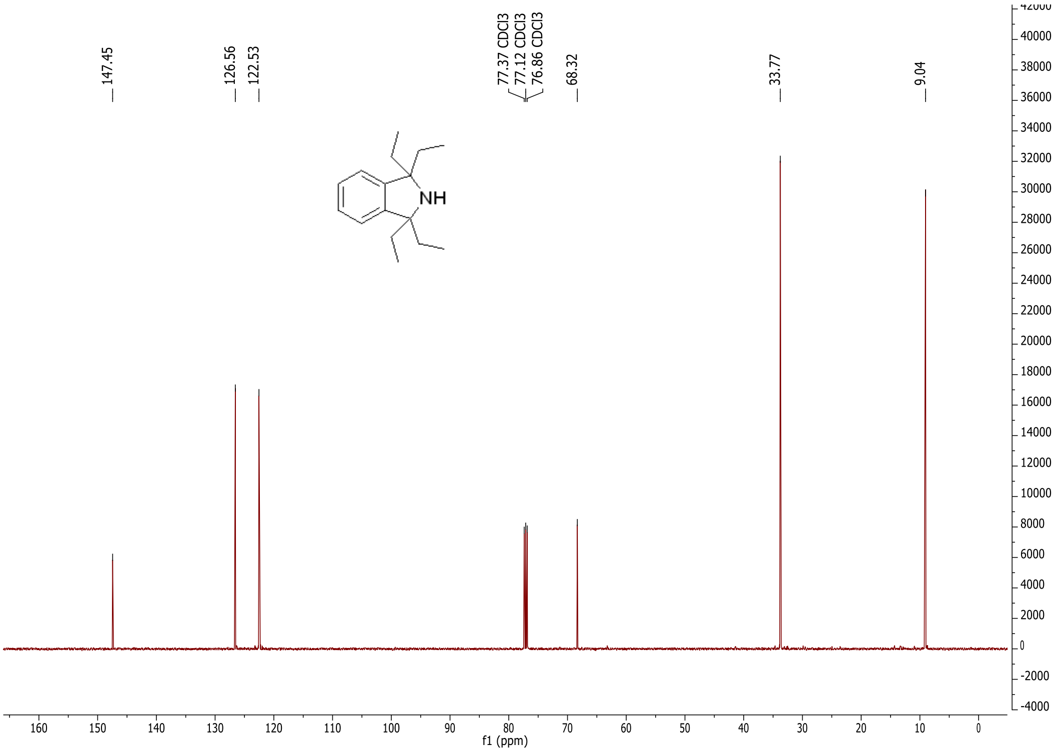

5-Nitro-1,1,3,3-tetramethylisoindoline (37)

^{1}H-NMR (400 MHz, $CDCl_3$):

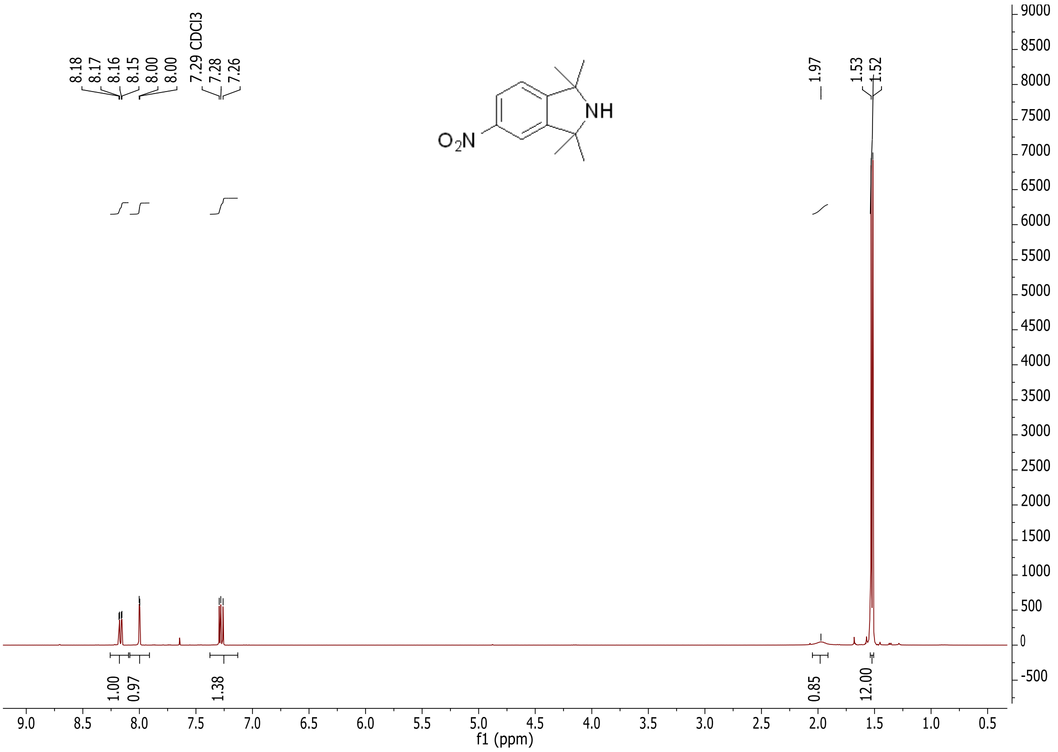

^{13}C-NMR (75.4 MHz, $CDCl_3$):

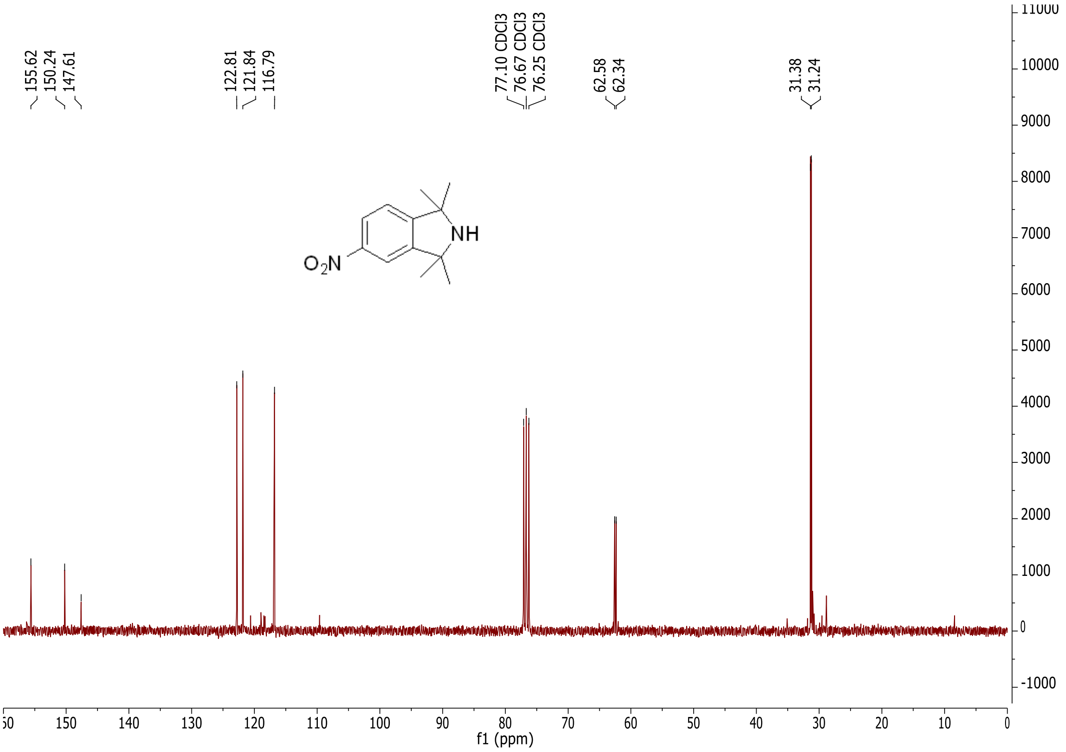

5-nitro-1,1,3,3-tetraethylisoindoline (38)

^{1}H-NMR (500 MHz, CDCl$_3$):

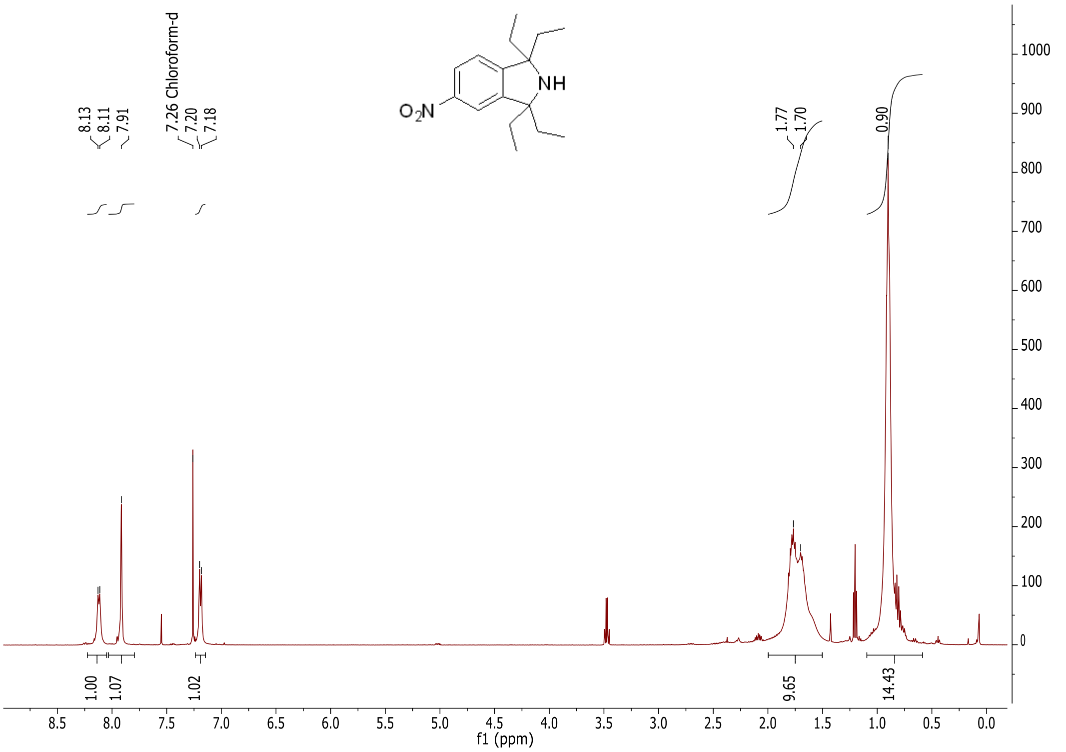

^{13}C-NMR (126 MHz, CDCl$_3$):

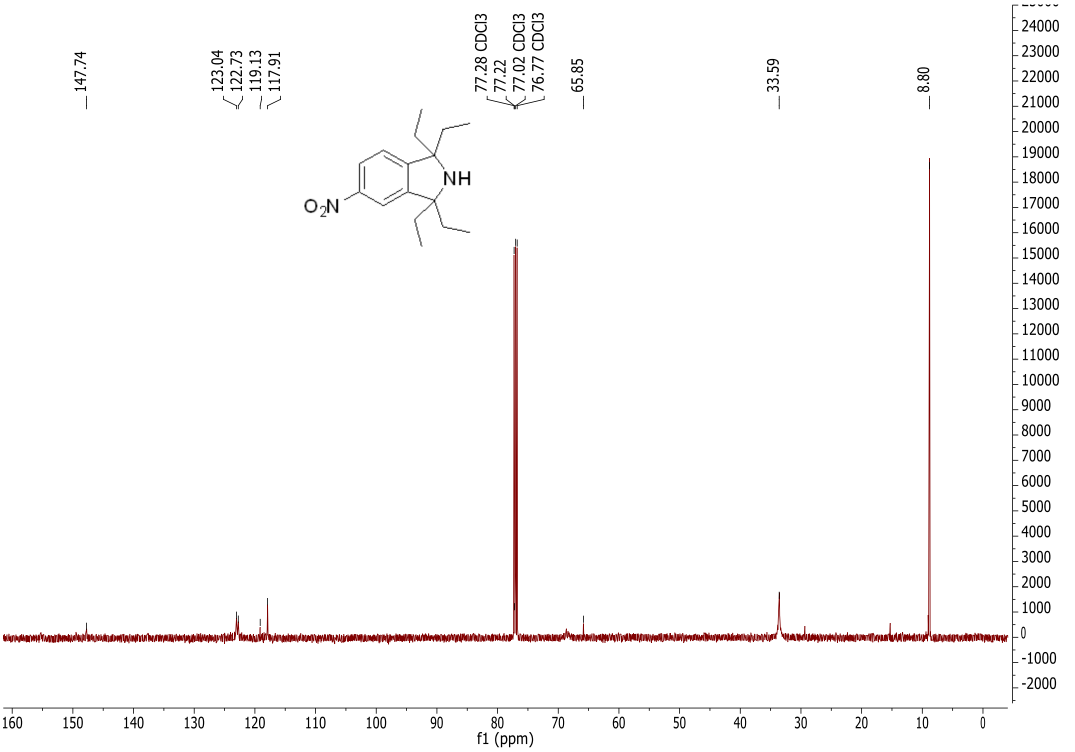

5-Amino-1,1,3,3-tetramethylisoindoline (39)

^{1}H-NMR (300 MHz, $CDCl_3$):

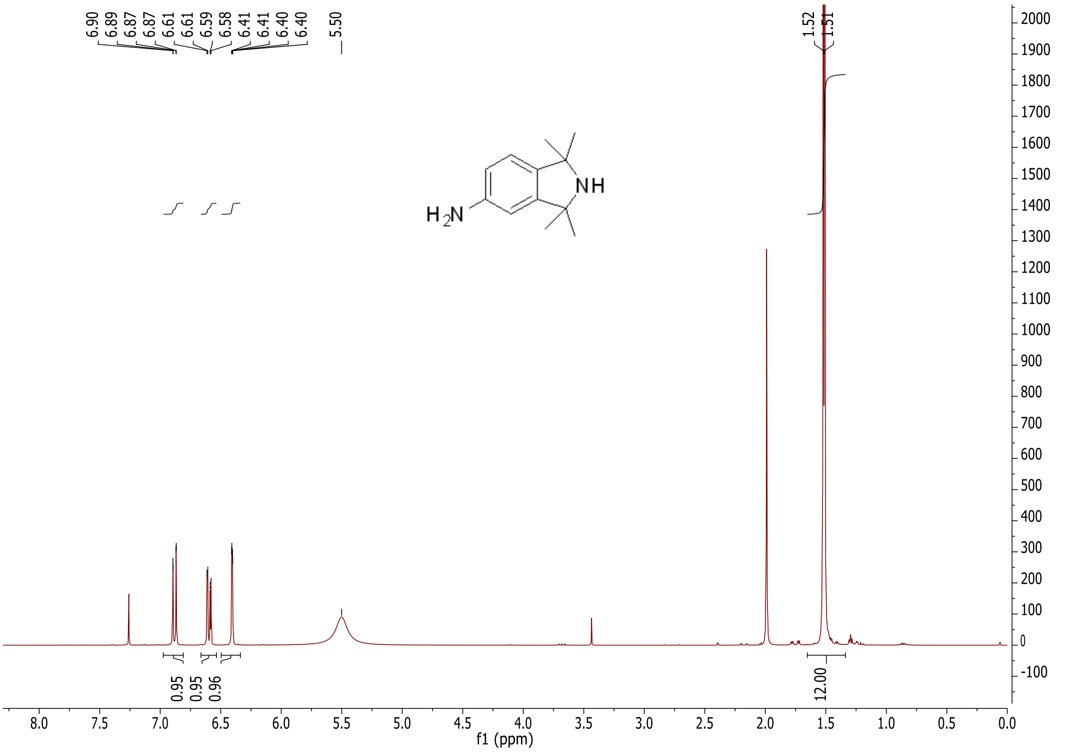

^{13}C-NMR (75.4 MHz, MeOH-d4):

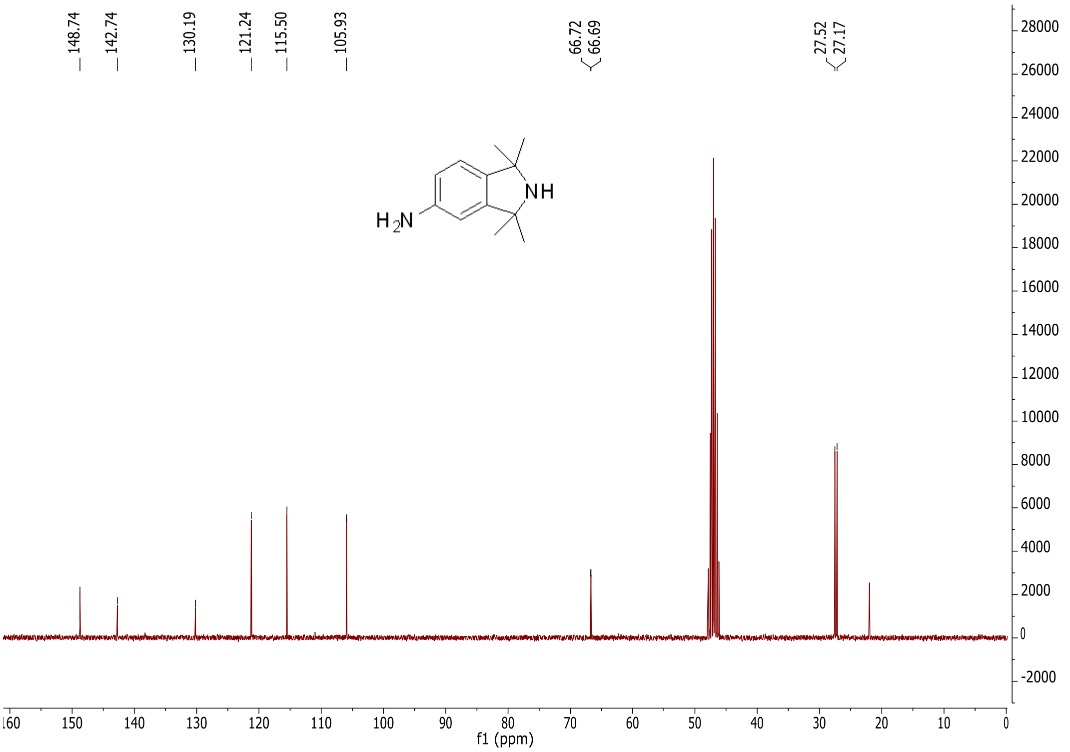

5-Amino-1,1,3,3-tetraethylisoindoline (40)

^{1}H-NMR (500 MHz, MeOH-d4):

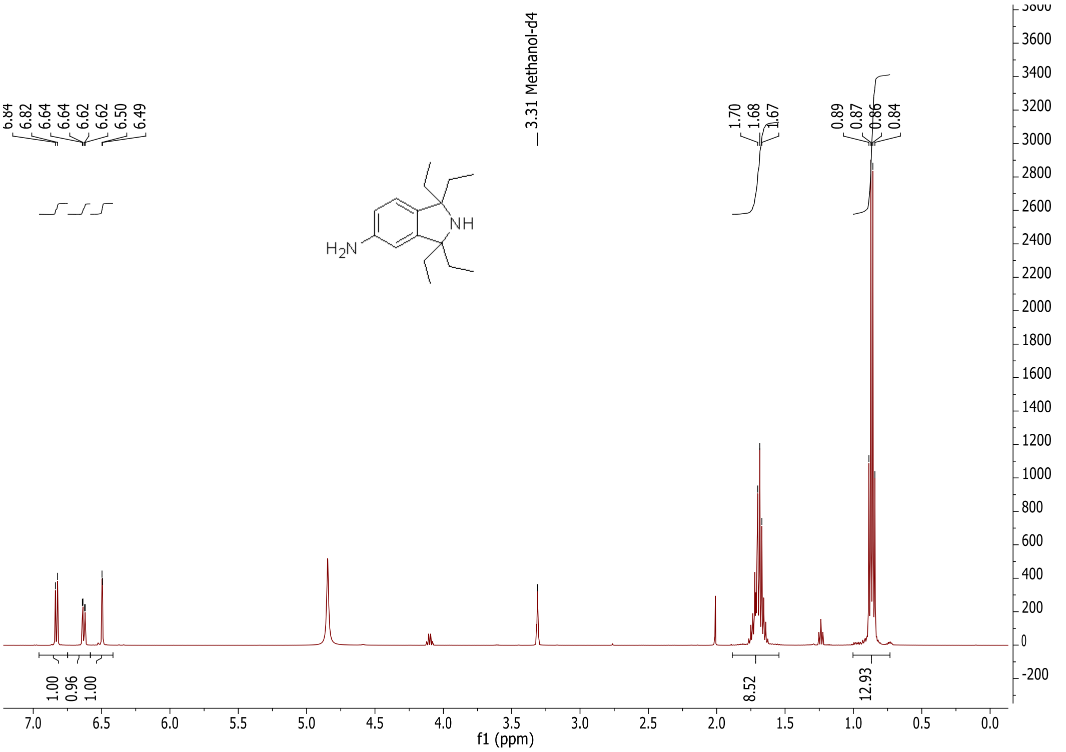

^{13}C-NMR (126 MHz, MeOH-d4):

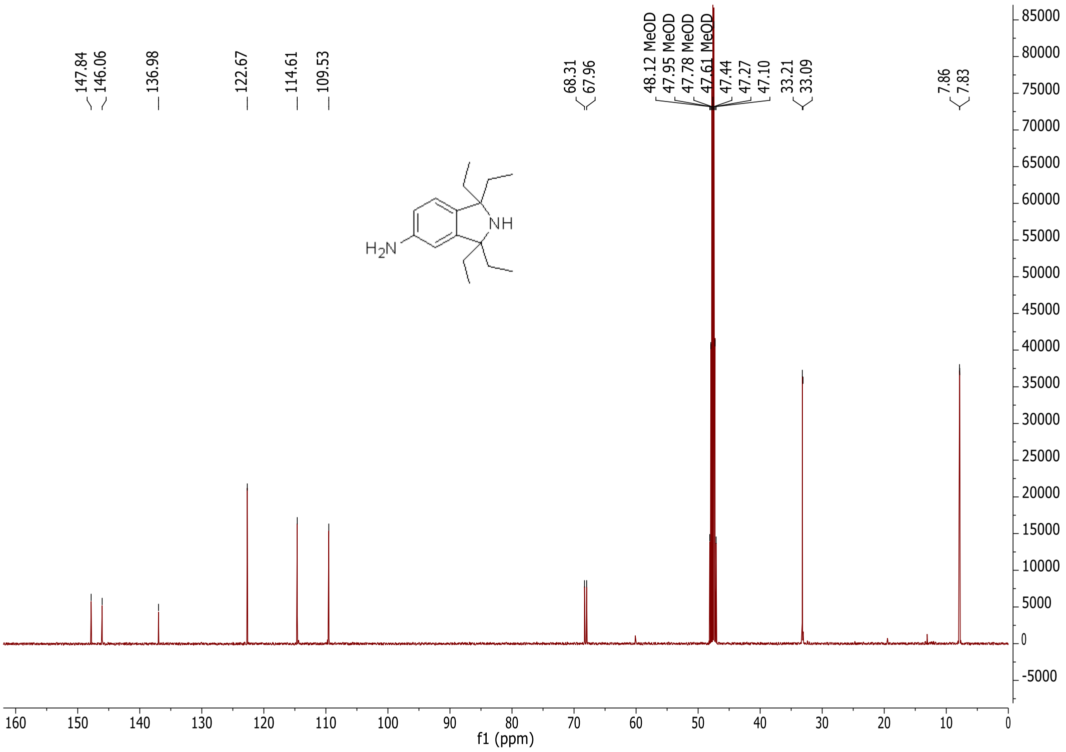

5-azido-1,1,3,3-tetramethylisoindoline (41)

^{1}H-NMR (300 MHz, CDCl$_3$):

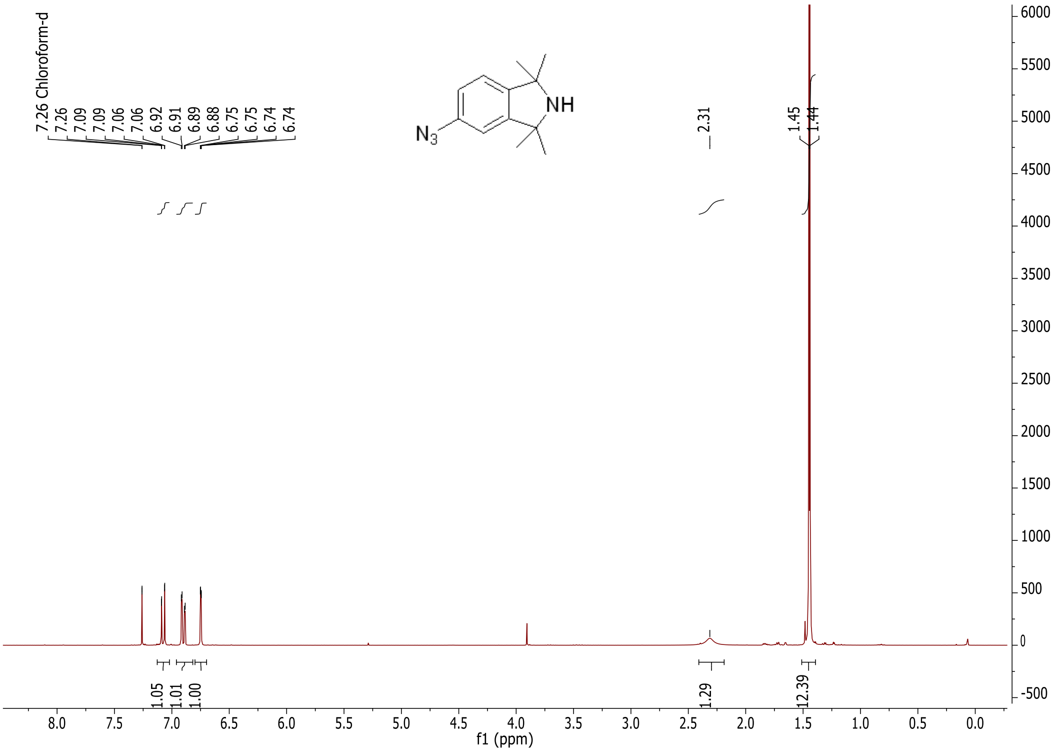

^{13}C-NMR (75.4 MHz, CDCl$_3$):

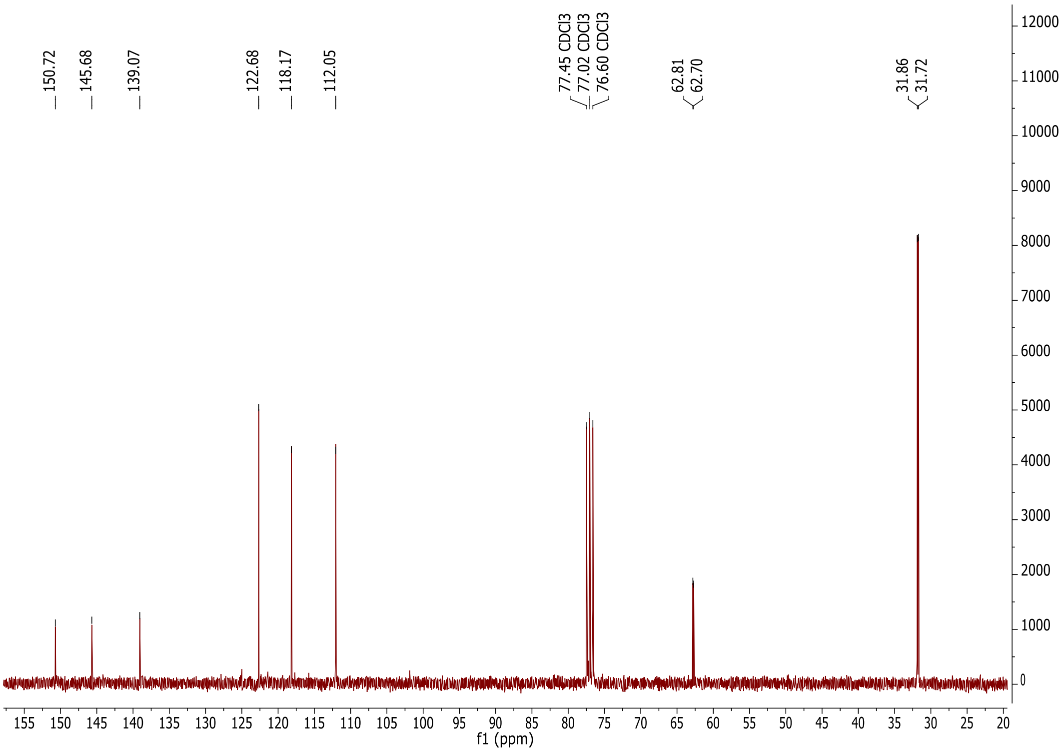

5-azido-1,1,3,3-tetraethylisoindoline (42)

^{1}H-NMR (500 MHz, CDCl$_3$):

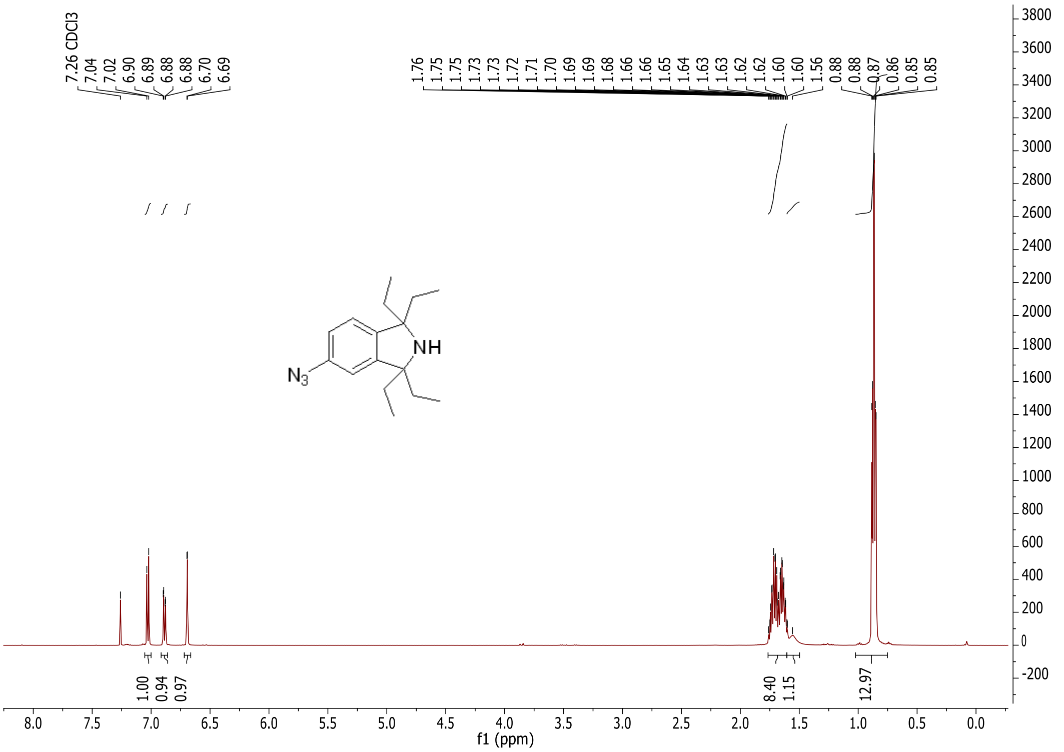

^{13}C-NMR (126 MHz, CDCl$_3$):

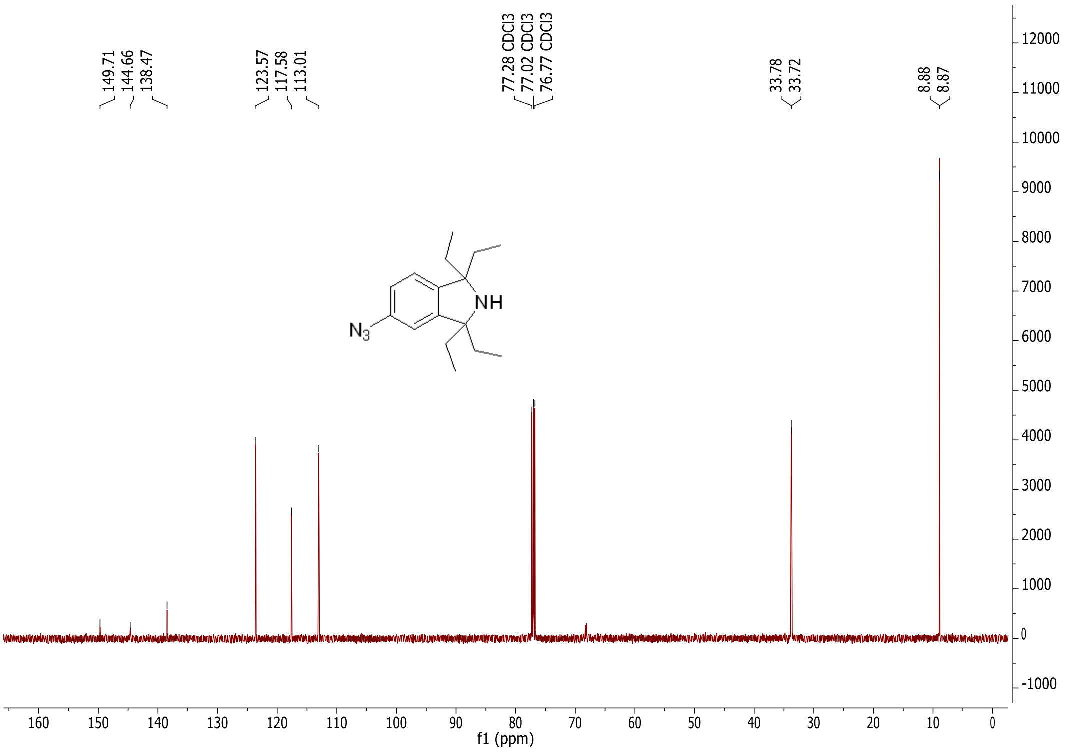

5-azido-1,1,3,3-tetramethylisoindolin-1-yloxyl (43)

^{1}H-NMR (300 MHz, $CDCl_3$):

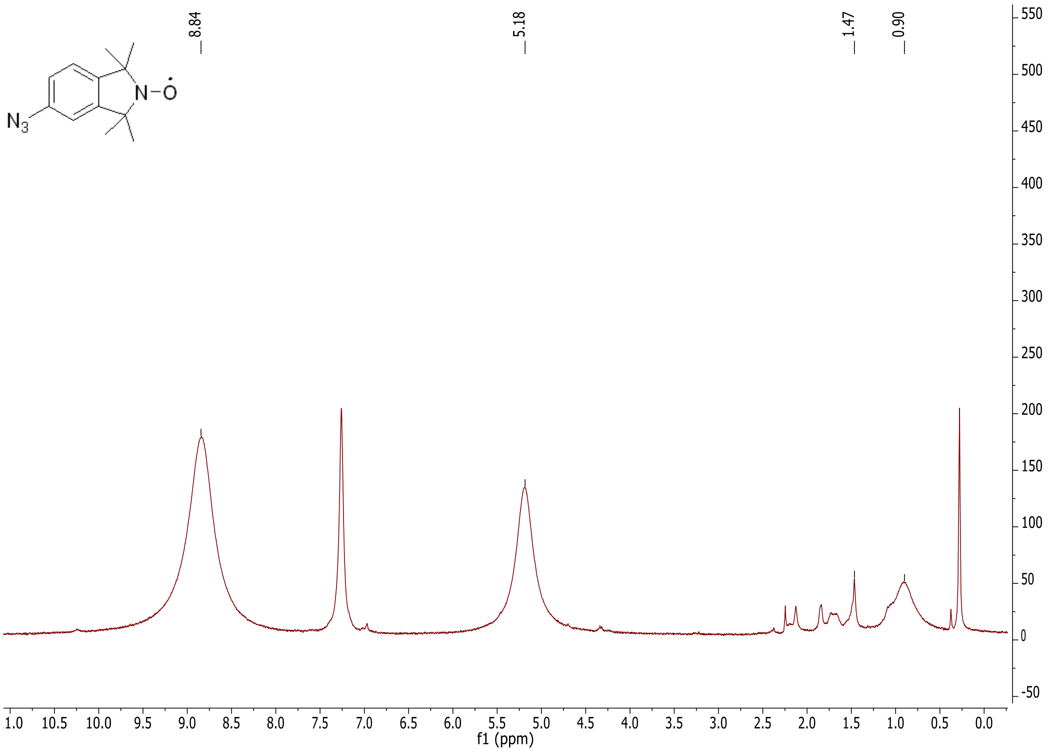

5-azido-1,1,3,3-tetraethylisoindolin-1-yloxyl (44)

^{1}H-NMR(500 MHz, $CDCl_3$):

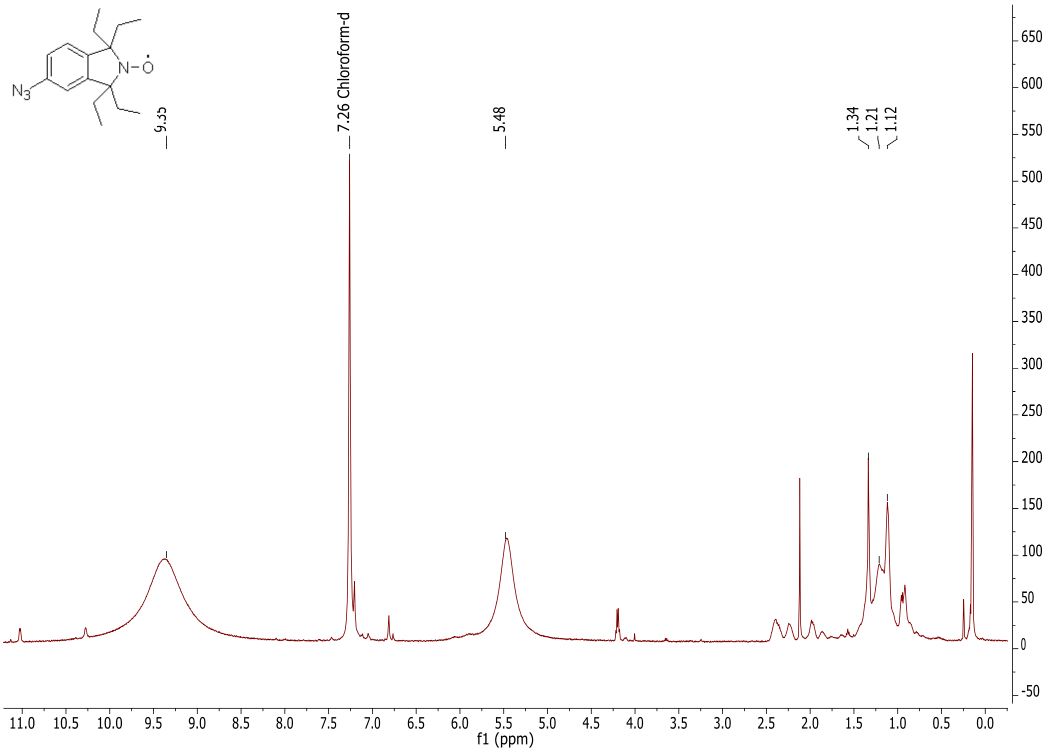

5-Iodo-2‘-O-methylcytidine (48)

^{1}H-NMR (400 MHz, MeOH-d4):

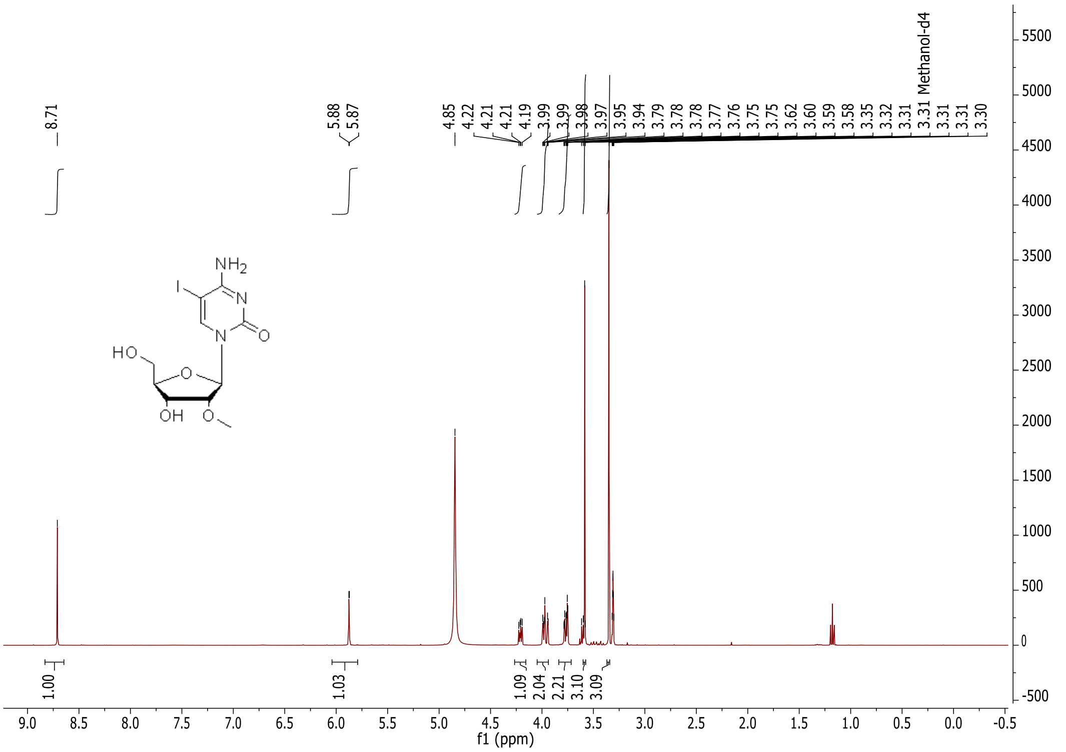

^{13}C-NMR (100.6 MHz, MeOH-d4):

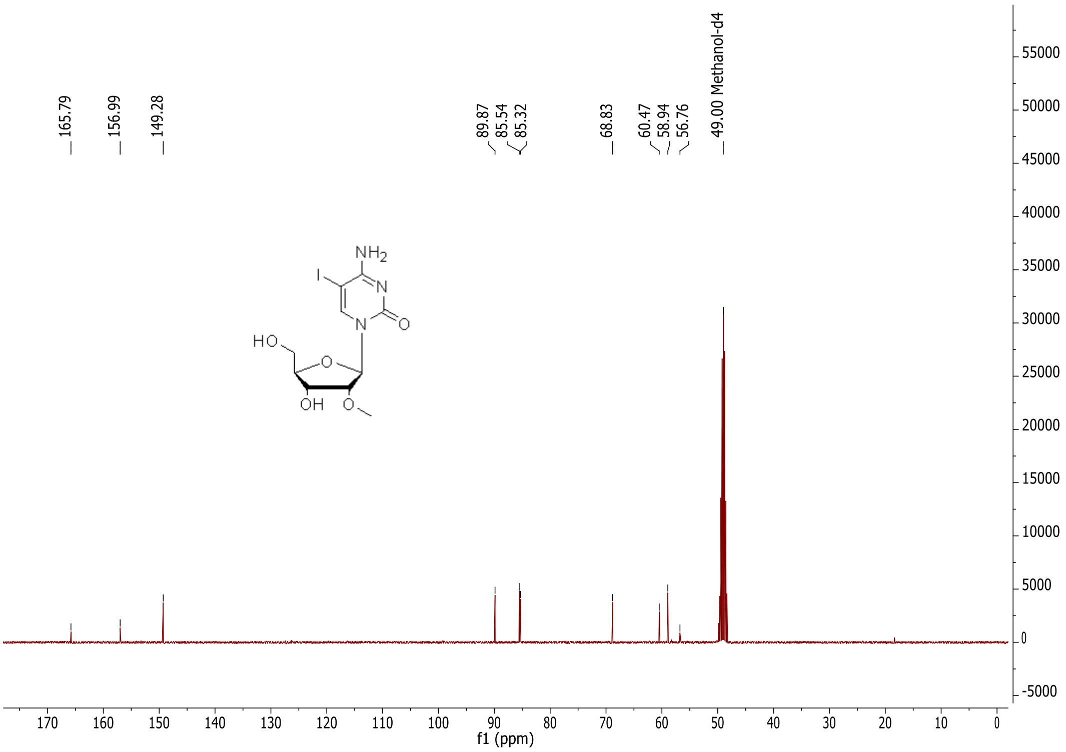

5-(Trimethylsilylethynyl)-2‘-O-methylcytidine (49)

^{1}H-NMR (400 MHz, DMSO-d$_6$):

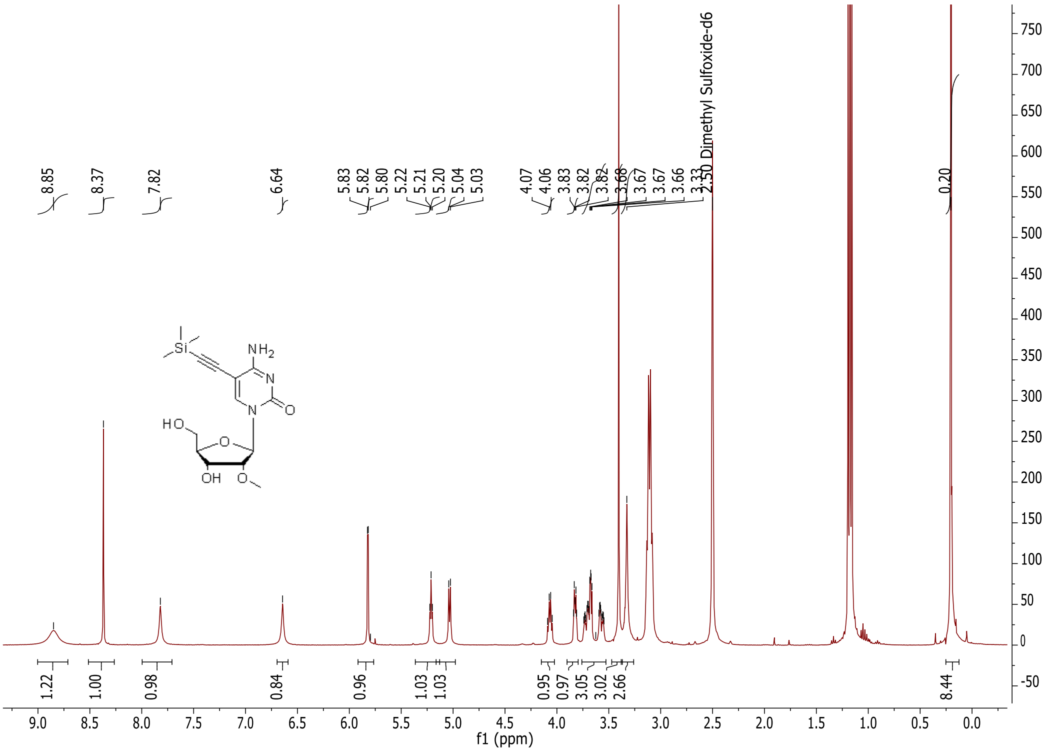

^{13}C-NMR (100.6 MHz, DMSO-d$_6$):

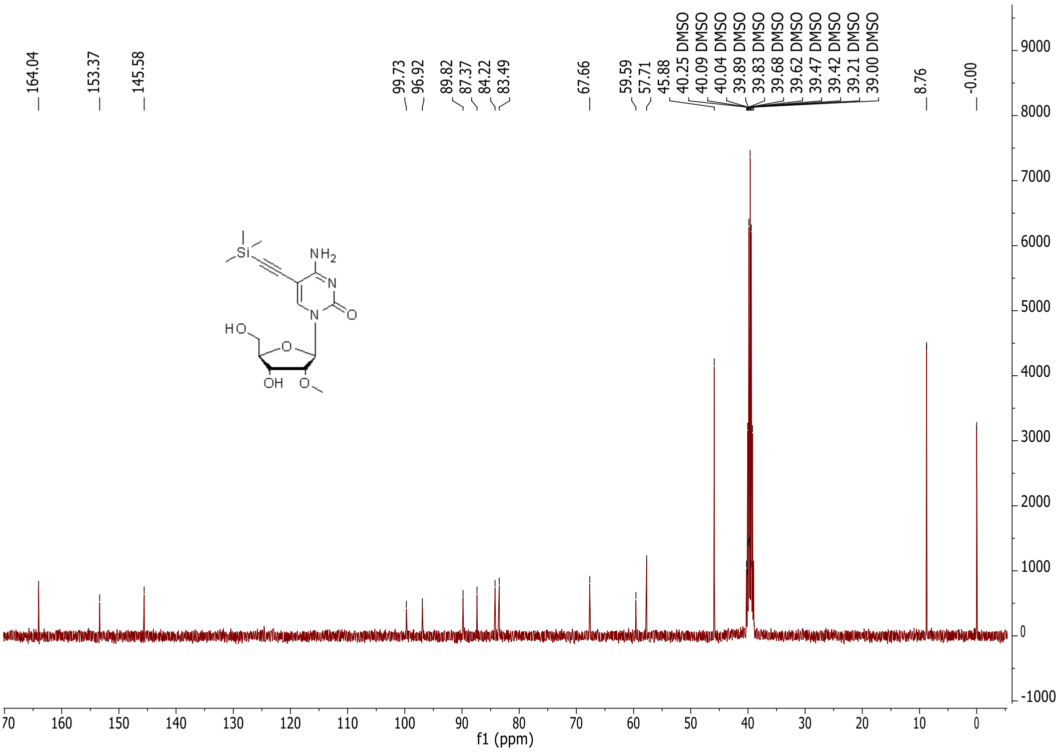

5-Ethynyl-2‘-O-methylcytidine (50)

^{1}H-NMR (400 MHz, DMSO-d$_6$):

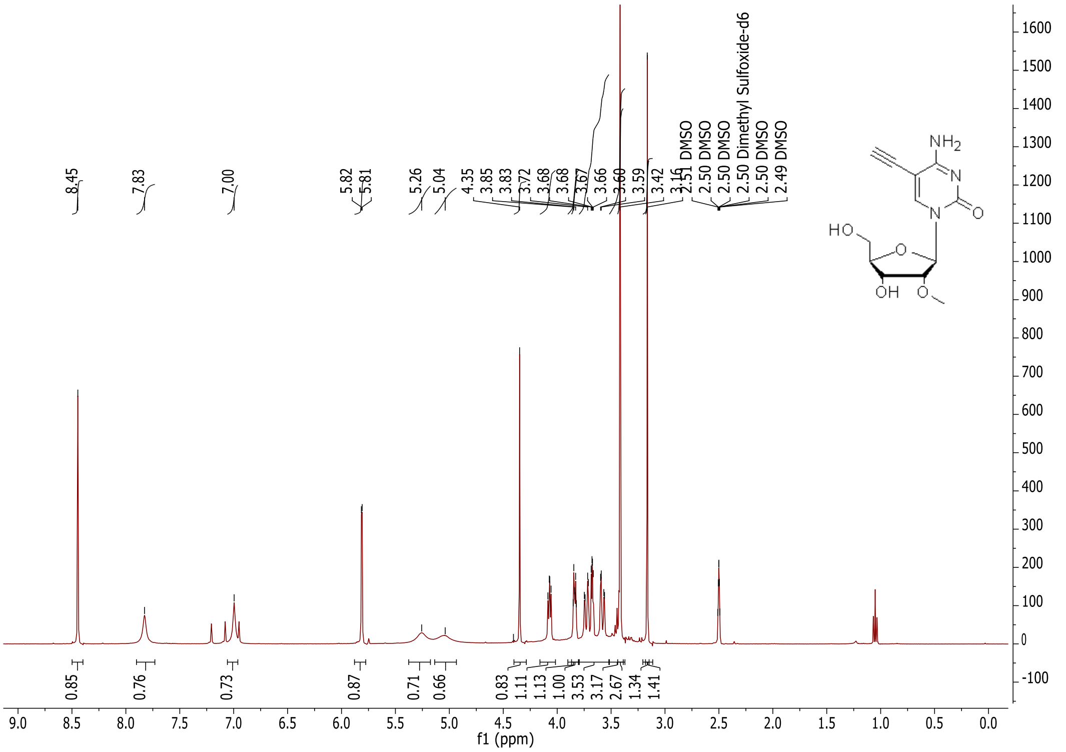

^{13}C-NMR (100.6 MHz, DMSO-d$_6$):

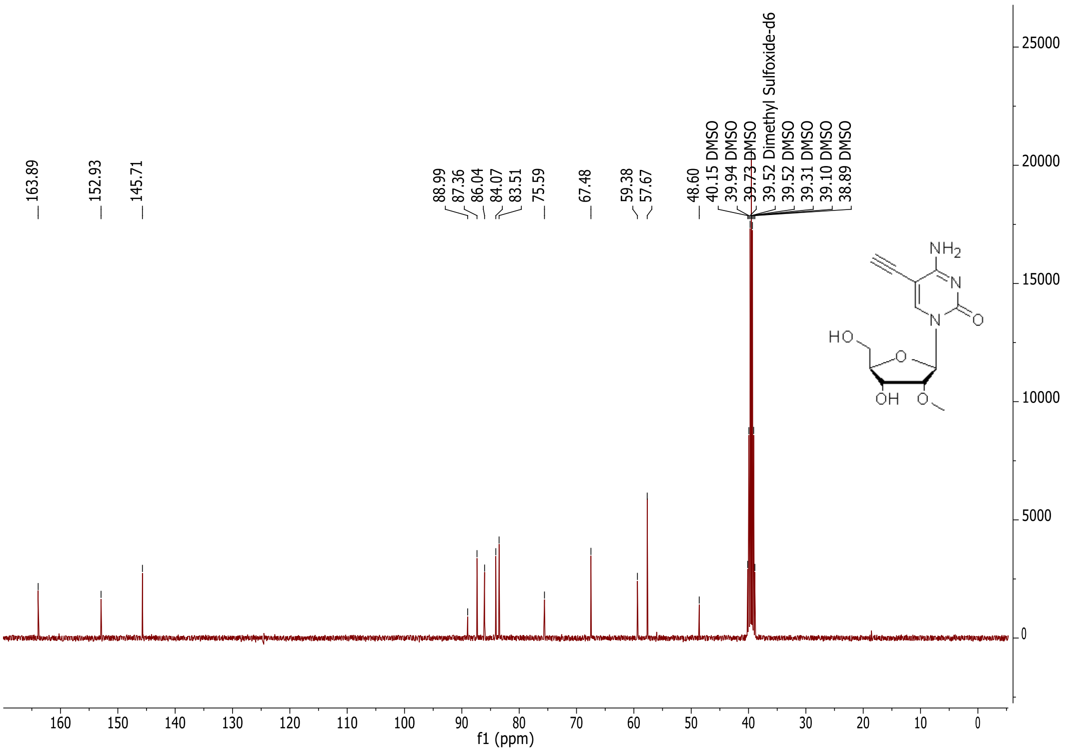

N_4-Acetyl-5-Ethynyl-2‘-O-methylcytidine (51)

^{1}H-NMR (500 MHz, DMSO-d_6):

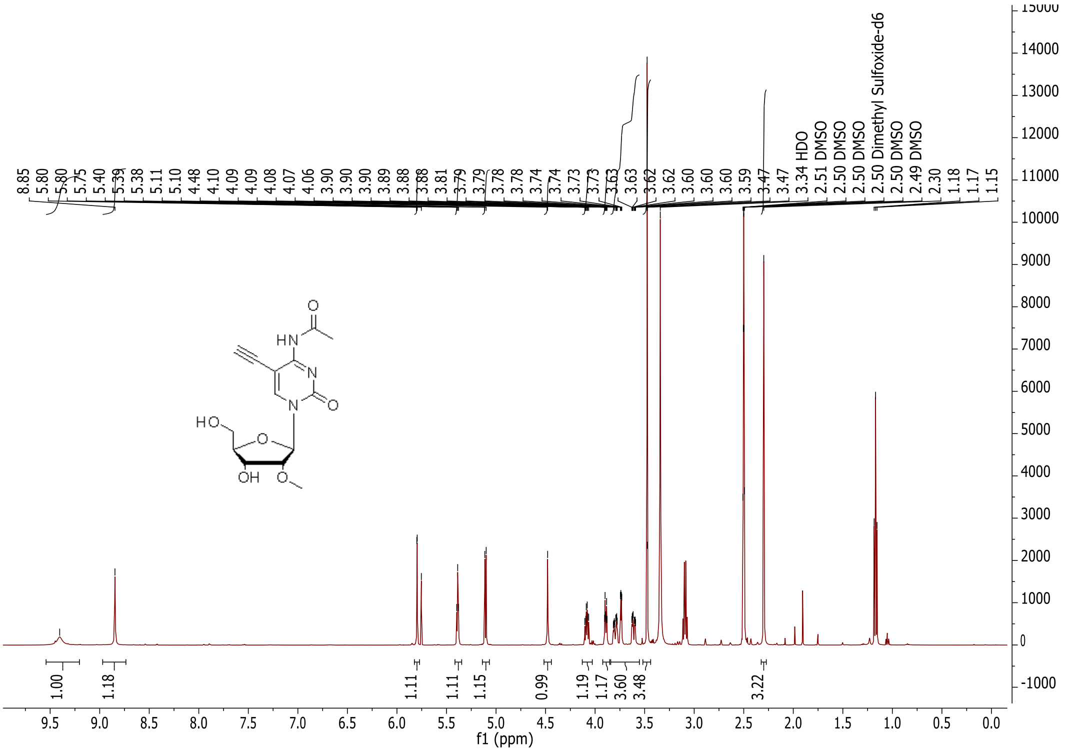

^{13}C-NMR (126 MHz, DMSO-d_6):

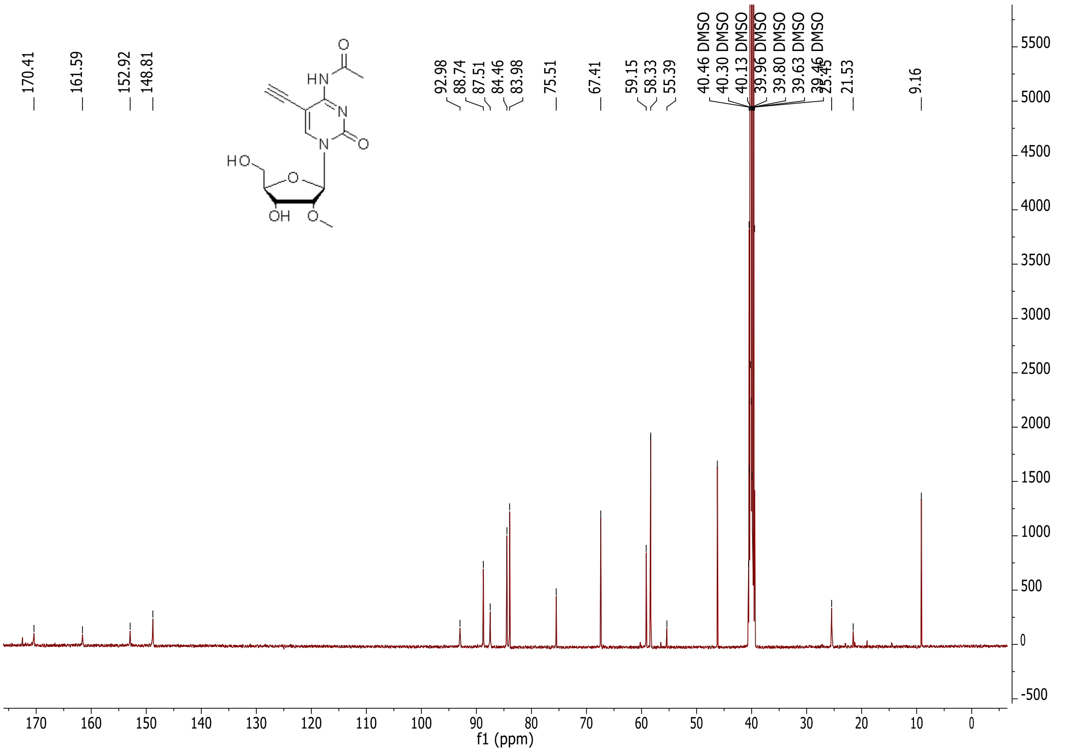

5’-O-Dimethoxytrityl-N$_4$-Acetyl-5-ethinyl-2’-O-methylcytidine (52)

^{1}H-NMR (500 MHz, CDCl$_3$):

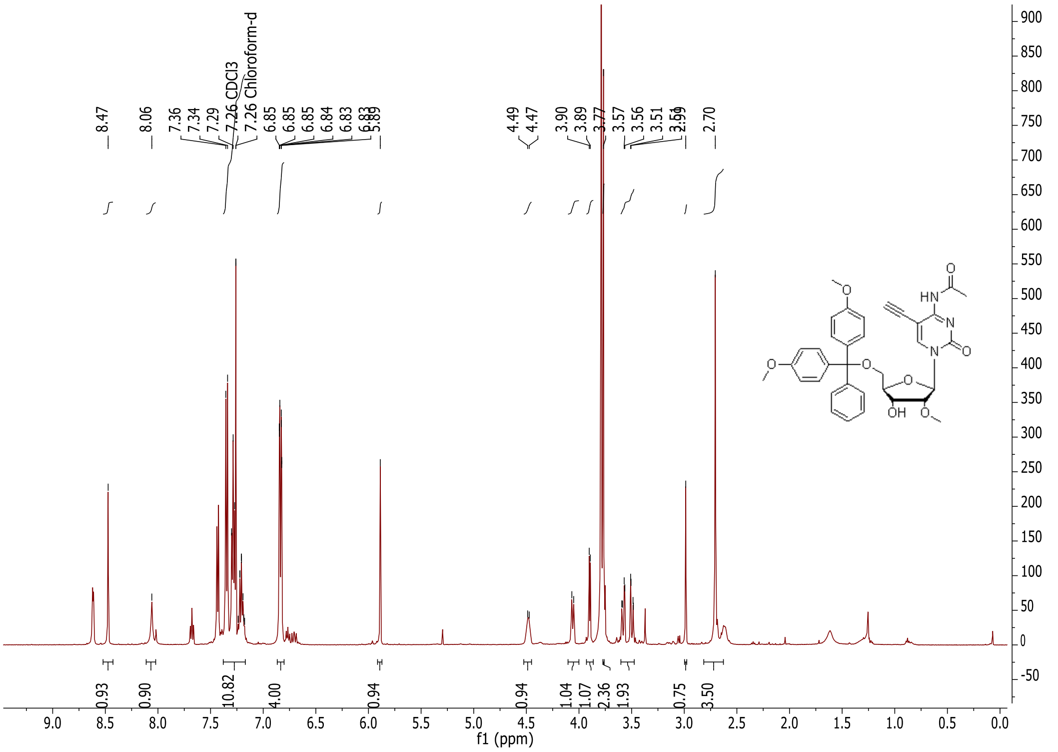

^{13}C-NMR (126 MHz, CDCl$_3$):

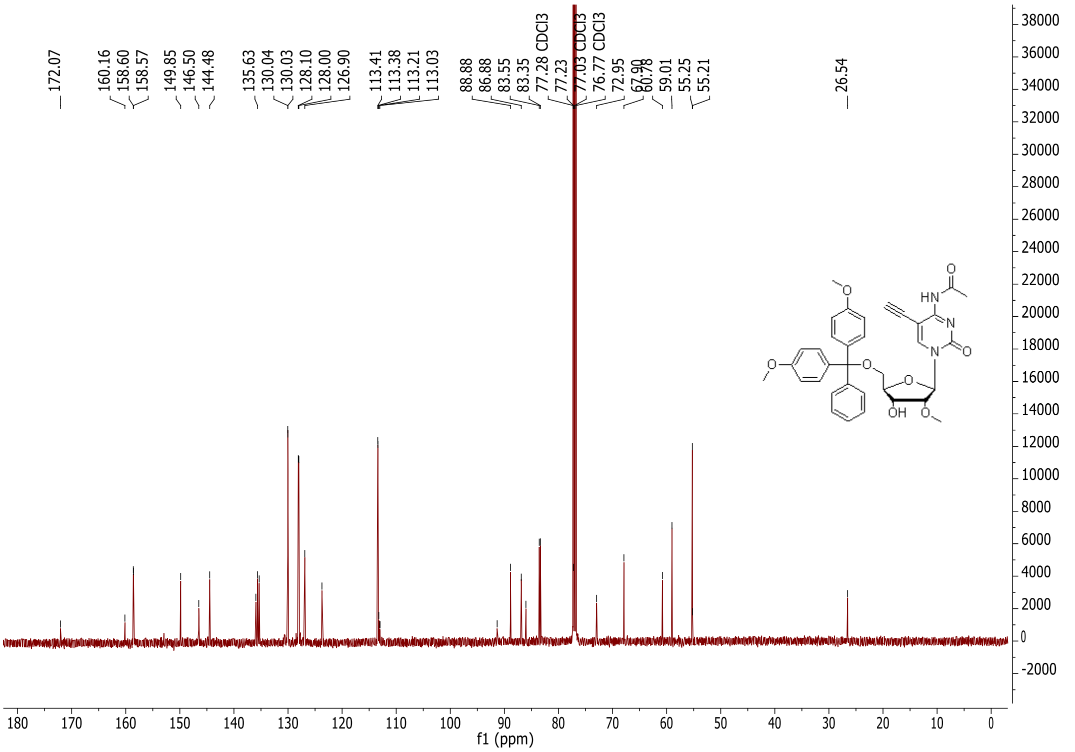

3’-O-[(2-Cyanoethyl)(N,N-diisopropylamino)phosphinyl]-5’-O-dimethoxytrityl-5-ethinyl -2’-O-methylcytidine (EmC)

^{1}H-NMR (500 MHz, $CDCl_3$):

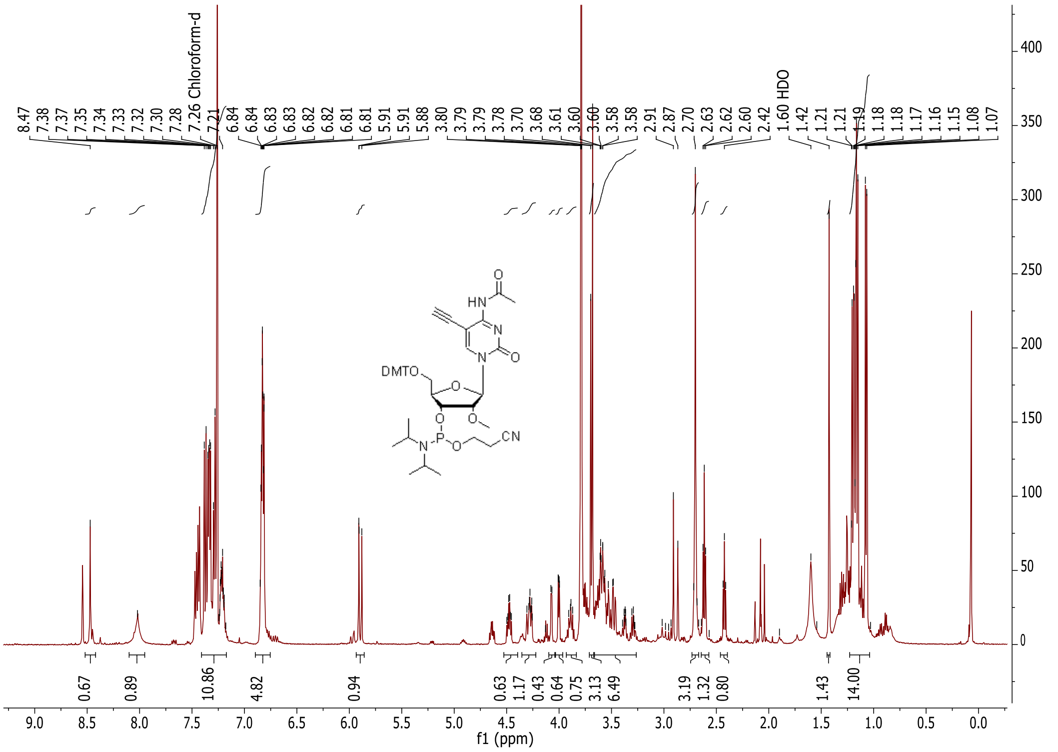

^{13}C-NMR (126 MHz, $CDCl_3$):

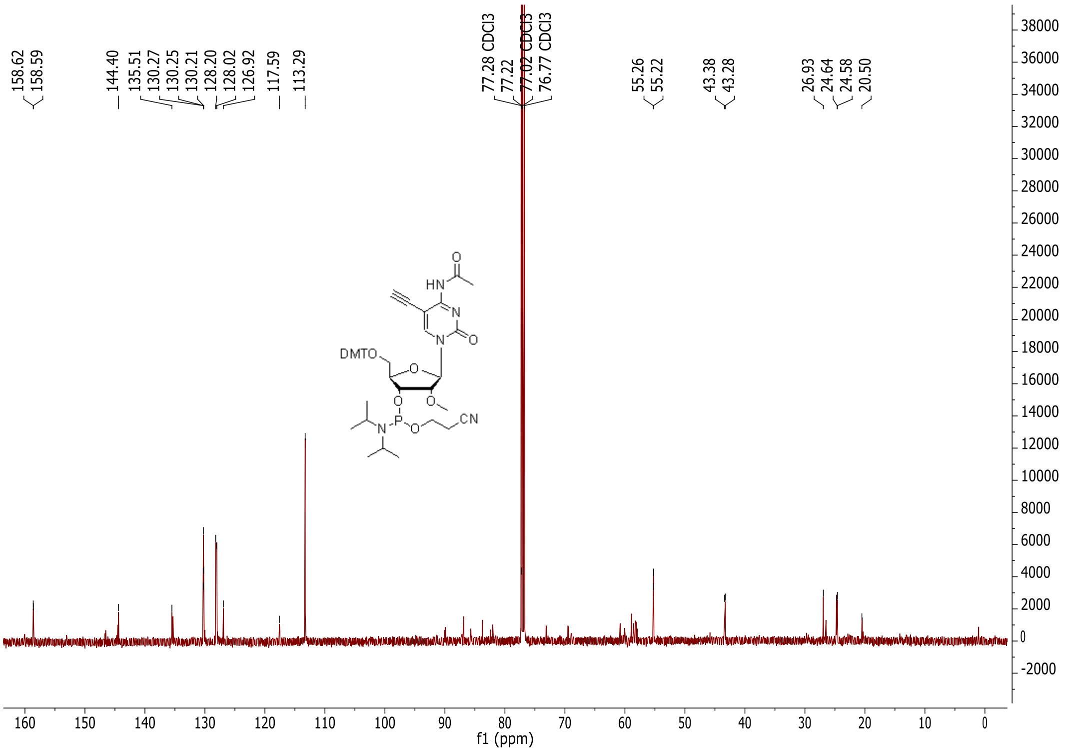

^{31}P-NMR (202.4 MHz, $CDCl_3$):

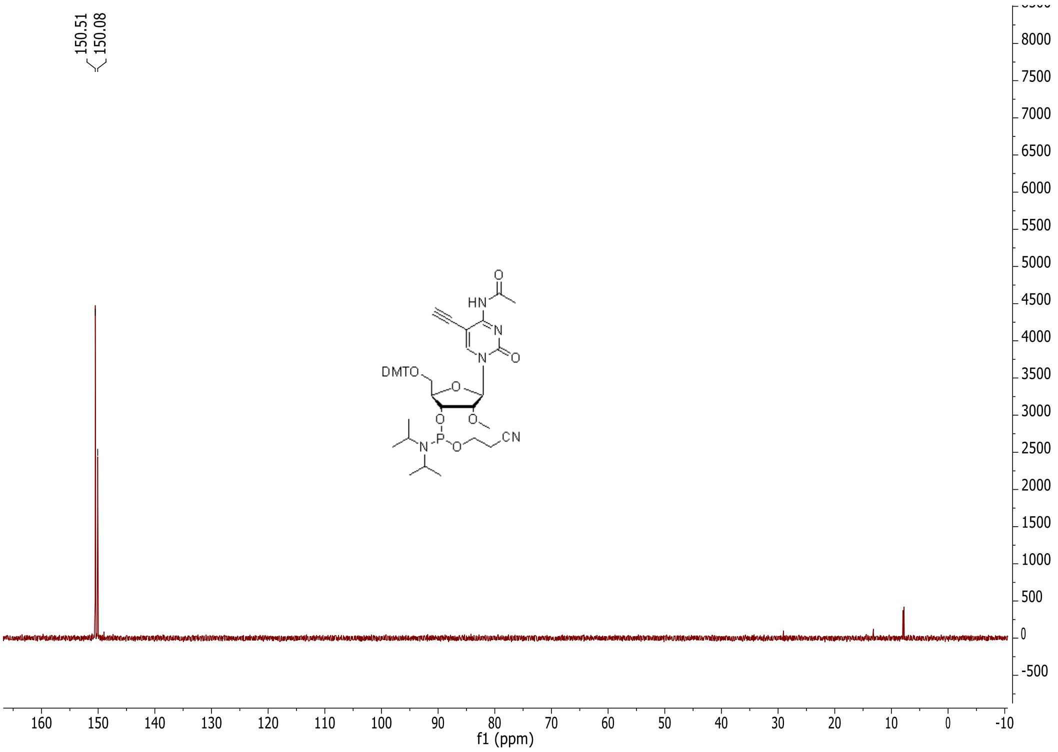

Hydroxy-1,1,3,3-tetramethylisoindoline (56)

In-situ ^{1}H-NMR (400 MHz, D_2O):

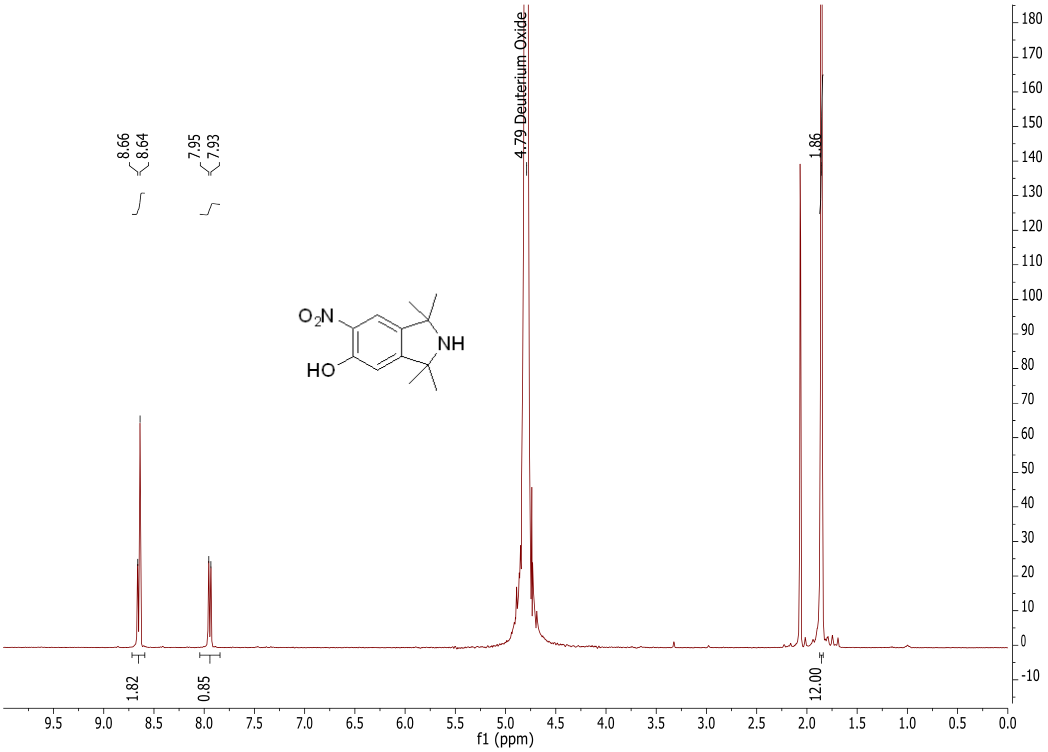

5-Hydroxy-6-nitro-1,1,3,3-tetramethylisoindoline (57)

^{1}H-NMR (400 MHz, $CDCl_3$):

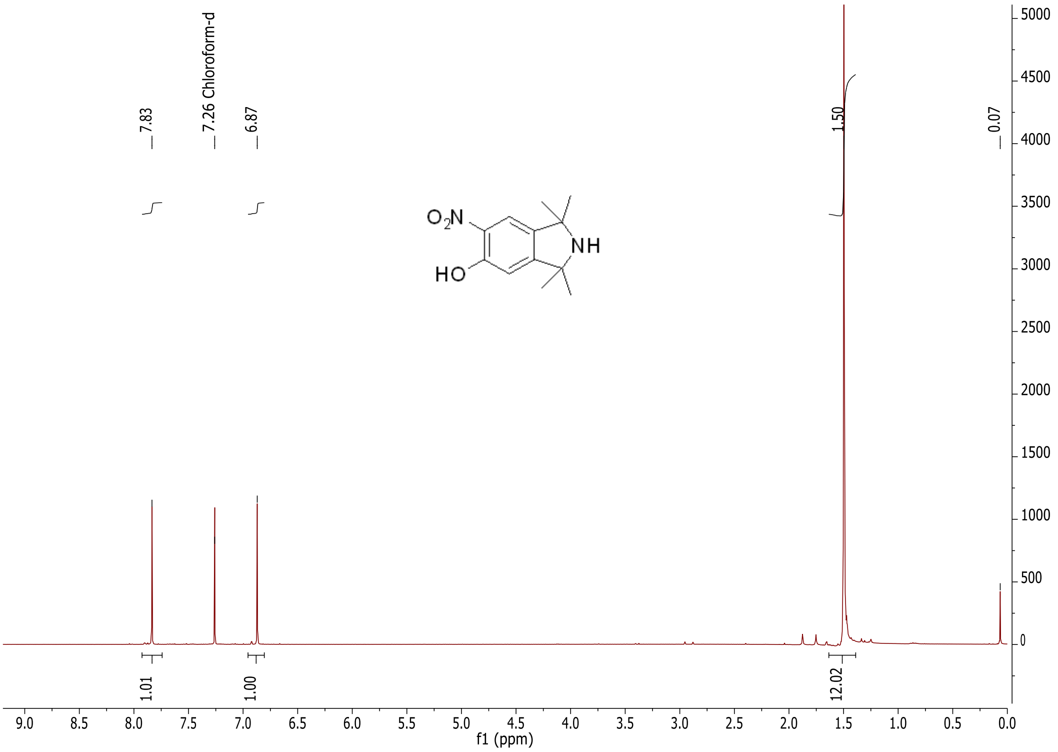

^{13}C-NMR (126 MHz, $CDCl_3$):

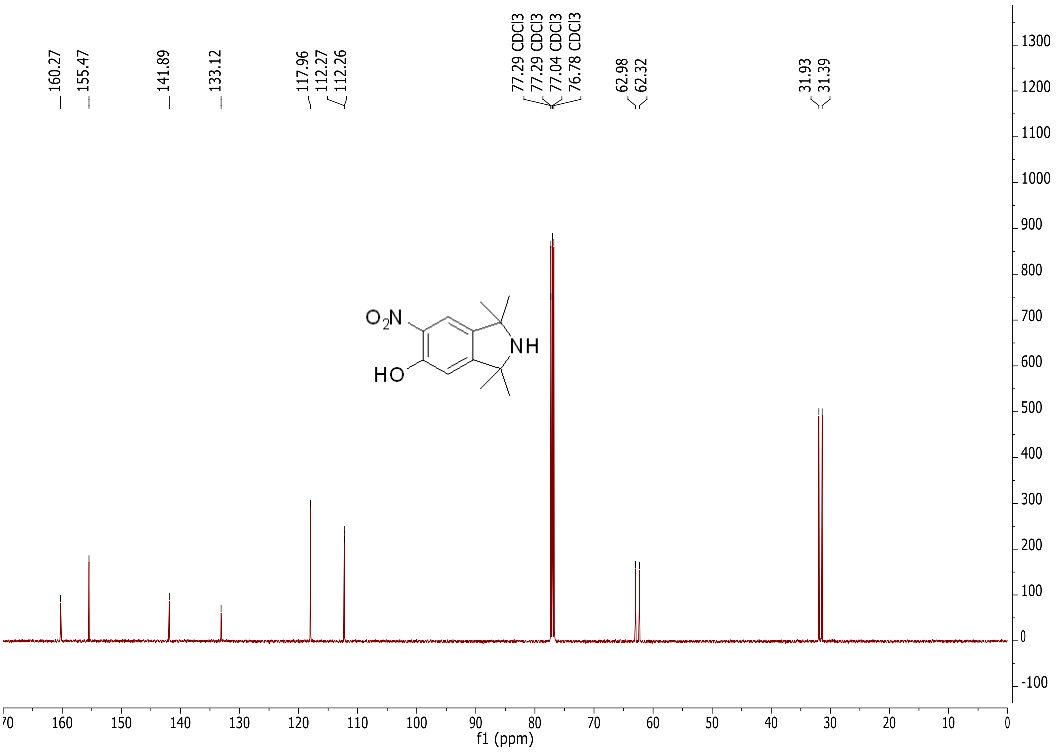

5-Hydroxy-6-amino-1,1,3,3-tetramethylisoindoline (58)

^{1}H-NMR (400 MHz, MeOH-d4):

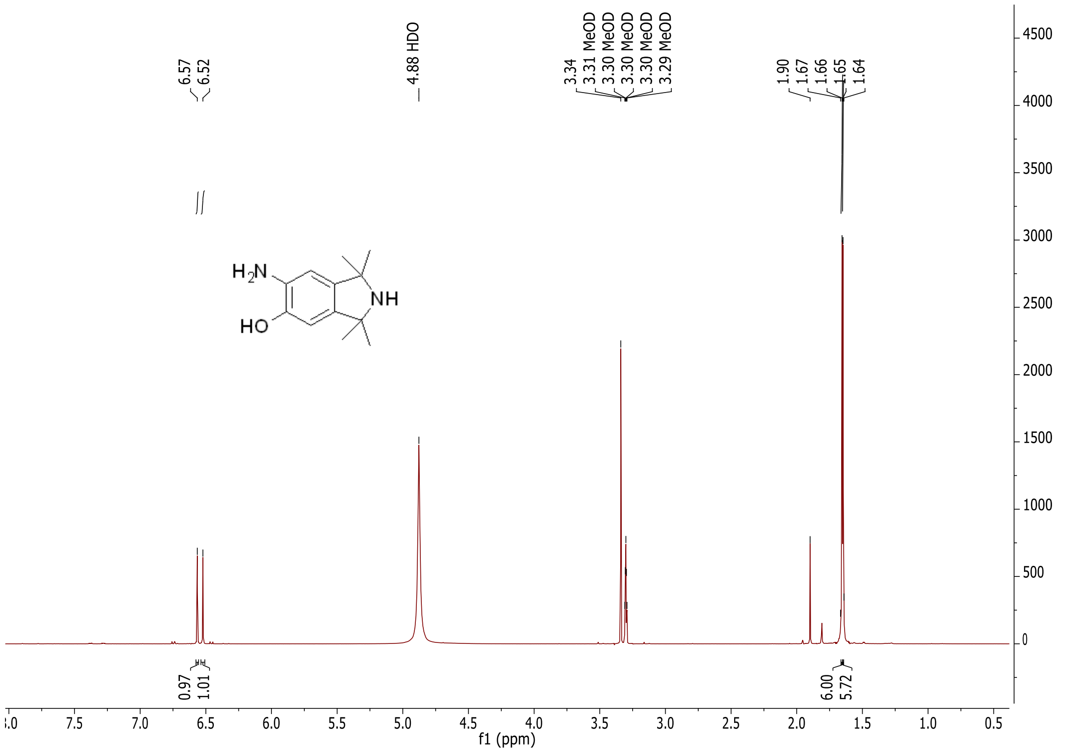

^{13}C-NMR (75.4 MHz, DMSO-d_6):

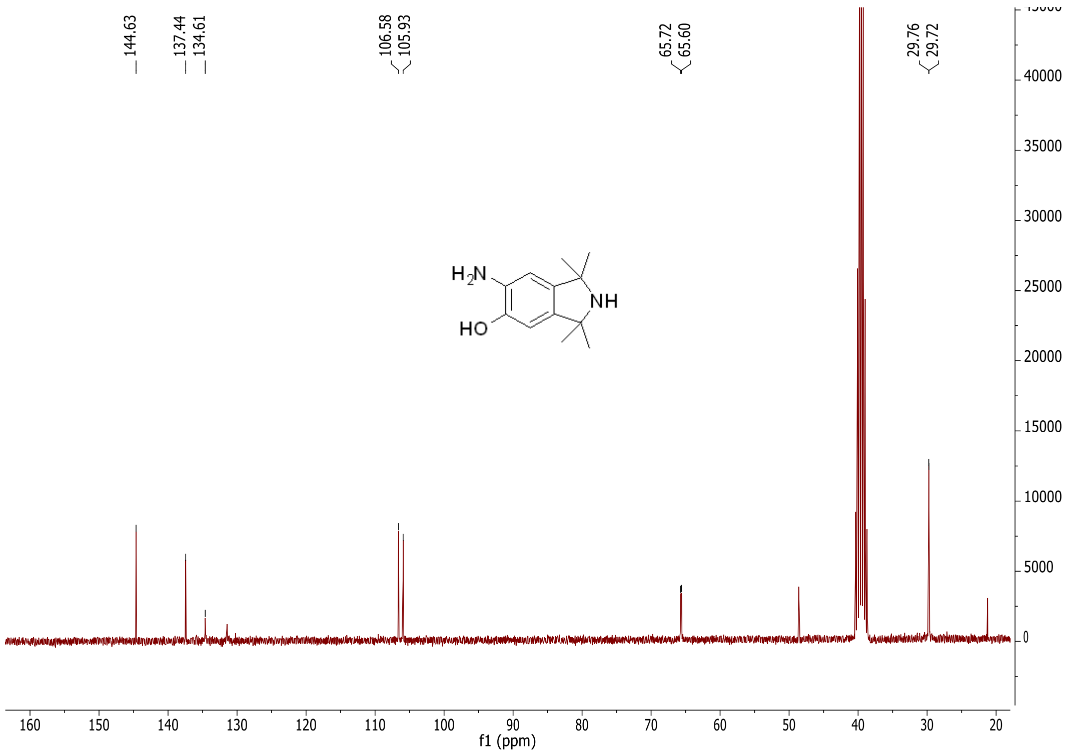

5-Bromo-2’-O-methyluridine (60)

^{1}H-NMR:

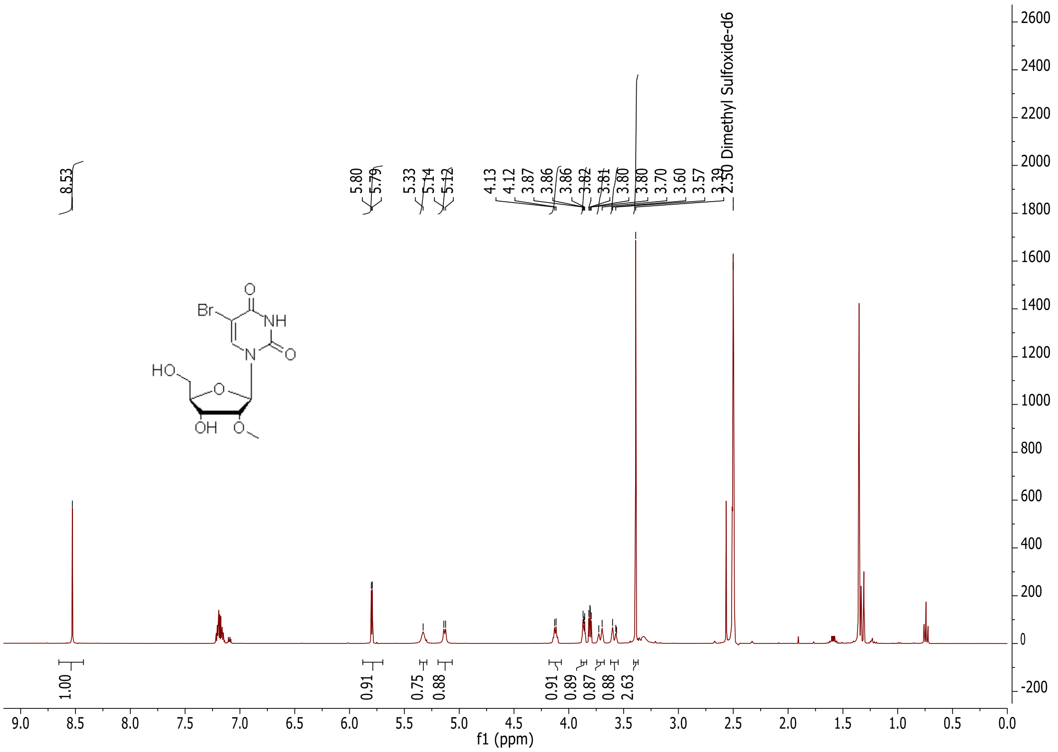

^{13}C-NMR (75.4 MHz, DMSO-d$_6$):

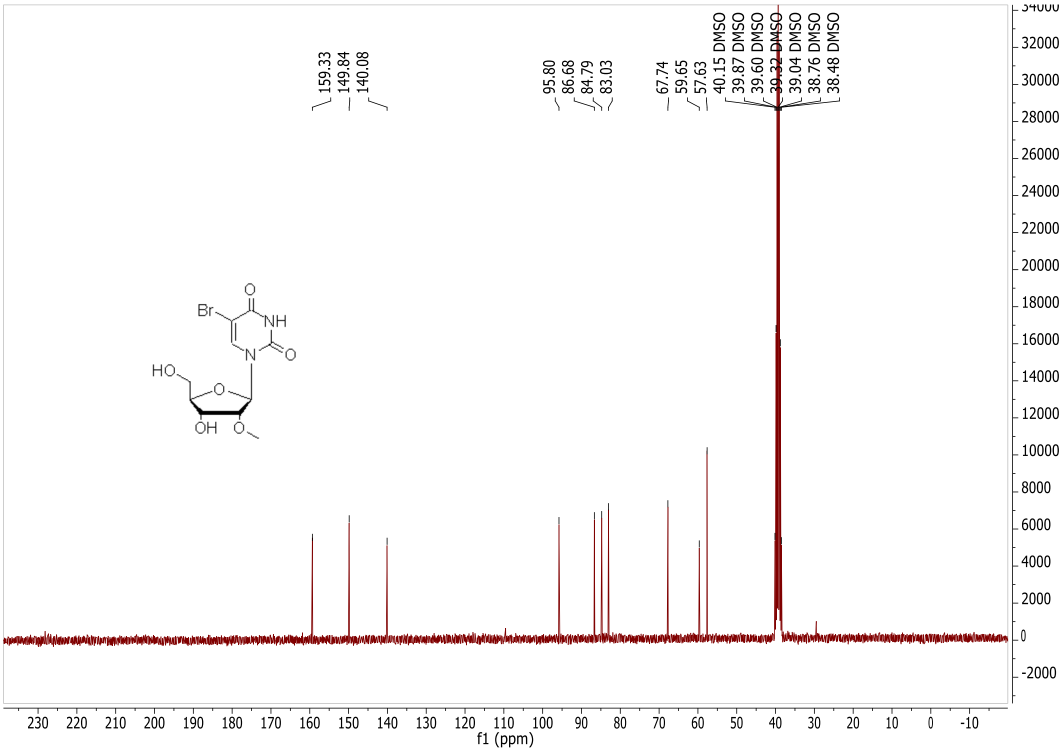

3′,5′-Diacetyl-5-bromo-2′-O-methyluridine (61)

^{1}H-NMR (400 MHz, CDCl$_3$):

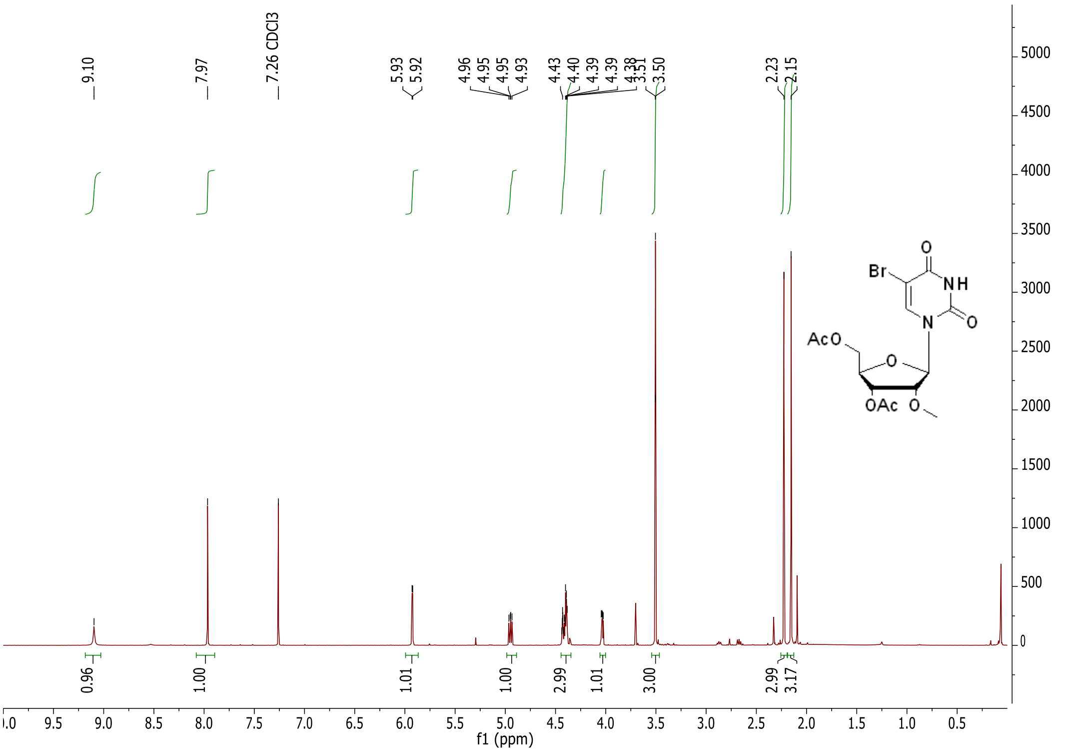

^{13}C-NMR (75.4 MHz, CDCl$_3$):

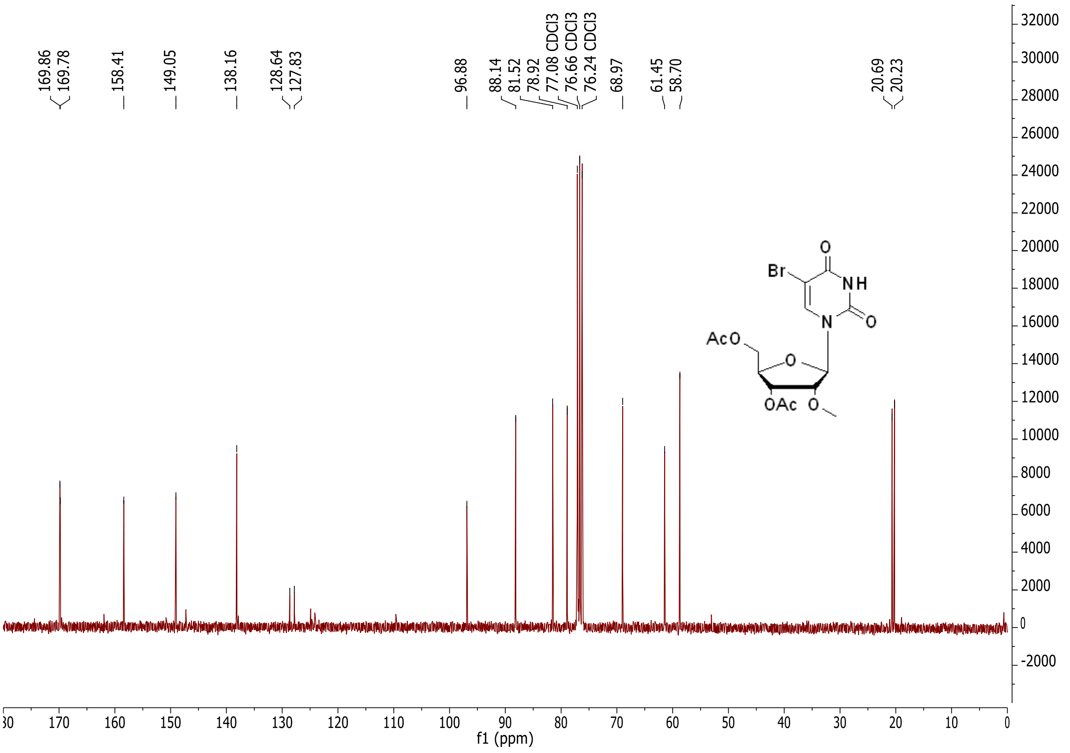

3′,5′-Diacetyl-5-bromo-4-chloro-2′-O-methyluridine (62)

^{1}H-NMR (300 MHz, CDCl$_3$):

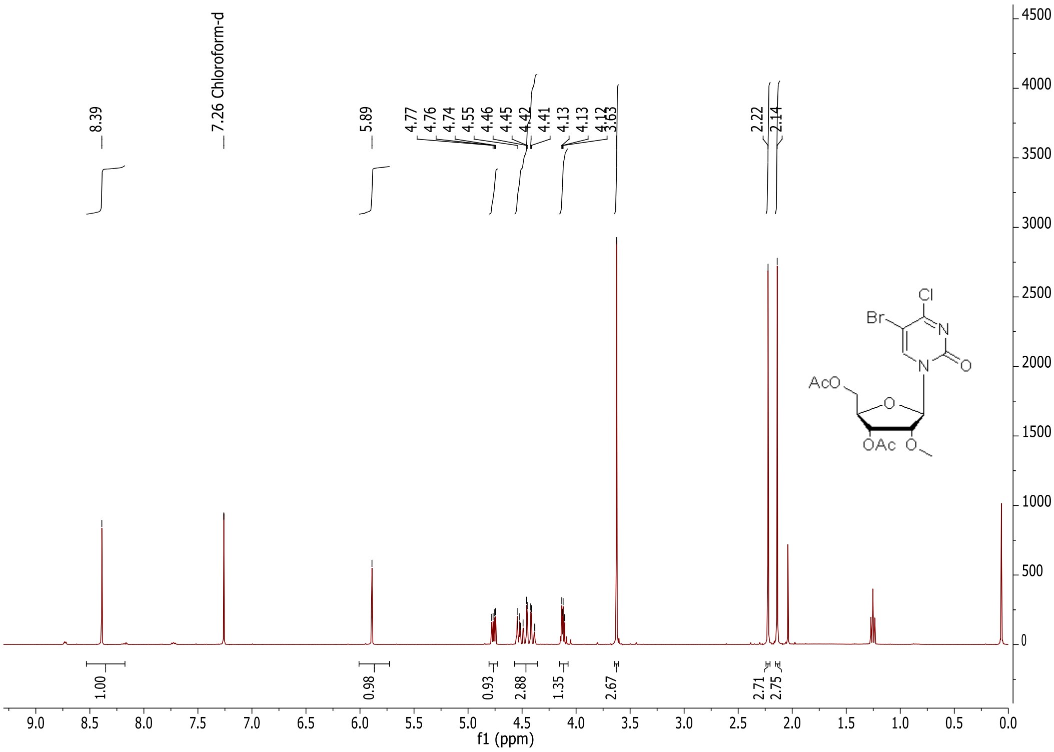

3´,5´-Diacetyl-5-bromo-N$_4$-(6-hydroxy-1,1,3,3-tetramethylisoindolinyl)-2´-O-methylcytidine (63)

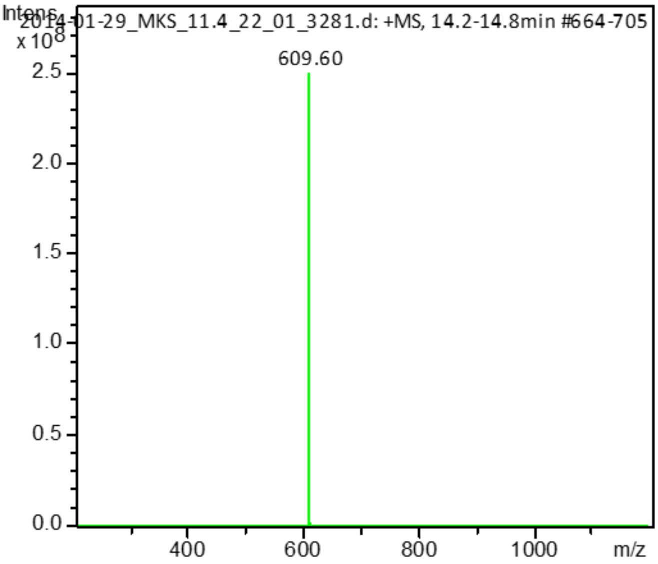

Phenoxazine derived nucleoside (64)

^{1}H-NMR (500 MHz, MeOH-d4):

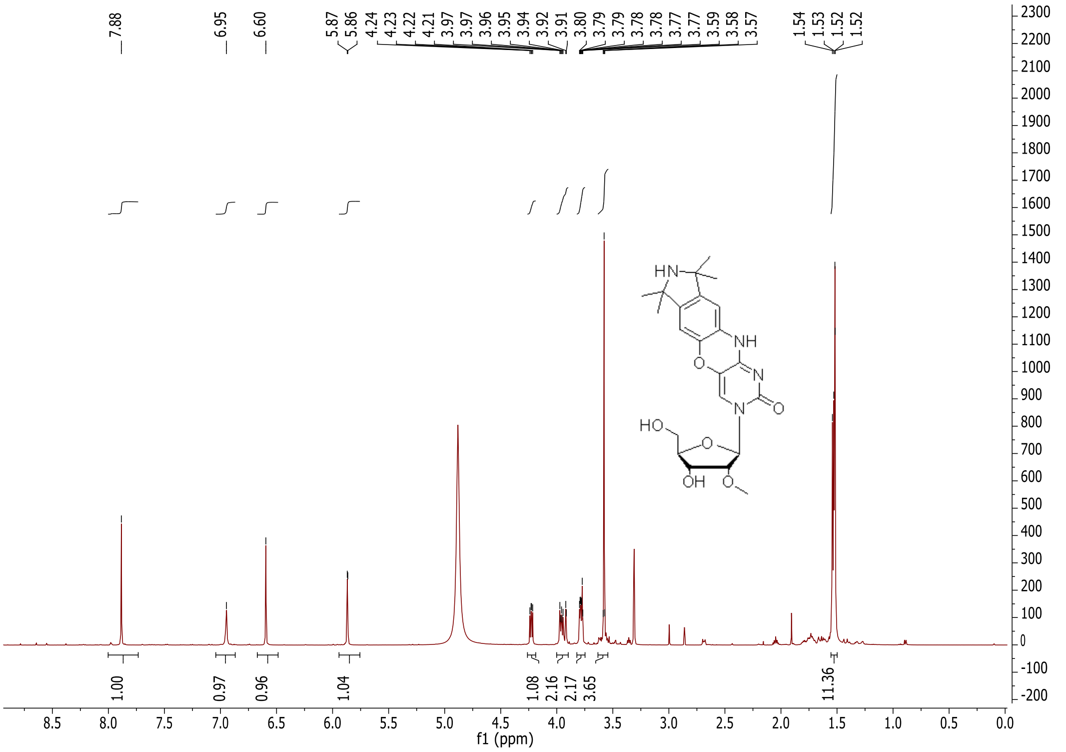

^{13}C-NMR(126 MHz, MeOH-d4):

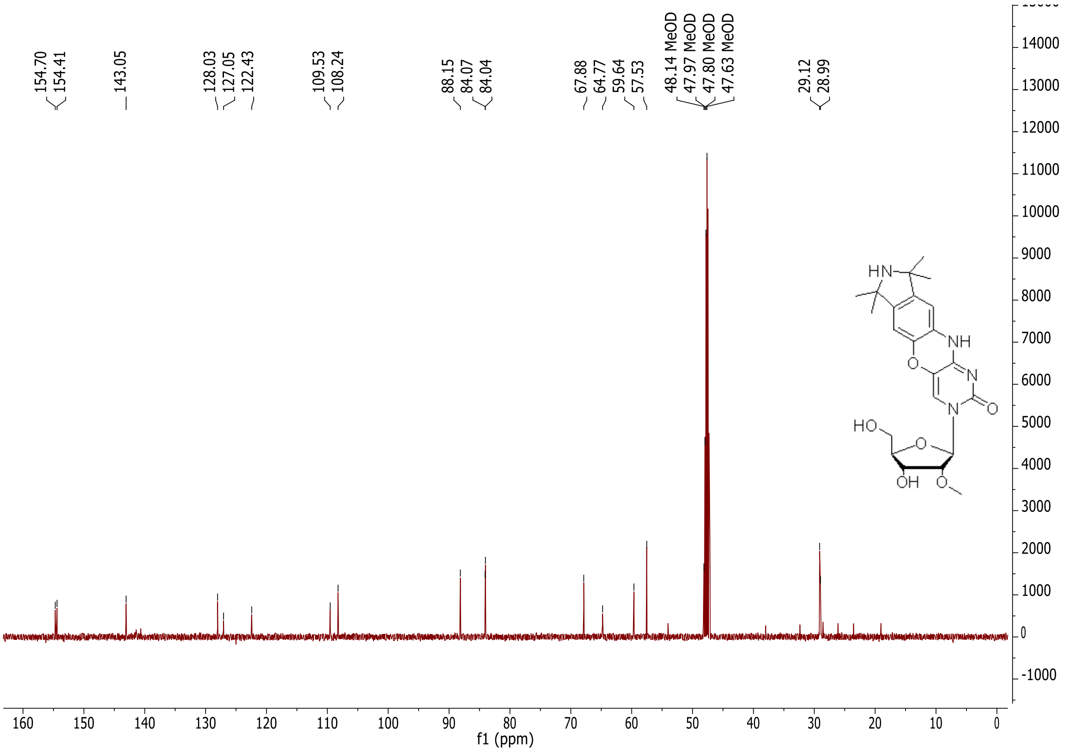

Spin-labeled nucleoside (Çm) (65)

^{1}H-NMR (500 MHz, DMSO-d$_6$):

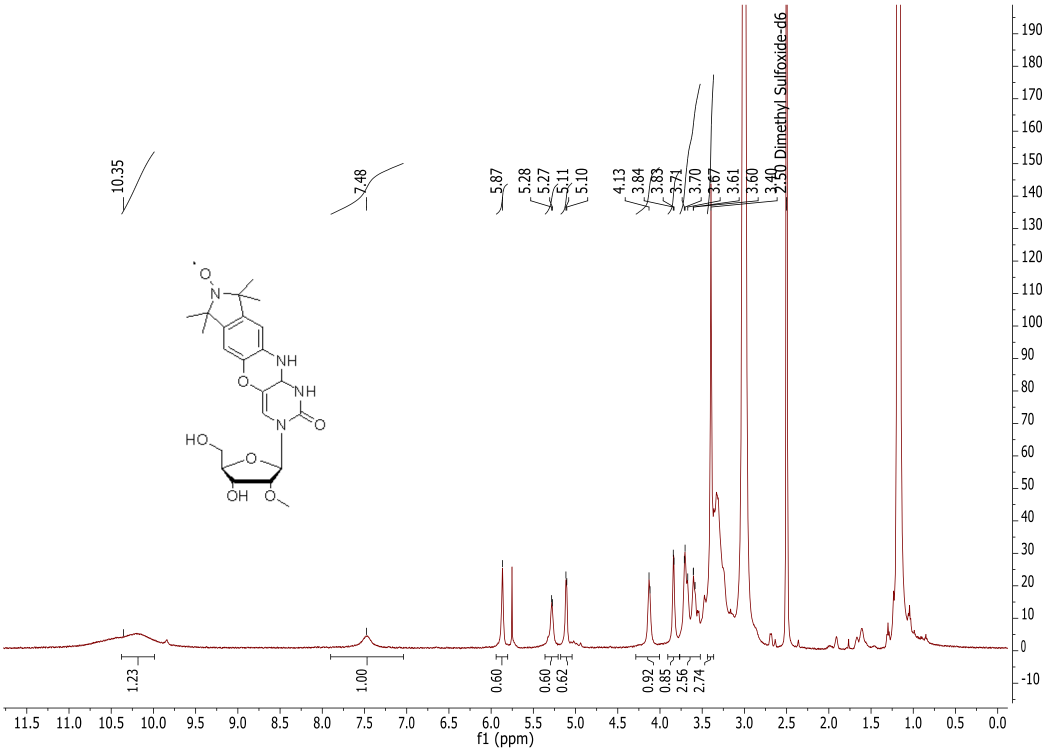

5’-Dimethoxytritylated, spin-labeled nucleoside Çm (66)

^{1}H-NMR (500 MHz, DMSO-d$_6$):

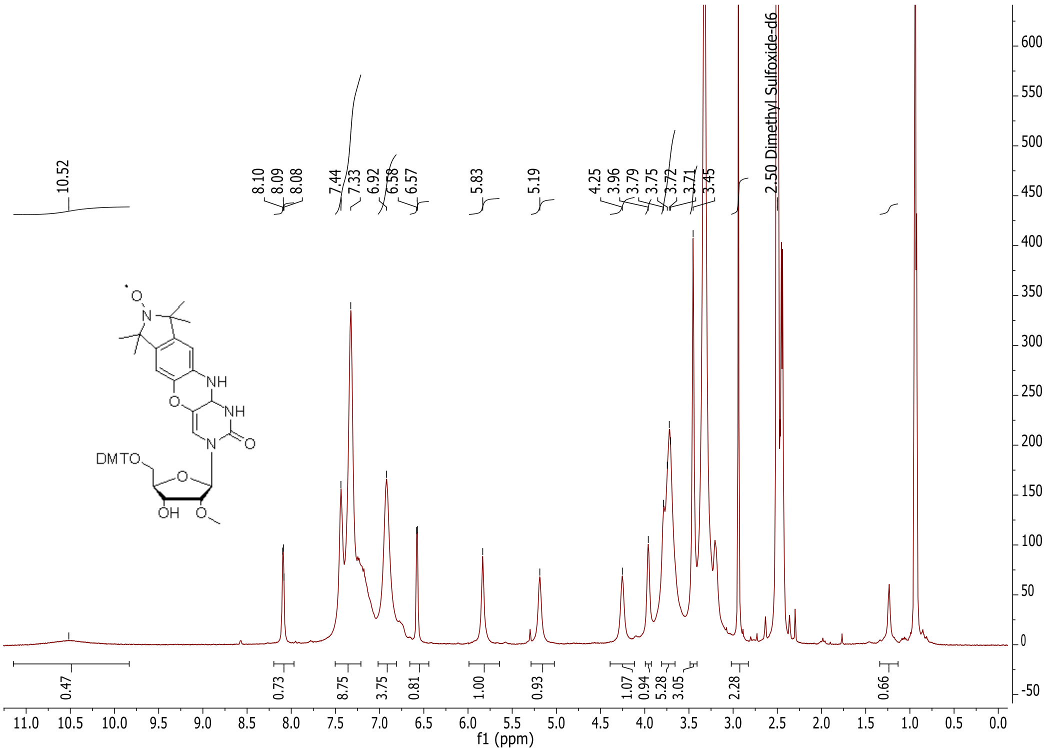

Spin-labeled phosphoramidite (Çm)

^{1}H-NMR (400 MHz, DMSO-d$_6$):

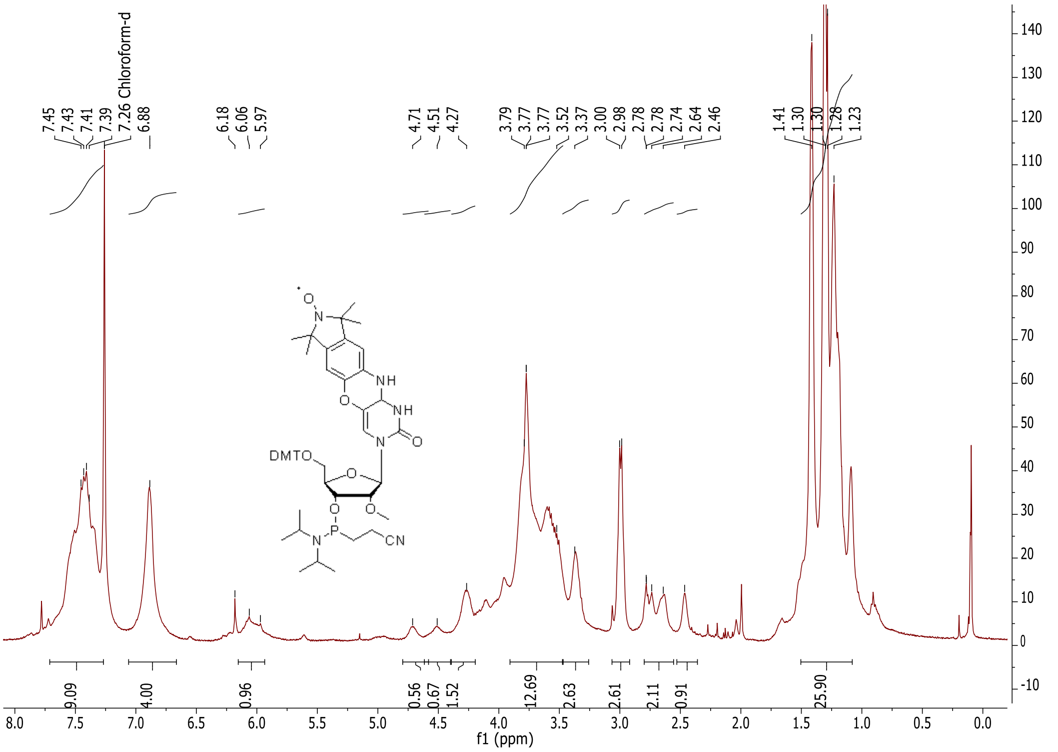

^{31}P-NMR (162 MHz, CDCl3):

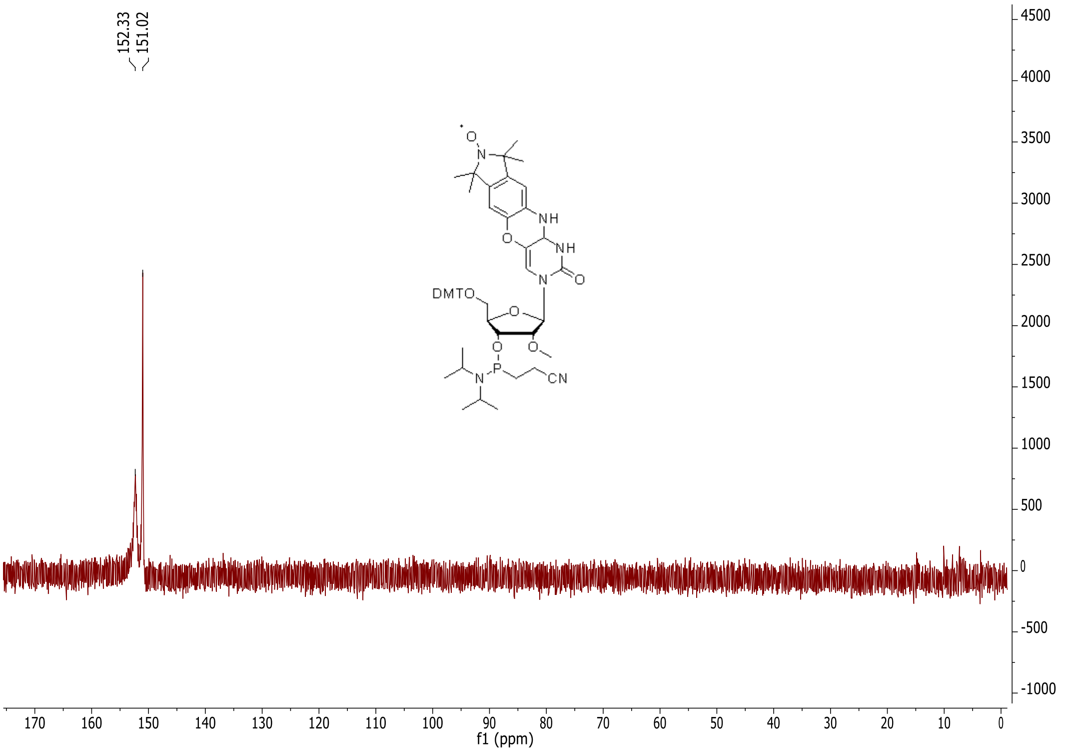

5-Iodo-2‘-O-methyluridine (68)

^{1}H-NMR (500 MHz, DMSO-d$_6$):

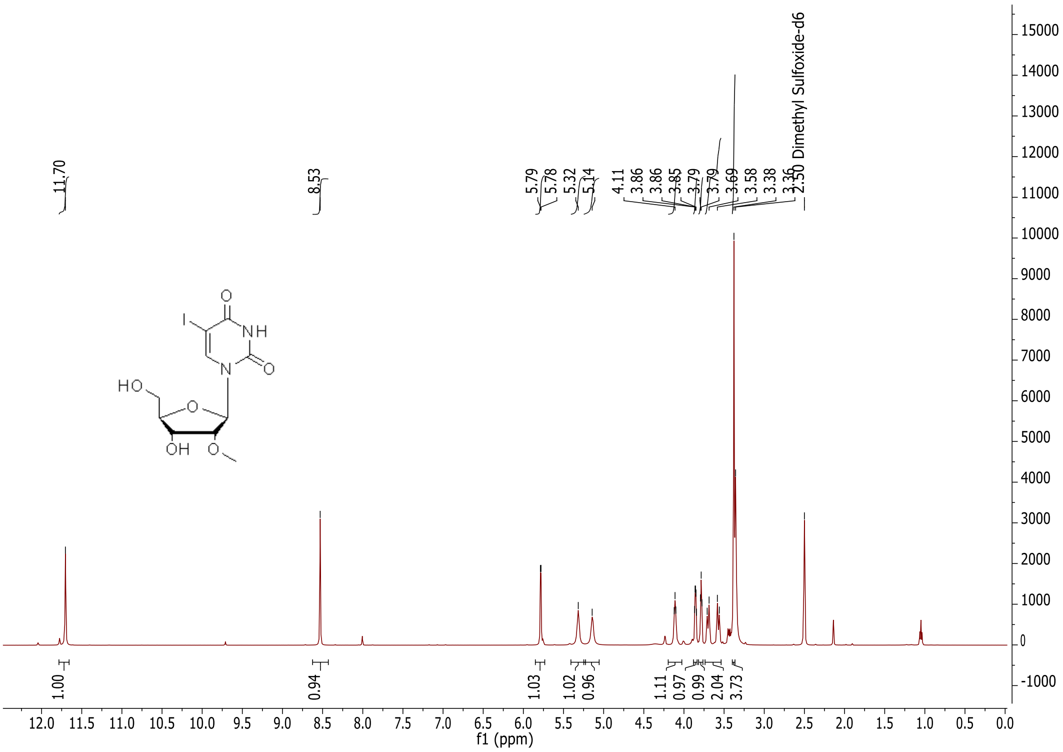

^{13}C-NMR (126 MHz, DMSO-d$_6$):

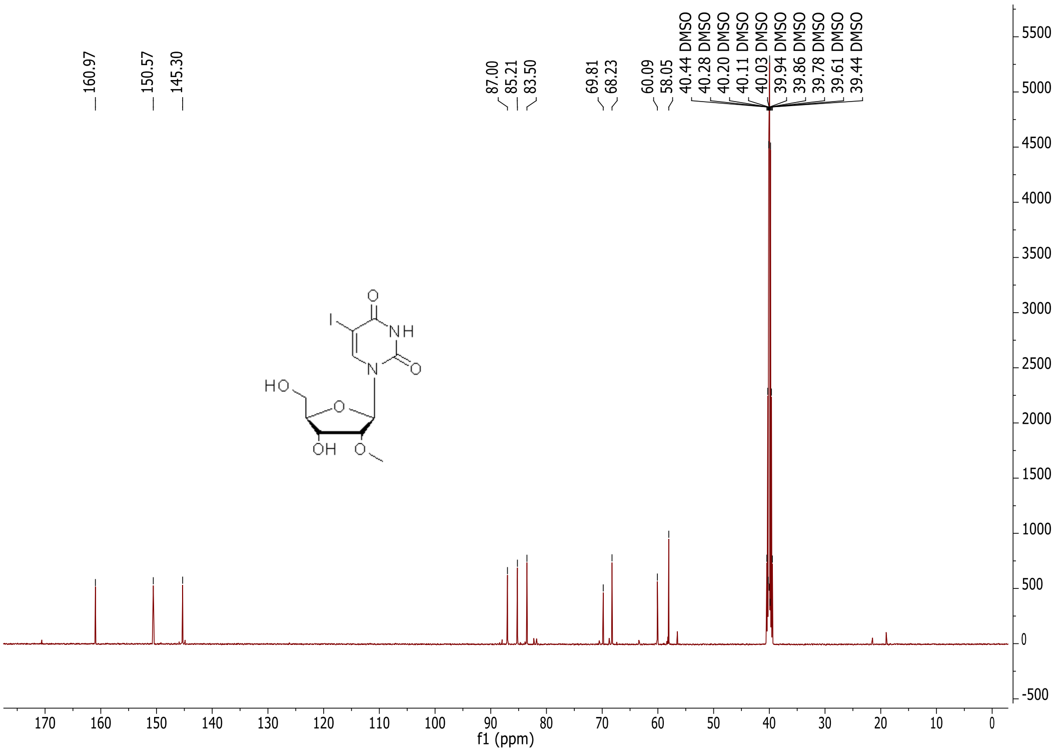

5-(Trimethylsilylethynyl)-2‘-O-methyluridine (69)

^{1}H-NMR (400 MHz, DMSO-d$_6$):

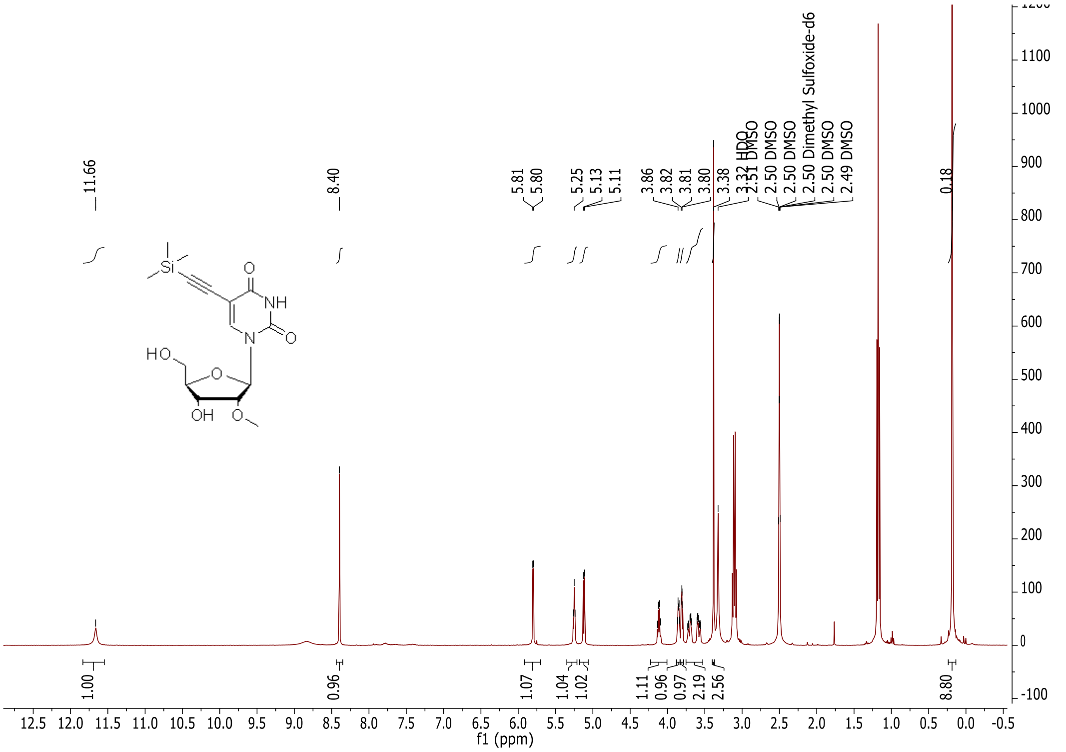

^{13}C-NMR (100.6 MHz, DMSO-d$_6$):

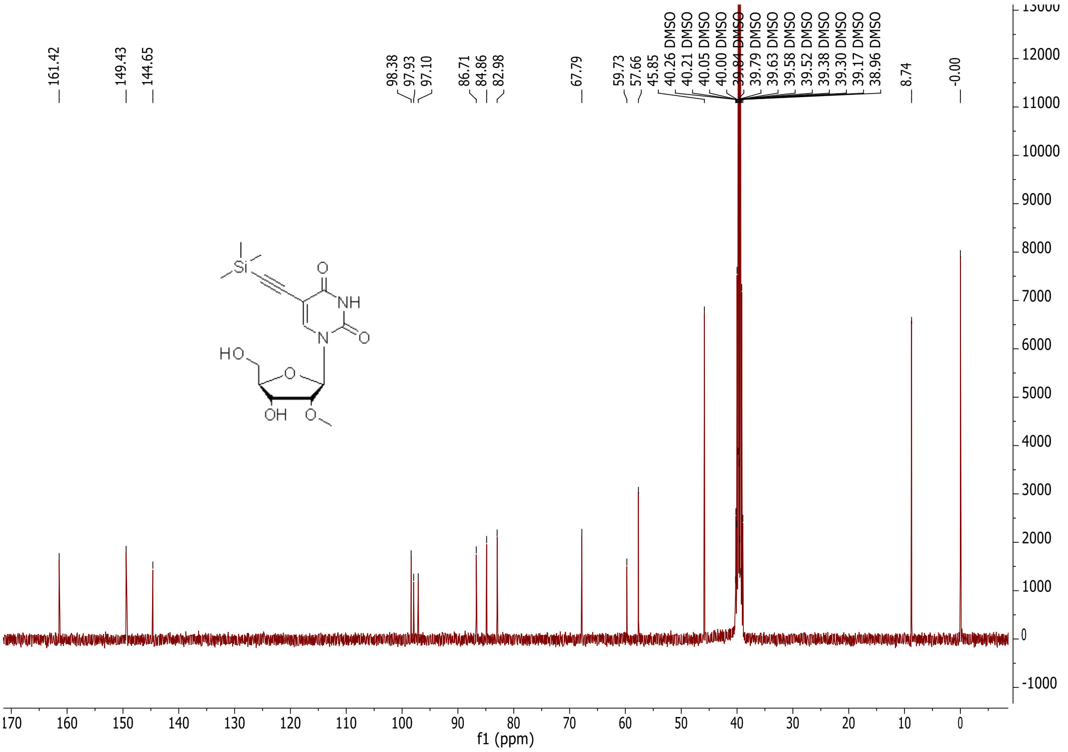

5-Ethynyl-2‘-O-methyluridine (70)

^{1}H-NMR (500 MHz, DMSO-d$_6$):

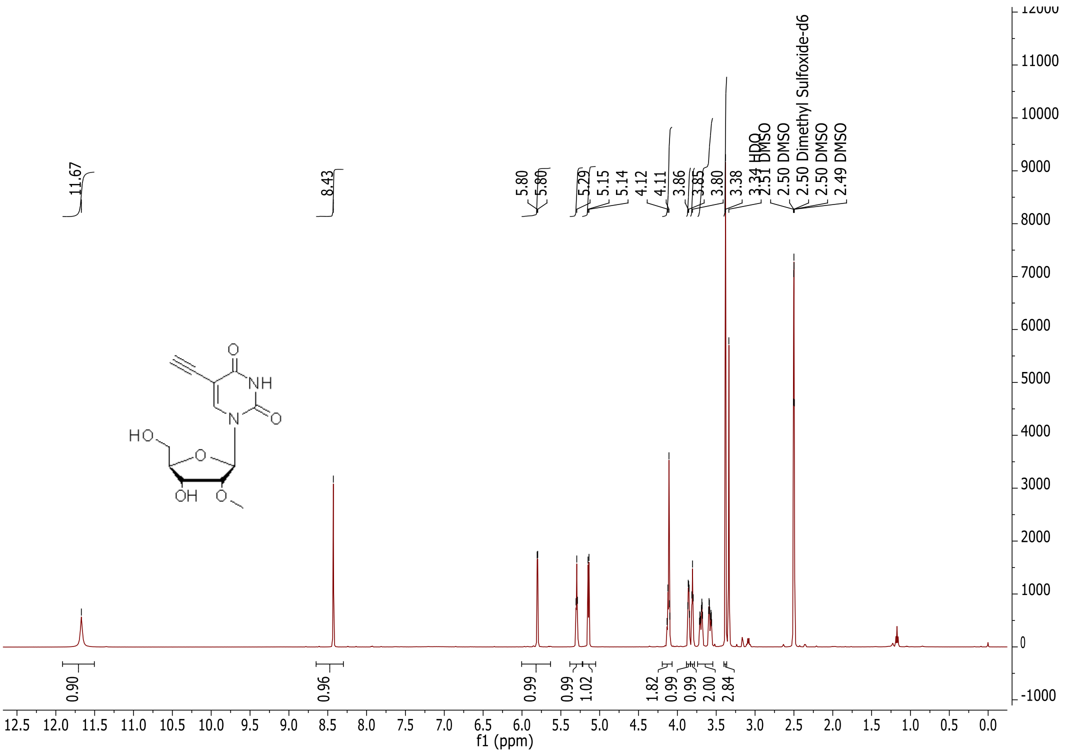

^{13}C-NMR (126 MHz, DMSO-d$_6$):

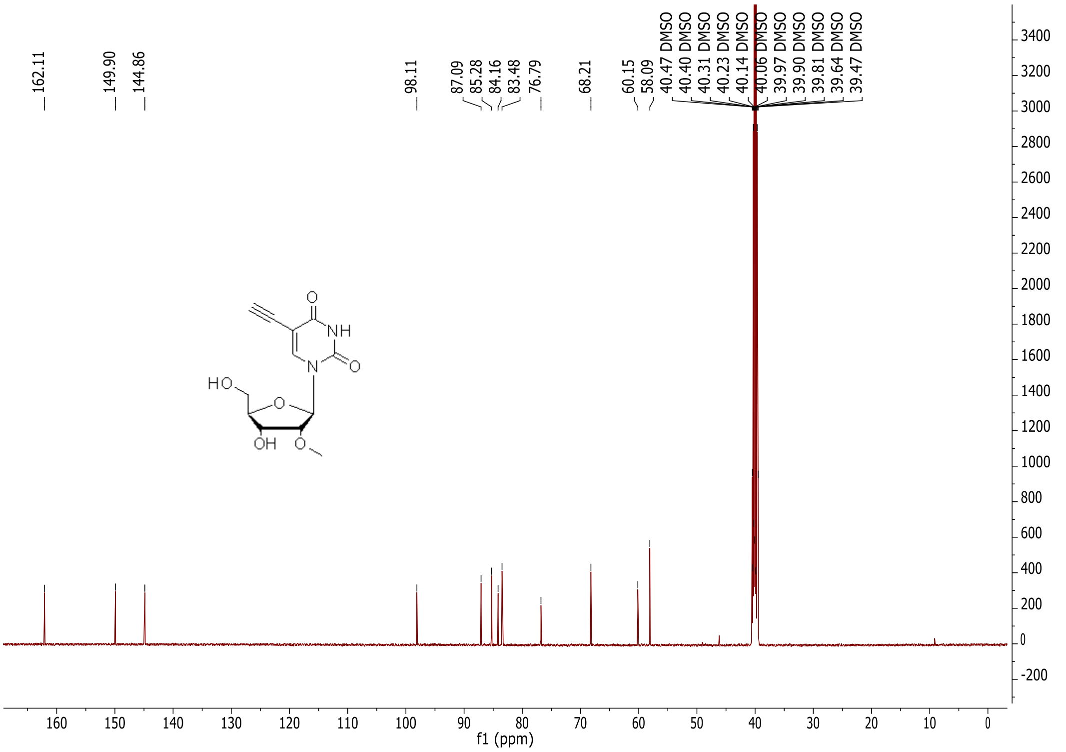

5’-O-Dimethoxytrityl-5-ethinyl-2’-O-methyluridine (71)

^{1}H-NMR (500 MHz, DMSO-d$_6$):

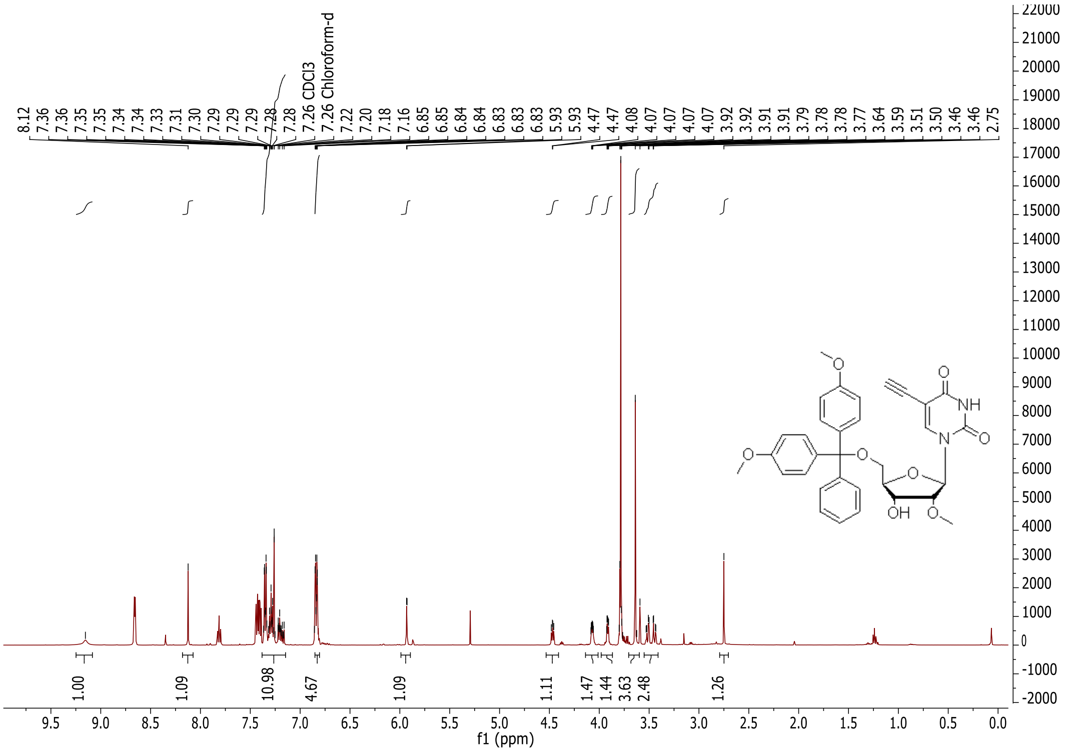

^{13}C-NMR (126 MHz, DMSO-d$_6$):

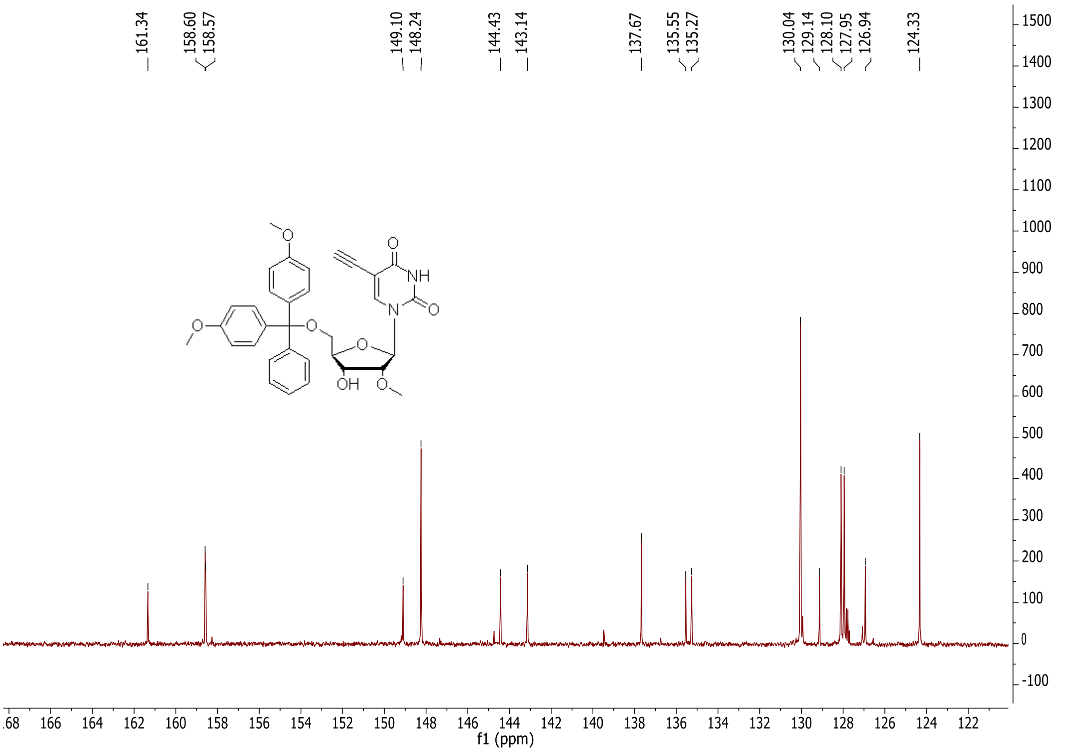

5’-O-Dimethoxytrityl-5-(1,1,3,3-tetramethyl-5-(4H-1,2,3-triazol-4-yl)-isoindolin-1-yloxyl)-2’-O-methyluridine (72)

^{1}H-NMR (500 MHz, $CDCl_3$):

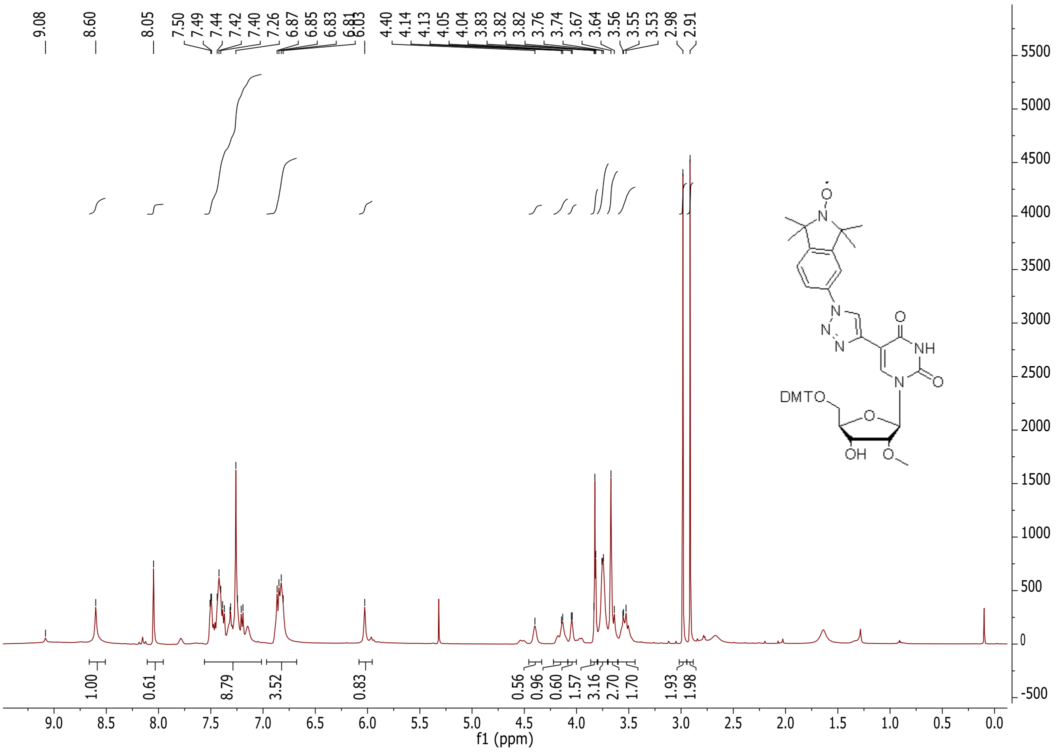

^{13}C-NMR (126 MHz, $CDCl_3$):

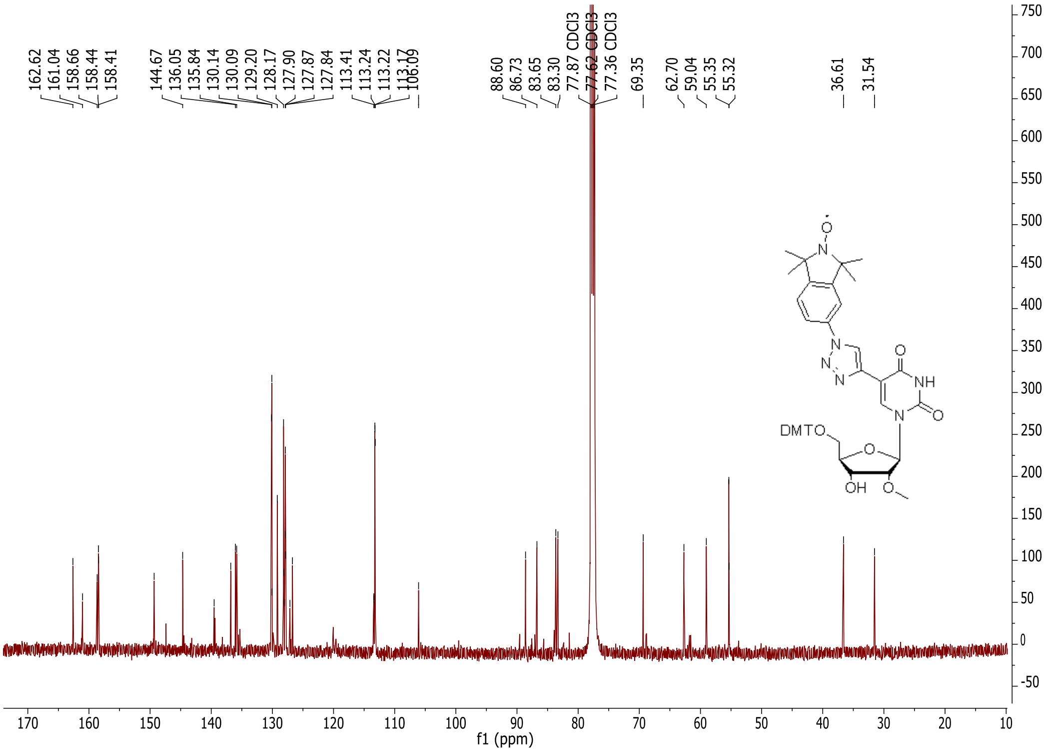

3’-O-[(2-Cyanoethyl)(N,N-diisopropylamino)phosphinyl]-5’-O-dimethoxytrityl-5-(1,1,3,3-tetramethyl-5-(4H-1,2,3-triazol-4-yl)-isoindolin-1-yloxyl)-2’-O-methyluridine (Ųm)

^{1}H-NMR (400 MHz, CDCl$_3$):

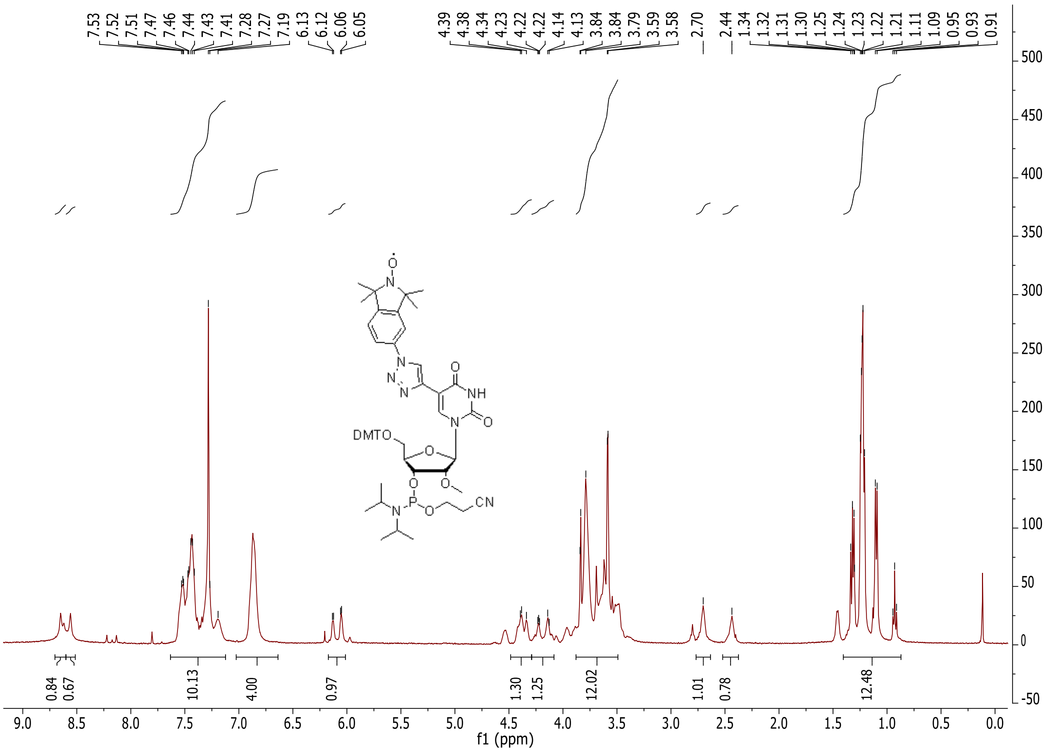

^{31}P-NMR (162 MHz, CDCl$_3$):

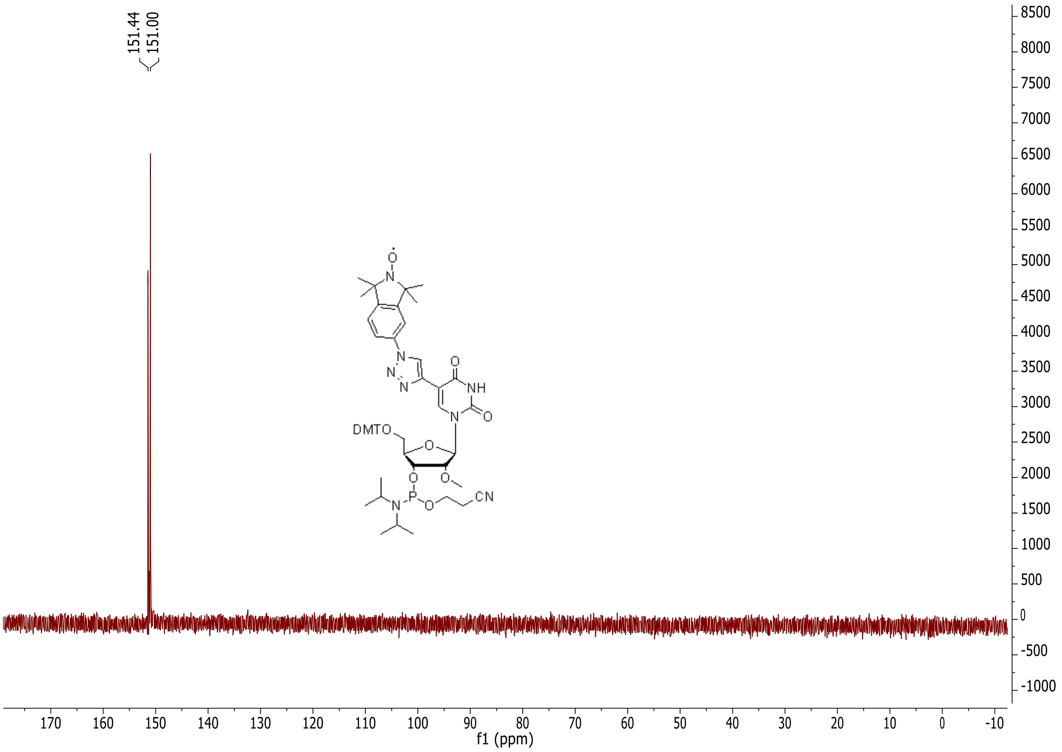

5’-O-Dimethoxytrityl-N$_4$-Acetyl-5-(1,1,3,3-tetramethyl-5-(4H-1,2,3-triazol-4-yl)-isoindolin-1-yloxyl)-2’-O-methylcytidine (74)

^{1}H-NMR (500 MHz, CDCl$_3$):

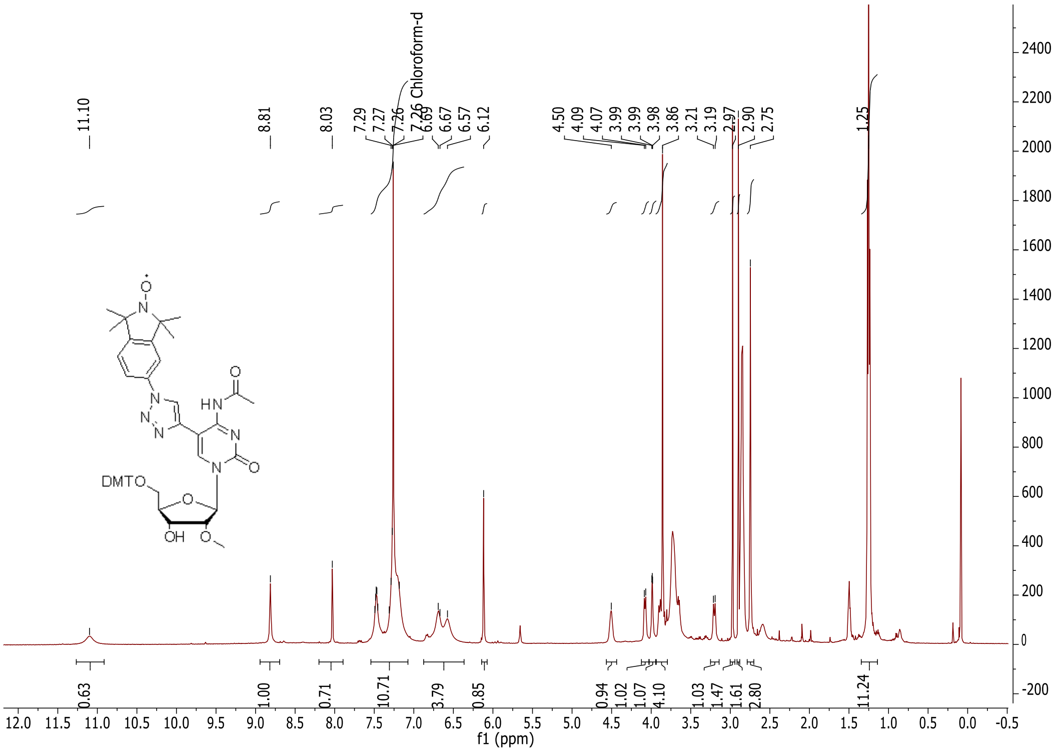

3’-O-[(2-Cyanoethyl)(N,N-diisopropylamino)phosphinyl]-5’- O-dimethoxytrityl-N$_4$-Acetyl-5-(1,1,3,3-tetramethyl-5-(4H-1,2,3-triazol-4-yl)-isoindolin-1-yloxyl)-2’-O-methylcytidine (Çm)

^{1}H-NMR (500 MHz, CDCl$_3$):

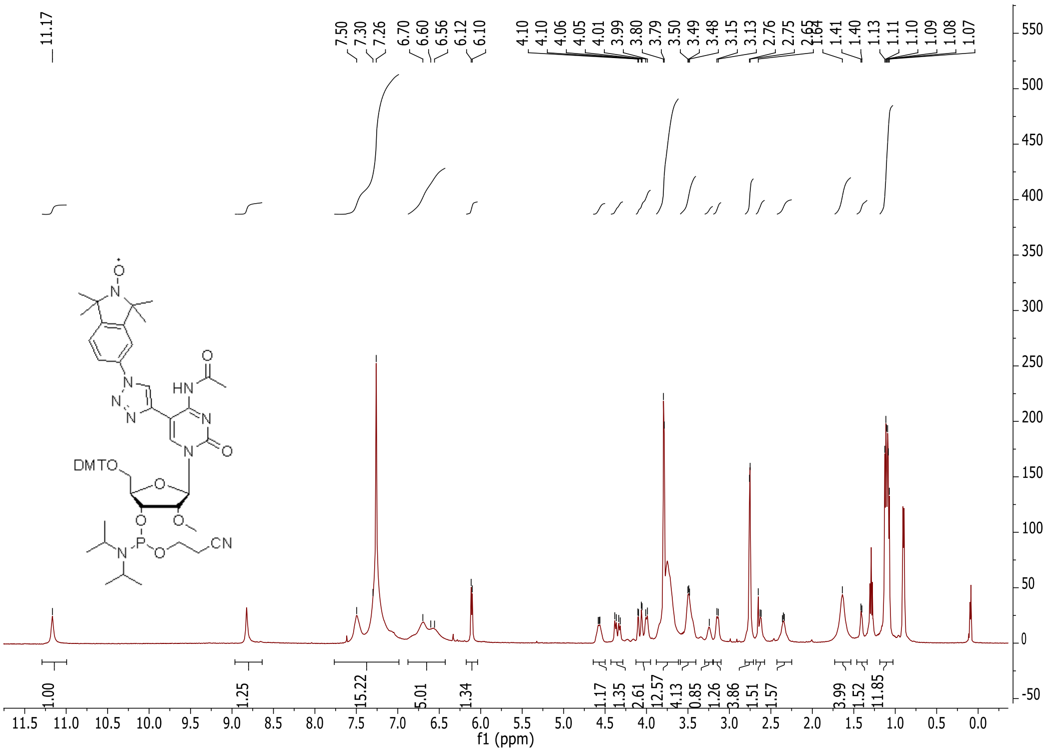

^{31}P-NMR (202.4 MHz, $CDCl_3$):

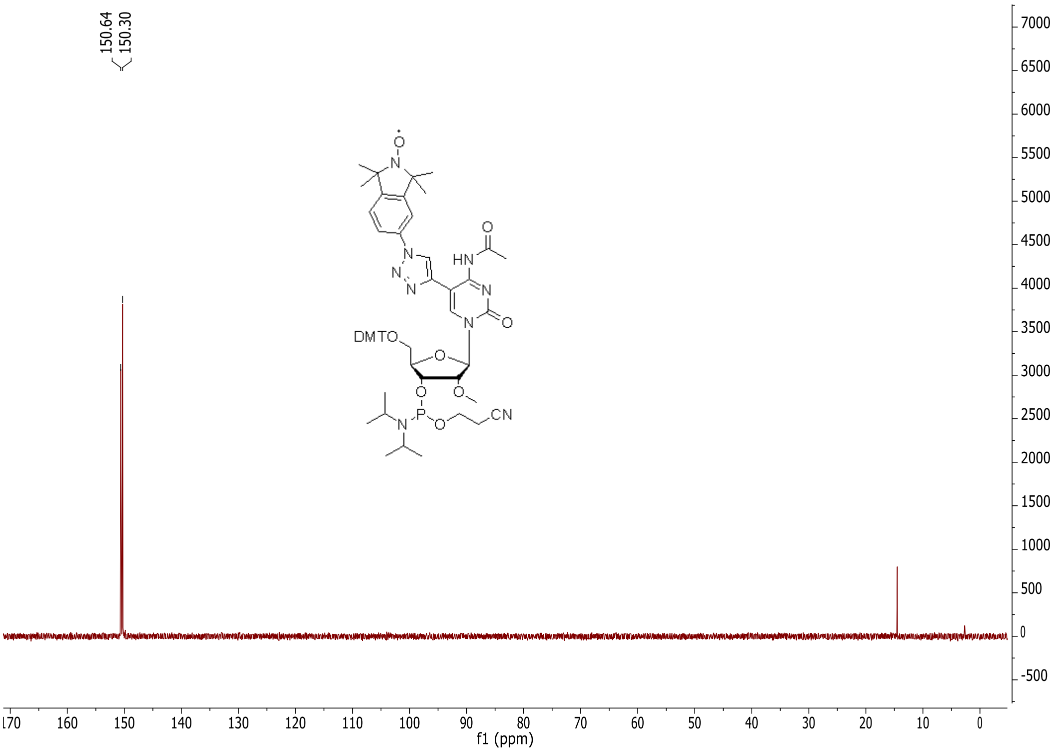

N-Isopropyl-2-propanaminium tetrazol-1-ide

^{1}H-NMR (600 MHz, CD_2Cl_2):

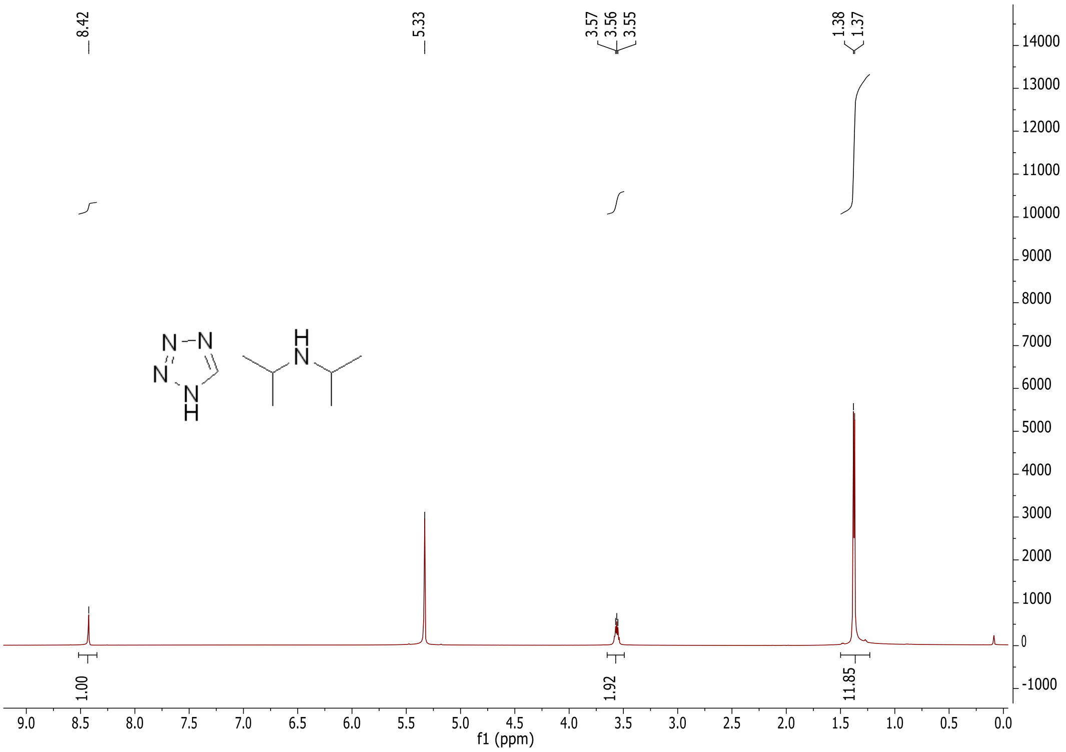

^{13}C-NMR (151 MHz, CD_2Cl_2):

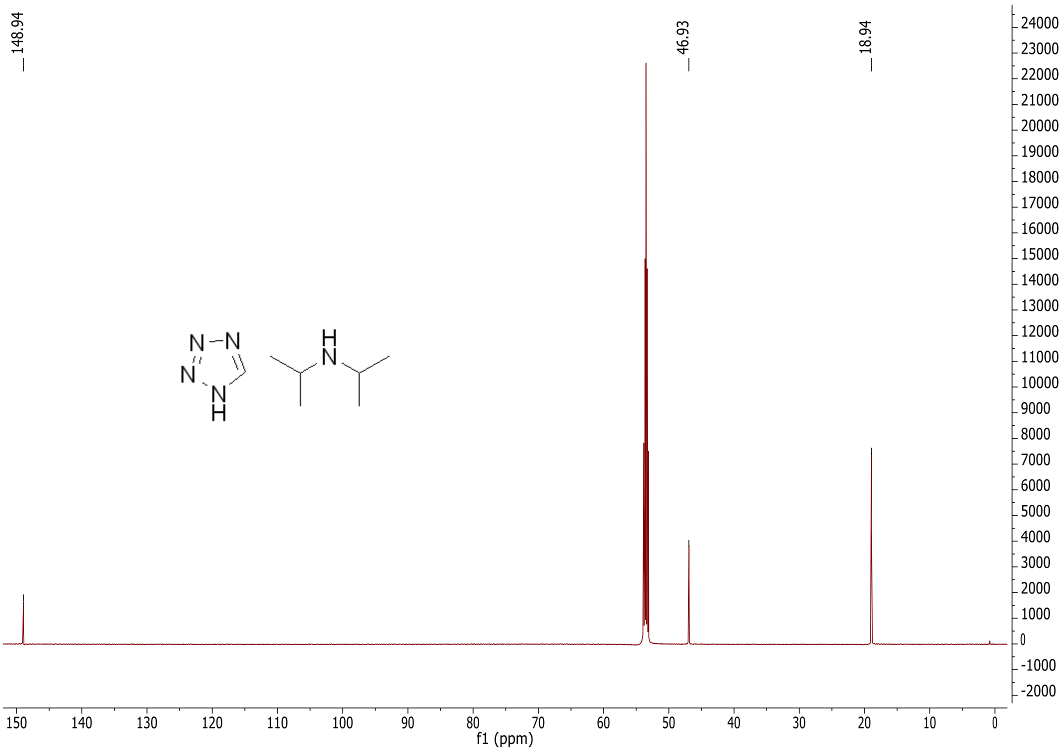

Imidazole-1-sulfonyl azide

^{1}H-NMR (400 MHz, D_2O):

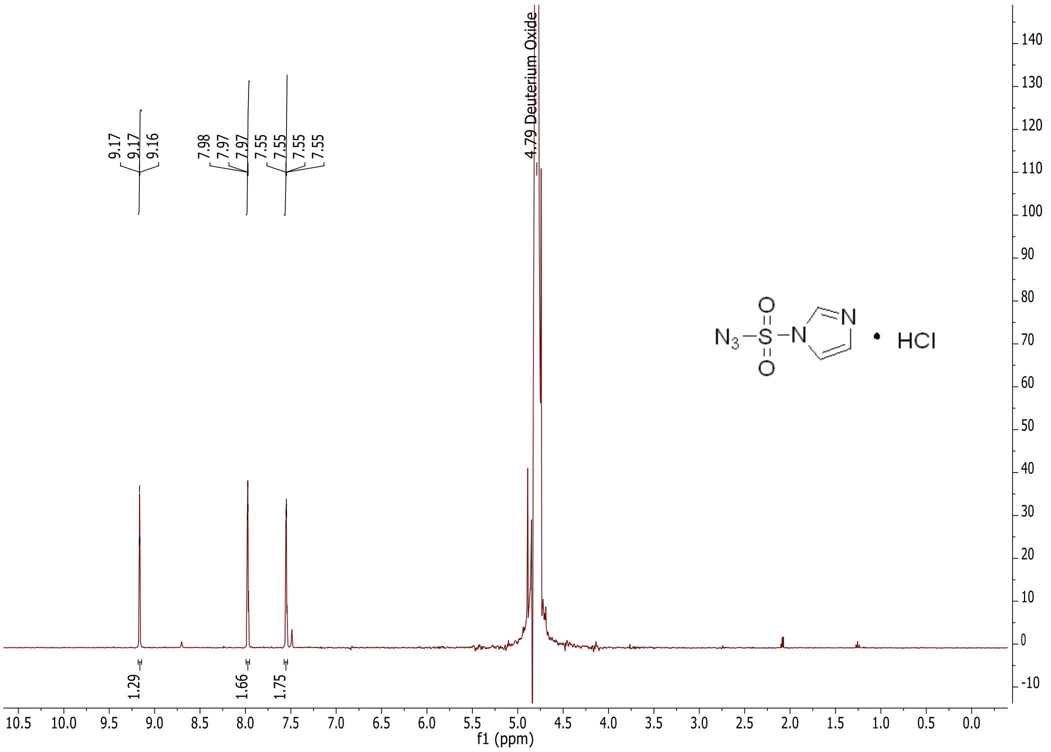

^{13}C-NMR (100.6 MHz, D_2O):

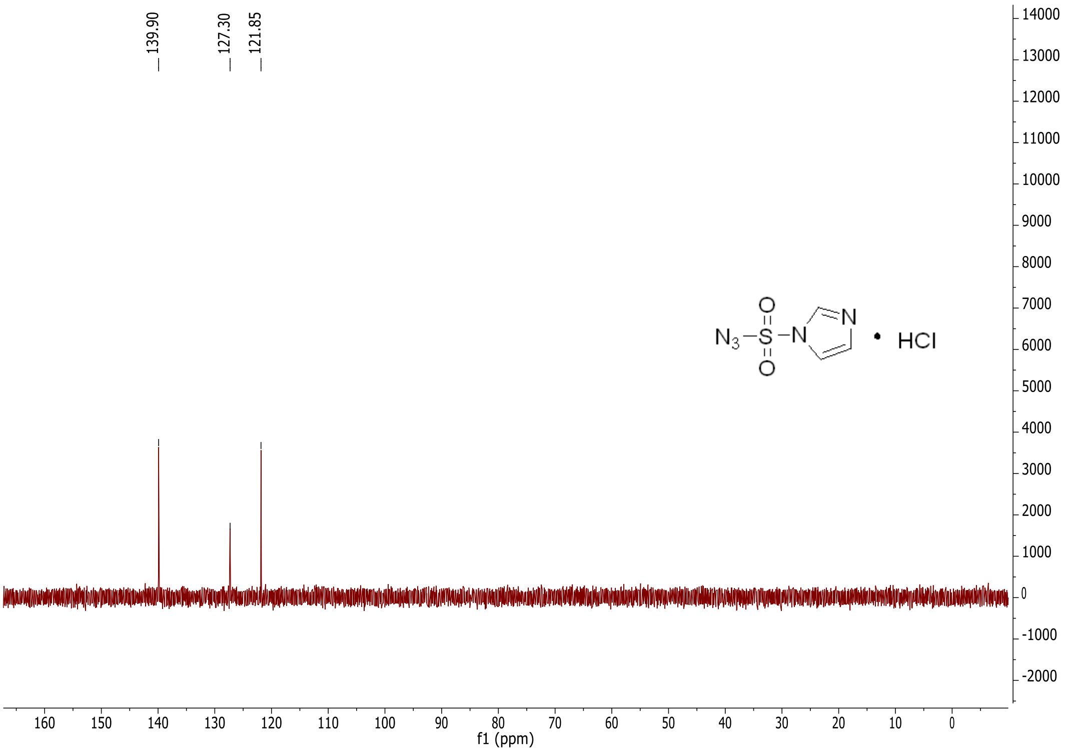

6.2 Melting denaturation experiments

Duplexes

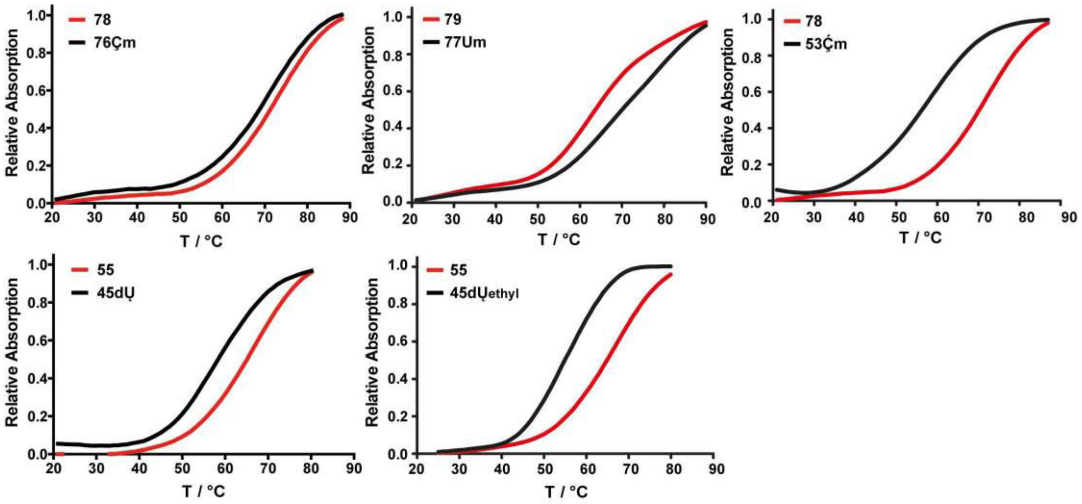

Figure 70: Melting curves of spin-labeled duplexes compared to their non-modified counterparts.

PreQ1 aptamer domain

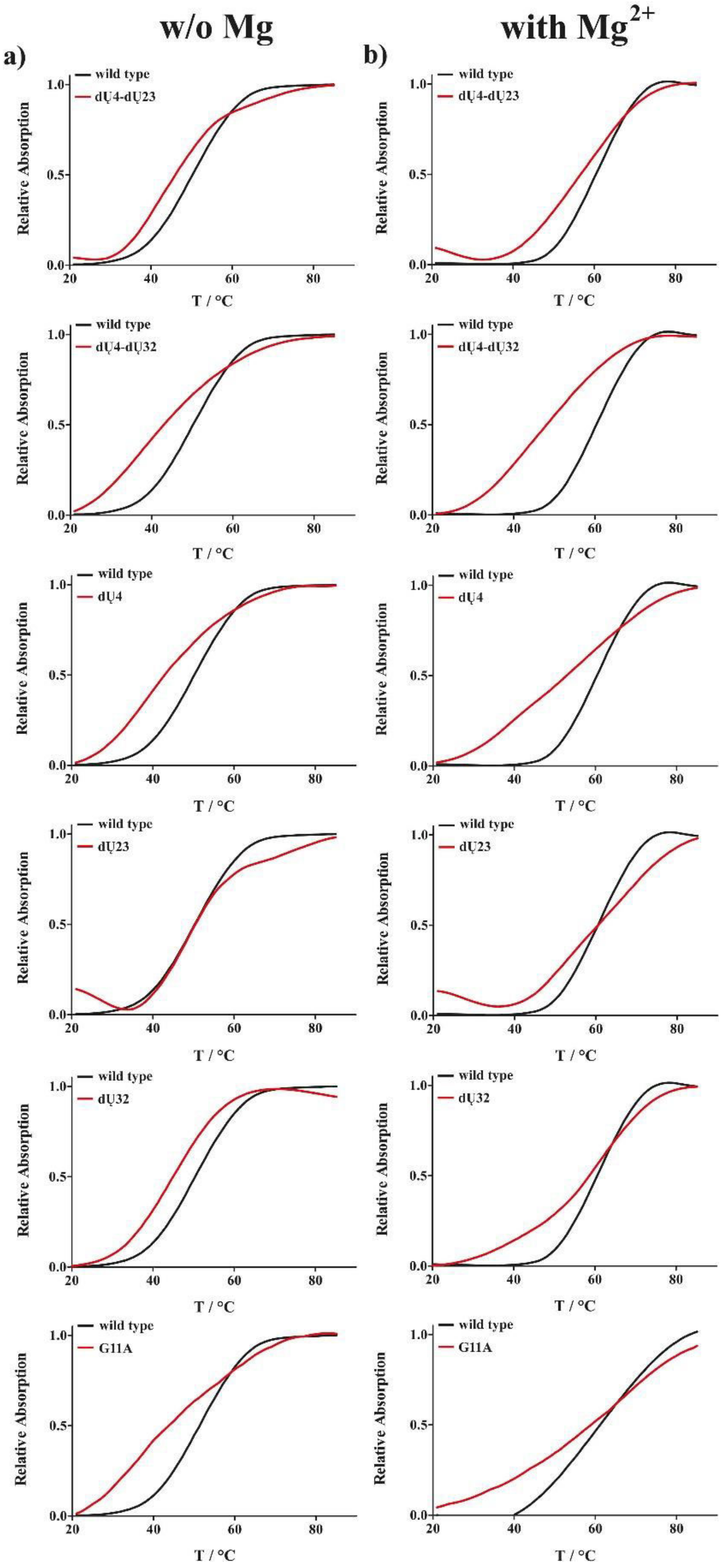

Figure 71: Melting curves of preQ1 mutants (red) compared to preQ1 wild type (black) without Mg a) and with Mg^{2+} b). Conditions: C_{RNA} = 1µM, C_{Mg2+} = 2 mM.

Table 17: Absolute Tm values for preQ1 wild type aptamer domain and its spin-labeled mutants derived from the melting curves (Figure 71).

preQ constructs	**ΔT_m [°C] w/o Mg^{2+}**	**ΔT_m [°C] with Mg^{2+}**
dŲ4	42.3 ± 0.3	54.5 ± 1.5
dŲ23	47.8 ±0.3	63.0 ± 1.0
dŲ32	45.2 ± 0.4	60.8 ± 1.8
dŲ4-dŲ23	48.5 ±1.0	56.5 ±1.5
dŲ4-dŲ32	40.5 ± 2.0	46.5 ± 1.5
dŲ4-dŲ32 (G11A)	47.3 ± 1.4	61.7 ±0.9
preQ1 **wild type**	50.5 ± 0.5	59.8 ±0.3

TPP aptamer domain

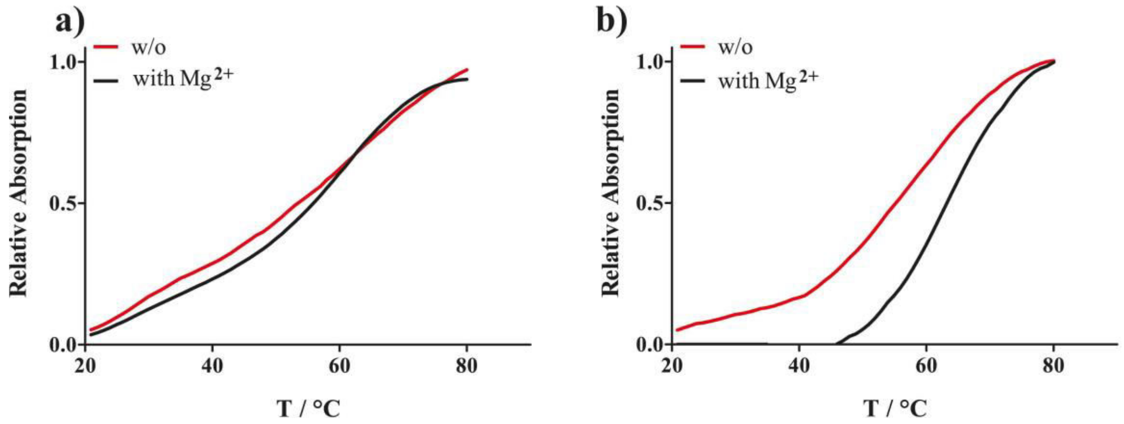

Figure 72: Melting curves of a) TPP wild type aptamer domain and b) spin-labeled TPP aptamer domain in the absence (black) and presence (red) of Mg^{2+}. Conditions: C_{RNA} = 1µM, C_{Mg2+} = 2 mM.

Table 18: Absolute Tm values for TPP wild type aptamer domain and its double-labeled mutant derived from the melting curves (Figure 72).

TPP constructs	**ΔT_m [°C] w/o Mg^{2+}**	**ΔT_m [°C] with Mg^{2+}**
TPP **wild type**	42.3 ± 0.3	54.5 ± 1.5
dŲ20-dŲ68	47.8 ±0.3	63.0 ± 1.0

6.3 Cw-EPR measurements

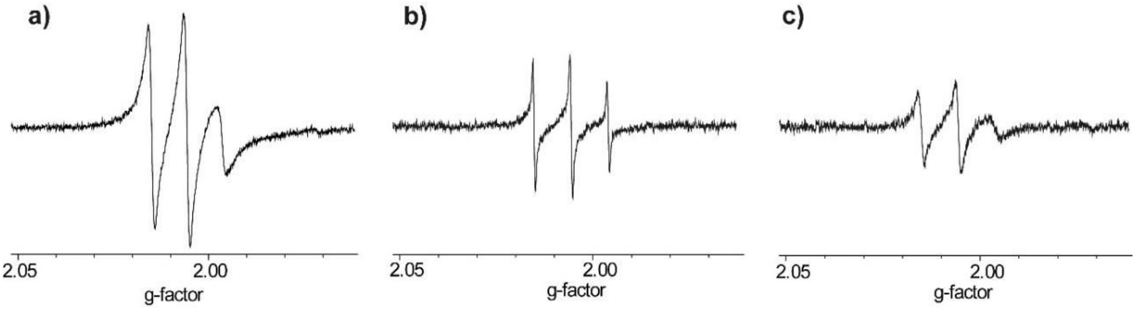

Figure 73: cw-EPR spectra of a) **46dŲ**, **53Ḉm** and c) **54dŲ**.

Table 19: Spin counting values for **45dŲ** and **76Çm**.

Spin-labeled constructs	Labeling efficiency [%]
45dŲ	112
76Çm	113

Table 20: Spin counting values for spin-labeled preQ1 and TPP aptamer domains.

Spin-labeled constructs	Labeling efficiency [%]
dŲ4	101
dŲ23	105
dŲ32	123
dŲ4-dŲ23	129
dŲ4-dŲ32	128
dŲ4-dŲ32 (G11A)	102
TPP dŲ20-dŲ68	123

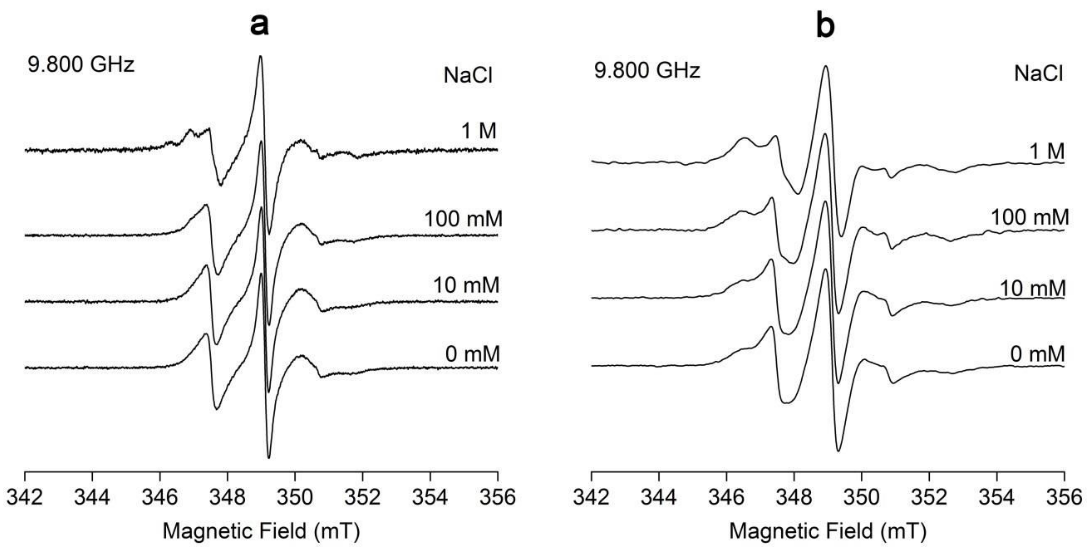

Figure 74: Dependence of the EPR spectrum of a) **45dŲ** and b) **76Çm** on the NaCl concentration in the samples.

Best-fit parameters for the spectral simulations of the cw-EPR spectra

Table 21: Parameters used for the simulation of the cw-EPR spectra of **45dŲ** and **76Çm** with the program MultiComponent

Parameter	**45dŲ**		**76Çm**	
	slow-motion fraction	fast-motion fraction	slow-motion fraction	fast-motion fraction
g[a]	[2.0086, 2.0064, 2.0026]		[2.0086, 2.0064, 2.0026]	
$A(^{15}N)$ (mT)[b]	[0.58, 0.58, 3.67]		[0.58, 0.58, 3.67]	
log(R) (s^{-1})[c]	[7.97, 1.66]	8.27	[7.32, 1.26]	8.31
τ_c (ns)[d]	1.8	0.9	7.9	0.8
S_{20}[e]	0.13	-	0.70	-
α_D, β_D, γ_D[f]	0°, 31°, 0°	-	0°, 42°, 0°	-
ΔH (mT)[g]	0.0		0.2	
Weight (%)	0.93	0.07	0.93	0.07

[a] The g-factor is given in a form [g_{xx}, g_{yy}, g_{zz}].

[b] The hyperfine coupling tensor is given in a form [A_{xx}, A_{yy}, A_{zz}].

[c] The diffusion tensor: axial for the slow-motion fraction of spin labels and isotropic for fast-motion fraction of spin labels.

[d] The effective rotational correlation time.

[e] The order parameter.

[f] A set of Euler angles describing the relative orientation of the diffusion tensor axes with respect to the nitroxide magnetic frame.

[g] The inhomogeneous line broadening.

preQ1 dŲ4-dŲ32

Table 22: Best-fit parameters for the spectral simulations of the cw-EPR spectra from the preQ1 **dŲ4-dŲ32.**

	slow-motion	fast-motion
g[a]	[2.0088, 2.0059, 2.0023]	
A (^{14}N) (mT)[b]	[0.57, 0.40, 3.83]	
log(R)[c]	[7.64, 7.34]	8.26
τ (ns)[d]	[3.8, 7.6]	0.9
α_D, β_D, γ_D[e]	[0°, 0°, 0°]	
weight (%) (without Mg)	41	59
weight (%) (with Mg)	71	29
weight (%) (with Mg+preq)	83	17

[a] The g-factor is given in a form [g_{xx}, g_{yy}, g_{zz}].

[b] The hyperfine coupling tensor is given in a form [A_{xx}, A_{yy}, A_{zz}].

[c] The logarithm of diffusion tensor R (s^{-1}): axial for the slow-motion fraction of spin labels and isotropic for fast-motion fraction of spin labels.

[d] The effective rotational correlation time.

[e] A set of Euler angles describing the relative orientation of the diffusion tensor axes with respect to the nitroxide magnetic frame.

preQ1 dŲ4 and dŲ32

Table 23: Best-fit parameters for the spectral simulations of the cw-EPR spectra from the preQ1 **dŲ4** and **dŲ32**.

	slow-motion	fast-motion
g[a]	[2.0088, 2.0059, 2.0023]	
A (^{14}N) (mT)[b]	[0.57, 0.40, 3.83]	
log(R)[c]	[7.60, 7.30]	8.35
t (ns)[d]	[4.2, 8.4]	0.7
α_D, β_D, γ_D[e]	[0°, 0°, 0°]	
weight (%) (without Mg)	29	71
weight (%) (with Mg)	63	37
weight (%) (with Mg+preq)	81	19

[a] The g-factor is given in a form [g_{xx}, g_{yy}, g_{zz}].

[b] The hyperfine coupling tensor is given in a form [A_{xx}, A_{yy}, A_{zz}].

[c] The logarithm of diffusion tensor R (s^{-1}): axial for the slow-motion fraction of spin labels and isotropic for fast-motion fraction of spin labels.

[d] The effective rotational correlation time.

[e] A set of Euler angles describing the relative orientation of the diffusion respect to the nitroxide magnetic frame.

preQ1 dŲ4-dŲ32(G11A)

Table 24: Best-fit parameters for the spectral simulations of the cw-EPR spectra from the preQ1 **dŲ4-dŲ32(G11A)**.

	slow-motion	fast-motion
g^a	[2.0088, 2.0059, 2.0023]	
A (^{14}N) (mT)^b	[0.57, 0.40, 3.83]	
log(R)^c	[7.59, 7.89]	8.59
τ (ns)^d	[2.1, 4.7]	0.43
α_D, β_D, γ_D^{e}	[0°, 0°, 0°]	[0°, 60°, 0°]
weight (%) (without Mg)	76	24
weight (%) (with Mg)	80	20
weight (%) (with Mg+preq)	85	15

[a] The g-factor is given in a form [g_{xx}, g_{yy}, g_{zz}].

[b] The hyperfine coupling tensor is given in a form [A_{xx}, A_{yy}, A_{zz}].

[c] The logarithm of diffusion tensor R (s^{-1}): axial for the slow-motion fraction of spin labels and isotropic for fast-motion fraction of spin labels.

[d] The effective rotational correlation time.

[e] A set of Euler angles describing the relative orientation of the diffusion respect to the nitroxide magnetic frame.

preQ1 dŲ23

Table 25: Best-fit parameters for the spectral simulations of the cw-EPR spectra from the preQ1 **dŲ23** in the absence of Mg^{2+} and preQ1.

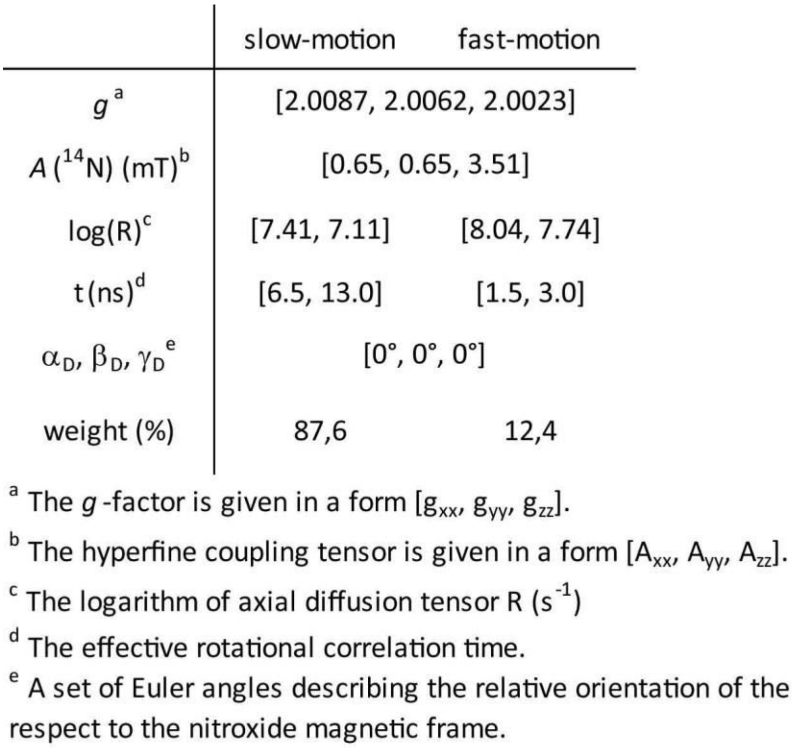

	slow-motion	fast-motion
g^a	[2.0087, 2.0062, 2.0023]	
A (^{14}N) (mT)^b	[0.65, 0.65, 3.51]	
log(R)^c	[7.41, 7.11]	[8.04, 7.74]
t(ns)^d	[6.5, 13.0]	[1.5, 3.0]
α_D, β_D, γ_D^{e}	[0°, 0°, 0°]	
weight (%)	87,6	12,4

[a] The g-factor is given in a form [g_{xx}, g_{yy}, g_{zz}].

[b] The hyperfine coupling tensor is given in a form [A_{xx}, A_{yy}, A_{zz}].

[c] The logarithm of axial diffusion tensor R (s^{-1})

[d] The effective rotational correlation time.

[e] A set of Euler angles describing the relative orientation of the respect to the nitroxide magnetic frame.

Table 26: Best-fit parameters for the spectral simulations of the cw-EPR spectra from the preQ1 **dŲ23** in the presence of only Mg^{2+} / both Mg^{2+} and preQ1.

	slow-motion	fast-motion
g [a]	[2.0087, 2.0062, 2.0023]	
A (^{14}N) (mT) [b]	[0.65, 0.65, 3.51]	
log(R) [c]	[7.36, 7.06]	[7.99, 6.99]
t (ns) [d]	[7.3, 14.5]	[1.7, 3.4]
α_D, β_D, γ_D [e]	[0°, 0°, 0°]	
weight (%)	90.4	9.6

[a] The g-factor is given in a form [g_{xx}, g_{yy}, g_{zz}].

[b] The hyperfine coupling tensor is given in a form [A_{xx}, A_{yy}, A_{zz}].

[c] The logarithm of axial diffusion tensor R (s^{-1})

[d] The effective rotational correlation time.

[e] A set of Euler angles describing the relative orientation of the diffusion respect to the nitroxide magnetic frame.

preQ1 dŲ4-dŲ23

Table 27: Best-fit parameters for the spectral simulations of the cw-EPR spectra from the preQ1 **dŲ4-dŲ23** in the absence of Mg^{2+} and preQ1.

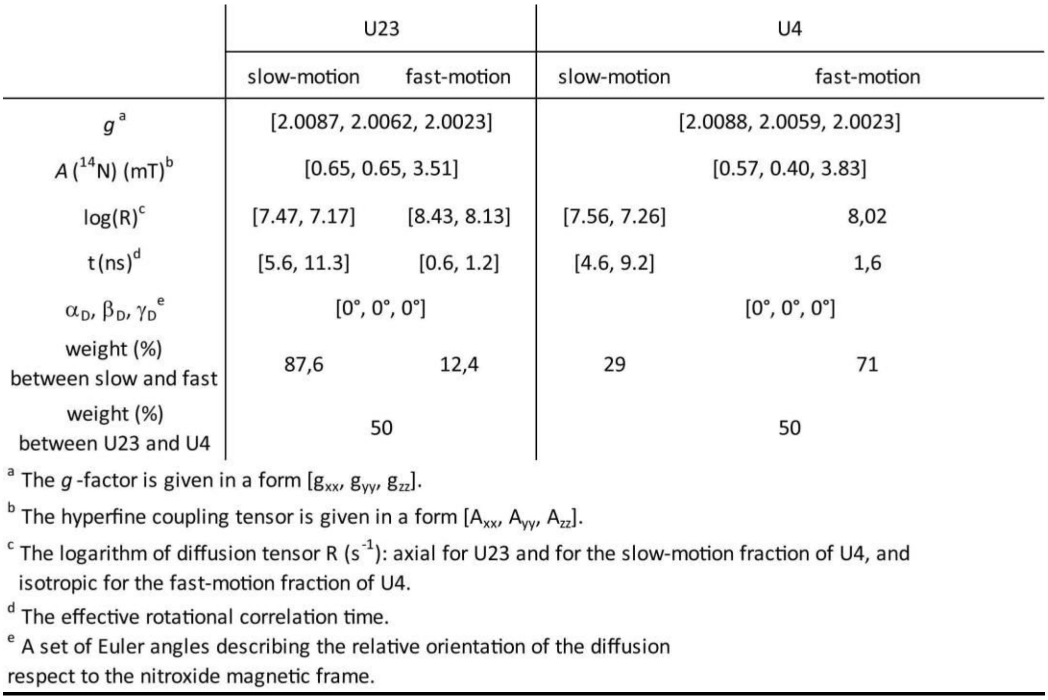

	U23		U4	
	slow-motion	fast-motion	slow-motion	fast-motion
g [a]	[2.0087, 2.0062, 2.0023]		[2.0088, 2.0059, 2.0023]	
A (^{14}N) (mT) [b]	[0.65, 0.65, 3.51]		[0.57, 0.40, 3.83]	
log(R) [c]	[7.47, 7.17]	[8.43, 8.13]	[7.56, 7.26]	8,02
t (ns) [d]	[5.6, 11.3]	[0.6, 1.2]	[4.6, 9.2]	1,6
α_D, β_D, γ_D [e]	[0°, 0°, 0°]		[0°, 0°, 0°]	
weight (%) between slow and fast	87,6	12,4	29	71
weight (%) between U23 and U4	50		50	

[a] The g-factor is given in a form [g_{xx}, g_{yy}, g_{zz}].

[b] The hyperfine coupling tensor is given in a form [A_{xx}, A_{yy}, A_{zz}].

[c] The logarithm of diffusion tensor R (s^{-1}): axial for U23 and for the slow-motion fraction of U4, and isotropic for the fast-motion fraction of U4.

[d] The effective rotational correlation time.

[e] A set of Euler angles describing the relative orientation of the diffusion respect to the nitroxide magnetic frame.

Table 28: Best-fit parameters for the spectral simulations of the cw-EPR spectra from the preQ1 **dŲ4-dŲ23** in the presence of only Mg^{2+} / both Mg^{2+} and preQ1.

	U23		U4	
	slow-motion	fast-motion	slow-motion	fast-motion
g [a]	[2.0087, 2.0062, 2.0023]		[2.0088, 2.0059, 2.0023]	
A (^{14}N) (mT) [b]	[0.65, 0.65, 3.51]		[0.57, 0.40, 3.83]	
log(R) [c]	[7.42, 7.11]	[8.21, 7.91]	[7.55, 7.25]	8,15
t(ns) [d]	[6.3, 12.6]	[1.0, 2.1]	[4.7, 9.3]	1,2
$\alpha_D, \beta_D, \gamma_D$ [e]	[0°, 0°, 0°]		[0°, 0°, 0°]	
weight (%) between slow and fast	90,4	9,6	63	37
weight (%) between U23 and U4	50		50	

[a] The g-factor is given in a form [g_{xx}, g_{yy}, g_{zz}].

[b] The hyperfine coupling tensor is given in a form [A_{xx}, A_{yy}, A_{zz}].

[c] The logarithm of diffusion tensor R (s^{-1}): axial for U23 and for the slow-motion fraction of U4, and isotropic for the fast-motion fraction of U4.

[d] The effective rotational correlation time.

[e] A set of Euler angles describing the relative orientation of the diffusion respect to the nitroxide magnetic frame.

Table 29: Best-fit parameters for the spectral simulations of the cw-EPR spectra from the preQ1 **dŲ4-dŲ23** in the presence of Mg^{2+} and preQ1.

	U23		U4	
	slow-motion	fast-motion	slow-motion	fast-motion
g [a]	[2.0087, 2.0062, 2.0023]		[2.0088, 2.0059, 2.0023]	
A (^{14}N) (mT) [b]	[0.65, 0.65, 3.51]		[0.57, 0.40, 3.83]	
log(R) [c]	[7.42, 7.11]	[8.21, 7.91]	[7.55, 7.25]	8,15
t(ns) [d]	[6.3, 12.6]	[1.0, 2.1]	[4.7, 9.3]	1,2
$\alpha_D, \beta_D, \gamma_D$ [e]	[0°, 0°, 0°]		[0°, 0°, 0°]	
weight (%) between slow and fast	90,4	9,6	63	37
weight (%) between U23 and U4	50		50	

[a] The g-factor is given in a form [g_{xx}, g_{yy}, g_{zz}].

[b] The hyperfine coupling tensor is given in a form [A_{xx}, A_{yy}, A_{zz}].

[c] The logarithm of diffusion tensor R (s^{-1}): axial for U23 and for the slow-motion fraction of U4, and isotropic for the fast-motion fraction of U4.

[d] The effective rotational correlation time.

[e] A set of Euler angles describing the relative orientation of the diffusion respect to the nitroxide magnetic frame.

TPP dŲ20-dŲ68

Table 30: Best-fit parameters for the spectral simulations of the cw-EPR spectra from the TPP **dŲ20-dŲ68** in the absence of Mg^{2+} and TPP ligand.

	slow-motion	fast-motion
g [a]	[2.0079, 2.0062, 2.0023]	
A (^{14}N) (mT) [b]	[0.72, 0.72, 3.54]	
log(R) [c]	[6.39, 6.09]	[7.70, 7.40]
t (ns) [d]	[67.9, 135.8]	[3.3, 6.6]
a_D, b_D, g_D [e]	[0°, 50°, 0°]	[0°, 50°, 0°]
weight (%)	36.5	63.5

[a] The g-factor is given in a form [g_{xx}, g_{yy}, g_{zz}].

[b] The hyperfine coupling tensor is given in a form [A_{xx}, A_{yy}, A_{zz}].

[c] The logarithm of axial diffusion tensor R (s^{-1})

[d] The effective rotational correlation time.

[e] A set of Euler angles describing the relative orientation of the diffusion tensor axes with respect to the nitroxide magnetic frame.

6.4 PELDOR measurements

Not baseline-corrected PELDOR time traces

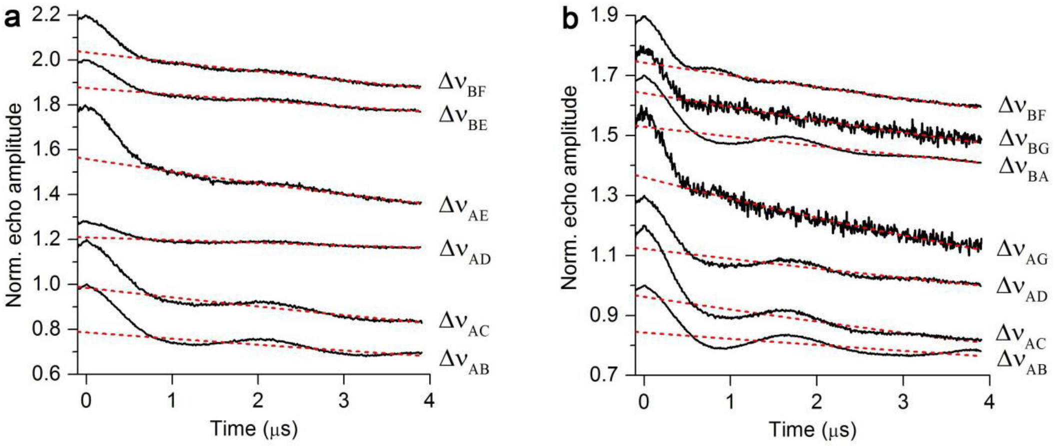

Figure 75: PELDOR time traces of a) **45dŲ** and b) **76Çm** (black lines) are overlaid with the background fits (red dashes).

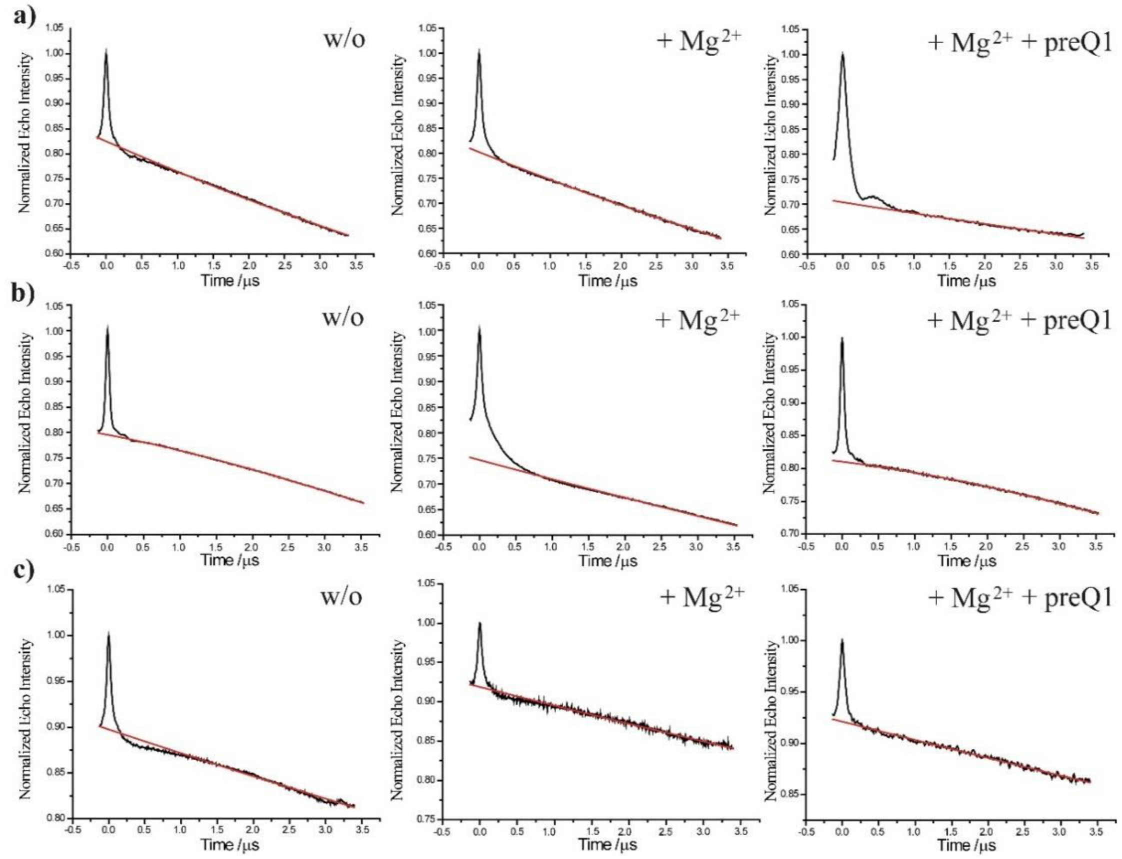

Figure 76: Not baseline-corrected Q-band PELDOR time traces of a) preQ1 **dŲ4-dŲ32**, b) preQ1 **dŲ4-dŲ23** and c) preQ1 **dŲ4-dŲ32(G11A)**. Left are shown time traces of the samples without Mg^{2+}, in the middle after addition of Mg^{2+} and right after addition of both Mg^{2+} and preQ1. Red line illustrates the background.

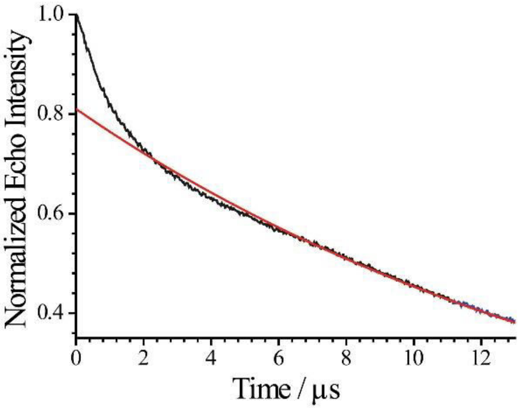

Figure 77: Not baseline-corrected Q-band PELDOR time trace of TPP **dŲ20-dŲ68**. Red line illustrates the background.

Orientation selective PELDOR measurements of preQ1 dŲ4-dŲ32.

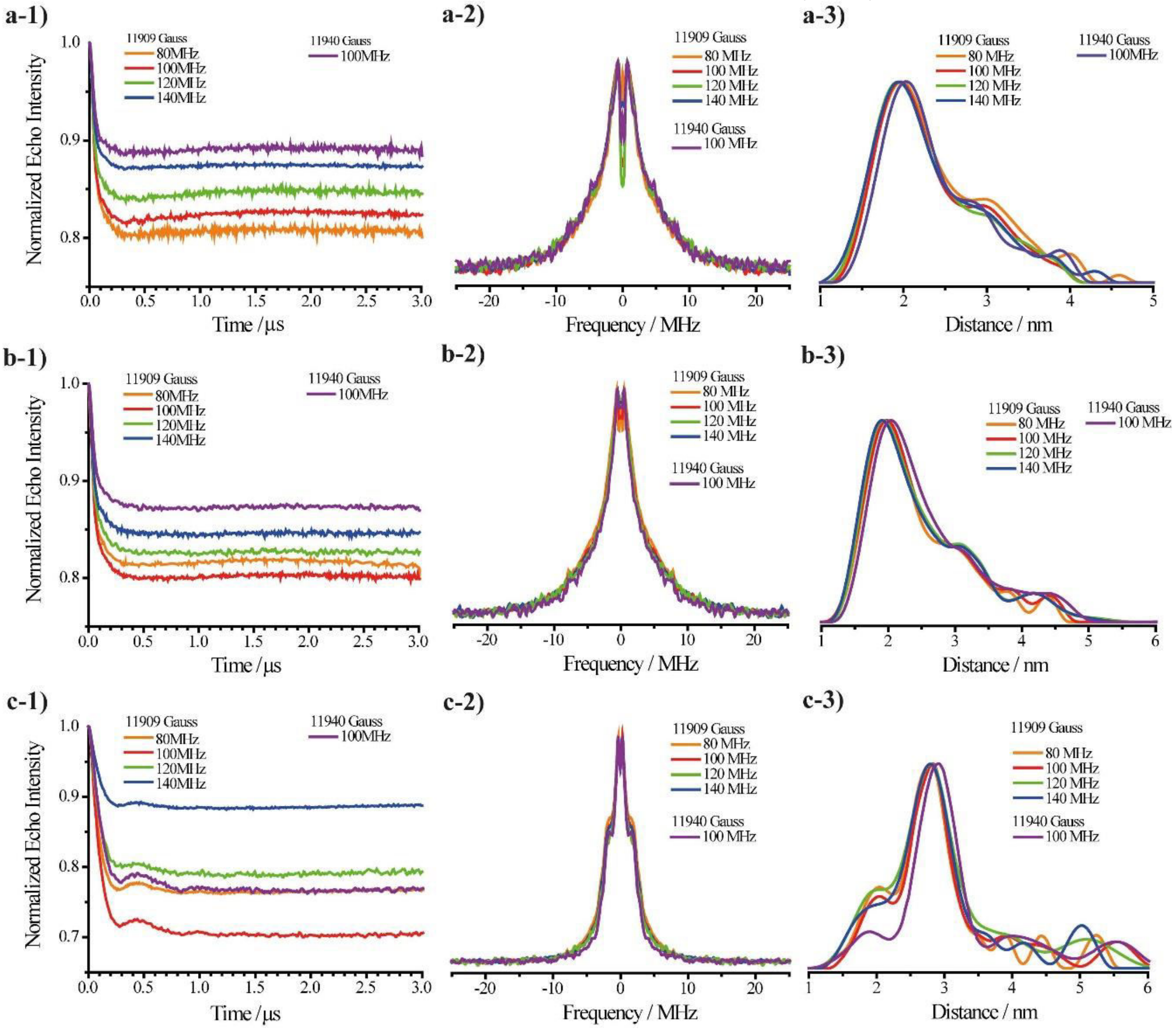

Figure 78: a, b, c-1) Baseline-corrected Q-band PELDOR time traces of preQ1 **dŲ4-dŲ32**. a-1) preQ1 **dŲ4-dŲ32** in the absence of preQ1 and Mg^{2+}, b-1) after addition of Mg^{2+} and c-1) after addition of Mg^{2+} and preQ1. a, b, c-2) The Fourier transforms of the PELDOR time traces from (a, b, c-1). a-2) preQ1 **dŲ4-dŲ32** in the absence of preQ1 and Mg^{2+}, (b-2) after addition of Mg^{2+} and c-2) after addition of Mg^{2+} and preQ1. a,b,b-3) The derived distance distributions from a, b, c-2). a-3) preQ1 **dŲ4-dŲ32** in the absence of preQ1 and Mg^{2}, b-3) after addition of Mg^{2+} and c-3) after addition of Mg^{2+} and preQ1.

PELDOR time traces of the preQ1 dŲ4-dŲ23 and preQ1 dŲ4-dŲ32(G11A)

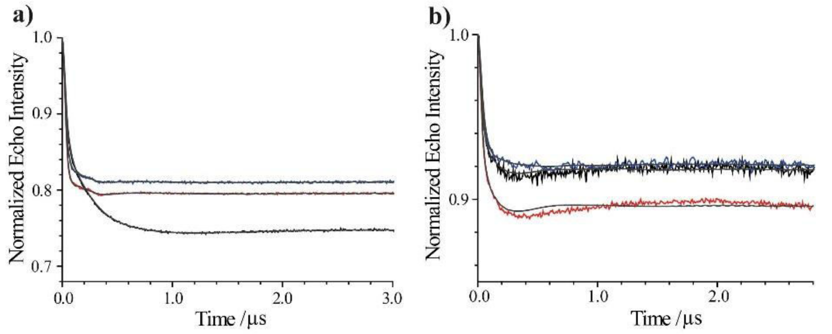

Figure 79: Baseline-corrected Q-band PELDOR time traces of a) preQ1 **dŲ4-dŲ23** and b) preQ1 **dŲ4-dŲ32(G11A)** in the absence of preQ1 and Mg^{2+} (red), after addition of Mg^{2+} (black) and after

addition of Mg^{2+} and preQ1 (blue) at 50K. The calculated time traces (gray) were obtained by the Tikhonov analysis of the experimental ones using DeerAnalysis.

6.5 B. List of Abbreviations

Abbreiation	**Full form**
ABI	Applied Biosystems
ACE	2'-Bis(2-acetoxyethoxy)methyl
ACN	Acetonitrile
APS	Ammonium persulfate solution
ASC	Ascorbate
ATP	Adenosine triphosphate
Bsu	*Bacillus subtilis*
BTT	5-(Benzylthio)-1H-tetrazole
CAP	Capping reagent
CD	Circular dichroism
CPG	Controlled pore glass
CIAP	Calf intestinal alkaline phosphatase
CuAAC	Cu(I)-catalyzed Azide-Alkyne cycloaddition
cw-EPR	continuous wave electron paramagnetic resonance
DCA	Dichloroacetic acid
DCM	Dichloromethane
DEER	Double Electron Electron Resonance
DEPC	Diethylopyrocarbonate
DFT	Density functional theory
DHA	Dehydroascorbic acid
DTT	Dithiothreitol

DMF	Dimethylformamide
DMSO	Dimethyl sulfoxide
DMT	Dimethoxytrityl
DNA	Deoxyribonucleic acid
EDTA	Ethylenediaminetetraacetic acid
EdA	Ethynyl-2’-deoxyadenine
EdG	Ethynyl-2’-deoxyguanine
EdC	5-Ethynyl-2’-deoxycytidine
E. coli	*Escherichia coli*
EdU	5-Ethynyl-2’-deoxyuridine
EmC	5-Ethynyl-2‘-O-methylcytidine
EPR	Electron paramagnetic resonance
ESI	Electrospray-ionisation
FRET	Fluorescence Resonance Energy Transfer
Fsu	*Fusobacterium nucleatum*
GMPS	Guanosine monophosphorthioate
HEPES	4-(2-Hydroxyethyl)-1-piperazineethanesulfonic acid
HIFP	Hexafluoroisopropanol
HPLC	High-performance liquid chromatography
IAP	3-(2-Iodoacetamido)-PROXYL spin label
IRES	Internal ribosome entry site
ISA	Imidazole-1-sulfonyl azide
ITC	Isothermal titration calorimetry
LC-MS	Liquid chromatography–mass spectrometry

lncRNA	long non-coding Ribonucleic acid
*m*CPBA	meta-Chloroperoxybenzoic acid
mRNA	messenger Ribonucleic acid
MST	Microscale thermophoresis
MTSL	S-(1-oxyl-2,2,5,5-tetramethyl-2,5-dihydro-1H-pyrrol-3-yl)methyl methanesulfonothioate
NMR	Nuclear magnetic resonance spectroscopy
PAGE	Polyacrylamide gel electrophoresis
PCR	Polymerase chain reaction
PELDOR	Pulsed Electron Electron Double Resonance
Pfu	*Pyrococcus furiosus*
PNK	Polynucleotide kinase
rRNA	ribosomal Ribonucleic acid
RNA	Ribonucleic acid
siRNA	small interfering ribonucleic acid
smFRET	small-molecule Fluorescence Resonance Energy Transfer
TBAF	Tetra-n-butylammonium fluoride
TBDMS	*Tert*-Butyldimethylsilyl
TBE	TRIS-Borat-EDTA
TBHP	*Tert*-butyl hydroperoxide
TBTA	Tris(benzyltriazolylmethyl)amine
TCA	Trichloroacetic acid
TEAA	Triethylammonium acetate
TEMED	Tetramethylethylenediamine

THPTA	Tris(3-hydroxypropyltriazolylmethyl)amine
THF	Tetrahydrofuran
TIPS	Triisopropylsilyl
TLC	Thin layer chromatography
TMSA	Trimethylsilylacetylene
TPA	2,2,5,5-tetramethylpyrrolin-1-yloxy-3-acetylene
TPP	Thiamine pyrophosphate
TRIS	Tris(hydroxymethyl)aminomethane
tRNA	transfer Ribonucleic acid
Tte	*Thermoanaerobacter tengcongensis*
UV	Ultraviolet

6.6 List of Figures

6.7 List of Schemes

6.8 List of Tables

7 Bibliography

(1) Dahm, R., Discovering DNA: Friedrich Miescher and the early years of nucleic acid research. *Hum Genet* **2008,** *122* (6), 565-81.

(2) Lindahl, T., Instability and Decay of the Primary Structure of DNA. *Nature* **1993,** *362* (6422), 709-715.

(3) Weber, F.; Wagner, V.; Rasmussen, S. B.; Hartmann, R.; Paludan, S. R., Double-stranded RNA is produced by positive-strand RNA viruses and DNA viruses but not in detectable amounts by negative-strand RNA viruses. *J Virol* **2006,** *80* (10), 5059-64.

(4) Beveridge, D. L.; Cheatham, T. E., 3rd; Mezei, M., The ABCs of molecular dynamics simulations on B-DNA, circa 2012. *J Biosci* **2012,** *37* (3), 379-97.

(5) Egli, M., Structural aspects of nucleic acid analogs and antisense oligonucleotides. *Angewandte Chemie-International Edition in English* **1996,** *35* (17), 1895-1910.

(6) Jaeger, J. A.; Santalucia, J.; Tinoco, I., Determination of Rna Structure and Thermodynamics. *Annu Rev Biochem* **1993,** *62*, 255-287.

(7) Emory, S. A.; Bouvet, P.; Belasco, J. G., A 5'-Terminal Stem Loop Structure Can Stabilize Messenger-Rna in Escherichia-Coli. *Gene Dev* **1992,** *6* (1), 135-148.

(8) Svoboda, P.; Di Cara, A., Hairpin RNA: a secondary structure of primary importance. *Cell Mol Life Sci* **2006,** *63* (7-8), 901-918.

(9) Nissen, P.; Ippolito, J. A.; Ban, N.; Moore, P. B.; Steitz, T. A., RNA tertiary interactions in the large ribosomal subunit: The A-minor motif. *P Natl Acad Sci USA* **2001,** *98* (9), 4899-4903.

(10) Staple, D. W.; Butcher, S. E., Pseudoknots: RNA structures with diverse functions. *Plos Biol* **2005,** *3* (6), 956-959.

(11) Chen, J. L.; Blasco, M. A.; Greider, C. W., Secondary structure of vertebrate telomerase RNA. *Cell* **2000,** *100* (5), 503-514.

(12) Theimer, C. A.; Blois, C. A.; Feigon, J., Structure of the human telomerase RNA pseudoknot reveals conserved tertiary interactions essential for function. *Mol Cell* **2005,** *17* (5), 671-682.

(13) Brierley, I.; Digard, P.; Inglis, S. C., Characterization of an Efficient Coronavirus Ribosomal Frameshifting Signal - Requirement for an Rna Pseudoknot. *Cell* **1989,** *57* (4), 537-547.

(14) Kruger, K.; Grabowski, P. J.; Zaug, A. J.; Sands, J.; Gottschling, D. E.; Cech, T. R., Self-Splicing Rna - Auto-Excision and Auto-Cyclization of the Ribosomal-Rna Intervening Sequence of Tetrahymena. *Cell* **1982,** *31* (1), 147-157.

(15) Guerriertakada, C.; Gardiner, K.; Marsh, T.; Pace, N.; Altman, S., The Rna Moiety of Ribonuclease-P Is the Catalytic Subunit of the Enzyme. *Cell* **1983,** *35* (3), 849-857.

(16) Fica, S. M.; Tuttle, N.; Novak, T.; Li, N. S.; Lu, J.; Koodathingal, P.; Dai, Q.; Staley, J. P.; Piccirilli, J. A., RNA catalyses nuclear pre-mRNA splicing. *Nature* **2013,** *503* (7475), 229-234.

817) Steitz, T. A.; Moore, P. B., RNA, the first macromolecular catalyst: the ribosome is a ribozyme. *Trends in Biochemical Sciences* **2003,** *28* (8), 411-418.

(18) He, L.; Hannon, G. J., Micrornas: Small RNAs with a big role in gene regulation. *Nat Rev Genet* **2004,** *5* (7), 522-531.

(19) Wienholds, E.; Plasterk, R. H. A., MicroRNA function in animal development. *Febs Letters* **2005,** *579* (26), 5911-5922.

(20) Ramachandran, P. V.; Ignacimuthu, S., RNA Interference-A Silent but an Efficient Therapeutic Tool. *Appl Biochem Biotech* **2013,** *169* (6), 1774-1789.

(21) Wahlestedt, C., Targeting long non-coding RNA to therapeutically upregulate gene expression. *Nat Rev Drug Discov* **2013,** *12* (6), 433-446.

(22) Mercer, T. R.; Mattick, J. S., Structure and function of long noncoding RNAs in epigenetic regulation. *Nat Struct Mol Biol* **2013,** *20* (3), 300-307.

(23) Winkler, W. C.; Breaker, R. R., Regulation of bacterial gene expression by riboswitches. *Annu Rev Microbiol* **2005,** *59*, 487-517.

(24) Gottesman, S., The small RNA regulators of Escherichia coli: roles and mechanisms*. *Annu Rev Microbiol* **2004,** *58*, 303-28.

(25) Mandal, M.; Breaker, R. R., Gene regulation by riboswitches. *Nat Rev Mol Cell Biol* **2004,** *5* (6), 451-63.

(26) Nudler, E.; Mironov, A. S., The riboswitch control of bacterial metabolism. *Trends Biochem Sci* **2004,** *29* (1), 11-7.

(27) Kubodera, T.; Watanabe, M.; Yoshiuchi, K.; Yamashita, N.; Nishimura, A.; Nakai, S.; Gomi, K.; Hanamoto, H., Thiamine-regulated gene expression of Aspergillus oryzae thiA requires splicing of the intron containing a riboswitch-like domain in the 5'-UTR. *FEBS Lett* **2003,** *555* (3), 516-20.

(28) Sudarsan, N.; Barrick, J. E.; Breaker, R. R., Metabolite-binding RNA domains are present in the genes of eukaryotes. *Rna* **2003,** *9* (6), 644-647.

(29) Matzner, D.; Mayer, G., (Dis)similar Analogues of Riboswitch Metabolites as Antibacterial Lead Compounds. *J Med Chem* **2015,** *58* (8), 3275-3286.

(30) Morris, K. V.; Mattick, J. S., The rise of regulatory RNA. *Nat Rev Genet* **2014,** *15* (6), 423-437.

(31) Wang, J. X.; Breaker, R. R., Riboswitches that sense S-adenosylmethionine and S-adenosylhomocysteine. *Biochem Cell Biol* **2008,** *86* (2), 157-168.

(32) Lee, E. R.; Baker, J. L.; Weinberg, Z.; Sudarsan, N.; Breaker, R. R., An Allosteric Self-Splicing Ribozyme Triggered by a Bacterial Second Messenger. *Science* **2010,** *329* (5993), 845-848.

(33) Chen, A. G. Y.; Sudarsan, N.; Breaker, R. R., Mechanism for gene control by a natural allosteric group I ribozyme. *Rna* **2011,** *17* (11), 1967-1972.

(34) Winkler, W.; Nahvi, A.; Breaker, R. R., Thiamine derivatives bind messenger RNAs directly to regulate bacterial gene expression. *Nature* **2002,** *419* (6910), 952-956.

(35) Breaker, R. R., Riboswitches and the RNA world. *Cold Spring Harb Perspect Biol* **2012,** *4* (2).

(36) McCown, P. J.; Corbino, K. A.; Stav, S.; Sherlock, M. E.; Breaker, R. R., Riboswitch diversity and distribution. *Rna* **2017,** *23* (7), 995-1011.

(37) Nahvi, A.; Sudarsan, N.; Ebert, M. S.; Zou, X.; Brown, K. L.; Breaker, R. R., Genetic control by a metabolite binding mRNA. *Chemistry & Biology* **2002,** *9* (9), 1043-1049.

(38) Epshtein, V.; Mironov, A. S.; Nudler, E., The riboswitch-mediated control of sulfur metabolism in bacteria. *P Natl Acad Sci USA* **2003,** *100* (9), 5052-5056.

(39) Mironov, A. S.; Gusarov, I.; Rafikov, R.; Lopez, L. E.; Shatalin, K.; Kreneva, R. A.; Perumov, D. A.; Nudler, E., Sensing small molecules by nascent RNA: A mechanism to control transcription in bacteria. *Cell* **2002,** *111* (5), 747-756.

(40) White, H. B., 3rd, Coenzymes as fossils of an earlier metabolic state. *J Mol Evol* **1976,** *7* (2), 101-4.

(41) Holbrook, S. R., Structural principles from large RNAs. *Annu Rev Biophys* **2008,** *37*, 445-64.

(42) Scott, L. G.; Hennig, M., RNA structure determination by NMR. *Methods Mol Biol* **2008,** *452*, 29-61.

(43) Lemay, J. F.; Penedo, J. C.; Tremblay, R.; Lilley, D. M.; Lafontaine, D. A., Folding of the adenine riboswitch. *Chem Biol* **2006,** *13* (8), 857-68.

(44) Esquiaqui, J. M.; Sherman, E. M.; Ye, J. D.; Fanucci, G. E., Site-Directed Spin-Labeling Strategies and Electron Paramagnetic Resonance Spectroscopy for Large Riboswitches. *Riboswitch Discovery, Structure and Function* **2014,** *549*, 287-311.

(45) Hunsicker-Wang, L.; Vogt, M.; DeRose, V. J., Epr Methods to Study Specific Metal-Ion Binding Sites in Rna. *Methods in Enzymology, Vol 468: Biophysical, Chemical, and Functional Probes of Rna Structure, Interactions and Folding, Pt A* **2009,** *468*, 335-367.

(46) Ubbink, M.; Worrall, J. A. R.; Canters, G. W.; Groenen, E. J. J.; Huber, M., Paramagnetic resonance of biological metal centers. *Annu Rev Bioph Biom* **2002,** *31*, 393-422.

(47) Jerabek-Willemsen, M.; Wienken, C. J.; Braun, D.; Baaske, P.; Duhr, S., Molecular Interaction Studies Using Microscale Thermophoresis. *Assay Drug Dev Techn* **2011,** *9* (4), 342-353.

(48) Kulshina, N.; Edwards, T. E.; Ferre-D'Amare, A. R., Thermodynamic analysis of ligand binding and ligand binding-induced tertiary structure formation by the thiamine pyrophosphate riboswitch. *Rna* **2010,** *16* (1), 186-196.

(49) Puglisi, J. D.; Tinoco, I., Jr., Absorbance melting curves of RNA. *Methods Enzymol* **1989,** *180*, 304-25.

(50) Johnson, K. H.; Gray, D. M., Analysis of an RNA pseudoknot structure by CD spectroscopy. *J Biomol Struct Dyn* **1992,** *9* (4), 733-45.

(51) Caruthers, M. H.; Beaucage, S. L.; Becker, C.; Efcavitch, J. W.; Fisher, E. F.; Galluppi, G.; Goldman, R.; deHaseth, P.; Matteucci, M.; McBride, L.; et al., Deoxyoligonucleotide synthesis via the phosphoramidite method. *Gene Amplif Anal* **1983,** *3*, 1-26.

(52) Ogilvie, K. K.; Beaucage, S. L.; Schifman, A. L.; Theriault, N. Y.; Sadana, K. L., Synthesis of Oligoribonucleotides .2. Use of Silyl Protecting Groups in Nucleoside and Nucleotide Chemistry .7. *Can J Chem* **1978,** *56* (21), 2768-2780.

(53) Beaucage, S. L.; Iyer, R. P., Advances in the Synthesis of Oligonucleotides by the Phosphoramidite Approach. *Tetrahedron* **1992,** *48* (12), 2223-2311.

(54) Cekan, P.; Smith, A. L.; Barhate, N.; Robinson, B. H.; Sigurdsson, S. T., Rigid spin-labeled nucleoside C: a nonperturbing EPR probe of nucleic acid conformation. *Nucleic Acids Research* **2008,** *36* (18), 5946-5954.

(55) Spaltenstein, A.; Robinson, B. H.; Hopkins, P. B., A Rigid and Nonperturbing Probe for Duplex DNA Motion. *J Am Chem Soc* **1988,** *110* (4), 1299-1301.

(56) Piton, N.; Mu, Y.; Stock, G.; Prisner, T. F.; Schiemann, O.; Engels, J. W., Base-specific spin-labeling of RNA for structure determination (vol 35, pg 3128, 2007). *Nucleic Acids Research* **2007,** *35* (17), 5985-5985.

(57) Gophane, D. B.; Sigurdsson, S. T., Hydrogen-bonding controlled rigidity of an isoindoline-derived nitroxide spin label for nucleic acids. *Chem Commun* **2013,** *49* (10), 999-1001.

(58) Miller, T. R.; Hopkins, P. B., Toward the Synthesis of a 2nd-Generation Nitroxide Spin-Probe for DNA Dynamics Studies. *Bioorg Med Chem Lett* **1994,** *4* (8), 981-986.

(59) Hobartner, C.; Sicoli, G.; Wachowius, F.; Gophane, D. B.; Sigurdsson, S. T., Synthesis and characterization of RNA containing a rigid and nonperturbing cytidine-derived spin label. *J Org Chem* **2012,** *77* (17), 7749-54.

(60) Schiemann, O.; Cekan, P.; Margraf, D.; Prisner, T. F.; Sigurdsson, S. T., Relative Orientation of Rigid Nitroxides by PELDOR: Beyond Distance Measurements in Nucleic Acids. *Angew Chem Int Edit* **2009,** *48* (18), 3292-3295.

(61) Marko, A.; Margraf, D.; Cekan, P.; Sigurdsson, S. T.; Schiemann, O.; Prisner, T. F., Analytical method to determine the orientation of rigid spin labels in DNA. *Phys Rev E* **2010,** *81* (2).

(62) Hara, H.; Horiuchi, T.; Saneyoshi, M.; Nishimura, S., 4thiouridine-Specific Spin-Labeling of E-Coli Transfer Rna. *Biochem Bioph Res Co* **1970,** *38* (2), 305-+.

(63) Ramos, A.; Varani, G., A new method to detect long-range protein-RNA contacts: NMR detection of electron-proton relaxation induced by nitroxide spin-labeled RNA. *J Am Chem Soc* **1998,** *120* (42), 10992-10993.

(64) Allerson, C. R.; Chen, S. L.; Verdine, G. L., A chemical method for site-specific modification of RNA: The convertible nucleoside approach. *J Am Chem Soc* **1997,** *119* (32), 7423-7433.

(65) Sicoli, G.; Wachowius, F.; Bennati, M.; Hobartner, C., Probing secondary structures of spin-labeled RNA by pulsed EPR spectroscopy. *Angew Chem Int Ed Engl* **2010,** *49* (36), 6443-7.

(66) Edwards, T. E.; Sigurdsson, S. T., Site-specific incorporation of nitroxide spin-labels into 2 '-positions of nucleic acids. *Nature Protocols* **2007,** *2* (8), 1954-1962.

(67) Qin, P. Z.; Butcher, S. E.; Feigon, J.; Hubbell, W. L., Quantitative analysis of the isolated GAAA tetraloop/receptor interaction in solution: a site-directed spin labeling study. *Biochemistry* **2001,** *40* (23), 6929-36.

(68) Shelke, S. A.; Sigurdsson, S. T., Noncovalent and Site-Directed Spin Labeling of Nucleic Acids. *Angew Chem Int Edit* **2010,** *49* (43), 7984-7986.

(69) Kamble, N. R.; Granz, M.; Prisner, T. F.; Sigurdsson, S. T., Noncovalent and site-directed spin labeling of duplex RNA. *Chem Commun* **2016,** *52* (100), 14442-14445.

(70) Shelke, S. A.; Sandholt, G. B.; Sigurdsson, S. T., Nitroxide-labeled pyrimidines for non-covalent spin-labeling of abasic sites in DNA and RNA duplexes. *Org Biomol Chem* **2014,** *12* (37), 7366-7374.

(71) Lang, K.; Micura, R., The preparation of site-specifically modified riboswitch domains as an example for enzymatic ligation of chemically synthesized RNA fragments. *Nature Protocols* **2008,** *3* (9), 1457-1466.

(72) Stark, M. R.; Pleiss, J. A.; Deras, M.; Scaringe, S. A.; Rader, S. D., An RNA ligase-mediated method for the efficient creation of large, synthetic RNAs. *Rna* **2006,** *12* (11), 2014-2019.

(73) Duss, O.; Yulikov, M.; Jeschke, G.; Allain, F. H. T., EPR-aided approach for solution structure determination of large RNAs or protein-RNA complexes. *Nat Commun* **2014,** *5*.

(74) Buttner, L.; Seikowski, J.; Wawrzyniak, K.; Ochmann, A.; Hobartner, C., Synthesis of spin-labeled riboswitch RNAs using convertible nucleosides and DNA-catalyzed RNA ligation. *Bioorgan Med Chem* **2013,** *21* (20), 6171-6180.

(75) Purtha, W. E.; Coppins, R. L.; Smalley, M. K.; Silverman, S. K., General deoxyribozyme-catalyzed synthesis of native 3 '-5 ' RNA linkages. *J Am Chem Soc* **2005,** *127* (38), 13124-13125.

(76) Lebars, I.; Vileno, B.; Bourbigot, S.; Turek, P.; Wolff, P.; Kieffer, B., A fully enzymatic method for site-directed spin labeling of long RNA. *Nucleic Acids Res* **2014,** *42* (15), e117.

(77) Babaylova, E. S.; Ivanov, A. V.; Malygin, A. A.; Vorobjeva, M. A.; Venyaminova, A. G.; Polienko, Y. F.; Kirilyuk, I. A.; Krumkacheva, O. A.; Fedin, M. V.; Karpova, G. G.; Bagryanskaya, E. G., A versatile approach for site-directed spin labeling and structural EPR studies of RNAs. *Org Biomol Chem* **2014,** *12* (19), 3129-3136.

(78) Babaylova, E. S.; Malygin, A. A.; Lomzov, A. A.; Pyshnyi, D. V.; Yulikov, M.; Jeschke, G.; Krumkacheva, O. A.; Fedin, M. V.; Karpova, G. G.; Bagryanskaya, E. G., Complementary-addressed site-directed spin labeling of long natural RNAs. *Nucleic Acids Research* **2016,** *44* (16), 7935-7943.

(79) Rostovtsev, V. V.; Green, L. G.; Fokin, V. V.; Sharpless, K. B., A stepwise Huisgen cycloaddition process: Copper(I)-catalyzed regioselective "ligation" of azides and terminal alkynes. *Angew Chem Int Edit* **2002,** *41* (14), 2596-+.

(80) Tornoe, C. W.; Christensen, C.; Meldal, M., Peptidotriazoles on solid phase: [1,2,3]-triazoles by regiospecific copper(I)-catalyzed 1,3-dipolar cycloadditions of terminal alkynes to azides. *Journal of Organic Chemistry* **2002,** *67* (9), 3057-3064.

(81) Wu, P.; Fokin, V. V., Catalytic azide-alkyne cycloaddition: Reactivity and applications. *Aldrichim Acta* **2007,** *40* (1), 7-17.

(82) Lee, B. Y.; Park, S. R.; Jeon, H. B.; Kim, K. S., A new solvent system for efficient synthesis of 1,2,3-triazoles. *Tetrahedron Lett* **2006,** *47* (29), 5105-5109.

(83) Chan, T. R.; Hilgraf, R.; Sharpless, K. B.; Fokin, V. V., Polytriazoles as copper(I)-stabilizing ligands in catalysis. *Organic Letters* **2004,** *6* (17), 2853-2855.

(84) El-Sagheer, A. H.; Brown, T., Click chemistry with DNA. *Chem Soc Rev* **2010,** *39* (4), 1388-1405.

(85) Rao, H.; Tanpure, A. A.; Sawant, A. A.; Srivatsan, S. G., Enzymatic incorporation of an azide-modified UTP analog into oligoribonucleotides for post-transcriptional chemical functionalization. *Nat Protoc* **2012,** *7* (6), 1097-112.

(86) Haugland, M. M.; El-Sagheer, A. H.; Porter, R. J.; Pena, J.; Brown, T.; Anderson, E. A.; Lovett, J. E., 2'-Alkynylnucleotides: A Sequence- and Spin Label-Flexible Strategy for EPR Spectroscopy in DNA. *J Am Chem Soc* **2016,** *138* (29), 9069-72.

(87) Jakobsen, U.; Shelke, S. A.; Vogel, S.; Sigurdsson, S. T., Site-directed spin-labeling of nucleic acids by click chemistry: detection of abasic sites in duplex DNA by EPR spectroscopy. *J Am Chem Soc* **2010,** *132* (30), 10424-8.

(88) Ding, P.; Wunnicke, D.; Steinhoff, H. J.; Seela, F., Site-directed spin-labeling of DNA by the azide-alkyne 'click' reaction: nanometer distance measurements on 7-deaza-2'-deoxyadenosine and 2'-deoxyuridine nitroxide conjugates spatially separated or linked to a 'dA-dT' base pair. *Chemistry* **2010,** *16* (48), 14385-96.

(89) Schlick, S., *Advanced ESR methods in polymer research*. Wiley-Interscience: Hoboken, N.J., 2006; p xiv, 353 p.

(90) Jeschke, G., Einführung in die ESR-Spektroskopie. **1998**.

(91) Schweiger, A.; Jeschke, G., *Principles of pulse electron paramagnetic resonance*. Oxford University Press: Oxford, UK ; New York, 2001; p xxvi, 578 p.

(92) Krstic, I.; Endeward, B.; Margraf, D.; Marko, A.; Prisner, T. F., Structure and Dynamics of Nucleic Acids. *Top Curr Chem* **2012,** *321*, 159-198.

(93) Budil, D. E.; Earle, K. A.; Freed, J. H., Full Determination of the Rotational Diffusion Tensor by Electron-Paramagnetic Resonance at 250 Ghz. *J Phys Chem-Us* **1993,** *97* (7), 1294-1303.

(94) Rabenstein, M. D.; Shin, Y. K., Determination of the Distance between 2 Spin Labels Attached to a Macromolecule. *P Natl Acad Sci USA* **1995,** *92* (18), 8239-8243.

(95) Jeschke, G.; Polyhach, Y., Distance measurements on spin-labelled biomacromolecules by pulsed electron paramagnetic resonance. *Phys Chem Chem Phys* **2007,** *9* (16), 1895-1910.

(96) Milov, A. D.; Salikhov, K. M.; Shirov, M. D., Application of Eldor in Electron-Spin Echo for Paramagnetic Center Space Distribution in Solids. *Fiz Tverd Tela+* **1981,** *23* (4), 975-982.

(97) Martin, R. E.; Pannier, M.; Diederich, F.; Gramlich, V.; Hubrich, M.; Spiess, H. W., Determination of end-to-end distances in a series of TEMPO diradicals of up to 2.8 nm length with a new four-pulse double electron electron resonance experiment. *Angew Chem Int Edit* **1998,** *37* (20), 2834-2837.

(98) El Mkami, H.; Norman, D. G., EPR Distance Measurements in Deuterated Proteins. *Electron Paramagnetic Resonance Investigations of Biological Systems by Using Spin Labels, Spin Probes, and Intrinsic Metal Ions, Pt B* **2015,** *564*, 125-152.

(99) Junk, M. J. N., Electron Paramagnetic Resonance Theory. *University of California* **2012**.

(100) Jeschke, G.; Panek, G.; Godt, A.; Bender, A.; Paulsen, H., Data analysis procedures for pulse ELDOR measurements of broad distance distributions. *Appl Magn Reson* **2004,** *26* (1-2), 223-244.

(101) Abdullin, D.; Hagelueken, G.; Hunter, R. I.; Smith, G. M.; Schiemann, O., Geometric model-based fitting algorithm for orientation-selective PELDOR data. *Mol Phys* **2015,** *113* (6), 544-560.

(102) Flaender, M.; Sicoli, G.; Fontecave, T.; Mathis, G.; Saint-Pierre, C.; Boulard, Y.; Gambarelli, S.; Gasparutto, D., Site-specific insertion of nitroxide-spin labels into DNA probes by click chemistry for structural analyses by ELDOR spectroscopy. *Nucleic Acids Symp Ser (Oxf)* **2008,** (52), 147-8.

(103) de Oliveira, K. N.; Costa, P.; Santin, J. R.; Mazzambani, L.; Burger, C.; Mora, C.; Nunes, R. J.; de Souza, M. M., Synthesis and antidepressant-like activity evaluation of sulphonamides and sulphonyl-hydrazones. *Bioorgan Med Chem* **2011,** *19* (14), 4295-4306.

(104) Goddard-Borger, E. D.; Stick, R. V., An efficient, inexpensive, and shelf-stable diazotransfer reagent: Imidazole-1-sulfonyl azide hydrochloride. *Organic Letters* **2007,** *9* (19), 3797-3800.

(105) Strauss, J. H.; Kelly, R. B.; Sinsheimer, R. L., Denaturation of Rna with Dimethyl Sulfoxide. *Biopolymers* **1968,** *6* (6), 793-+.

(106) El-Sagheer, A. H.; Brown, T., New strategy for the synthesis of chemically modified RNA constructs exemplified by hairpin and hammerhead ribozymes. *Proc Natl Acad Sci U S A* **2010,** *107* (35), 15329-34.

(107) Jao, C. Y.; Salic, A., Exploring RNA transcription and turnover in vivo by using click chemistry. *Proc Natl Acad Sci U S A* **2008,** *105* (41), 15779-84.

(108) Paredes, E.; Das, S. R., Click chemistry for rapid labeling and ligation of RNA. *Chembiochem* **2011,** *12* (1), 125-31.

(109) Ingale, S. A.; Mei, H.; Leonard, P.; Seela, F., Ethynyl side chain hydration during synthesis and workup of "clickable" oligonucleotides: bypassing acetyl group formation by triisopropylsilyl protection. *J Org Chem* **2013,** *78* (22), 11271-82.

(110) Sosnovsky, G.; Konieczny, M., Preparation of 4-Phosphorylated 1,4-Dihydroxy-2,2,6,6-Tetramethylpiperidines by Reduction of Nitroxyls with L-Ascorbic-Acid. *Synthesis-Stuttgart* **1977,** (9), 619-622.

(111) Paleos, C. M.; Litsas, S. B., Reduction of Some Nitroxide Free-Radicals by Tert-Butylhydroquinones and Di-Tert-Butylhydroquinones. *Chem Scripta* **1977,** *12* (4-5), 125-127.

(112) Kinoshita, Y.; Yamada, K.; Yamasaki, T.; Sadasue, H.; Sakai, K.; Utsumi, H., Development of novel nitroxyl radicals for controlling reactivity with ascorbic acid. *Free Radic Res* **2009,** *43* (6), 565-71.

(113) Biaglow, J. E.; Manevich, Y.; Uckun, F.; Held, K. D., Quantitation of hydroxyl radicals produced by radiation and copper-linked oxidation of ascorbate by 2-deoxy-D-ribose method. *Free Radic Biol Med* **1997,** *22* (7), 1129-38.

(114) Tabbi, G.; Fry, S. C.; Bonomo, R. P., ESR study of the non-enzymic scission of xyloglucan by an ascorbate-H2O2-copper system: the involvement of the hydroxyl radical and the degradation of ascorbate. *J Inorg Biochem* **2001,** *84* (3-4), 179-87.

(115) Zepp, R. G.; Faust, B. C.; Hoigne, J., Hydroxyl Radical Formation in Aqueous Reactions (Ph 3-8) of Iron(Ii) with Hydrogen-Peroxide - the Photo-Fenton Reaction. *Environ Sci Technol* **1992,** *26* (2), 313-319.

(116) Seela, F.; Zulauf, M., Palladium-catalyzed cross coupling of 7-iodo-2'-deoxytubercidin with terminal alkynes. *Synthesis-Stuttgart* **1996,** (6), 726-&.

(117) Munzel, M.; Globisch, D.; Trindler, C.; Carell, T., Efficient synthesis of 5-hydroxymethylcytosine containing DNA. *Org Lett* **2010,** *12* (24), 5671-3.

(118) Andersen, N. K.; Dossing, H.; Jensen, F.; Vester, B.; Nielsen, P., Duplex and Triplex Formation of Mixed Pyrimidine Oligonucleotides with Stacking of Phenyl-triazole Moieties in the Major Groove. *Journal of Organic Chemistry* **2011,** *76* (15), 6177-6187.

(119) Barhate, N.; Cekan, P.; Massey, A. P.; Sigurdsson, S. T., A nucleoside that contains a rigid nitroxide spin label: a fluorophore in disguise. *Angew Chem Int Ed Engl* **2007,** *46* (15), 2655-8.

(120) Asakura, J.; Robins, M. J., Cerium(Iv)-Mediated Halogenation at C-5 of Uracil Derivatives. *Journal of Organic Chemistry* **1990,** *55* (16), 4928-4933.

(121) Gannett, P. M.; Darian, E.; Powell, J.; Johnson, E. M.; Mundoma, C.; Greenbaum, N. L.; Ramsey, C. M.; Dalal, N. S.; Budil, D. E., Probing triplex formation by EPR spectroscopy using a newly synthesized spin label for oligonucleotides. *Nucleic Acids Research* **2002,** *30* (23), 5328-5337.

(122) Steely, H. T., Jr.; Gray, D. M.; Lang, D.; Maestre, M. F., Circular dichroism of double-stranded RNA in the presence of salt and ethanol. *Biopolymers* **1986,** *25* (1), 91-117.

(123) Sabahi, A.; Guidry, J.; Inamati, G. B.; Manoharan, M.; Wittung-Stafshede, P., Hybridization of 2 '-ribose modified mixed-sequence oligonucleotides: thermodynamic and kinetic studies. *Nucleic Acids Research* **2001,** *29* (10), 2163-2170.

(124) Egli, M.; Pallan, P. S., Insights from crystallographic studies into the structural and pairing properties of nucleic acid analogs and chemically modified DNA and RNA oligonucleotides. *Annu Rev Bioph Biom* **2007,** *36*, 281-305.

(125) Freier, S. M.; Altmann, K. H., The ups and downs of nucleic acid duplex stability: structure-stability studies on chemically-modified DNA:RNA duplexes. *Nucleic Acids Research* **1997,** *25* (22), 4429-4443.

(126) SantaLucia, J.; Allawi, H. T.; Seneviratne, A., Improved nearest-neighbor parameters for predicting DNA duplex stability. *Biochemistry* **1996,** *35* (11), 3555-3562.

(127) Yakovchuk, P.; Protozanova, E.; Frank-Kamenetskii, M. D., Base-stacking and base-pairing contributions into thermal stability of the DNA double helix (vol 34, pg 564, 2006). *Nucleic Acids Research* **2006,** *34* (3), 1082-+.

(128) Lopez, C. J.; Yang, Z. Y.; Altenbach, C.; Hubbell, W. L., Conformational selection and adaptation to ligand binding in T4 lysozyme cavity mutants. *P Natl Acad Sci USA* **2013,** *110* (46), E4306-E4315.

(129) Tan, Z. J.; Chen, S. J., Nucleic acid helix stability: Effects of salt concentration, cation valence and size, and chain length. *Biophys J* **2006,** *90* (4), 1175-1190.

(130) Tkach, I.; Pornsuwan, S.; Hobartner, C.; Wachowius, F.; Sigurdsson, S. T.; Baranova, T. Y.; Diederichsen, U.; Sicoli, G.; Bennati, M., Orientation selection in distance measurements between nitroxide spin labels at 94 GHz EPR with variable dual frequency irradiation. *Phys Chem Chem Phys* **2013,** *15* (10), 3433-3437.

(131) Marko, A.; Denysenkov, V.; Margraft, D.; Cekan, P.; Schiemann, O.; Sigurdsson, S. T.; Prisner, T. F., Conformational Flexibility of DNA. *J Am Chem Soc* **2011,** *133* (34), 13375-13379.

(132) Prisner, T. F.; Marko, A.; Sigurdsson, S. T., Conformational dynamics of nucleic acid molecules studied by PELDOR spectroscopy with rigid spin labels. *J Magn Reson* **2015,** *252*, 187-198.

(133) Kerzhner, M.; Abdullin, D.; Wiecek, J.; Matsuoka, H.; Hagelueken, G.; Schiemann, O.; Famulok, M., Post-synthetic Spin-Labeling of RNA through Click Chemistry for PELDOR Measurements. *Chem-Eur J* **2016,** *22* (34), 12113-12121.

(134) Kocalka, P.; Andersen, N. K.; Jensen, F.; Nielsen, P., Synthesis of 5-(1,2,3-triazol-4-yl)-2'deoxyuridines by a click chemistry approach: Stacking of triazoles in the major groove gives increased nucleic acid duplex stability. *Chembiochem* **2007,** *8* (17), 2106-2116.

(135) Lu, X. J.; Olson, W. K., 3DNA: a software package for the analysis, rebuilding and visualization of three-dimensional nucleic acid structures. *Nucleic Acids Research* **2003,** *31* (17), 5108-5121.

(136) Hagelueken, G.; Ward, R.; Naismith, J. H.; Schiemann, O., MtsslWizard: In Silico Spin-Labeling and Generation of Distance Distributions in PyMOL. *Appl Magn Reson* **2012,** *42* (3), 377-391.

(137) Hagelueken, G.; Abdullin, D.; Ward, R.; Schiemann, O., mtsslSuite: In silico spin labelling, trilateration and distance-constrained rigid body docking in PyMOL. *Mol Phys* **2013,** *111* (18-19), 2757-2766.

(138) Hagelueken, G.; Abdullin, D.; Schiemann, O., mtsslSuite: Probing Biomolecular Conformation by Spin-Labeling Studies. *Method Enzymol* **2015,** *563*, 595-622.

(139) Adamiak, D. A.; Milecki, J.; Popenda, M.; Adamiak, R. W.; Dauter, Z.; Rypniewski, W. R., Crystal structure of 2'-O-Me(CGCGCG)(2), an RNA duplex at 1.30 angstrom resolution. Hydration pattern of 2'-O-methylated RNA. *Nucleic Acids Research* **1997,** *25* (22), 4599-4607.

(140) Rieder, U.; Lang, K.; Kreutz, C.; Polacek, N.; Micura, R., Evidence for Pseudoknot Formation of Class I preQ(1) Riboswitch Aptamers. *Chembiochem* **2009,** *10* (7), 1141-1144.

(141) Roth, A.; Winkler, W. C.; Regulski, E. E.; Lee, B. W. K.; Lim, J.; Jona, I.; Barrick, J. E.; Ritwik, A.; Kim, J. N.; Welz, R.; Iwata-Reuyl, D.; Breaker, R. R., A riboswitch selective for the queuosine precursor preQ(1) contains an unusually small aptamer domain. *Nat Struct Mol Biol* **2007,** *14* (4), 308-317.

(142) Santner, T.; Rieder, U.; Kreutz, C.; Micura, R., Pseudoknot Preorganization of the PreQ(1) Class I Riboswitch. *J Am Chem Soc* **2012,** *134* (29), 11928-11931.

(1439 Rieder, U.; Kreutz, C.; Micura, R., Folding of a transcriptionally acting PreQ(1) riboswitch. *P Natl Acad Sci USA* **2010,** *107* (24), 10804-10809.

(144) Resendiz, M. J.; Schon, A.; Freire, E.; Greenberg, M. M., Photochemical control of RNA structure by disrupting pi-stacking. *J Am Chem Soc* **2012,** *134* (30), 12478-81.

(145) Stoll, S.; Schweiger, A., EasySpin, a comprehensive software package for spectral simulation and analysis in EPR. *J Magn Reson* **2006,** *178* (1), 42-55.

(146) Suddala, K. C.; Rinaldi, A. J.; Feng, J.; Mustoe, A. M.; Eichhorn, C. D.; Liberman, J. A.; Wedekind, J. E.; Al-Hashimi, H. M.; Brooks, C. L.; Walter, N. G., Single transcriptional and translational preQ(1) riboswitches adopt similar pre-folded ensembles that follow distinct folding pathways into the same ligand-bound structure. *Nucleic Acids Research* **2013,** *41* (22), 10462-10475.

(147) Suddala, K. C.; Wang, J. R.; Hou, Q.; Water, N. G., Mg2+ Shifts Ligand-Mediated Folding of a Riboswitch from Induced-Fit to Conformational Selection. *J Am Chem Soc* **2015,** *137* (44), 14075-14083.

(148) Jenkins, J. L.; Krucinska, J.; McCarty, R. M.; Bandarian, V.; Wedekind, J. E., Comparison of a preQ1 riboswitch aptamer in metabolite-bound and free states with implications for gene regulation. *J Biol Chem* **2011,** *286* (28), 24626-37.

(149) Haller, A.; Altman, R. B.; Souliere, M. F.; Blanchard, S. C.; Micura, R., Folding and ligand recognition of the TPP riboswitch aptamer at single-molecule resolution. *P Natl Acad Sci USA* **2013,** *110* (11), 4188-4193.

(150) Lang, K.; Rieder, R.; Micura, R., Ligand-induced folding of the thiM TPP riboswitch investigated by a structure-based fluorescence spectroscopic approach. *Nucleic Acids Research* **2007,** *35* (16), 5370-5378.

(151) Warner, K. D.; Homan, P.; Weeks, K. M.; Smith, A. G.; Abell, C.; Ferre-D'Amare, A. R., Validating fragment-based drug discovery for biological RNAs: lead fragments bind and remodel the TPP riboswitch specifically. *Chem Biol* **2014,** *21* (5), 591-5.

(152) Rentmeister, A.; Mayer, G.; Kuhn, N.; Famulok, M., Conformational changes in the expression domain of the Escherichia coli thiM riboswitch. *Nucleic Acids Research* **2007,** *35* (11), 3713-3722.

(153) Milligan, J. F.; Uhlenbeck, O. C., Synthesis of small RNAs using T7 RNA polymerase. *Methods Enzymol* **1989,** *180*, 51-62.

(154) Birikh, K. R.; Heaton, P. A.; Eckstein, F., The structure, function and application of the hammerhead ribozyme. *Eur J Biochem* **1997,** *245* (1), 1-16.

(155) ClouetdOrval, B.; Uhlenbeck, O. C., Hammerhead ribozymes with a faster cleavage rate. *Biochemistry* **1997,** *36* (30), 9087-9092.

(156) Stage-Zimmermann, T. K.; Uhlenbeck, O. C., Hammerhead ribozyme kinetics. *Rna* **1998,** *4* (8), 875-889.

(157) Kathirvelu, V.; Smith, C.; Parks, C.; Mannan, M. A.; Miura, Y.; Takeshita, K.; Eaton, S. S.; Eaton, G. R., Relaxation rates for spirocyclohexyl nitroxyl radicals are suitable for interspin distance measurements at temperatures up to about 125 K. *Chem Commun* **2009,** (4), 454-456.

(158) Kirilyuk, I. A.; Polienko, Y. F.; Krumkacheva, O. A.; Strizhakov, R. K.; Gatilov, Y. V.; Grigor'ev, I. A.; Bagryanskaya, E. G., Synthesis of 2,5-Bis(spirocyclohexane)-Substituted Nitroxides of Pyrroline and Pyrrolidine Series, Including Thiol-Specific Spin Label: An Analogue of MTSSL with Long Relaxation Time. *Journal of Organic Chemistry* **2012,** *77* (18), 8016-8027.

(159) Fulmer, G. R.; Miller, A. J. M.; Sherden, N. H.; Gottlieb, H. E.; Nudelman, A.; Stoltz, B. M.; Bercaw, J. E.; Goldberg, K. I., NMR Chemical Shifts of Trace Impurities: Common Laboratory Solvents, Organics, and Gases in Deuterated Solvents Relevant to the Organometallic Chemist. *Organometallics* **2010,** *29* (9), 2176-2179.

160. Bradley, D.; Williams, G.; Lawton, M., Drying of Organic Solvents: Quantitative Evaluation of the Efficiency of Several Desiccants. *Journal of Organic Chemistry* **2010,** *75* (24), 8351-8354.

(161) Sun, Y. W.; Chen, K. M.; Kwon, C. H., Sulfonyl-containing nucleoside phosphotriesters and phosphoramidates as novel anticancer prodrugs of 5-fluoro-2'-deoxyuridine 5'-monophosphate (FdUMP). *Mol Pharm* **2006,** *3* (2), 161-73.

(162) Hill, J. G.; Rossiter, B. E.; Sharpless, K. B., Anhydrous Tert-Butyl Hydroperoxide in Toluene - the Preferred Reagent for Applications Requiring Dry Tbhp. *Journal of Organic Chemistry* **1983,** *48* (20), 3607-3608.

(163) Budil, D. E.; Lee, S.; Saxena, S.; Freed, J. H., Nonlinear-least-squares analysis of slow-motion EPR spectra in one and two dimensions using a modified Levenberg-Marquardt algorithm. *J Magn Reson Ser A* **1996,** *120* (2), 155-189.

(164) Jeschke, G.; Chechik, V.; Ionita, P.; Godt, A.; Zimmermann, H.; Banham, J.; Timmel, C. R.; Hilger, D.; Jung, H., DeerAnalysis2006 - a comprehensive software package for analyzing pulsed ELDOR data. *Appl Magn Reson* **2006,** *30* (3-4), 473-498.

165. Neese, F., The ORCA program system. *wires computational molecular science* **2012,** (2), 73-78.